IRE Transactions

on Microwave Theory and Techniques

Volume MTT-9 **MARCH, 1961** Number 2

Published Bimonthly

In This Issue

PUBLISHED BY THE
Professional Group on Microwave Theory and Techniques

IRE PROFESSIONAL GROUP ON MICROWAVE THEORY AND TECHNIQUES

The Professional Group on Microwave Theory and Techniques is an association of IRE members with professional interest in the field of Microwave Theory and Techniques. All IRE members are eligible for membership and will receive all Group publications upon payment of the prescribed annual fee of $3.00. Members of the American Physical Society and the Institution of Electrical Engineers of Great Britain may become affiliated with PGMTT and receive all Group publications upon payment of the Affiliate fee of $7.50 per year.

IRE TRANSACTIONS®
on Microwave Theory and Techniques

Published by The Institute of Radio Engineers, Inc., for the Professional Group on Microwave Theory and Techniques, at 1 East 79 Street, New York 21, N.Y. Responsibility for the contents rests upon the authors, and not upon the IRE, the Group, or its members. Individual copies of this issue and all available back issues may be purchased at the following prices: IRE members (one copy) $2.25, libraries and colleges $3.25, all others $4.50. Annual subscription price: non-members, $17.00; colleges and public libraries, $12.75.

Address all manuscripts to Donald D. King, PGMTT Editor, Electronic Communications, Inc., 1830 York Road, Timonium, Md. Submission of three copies of manuscripts, including figures, will expedite the review.

IRE Transactions on Microwave Theory and Techniques

Volume MTT-9 MARCH, 1961 Number 2
Published Bimonthly

TABLE OF CONTENTS

CONTRIBUTIONS

CORRESPONDENCE

Dynamic Interaction Fields in a Two-Dimensional Lattice*

R. E. COLLIN†, MEMBER, IRE, AND W. H. EGGIMANN†

Summary—In the theory of artificial dielectrics and aperture coupling in rectangular waveguides, a knowledge of the dynamic interaction fields is required in order to evaluate the polarizing fields. This paper presents suitable methods for evaluating the dynamic interaction fields in a two-dimensional lattice. Both electric and magnetic dipoles are considered. The results are presented in closed form apart from correction terms involving rapidly converging series. Cross-polarization interaction constants are also evaluated.

Introduction

TWO-DIMENSIONAL periodic lattice structures are encountered in the field of artificial dielectric media, aperture coupling in rectangular waveguides, and elsewhere. Fig. 1(a) illustrates a disk-type artificial dielectric. Each plane array of disks may be represented as an equivalent shunt susceptance B which loads a transmission line periodically along the z direction. Fig. 1(b) illustrates an aperture in a transverse wall in a rectangular guide, together with the images of the aperture in the guide walls. The shunt susceptance of planar arrays of the above type disks or apertures is usually determined by using the small aperture theory of Bethe (or its dual for the obstacle problem).[1] In this theory, each obstacle or aperture is replaced by an equivalent set of electric and magnetic dipoles, with moments given by the product of the incident field and a suitable polarizability constant which is dependent on the obstacle geometry only.[2] A limitation of the simple theory is that the obstacle size must be small and the spacing must be large, so that interaction between neighboring elements can be neglected.

In practice, it is usually desirable to employ such element spacings that the mutual interaction cannot be neglected. In such cases, the effective polarizing fields are the sum of the incident field and the field radiated by the induced dipoles in all the neighboring elements. For sufficiently small element spacing, the interaction field may be approximated by a static field. The evaluation of the interaction constant for a static interaction field has been carried out by Brown.[3] In this paper, suitable methods for evaluating the dynamic interaction field in closed form will be presented, and a restricted problem will be analyzed in detail. However, it should be noted that the methods of summing the series involved may be applied without difficulty to a general two-dimensional lattice with a field incident at any arbitrary angle.

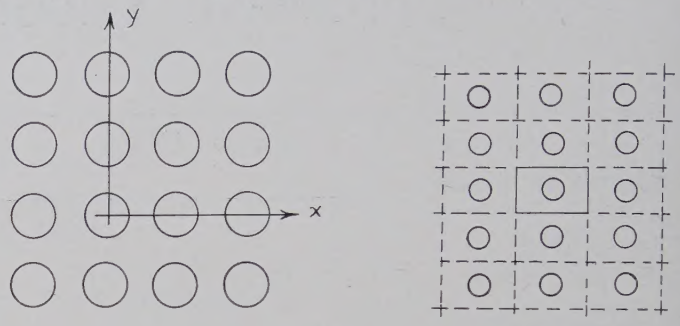

Fig. 1—Periodic arrays of similar elements.

An Array of Circular Disks

Fig. 2 illustrates a two-dimensional array of circular conducting disks such as is encountered in the field of artificial dielectric media. The spacing between disks is a along the x axis and b along the y axis. A perpendicular polarized TEM wave is assumed incident at an angle θ_i, relative to the z axis, in the xz plane. The incident field is

$$E_{\text{inc}} = E_y = e^{-jhx-\Gamma_0 z}, \tag{1a}$$

$$H_{\text{inc}} = H_z = \frac{h}{k_0} Y_0 E_{\text{inc}}, \tag{1b}$$

where $h = k_0 \sin \theta_i$, $\Gamma_0 = jk_0 \cos \theta_i$, $Y_0 = (\epsilon_0/\mu_0)^{1/2}$. In (1) the x component of the magnetic field has not been written down. This incident field induces y-directed electric dipoles of moment P in each disk, as well as z-directed magnetic dipoles of moment M in each disk. In view of the nature of the incident field, the induced moment in the disk at $x = ma$ has a phase e^{-jhma} relative to the dipole located at $x = 0$. The effective fields acting to polarize each disk are the sum of the incident fields plus the interaction field due to the fields radiated (scattered) by all of the neighboring disks. The interaction fields are proportional to the dipole strengths, and hence also proportional to the amplitude of the incident field.

The y-directed dipole moment P of each neighboring disk produces a y-directed electric interaction field E_{ie}

* Received by the PGMTT, October 8, 1960. The work reported in this paper was sponsored by AF Cambridge Res. Ctr. under contract AF 19(604)3887 and is based on Sci. Rept. No. 12 issued under this contract.

† Case Inst. Tech., Cleveland, Ohio.

[1] H. A. Bethe, "Theory of diffraction by small holes," *Phys. Rev.*, vol. 66, pp. 163–182; February, 1944.

[2] A. A. Oliner, "Equivalent circuits for small symmetrical longitudinal apertures and obstacles," IRE TRANS. ON MICROWAVE THEORY AND TECHNIQUES, vol. MTT-8, pp. 72–80; January, 1960.

[3] J. Brown and W. Jackson, "The relative permittivity of tetragonal arrays of perfectly conducting thin disks," *Proc. IEE*, vol. 102, Pt. B, pp. 37–42; January, 1955.

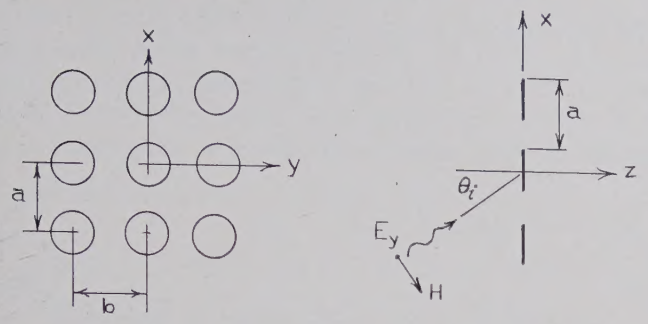

Fig. 2—Two-dimensional array of circular disks.

and a z-directed magnetic interaction field H_{ie} at the center of the disk, at the origin. Similarly, a z-directed magnetic dipole M in each neighboring disk produces a z-directed magnetic interaction field H_{im} and a y-directed electric interaction field E_{im} at the center of the disk at the origin. In addition, x- and y-directed magnetic interaction fields and x- and z-directed electric interaction fields are produced in general. This results in additional dipole moments in each obstacle. These cross-polarized dipole moments are small, however, since they are produced by the interaction fields only and do not have a contribution from the incident field. In most practical cases, these additional dipole moments may be neglected. The fact that they are present to some extent shows that even an array of isotropic particles in a cubical lattice structure will have anisotropic properties (structural anisotropy).[4]

In view of the linear relationship between the quantities involved, it is possible to write

$$E_i = E_{ie} + E_{im} = C_{ee}\frac{P}{\epsilon_0} + C_{em}Z_0M, \tag{2a}$$

$$H_i = H_{ie} + H_{im} = C_{me}Y_0\frac{P}{\epsilon_0} + C_{mm}M, \tag{2b}$$

where the interaction constants C_{ee}, C_{em}, C_{me} and C_{mm} are constants defined by these equations. The intrinsic impedance $Z_0=(\mu_0/\epsilon_0)^{1/2}$ and its reciprocal Y_0 is introduced in order to make C_{em} and C_{me} have the dimensions of meters^{-3}. The total y-directed electric interaction field is E_i, while H_i is the total z-directed magnetic interaction field. The effective field acting to polarize each disk is the sum of the incident field plus the total interaction field.

The electric dipole moment induced in the disk in the y direction is given by

$$\begin{aligned} P &= \alpha_e\epsilon_0[E_{\text{inc}} + E_{ie} + E_{im}] \\ &= \alpha_e\epsilon_0E_{\text{inc}} + \alpha_eC_{ee}P + \alpha_eC_{em}(\mu_0\epsilon_0)^{1/2}M. \end{aligned} \tag{4a}$$

Similarly, the magnetic dipole moment induced in the z direction is found to be

$$M = \alpha_mH_{\text{inc}} + \alpha_mC_{mm}M + \alpha_mC_{me}(\mu_0\epsilon_0)^{-1/2}P, \tag{4b}$$

where α_e and α_m are the electric and magnetic polarizabilities of the disk, respectively. Solving for P and M gives

$$P = \frac{(1-\alpha_mC_{mm})\alpha_e\epsilon_0E_{\text{inc}} + \alpha_e\alpha_m\epsilon_0C_{em}Z_0H_{\text{inc}}}{(1-\alpha_eC_{ee})(1-\alpha_mC_{mm}) - \alpha_e\alpha_mC_{em}C_{me}}, \tag{5a}$$

$$M = \frac{(1-\alpha_eC_{ee})\alpha_mH_{\text{inc}} + \alpha_e\alpha_mC_{me}Y_0E_{\text{inc}}}{(1-\alpha_eC_{ee})(1-\alpha_mC_{mm}) - \alpha_e\alpha_mC_{em}C_{me}}. \tag{5b}$$

In practice, the terms α_eC_{em}, α_mC_{me}, and $\alpha_e\alpha_m$ are small so that (5a) and (5b) reduce approximately to the more familiar expressions

$$P = \frac{\alpha_e\epsilon_0E_{\text{inc}}}{1-\alpha_eC_{ee}}, \tag{6a}$$

$$M = \frac{\alpha_mH_{\text{inc}}}{1-\alpha_mC_{mm}}. \tag{6b}$$

These results are equivalent to a neglect of the interaction between the electric and magnetic dipoles. The analysis to follow will give expressions for the interaction constants C_{ee}, C_{em}, C_{me} and C_{mm} [see (28), (31), and (40)].

Derivation of Interaction Constants

Consider an infinite two-dimensional array of magnetic dipoles Ma_z with a relative phase e^{-jhma} along the x axis. From symmetry considerations, the scattered field is such that conducting planes can be inserted into the lattice at $y=\pm b/2$ as in Fig. 2.

The field scattered by a single z-directed magnetic dipole, located at the origin, will be determined first. This field may be found from a magnetic Hertzian potential Π_z' as follows:

$$\boldsymbol{E} = -j\omega\mu_0\nabla \times \boldsymbol{a}_z\Pi_z', \tag{7a}$$

$$\boldsymbol{H} = k_0^2\Pi_z'\boldsymbol{a}_z + \nabla\nabla\cdot\boldsymbol{a}_z\Pi_z', \tag{7b}$$

where

$$\nabla^2\Pi_z' + k_0^2\Pi_z' = -M\delta(x)\delta(y)\delta(z), \tag{8}$$

and $\delta(x)$, etc., is the unit impulse function. Since E_z must vanish at $y=\pm b/2$, a suitable form for Π_z' is

$$\Pi_z' = \sum_{n=0}^{\infty} f_n(r)\cos 2n\pi y/b, \tag{9}$$

where $f_n(r)$ is a suitable function of $r=(x^2+z^2)^{1/2}$ to be determined. Substituting (9) into (8), multiplying both sides by $\cos 2n\pi y/b$, and integrating over $-b/2\leq y\leq b/2$ gives

$$\frac{1}{r}\frac{\partial}{\partial r}r\frac{\partial f_n}{\partial r} + \left[k_0^2 - \left(\frac{2n\pi}{b}\right)^2\right]f_n = -\frac{\epsilon_{0n}}{b}M\delta(r), \tag{10}$$

where $\delta(r)=\delta(x)\delta(z)$ and $\epsilon_{0n}=1$; $n=0$ and $\epsilon_{0n}=2$ for $n>0$. The solution to (10) which is bounded as $r\to\infty$ is

[4] Z. A. Kaprielian, "Anisotropic effects in geometrically isotropic lattices," *J. Appl. Phys.*, vol. 29, pp. 1052–1063; July, 1958.

$f_n(r) = a_n K_0(\gamma_n r)$ where K_0 is the modified Bessel function of the second kind, and $\gamma_n^2 = (2n\pi/b)^2 - k_0^2$. As $r \to 0$ the solution must have a logarithmic singularity of strength $-\epsilon_{0n} M/2\pi b \ln r$ and since $K_0(\gamma_n r) \to -\ln r$ as $r \to 0$ the coefficient a_n is given by

$$a_n = \frac{\epsilon_{0n} M}{2\pi b}. \tag{11}$$

Hence, the potential due to a single dipole is

$$\Pi_z' = \frac{M}{2\pi b}\left[K_0(jk_0 r) + 2\sum_{n=1}^{\infty} K_0(\gamma_n r)\cos 2n\pi y/b\right], \tag{12}$$

since $\gamma_0 = jk_0$. The Bessel function K_0 with imaginary argument is proportional to the Hankel function $H_0^2(k_0 r)$.

For dipoles at $x = ma$, $m = \pm 1, \pm 2, \cdots$, and having a relative phase $\exp(-jhma)$, the required potential is readily obtained by using (12) and is

$$\Pi_{z1} = \frac{M}{2\pi b}\left[\sum_{m=-\infty}^{\infty}{}' e^{-jhma} K_0(jk_0\sqrt{z^2 + (ma - x)^2}) \right. \tag{13}$$

$$\left. + 2\sum_{m=-\infty}^{\infty}{}' \sum_{n=1}^{\infty} e^{-jhma}\cos(2n\pi y/b) K_0(\gamma_n\sqrt{z^2 + (ma - x)^2})\right].$$

The prime means omission of the term $m = 0$. The double series converges very rapidly, since b is limited to be less than a half wavelength; hence, γ_n is real for $n > 0$ and K_0 decays rapidly. The single series will be transformed to a more rapidly converging form by an application of the Poisson summation formula.

Consider the series

$$\sum_{m=-\infty}^{\infty} S_0(ma) = \sum_{m=-\infty}^{\infty} K_0(jk_0\sqrt{z^2 + (ma)^2}). \tag{14}$$

To apply the Poisson summation formula, the following Fourier transform is required

$$\int_{-\infty}^{\infty} e^{-jwu} K_0(jk_0\sqrt{z^2 + u^2})\,du$$

$$= \pi \frac{\exp - |z|\sqrt{w^2 - k_0^2}}{\sqrt{w^2 - k_0^2}}. \tag{15}$$

According to the Poisson summation formula

$$\sum_{m=-\infty}^{\infty} S_0(ma) = \frac{1}{a}\sum_{m=-\infty}^{\infty} g(2m\pi/a), \tag{16}$$

where $g(w)$ is the Fourier transform of $S_0(u)$. Thus, (14) becomes

$$\sum_{m=-\infty}^{\infty} K_0(jk_0\sqrt{z^2 + (ma)^2})$$

$$= \frac{\pi}{a}\sum_{m=-\infty}^{\infty} \frac{\exp - |z|\sqrt{(2m\pi/a)^2 - k_0^2}}{\sqrt{(2m\pi/a)^2 - k_0^2}}. \tag{17}$$

Multiplying each term in (14) by e^{-jhma} replaces $(2m\pi/a)$ by $(2m\pi/a) + h$ in the transformed series. Replacing (ma) in (14) by $(ma - x)$ is equivalent to multiplying each term in the transformed series by $e^{-j2m\pi x/a}$. With the aid of these operational formulas, it is found that

$$\sum_{m=-\infty}^{\infty} e^{-jhma} K_0[jk_0\sqrt{z^2 + (ma - x)^2}]$$

$$= e^{-jhx}\sum_{m=-\infty}^{\infty} e^{-jh(ma-x)} K_0[jk_0\sqrt{z^2 + (ma - x)^2}]$$

$$= e^{-jhx}\frac{\pi}{a}\sum_{m=-\infty}^{\infty} \frac{e^{-\Gamma_m|z| - j2m\pi x/a}}{\Gamma_m}, \tag{18}$$

where

$$\Gamma_m^2 = [(2m\pi/a) + h]^2 - k_0^2.$$

The potential arising from dipoles at $x = ma$; $m = \pm 1, \pm 2, \cdots$, may now be expressed as

$$\Pi_{z1} = \frac{M}{2\pi b}\left[\frac{\pi}{a}\sum_{m=-\infty}^{\infty} \frac{e^{-\Gamma_m|z|}e^{-j(h+2m\pi/a)x}}{\Gamma_m}\right.$$

$$- K_0(jk_0\sqrt{x^2 + z^2}) + 2\sum_{m=-\infty}^{\infty}{}' \sum_{n=1}^{\infty} e^{-jhma}$$

$$\left. \cdot \cos(2n\pi y/b) K_0(\gamma_n\sqrt{z^2 + (ma - x)^2})\right]. \tag{19}$$

To obtain the potential due to all the dipoles in the lattice, except the dipole at the origin, the potential from dipoles located at $y = \pm mb$; $m = 1, 2, \cdots$; $x = z = 0$ must be added to (19). These dipoles are the images of the dipole at the origin, and the partial potential contributed by these is

$$\Pi_{z2} = \frac{M}{4\pi}\sum_{m=-\infty}^{\infty}{}' \frac{\exp - jk_0\sqrt{x^2 + z^2 + (mb - y)^2}}{\sqrt{x^2 + z^2 + (mb - y)^2}}. \tag{20}$$

Consider next the field scattered from y-directed electric dipoles of moment P and having a relative phase e^{-jhma}. The scattered field may be obtained from a vector potential A_y' with a single y component by means of the equations

$$\boldsymbol{E} = (j\omega\mu_0\epsilon_0)^{-1}(k_0^2 \boldsymbol{a}_y A_y' + \nabla\nabla\cdot \boldsymbol{a}_y A_y'), \tag{21a}$$

$$\boldsymbol{B} = \nabla \times \boldsymbol{a}_y A_y', \tag{21b}$$

and

$$\nabla^2 A_y' + k_0^2 A_y' = -j\omega\mu_0 P\delta(x)\delta(y)\delta(z), \tag{21c}$$

for a single dipole at the origin. The boundary conditions on A_y' are the same as those for Π_z', and (21c) is similar to (8). Therefore, the solution for the total vector potential A_y from all dipoles except the dipole at the origin is the same as the solution for $\Pi_{z1} + \Pi_{z2}$ but with M replaced by $j\omega\mu_0 P$. Thus,

$$A_y = \frac{j\omega\mu_0 P}{2\pi b}\left[\frac{\pi}{a}\sum_{m=-\infty}^{\infty}\frac{e^{-\Gamma_m|z|}e^{-j(h+2m\pi/a)x}}{\Gamma_m} - K_0(jk_0\sqrt{x^2+z^2}) + 2\sum_{m=-\infty}^{\infty}{}'\sum_{n=1}^{\infty} e^{-jhma}\cdot\cos(2n\pi y/b)K_0(\gamma_n\sqrt{z^2+(ma-x)^2})\right]$$

$$+\frac{j\omega\mu_0 P}{4\pi}\left[\sum_{m=-\infty}^{\infty}{}'\frac{\exp -jk_0\sqrt{x^2+z^2+(mb-y)^2}}{\sqrt{x^2+z^2+(mb-y)^2}}\right]. \quad (22)$$

The y-directed interaction field E_{ie} is given by

$$E_{ie} = (j\omega\mu_0\epsilon_0)^{-1}\left(k_0^2 + \frac{\partial^2}{\partial y^2}\right)A_y. \quad (23)$$

Using (22) and carrying out the operations indicated in (23), placing $x=y=0$, and letting z tend to zero, it is found that

$$E_{ie} = \lim_{z\to 0}\frac{k_0^2 P}{2\pi\epsilon_0 b}\left[\frac{\pi}{a}\sum_{m=-\infty}^{\infty}\frac{e^{-\Gamma_m|z|}}{\Gamma_m} - K_0(jk_0|z|)\right] - \frac{2P}{\pi\epsilon_0 b}\sum_{n=1}^{\infty}\sum_{m=1}^{\infty}\cos(hma)\gamma_n^2 K_0(\gamma_n ma) + \frac{P}{4\pi\epsilon_0}\left[4jk_0\sum_{m=1}^{\infty}\frac{e^{-jk_0 mb}}{(mb)^2} + 4\sum_{m=1}^{\infty}\frac{e^{-jk_0 mb}}{(mb)^3}\right]. \quad (24)$$

Now

$$\Gamma_m^{-1} = \frac{a}{2|m|\pi}\left[1 + \frac{ha}{m\pi} - \frac{k_0^2 - h^2}{(2m\pi)^2}a^2\right]^{-1/2} = \frac{a}{2|m|\pi} + 0\left[\frac{1}{m^2}\right]. \quad (25)$$

Thus, the dominant part of the series

$$\frac{\pi}{a}\sum_{m=-\infty}^{\infty}{}'\frac{e^{-\Gamma_m|z|}}{\Gamma_m}$$

is

$$\frac{\pi}{a}\sum_{m=-\infty}^{\infty}{}'\frac{e^{-2|m|\pi|z|/a}}{2|m|\pi/a} = \sum_{m=1}^{\infty}\frac{e^{-2\pi|z|m/a}}{m}.$$

This series is readily summed by standard methods to give[5]

$$\sum_{m=1}^{\infty}\frac{e^{-2\pi m|z|/a}}{m} = -\ln 2\sinh\frac{\pi|z|}{a} + \frac{\pi|z|}{a} \to -\ln 2\pi|z|/a \text{ as } z\to 0. \quad (26)$$

Also,

$$\lim_{z\to 0}K_0(jk_0|z|) = -(\gamma + \ln jk_0|z|/2) = -\gamma - j\pi/2 - \ln k_0|z|/2, \quad (27)$$

[5] R. E. Collin, "Field Theory of Guided Waves," McGraw-Hill Book Co., Inc., New York, N. Y.; 1960. See especially Sec. A-6.

where $\gamma = 0.577$ is Euler's constant. Thus, the logarithmic singularity due to the Bessel function $K_0(jk_0|z|)$ is cancelled by the logarithmic singularity arising from the dominant part of the series, *i.e.* from (26).

In (24), the first series may be written as a dominant series and a rapidly converging series. The series over $(mb)^{-2}$ and $(mb)^{-3}$ are readily summed. After summing these series and making use of (26) and (27), the following final result is obtained:

$$E_{ie} = \frac{k_0^2 P}{2ab\epsilon_0}\left[-\frac{a}{\pi}\left(\ln\frac{4\pi}{k_0 a} - \gamma\right) + j\left(\frac{a}{2} - \frac{1}{\sqrt{k_0^2 - h^2}}\right) + \sum_{m=1}^{\infty}\left(\frac{1}{\Gamma_m} + \frac{1}{\Gamma_{-m}} - \frac{a}{m\pi}\right)\right] - \frac{2P}{\pi b\epsilon_0}\sum_{n=1}^{\infty}\sum_{m=1}^{\infty}\gamma_n^2\cos(hma)K_0(\gamma_n ma) + \frac{P}{\pi\epsilon_0 b^3}\left[1.2 - \frac{k_0^2 b^2}{2}\ln k_0 b + \frac{k_0^2 b^2}{4} + \frac{k_0^4 b^4}{96} - j\left(\frac{\pi}{4}k_0^2 b^2 - \frac{k_0^3 b^3}{6}\right)\right] = C_{ee}\frac{P}{\epsilon_0}. \quad (28)$$

This equation determines the dynamic interaction constant C_{ee}. The double series involving K_0 converges very rapidly.

Determination of the interaction constant C_{me} requires evaluation of the interaction field H_{ie} at the origin. This interaction field is given by

$$H_{ie} = \mu_0^{-1}\frac{\partial A_y}{\partial x} = \frac{j\omega P}{2\pi b}\left[-j\frac{\pi}{a}\sum_{m=-\infty}^{\infty}e^{-\Gamma_m|z|}e^{-j(h+2m\pi/a)x}\frac{h+2m\pi/a}{\Gamma_m} + \frac{jk_0 x}{r}K_1(jk_0 r) + 2\sum_{m=-\infty}^{\infty}{}'\sum_{n=1}^{\infty}\cdot e^{-jhma}\frac{\gamma_n|(ma-x)|}{\sqrt{z^2+(ma-x)^2}}K_1(\gamma_n\sqrt{z^2+(ma-x)^2})\right] + \frac{j\omega P}{4\pi}\sum_{m=-\infty}^{\infty}{}'\left[-jk_0\frac{e^{-jk_0 r_m}}{r_m} - \frac{e^{-jk_0 r_m}}{r_m^2}\right]\frac{x}{r_m}, \quad (29)$$

where $r^2 = x^2+z^2$, $r_m^2 = z^2+x^2+(mb-y)^2$. As x and z tend to zero,

$$H_{ie} = \lim_{z\to 0}\frac{j\omega P}{2\pi b}\left[-j\frac{\pi}{a}\sum_{m=-\infty}^{\infty}e^{-\Gamma_m|z|}\frac{h+2m\pi/a}{\Gamma_m} - 4j\sum_{n=1}^{\infty}\sum_{m=1}^{\infty}\sin(hma)\gamma_n K_1(\gamma_n ma)\right]. \quad (30)$$

Now,

$$\Gamma_m^{-1} = \frac{a}{2|m|\pi}\left(1 - \frac{ha}{2m\pi}\right) + 0\left(\frac{1}{m^3}\right);$$

and hence the dominant part of the first series in (30) is

$$\sum_{m=-\infty}^{\infty}{}' e^{-2|m\pi z|/a}\frac{2m\pi}{a}\left(\frac{a}{2|m|\pi}-\frac{ha^2\,\mathrm{sg}\,m}{(2m\pi)^2}\right)+\sum_{m=-\infty}^{\infty}{}' e^{-2|m\pi z|/a}\frac{ha}{2|m|\pi},$$

while the correction series is

$$\sum_{m=-\infty}^{\infty}\left[\frac{2m\pi}{\Gamma_m a}-\frac{2m\pi}{a}\left(\frac{a}{2|m|\pi}-\frac{ha^2\,\mathrm{sg}\,m}{(2m\pi)^2}\right)\right]+\sum_{m=-\infty}^{\infty}{}'\left[\frac{h}{\Gamma_m}-\frac{ha}{2|m|\pi}\right],$$

where $\mathrm{sg}\,m=1$ for $m>0$ and -1 for $m<0$. The dominant part of the series vanishes, since the terms are odd functions of m. Thus, only the correction series and the double series in (30) contribute, and the final result for H_{ie} is

$$H_{ie}=\frac{\omega P}{2\pi b}\left[-j\frac{\pi}{a}\frac{h}{\sqrt{k_0^2-h^2}}+\frac{\pi}{a}\sum_{m=1}^{\infty}\left(\frac{h+2m\pi/a}{\Gamma_m}+\frac{h-2m\pi/a}{\Gamma_{-m}}\right)+4\sum_{n=1}^{\infty}\sum_{m=1}^{\infty}\gamma_n\sin(hma)K_1(\gamma_n ma)\right]=\frac{C_{me}\omega P}{k_0}. \quad (31)$$

The double series converges very rapidly and only one or two terms is usually required. From (2b) it is seen that $H_{ie}=C_{me}Y_0P/\epsilon_0$ and hence the right hand side of (31) when divided by Y_0P/ϵ_0 gives the interaction constant C_{me}.

The y-directed electric interaction field E_{im} due to the magnetic dipoles may be obtained from (31) by replacing P by $\mu_0 M$. When this is done and (2a) is used, it is found that

$$C_{em}=C_{me}. \quad (32)$$

As a final step, the interaction constant C_{mm} must be found. The interaction field H_{im} is given by

$$H_{im}=\left(k_0^2+\frac{\partial^2}{\partial z^2}\right)\Pi_z,\quad x=y=z=0, \quad (33)$$

where $\Pi_z=\Pi_{z1}+\Pi_{z2}$ and Π_{z1} is given by (19) and Π_{z2} by (20). The second term in (33) gives

$$\left.\frac{\partial^2\Pi_z}{\partial z^2}\right|_0=\lim_{z\to 0}\frac{M}{2\pi b}\left[\frac{\pi}{a}\sum_{m=-\infty}^{\infty}\Gamma_m e^{-\Gamma_m|z|}+k_0^2\left(K_0(jk_0|z|)+\frac{K_1(jk_0|z|)}{jk_0|z|}\right)\right]-\frac{M}{\pi b}\sum_{n=1}^{\infty}\sum_{m=-\infty}^{\infty}{}'\frac{\gamma_n}{|m|a}e^{-jhma}K_1(\gamma_n ma)-\frac{M}{2\pi}\sum_{m=1}^{\infty}\left[\frac{jk_0e^{-jk_0mb}}{(mb)^2}+\frac{e^{-jk_0mb}}{(mb)^3}\right]. \quad (34)$$

In order to evaluate the limiting value of this expression, the dominant part of the first series must be found first. Since

$$\Gamma_m=\frac{2|m|\pi}{a}+h\,\mathrm{sg}\,m-\frac{k_0^2a}{4|m|\pi}+0\left(\frac{1}{m^2}\right),$$

the series

$$\frac{\pi}{a}\sum_{m=-\infty}^{\infty}{}'\Gamma_m e^{-\Gamma_m z}$$

may be written as a dominant series,

$$\frac{\pi}{a}\sum_{m=-\infty}^{\infty}{}' e^{-2|mz|\pi/a}\left[\frac{2|m|\pi}{a}+h\,\mathrm{sg}\,m-\frac{k_0^2a}{4|m|\pi}\right],$$

plus a correction series

$$\frac{\pi}{a}\Gamma_0+\frac{\pi}{a}\sum_{m=-\infty}^{\infty}{}'\left[\Gamma_m-\frac{2|m|\pi}{a}-h\,\mathrm{sg}\,m+\frac{k_0^2a}{4|m|\pi}\right]=j\frac{\pi}{a}\sqrt{k_0^2-h^2}+\frac{\pi}{a}\sum_{m=1}^{\infty}\left[\Gamma_m+\Gamma_{-m}-\frac{4m\pi}{a}+\frac{k_0^2a}{2m\pi}\right]. \quad (35)$$

The dominant part of the series sums to

$$\left(\frac{2\pi}{a}\right)^2\sum_{m=1}^{\infty}me^{-2m\pi|z|/a}-\frac{k_0^2}{2}\sum_{m=1}^{\infty}\frac{e^{-2m\pi|z|/a}}{m}=\left(\frac{2\pi}{a}\right)^2\frac{1}{4\sinh^2\pi|z|/a}+\frac{k_0^2}{2}\left[\ln 2\sinh\frac{\pi|z|}{a}-\frac{\pi|z|}{a}\right]\to\frac{1}{|z|^2}-\frac{\pi^2}{3a^2}+\frac{k_0^2}{2}\ln 2\pi|z|/a, \quad (36)$$

since

$$(\sinh^2\pi|z|/a)^{-1}\to\frac{a^2}{\pi^2|z|^2}-\frac{1}{3}\quad\text{as } z\to 0.$$

The limiting form of the Bessel function term in the first part of (34) is

$$k_0^2\left[K_0(jk_0|z|)+\frac{K_1(jk_0|z|)}{jk_0|z|}\right]\to k_0^2\left[-\frac{\gamma}{2}-\frac{1}{2}\ln\frac{jk_0|z|}{2}-\frac{1}{k_0^2|z|^2}-\frac{1}{4}\right],$$

as $z\to 0$.

By adding the above to the series term (35) and (36), the singular terms cancel and one obtains the result

$$\frac{M}{2\pi b}\left[j\frac{\pi}{a}\sqrt{k_0^2-h^2}-\frac{\pi^2}{3a^2}+\frac{k_0^2}{2}\ln\frac{4\pi}{k_0a}-\frac{\gamma k_0^2}{2}-j\frac{k_0^2\pi}{4}-\frac{k_0^2}{4}+\frac{\pi}{a}\sum_{m=1}^{\infty}\left(\Gamma_m+\Gamma_{-m}-\frac{4m\pi}{a}+\frac{k_0^2a}{2m\pi}\right)\right], \quad (37)$$

after multiplying by $M/2\pi b$.

The remaining part of (34) may be summed to give

$$-\frac{2M}{\pi b}\sum_{n=1}^{\infty}\sum_{m=1}^{\infty}\frac{\gamma_n}{ma}\cos(hma)K_1(\gamma_n ma)$$
$$-\frac{M}{2\pi b^3}\left[1.2-\frac{k_0^2b^2}{2}\ln k_0b+\frac{k_0^2b^2}{4}+\frac{k_0^4b^4}{96}\right.$$
$$\left.-j\left(\frac{\pi}{4}k_0^2b^2-\frac{k_0^3b^3}{6}\right)\right]. \tag{38}$$

The only part left to be evaluated to obtain H_{im} is the term $k_0^2\Pi_z$. The evaluation of this term is similar to the evaluation of $k_0^2A_y$ given earlier. The final result for $x=y=z=0$, is

$$k_0^2\Pi_z=\frac{k_0^2M}{2\pi b}\left[-\ln\frac{4\pi}{k_0a}+\gamma+j\frac{\pi}{2}-j\frac{\pi}{a\sqrt{k_0^2-h^2}}\right.$$
$$+\frac{\pi}{a}\sum_{m=1}^{\infty}\left(\frac{1}{\Gamma_m}+\frac{1}{\Gamma_{-m}}-\frac{a}{m\pi}\right)$$
$$\left.+4\sum_{n=1}^{\infty}\sum_{m=1}^{\infty}\cos(hma)K_0(\gamma_nma)\right]$$
$$-\frac{k_0^2M}{2\pi b}\left[-j\frac{k_0b}{2}+j\frac{\pi}{2}+\ln 2\sin k_0b/2\right]. \tag{39}$$

The field H_{im} is given by the sum of (37), (38) and (39) and is equal to $C_{mm}M$. Hence, the interaction constant C_{mm} is given by

$$C_{mm}=-\frac{1}{2\pi b}\left\{\left[\frac{1.2}{b^2}+\frac{\pi^2}{3a^2}+\frac{k_0^2}{2}(1-\gamma)+\frac{k_0^4b^2}{96}\right.\right.$$
$$\left.+\frac{k_0^2}{2}\ln\frac{8\pi}{k_0^2ab}(1-\cos k_0b)\right]$$
$$-\frac{k_0^2\pi}{a}\sum_{m=1}^{\infty}\left[\frac{1}{\Gamma_m}+\frac{1}{\Gamma_{-m}}+\frac{\Gamma_m+\Gamma_{-m}}{k_0^2}-\frac{a}{2m\pi}-\frac{4m\pi}{k_0^2a}\right]$$
$$-4k_0^2\sum_{n=1}^{\infty}\sum_{m=1}^{\infty}\cos(hma)\left[K_0(\gamma_nma)-\frac{\gamma_n}{mk_0^2a}K_1(\gamma_nma)\right]$$
$$\left.-j\left[\frac{k_0^3b}{3}-\frac{\pi h^2}{a(k_0^2-h^2)^{1/2}}\right]\right\}. \tag{40}$$

This completes the derivation of the dynamic field interaction constants.

When the lattice spacings a and b are small compared with the wavelength λ_0, static field interaction constants may be used. These may be obtained by placing k_0^2 equal to zero in the expressions for C_{ee}, C_{em}, C_{me} and C_{mm}. It is readily found that

$$C_{ee}'=\frac{1.2}{\pi b^3}-\frac{8\pi}{b^3}\sum_{n=1}^{\infty}\sum_{m=1}^{\infty}n^2K_0(2nm\pi a/b), \tag{41a}$$
$$C_{em}'=C_{me}'=0, \tag{41b}$$
$$C_{mm}'=-\frac{0.6}{\pi b^3}-\frac{\pi}{6a^2b}$$
$$-\frac{4}{ab^2}\sum_{n=1}^{\infty}\sum_{m=1}^{\infty}\frac{n}{m}K_1(2nm\pi a/b), \tag{41c}$$

where the prime denotes static interaction constants. The static-field case C_{mm}' should be symmetrical in the variables a and b because of the symmetry involved in the two-dimensional lattice structure. Although (41c) seems to violate this condition, it may be shown that C_{mm}' as given by (41c) is also equal to[6]

$$C_{mm}'=-\frac{1.2}{\pi b^3}-\frac{1.2}{\pi a^3}+8\pi\sum_{n=1}^{\infty}\sum_{m=1}^{\infty}$$
$$\cdot\left[\frac{m^2}{b^3}K_0(2nm\pi a/b)+\frac{m^2}{a^3}K_0(2nm\pi b/a)\right]. \tag{42}$$

Conclusions

Suitable methods for evaluating the dynamic interaction fields in a two-dimensional lattice have been given. The final results for a particular case have been presented in terms of a set of interaction constants whose numerical values are readily computed. Reference to (5) shows that interaction fields will be of importance whenever the product of the element polarizability and the appropriate interaction constant is not negligible, compared to unity. This usually implies elements (such as disks and apertures) which are an appreciable fraction of a wavelength in size. For such elements, the polarizabilities are not, in general, given very accurately by the static formulas. Full advantage in the use of the dynamic interaction field analysis presented here is therefore limited to those elements for which higher order approximations to the polarizabilities are available. For the circular disk and aperture, the polarizabilities α_e and α_m have been evaluated up to and including terms in $(k_0r)^2$ where r is the disk radius.[7] Application of the results presented here will be discussed in a future paper.

[6] R. E. Collin and W. Eggimann, "Evlauation of Dynamic Interaction Fields in a Two Dimensional Lattice," Case Inst. Tech., Cleveland, Ohio, Sci. Rept. No. 12, issued under Contract AF 19(604)3887, March, 1960.

[7] W. H. Eggimann, "Higher order evaluation of dipole moments of a small circular disk," IRE Trans. on Microwave Theory and Techniques, vol. MTT-8, (Correspondence), p. 573; September, 1960.

TEM Impedance and Cross Coupling for Small Circular Center Conductors in a Double Ridged Waveguide*

J. E. STORER†, SENIOR MEMBER, IRE, AND T. W. THOMPSON†, STUDENT MEMBER, IRE

Summary—**The even and odd mode TEM impedances and cross-coupling coefficient were found for two small circular center conductors in a double ridge waveguide structure. Expressions were found by the use of a variational approximation for the case where the centers of the circular conductors lie on the horizontal center line of the guide; the conductors were placed symmetrically about the vertical plane of symmetry of the guide, and the conductors were placed a reasonable distance from the guide and from the region between the ridges. Results calculated from these expressions agree reasonably well with experimental data.**

The experimental and theoretical results tend to indicate that proper placement of the two conductors in a double ridge guide could be used as a method of transmitting three different messages inside a single closed waveguide.

Introduction and Basic Equations

WITH the problems of conserving weight and space in today's aircraft and missiles, the use of one waveguide for several different transmission systems would be advantageous. Suppose we consider the waveguide system shown in Fig. 1. By launching TEM modes on conductors C_1 and C_2 and using the dominant waveguide mode, this system could transmit three different messages instead of the one message for the usual application of the ridged guide. For ideal conductors (conductivity $= \infty$) and no discontinuities in the guiding structures, there will be no coupling between the TE waveguide mode and the TEM modes. If the cross coupling between the TEM modes on C_1 and C_2 is small and the mode conversion due to discontinuities and imperfect conductors is small, this system would be a practical method of using one waveguide for three communication channels. This article will consider only the TEM even and odd mode impedances and the cross coupling between C_1 and C_2 for the case where the conductors C_1 and C_2 satisfy the requirements mentioned in the summary.

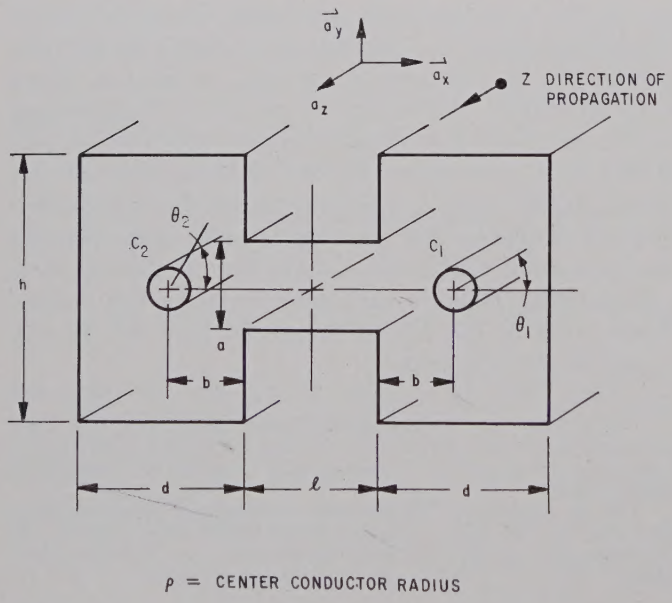

Fig. 1—Cross section of a waveguide system of two small circular center conductors inside a double ridge waveguide.

* Received by the PGMTT, May 19, 1960; revised manuscript received, September 23, 1960. This work was sponsored by AF Cambridge Res. Ctr., Air Res. and Dev. Command, Bedford, Mass., under Contract No. AF 19(604)-5474.

† Sylvania Electronic Sys., Waltham, Mass.

Basic Equations

The electric and magnetic field of the TEM modes of the system shown in Fig. 1 lie entirely in the transverse plane and are given by the following expressions:

$$\boldsymbol{E} = \text{Re}\left[-e^{j(kz-\omega t)}\nabla\phi(x, y)\right], \tag{1a}$$

$$\boldsymbol{H} = \frac{1}{\eta}(\boldsymbol{a}_z \times \boldsymbol{E}), \tag{1b}$$

where

$\boldsymbol{E}$ = electric field vector,

$\boldsymbol{H}$ = magnetic field vector,

$$\nabla = \boldsymbol{a}_x\frac{\partial}{\partial x} + \boldsymbol{a}_y\frac{\partial}{\partial y},$$

and

Re $e^{j(kz-\omega t)}$ = time and space variation of a wave travelling in the positive Z direction with a velocity ω/k.

The unit vectors in the x, y, and z directions will be noted by $\boldsymbol{a}_x$, $\boldsymbol{a}_y$, and $\boldsymbol{a}_z$, respectively. The quantity η is the characteristic impedance of uniform plane waves in the dielectric which fills the guide.

$$\eta = \sqrt{\frac{\mu}{\epsilon}}, \tag{1c}$$

where

μ = permeability of the dielectric filling the guide,

ϵ = dielectric constant of the dielectric filling the guide.

Also, the potential function $\phi(x, y)$ satisfies the two-dimensional Laplacian equation,

$$\nabla^2\phi(x, y) = \left(\frac{\partial^2}{\partial x^2} + \frac{\partial^2}{\partial y^2}\right)\phi(x, y) = 0. \tag{2}$$

The current in the center conductors will be given by i. It will be assumed that the current distribution varies angularly over the surface of the conductor. Thus,

$$i = \text{Re}\,[e^{j(kz-\omega t)}I(\theta)]\mathbf{a}_z,$$

where θ is shown in Fig. 1.

The impedance of one wire to ground will be defined as

$$Z = \frac{\int_{\text{conductor}}^{\text{wall}} \boldsymbol{E}\cdot\boldsymbol{ds}}{\int_{\substack{\text{conductor}\\ \text{surface}}} \boldsymbol{i}\cdot\boldsymbol{dA}}, \tag{3}$$

where

$$\boldsymbol{ds} = dx\mathbf{a}_x + dy\mathbf{a}_y,$$

$$\boldsymbol{dA} = \rho d\theta\mathbf{a}_z.$$

The coupling coefficient will be given by C and will be defined as

$$C = \frac{Z^e - Z^o}{Z^e - Z^o}. \tag{4}$$

The superscripts e and o denote the even and odd modes, respectively. If no superscript appears, then the equation will be considered to be applicable to either mode (with suitable modifications). For the even mode, at any transverse plane, conductors C_1 and C_2 will be raised to the same potential with respect to the outer conductor. The current flow in C_1 and C_2 will be equal and in the same direction. For the odd mode, at any transverse plane, conductors C_1 and C_2 will be raised to opposite potentials. The resulting current flow in C_1 and C_2 will be equal in magnitude and opposite in direction. The coupling coefficient defined by (4) has been discussed in previous articles[1,2] for balanced transmission systems—thus the requirement that conductors be placed symmetrically about the vertical plane of symmetry.

Let us consider the region to the right of the vertical plane of symmetry as shown in Fig. 2. The origin of cartesian co-ordinate system will be taken as the center of the aperture. It is easily shown that potential function $\phi(x, y)$ must satisfy the following boundary conditions:

$[\phi(x, y)]_{C_1}$ = potential on the center conductor surface

$$= V_0 \tag{5a}$$

$[\phi(x, y)]_C$ = potential on all conductor surfaces other than $C_1 = 0$, (5b)

$$\left[\frac{\partial\phi^e(x, y)}{\partial x}\right]_{x=-l/2} = 0, \tag{5c}$$

$$[\phi^o(x, y)]_{x=-l/2} = 0. \tag{5d}$$

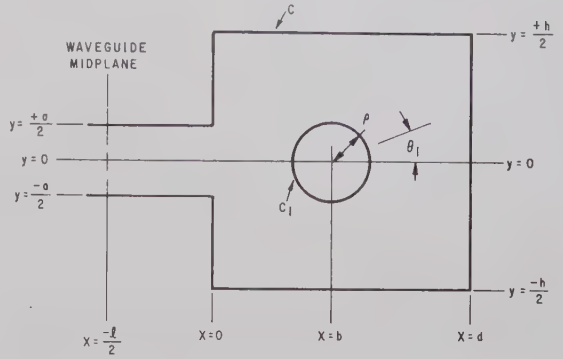

Fig. 2—Cartesian co-ordinate system in the transverse plane with the origin (0, 0) at center of the aperture.

Letting $\boldsymbol{n}_i$ denote a unit inwardly directed normal to the conductor surface and the subscript C_1 denote the value of the quantities at the surface of C_1, we can write the following boundary condition for the magnetic field at the surface of C_1:

$$i_{C_1} = -\boldsymbol{n}_i \times \boldsymbol{H}_{C_1}.$$

Using (1a) and (1b) and noting that the transverse current distribution is dependent only upon θ, it can easily be shown from the above that

$$I(\theta) = \frac{1}{\eta}\left[\frac{\partial}{\partial n_i}\phi(x, y)\right]_{x,y \text{ on } C_1}. \tag{5e}$$

It is readily apparent that this problem is not easily solved considering the differential equations. However, by considering an admittance Y defined as $1/Z$ and replacing the differential equations by integral equations and using a variational approximation, expressions for Z and C can be found. Thus, considering Y, we have

$$Y = \frac{1}{Z} = \frac{1}{V_0}\int_0^{2\pi} I(\theta)\rho d\theta$$

$$= \frac{1}{V_0\eta}\int_0^{2\pi}\left[\frac{\partial\phi(x, y)}{\partial n_i}\right]_{x,y \text{ on } C_1}\rho d\theta. \tag{6a}$$

The expression for the coupling coefficient now becomes

$$C = \frac{Y^o - Y^e}{Y^o + Y^e}. \tag{6b}$$

[1] B. M. Oliver, "Directional electromagnetic couplers," Proc. IRE, vol. 42, pp. 1686–1692; November, 1954.

[2] E. M. T. Jones and J. T. Bolljahn, "Coupled-strip-transmission-line filters and directional couplers," IRE Trans. on Microwave Theory and Techniques, vol. MTT-4, pp. 75–81; April, 1956.

Formulation of the Integral Equations

Let us consider a region 1 to be the rectangular area enclosed by the lines

$$x = 0, \quad x = d, \quad y = \frac{+h}{2}, \quad y = \frac{-h}{2}.$$

For this region, a Green's function can be defined such that

$$\nabla^2 G_1(x, x_0, y, y_0) = -\delta(x - x_0, y - y_0), \tag{7a}$$

$$G_1 = 0 \text{ on all boundaries of Region 1.} \tag{7b}$$

The function G_1 can be thought of as the two-dimensional potential for a negative line charge located at x_0, y_0 inside a conductor having the same boundaries as Region 1. The delta function in (7a) has the property

$$\iint f(x, y)\delta(x - x_0, y - y_0)dxdy = \begin{cases} f(x_0, y_0) \text{ if the area integrated over includes} \\ \text{the point } x_0, y_0\text{; zero if the area integrated} \\ \text{over does not include the point } x_0, y_0. \end{cases}$$

A solution to (7a) and (7b) in terms of a Fourier series expansion in y is

$$G_1(x, x_0, y, y_0) = 2\sum_{n=0}^{\infty} \frac{\cos\left(a_n \frac{y}{h}\right)\cos\left(a_n \frac{y_0}{h}\right)\sinh\left(a_n \frac{X^<}{h}\right)\sinh\left(a_n \frac{d - X^>}{h}\right)}{a_n \sinh\left(a_n \frac{d}{h}\right)}, \tag{7c}$$

where

$a_n = (2n+1)\pi$,
$X^<$ is the lesser of x, x_0,
$X^>$ is the greater of x, x_0.

Let Region 1′ be Region 1 excluding the center conductor cross section. If x_0, y_0 is supposed to lie in Region 1′ then

$$\phi_1(x_0, y_0) = \iint_{\text{Region 1}'} [G_1\nabla^2\phi - \phi\nabla^2 G_1]dxdy.$$

The above integral can be reduced from an area integral to line integral over the boundary by the use of Green's second identity. Thus

$$\iint_{\text{Region 1}'} [G_1\nabla^2\phi - \phi\nabla^2 G_1]dxdy = \int_{\text{boundary of Region 1}'} \left[G_1 \frac{\partial\phi}{\partial n} - \phi \frac{\partial G_i}{\partial n}\right] dl,$$

where the partial derivatives are with respect to an outwardly directed normal at the boundaries. The integrals above are reduced, noting the boundary conditions on ϕ and G_1 at the surface indicated. Thus,

$$\phi_1(x_0, y_0) = \int_{-a/2}^{a/2} \psi(y)\left[\frac{\partial G_1}{\partial x}\right]_{x=0} dy + \eta\int_0^{2\pi} (G_1)_{c_1} I(\theta)\rho d\theta - V_0\int_0^{2\pi}\left[\frac{\partial G_1}{\partial n}\right] C_1\rho d\theta,$$

where

$$\psi(y) = \phi(0, y) \quad \text{for } -a/2 \le y \le +a/2.$$

The last term in the expression above can be shown to be zero by the use of Green's second identity. Thus, for Region 1,

$$\phi_1(x_0, y_0) = \int_{-a/2}^{a/2} \psi(y)\left[\frac{\partial G_1}{\partial x}\right]_{x=0} dy + \eta\int_0^{2\pi} (G_1)_{x,y\to c_1} I(\theta)\rho d\theta. \tag{7d}$$

Turn now to a Region 2 which will be that area bounded by the lines $x = -l/2$, $x = 0$, $y = +a/2$, and $y = -a/2$. For this region we will define a second Green's function such that

$$\nabla^2 G_2(x, x_0, y, y_0) = -\delta(x - x_0, y - y_0)$$

$$G_2 = 0 \qquad \text{for } y = \pm a/2, \quad (-l/2 \le x \le 0)$$

$$\text{for } x = 0, \quad (-a/2 \le y \le +a/2)$$

$$\frac{\partial G_2^e}{\partial x} = G_2^o = 0 \quad \text{for } x = -l/2, \quad (-a/2 \le y \le +a/2),$$

where now x_0, y_0 is supposed to lie somewhere in Region 2. Writing G_2 as a Fourier series expansion

$$G_2^o = -2\sum_{n=0}^{\infty} \frac{\cos\left(a_n \frac{y}{a}\right)\cos\left(a_n \frac{y_0}{a}\right)\sinh\left[a_n \frac{\frac{l}{2}+X^<}{a}\right]\sinh\left(a_n \frac{X^>}{a}\right)}{a_n \sinh\left(a_n \frac{l}{2a}\right)}, \tag{8a}$$

$$G_2^e = -2\sum_{n=0}^{\infty} \frac{\cos\left(a_n \frac{y}{a}\right)\cos\left(a_n \frac{y_0}{a}\right)\cosh\left[a_n \frac{\frac{l}{2}+X^<}{a}\right]\sinh\left(a_n \frac{X^>}{a}\right)}{a_n \cosh\left(a_n \frac{l}{2a}\right)}, \tag{8b}$$

where $X^<$, and $X^>$ are those defined for G_1. By considering an analysis similar to that done for Region 1, it is easily shown that

$$\phi_2(x_0, y_0) = -\int_{-a/2}^{a/2} \psi(y)\left[\frac{\partial G_2}{\partial x}\right]_{x=0} dy. \tag{9}$$

By demanding that ϕ_1 reduce to V_0 on the conductor surface and that $\partial\phi_1/\partial x_0$ and $\partial\phi_2/\partial x_0$ be equal across the aperture $(x_0=0)$,[3] we obtain the following integral equations

$$V_0 = \eta\int_0^{2\pi}\left[\lim_{x_0,y_0\to C_1}(G_1)_{C_1}\right]I(\theta)\rho d\theta + \int_{-a/2}^{a/2}\psi(y)\left[\frac{\partial G_1}{\partial x}\right]_{x=0} dy \tag{10a}$$

$$0 = \eta\int_0^{2\pi}\left[\frac{\partial}{\partial x_0}(G_1)_{C_1}\right]_{x_0=0} I(\theta)\rho d\theta + \int_{-a/2}^{a/2}\psi(y)\left[\lim_{x_0\to 0}\frac{\partial}{\partial x_0}\left(\frac{\partial G_1}{\partial x}+\frac{\partial G_2}{\partial x}\right)_{x=0}\right]dy. \tag{10b}$$

These equations are sufficiently complicated to exclude an explicit expression for $I(\theta)$. However, an expression for Y can be found which is stationary with respect to $\psi(y)$ and $I(\theta)$ and a variational principle can be applied using this expression.

Variational Approximation

Using (6a), (10a), and (10b) together with the symmetry properties of the Green's function, it can be shown that Y can be written as

$$Y = \frac{+2}{V_0}\int_0^{2\pi} I(\theta)\rho d\theta - \frac{\eta}{V_0^2}\int_0^{2\pi}\int_0^{2\pi}[(G_1)_{C_1}]_{x_0,y_0\to C_1} I(\theta)I(\theta_0)\rho^2 d\theta d\theta_0 - \frac{2}{V_0^2}\int_0^{2\pi}\int_{-a/2}^{a/2}\left[\frac{\partial}{\partial x_0}(G_1)_{C_1}\right]_{x_0=0} I(\theta)\psi(y_0)\rho d\theta dy_0 - \frac{1}{\eta V_0^2}\int_{-a/2}^{a/2}\int_{-a/2}^{a/2}\left[\frac{\partial}{\partial x_0}\left(\frac{\partial G_1}{\partial x}+\frac{\partial G_2}{\partial x}\right)_{x=0}\right]_{x_0=0} \cdot\psi(y)\psi(y_0)dydy_0. \tag{11a}$$

This expression can be shown to be stationary with respect to independent variations of $I(\theta)$ and $\psi(y)$. To study an amplitude invariant form, let

$$I(\theta) = \frac{I_0}{2\pi\rho}K(\theta),$$

$$\psi(y) = \psi_0\Psi(y).$$

The expression for Y given by (11a) becomes

$$Y = \frac{2I_0}{V_0}\overline{R} - \frac{\eta I_0^2}{V_0^2}\Gamma_{11} - \frac{2I_0\psi_0}{V_0^2}\Gamma_{12} - \frac{\psi_0^2}{\eta V_0^2}\Gamma_{22}, \tag{11b}$$

where

$$\overline{R} = \frac{1}{2\pi}\int_0^{2\pi} K(\theta)d\theta,$$

$$\Gamma_{11} = \frac{1}{4\pi^2}\int_0^{2\pi}\int_0^{2\pi}[(G_1)_{C_1}]_{x_0,y_0\to C_1}K(\theta)K(\theta_0)d\theta d\theta_0, \tag{11c}$$

$$\Gamma_{12} = \frac{1}{2\pi}\int_0^{2\pi}\int_{-a/2}^{a/2}\left[\frac{\partial}{\partial x_0}(G_1)_{C_1}\right]_{x_0=0} K(\theta)\Psi(y_0)d\theta dy_0, \tag{11d}$$

$$\Gamma_{22} = \int_{-a/2}^{a/2}\int_{-a/2}^{a/2}\left[\frac{\partial}{\partial x_0}\left(\frac{\partial G_1}{\partial x}+\frac{\partial G_2}{\partial x}\right)_{x=0}\right]_{x_0=0} \Psi(y)\Psi(y_0)dydy_0. \tag{11e}$$

[3] It should be noted that ϕ_1 and ϕ_2 given by (7d) and (9) satisfy the boundary conditions given by (5b), (5c) and (5d).

The values of I_0 and ψ_0 can be found by setting $\partial Y/\partial I_0$ and $\partial Y/\partial \psi_0$ equal to zero. The resulting values of I_0, ψ_0 and Y are

$$I_0 = \frac{V_0 \overline{R} \Gamma_{22}}{\eta(\Gamma_{11}\Gamma_{22} - \Gamma_{12}^2)}, \tag{12a}$$

$$\psi_0 = \frac{V_0 \overline{R} \Gamma_{12}}{(\Gamma_{12}^2 - \Gamma_{11}\Gamma_{22})}, \tag{12b}$$

$$Y = \frac{1}{Z} = \frac{(\overline{R})^2 \Gamma_{22}}{\eta(\Gamma_{11}\Gamma_{22} - \Gamma_{12}^2)}. \tag{12c}$$

For most accurate results, the potential and current distributions should be studied experimentally and some analytic function picked to represent these distributions. However, in other problems of this sort, a uniform current distribution is usually chosen and good results obtained. This then will be our choice. We cannot say much about the potential distribution except

1) $\psi(y) = 0$ at $y = \pm a/2$,
2) $\psi(y)$ is symmetrical about $y = 0$,
3) $\psi(y)$ is maximum at $y = 0$.

Note that conditions 2) and 3) presuppose that the circular conductors lie midway between the top and bottom of the ridge guide. A potential function satisfying the above conditions is the triangular form,

$$\Psi(y) = 1 - \frac{2}{a} |y| .$$

This form is easy to handle mathematically and yielded good results. Thus the trial functions should suffice as long as the following conditions are met:

1) The aperture is not too large,
2) The distance from every point on the boundary of Region 1 to the conductor is at least equal to the conductor radius, and
3) The aperture is not a dominant influence on the current distribution.

Using the above-mentioned trial functions, the expressions for $\overline{R}$, Γ_{11}, Γ_{12}, Γ_{22}, become $\overline{R} = 1$.

$$\Gamma_{11} = \frac{-1}{2\pi} \ln\left(\frac{\pi\rho}{2h}\right) + \sum_{n=0}^{\infty} \frac{e^{-a(d/nh)} - \cosh\left(a_n \dfrac{d-2b}{h}\right)}{a_n \sinh\left(a_n \dfrac{d}{h}\right)}, \tag{13a}$$

$$\Gamma_{12} = 16\left(\frac{h}{a}\right) \sum_{n=0}^{\infty} \frac{\sinh\left(a_n \dfrac{d-b}{h}\right) \sin^2\left(a_n \dfrac{a}{4h}\right)}{a_n^2 \sinh\left(a_n \dfrac{d}{h}\right)}, \tag{13b}$$

$$\Gamma_{22} = -128 \sum_{n=0}^{\infty} \frac{4\left[\tanh\left(a_n \dfrac{l}{2a}\right)\right]^{\Gamma} + \left(\dfrac{h^2}{a^2}\right) \coth\left(a_n \dfrac{d}{h}\right) \sin^4\left(a_n \dfrac{a}{4h}\right)}{a_n^3}, \tag{13c}$$

where $a_n = (2n+1)\pi$.

For the even mode, $\Gamma = \Gamma^e = +1$.
For the odd mode, $\Gamma = \Gamma^o = -1$.

The above series converges quickly. The evaluation of Γ_{11} is shown in the Appendix. The evaluation of Γ_{11} and Γ_{12} was simplified by the fact that G_1 is essentially a potential function and its average over conductor surface is its value at center of the conductor ($x = b$, $y = 0$).

From the expressions for Y^e and Y^o, direct computation of the coupling coefficient from (6b) would be difficult and the values found probably erroneous. However, an expression for the difference $(Y^o - Y^e)$ can be found and the coupling coefficient found using the second form of (6a).

Evaluation of Mode Coupling

For the waveguide system shown in Fig. 1 to be used as a three-channel communication system, we would use the dominant waveguide mode and the TEM modes associated with conductors C_1 and C_2. The waveguide mode will be operated in a frequency range such that all waveguide modes except the dominant mode are below cutoff (if the center conductors are small and located away from the region between the ridges, the change in cutoff frequency of the dominant waveguide mode is less than 10 per cent[4]). Under ideal conditions, the TE and TEM are considered orthogonal[5] and thus they will propagate independently. For an actual system, there

[4] Both experimental and theoretical results carried out by the authors and James D. Kellett under Contract No. AF 19(604)-5474, AF Cambridge Res. Ctr., Air Res. and Dev. Command, Bedford, Mass.

[5] See for example, N. Maruuvitz, "Waveguide Handbook," in "M.I.T. Radiation Laboratory Series," McGraw-Hill Book Co., Inc., New York, N. Y., vol. 10; 1951. See especially Sec. 1.2.

will be discontinuities and asymmetries resulting in mode conversion. This conversion is difficult to handle mathematically and this paper will be concerned only with the coupling between the TEM modes for ideal conductors as given by (4) and (6b). Thus, the coupling considered in this section is only that between the TEM modes.

Let us consider the following integral

$$\iint_{\text{region } 1'+\text{region } 2} [\phi^e \nabla^2 \phi^o - \phi^o \nabla^2 \phi^e] dx dy.$$

It is readily apparent that the above integral is identically equal to zero. However, by the use of Green's second identity, the above integral reduces to

$$0 = \int_0^{2\pi} \left[\phi^e \frac{\partial \phi^o}{\partial n_i} - \phi^o \frac{\partial \phi^e}{\partial n_i} \right]_{C_1} \rho d\theta + \int_{-a/2}^{a/2} \left[-\phi^e \frac{\partial \phi^o}{\partial x} + \phi^o \frac{\partial \phi^e}{\partial x} \right]_{x=-l/2} dy.$$

By the use of (5a), (5c), and (6a) it is easily shown that

$$Y^o - Y^e = \frac{1}{\eta V_0{}^e V_0{}^o} \int_{-a/2}^{a/2} \left[\phi^e \frac{\partial \phi^o}{\partial x} \right]_{x=-l/2} dy.$$

Substituting the form of ϕ given by (9), the previous equation yields

$$Y^o - Y^e = \frac{4}{\eta a^2} \sum_{n=0}^{\infty} \left\{ \left[\frac{a_n}{\sinh\left(a_n \frac{1}{a}\right)} \right] \times \left[\int_{-a/2}^{a/2} \frac{\psi^e(y)}{V_0{}^e} \cos\left(a_n \frac{y}{a}\right) dy \right] \times \left[\int_{-a/2}^{a/2} \frac{\psi^o(y)}{V_0{}^o} \cos\left(a_n \frac{y}{a}\right) dy \right] \right\}.$$

The above series converges very quickly so that only the first term need be considered. Thus,

$$Y^o - Y^e \approx \frac{64}{\eta \pi^3 \sinh\left(\frac{\pi 1}{a}\right)} \left[\frac{\Gamma_{12}}{\Gamma_{11}\Gamma_{22} - \Gamma_{12}{}^2} \right]^e \times \left[\frac{\Gamma_{12}}{\Gamma_{11}\Gamma_{22} - \Gamma_{12}} \right]^o. \quad (14)$$

Since the quantity $(Y^o - Y^e)$ will be a very small quantity, the sum $(Y^o + Y^e)$ can be replaced by some average value $2\overline{Y}$. This is calculated using (12c) and replacing Γ_{22} by $\overline{\Gamma}_{22}$ where

$$\overline{\Gamma}_{22} = -128 \sum_{m=0}^{\infty} \frac{4 + \left(\frac{h^2}{a^2}\right) \coth\left(a_n \frac{d}{h}\right) \sin^4\left(\frac{a_n a}{4h}\right)}{a_n{}^3}.$$

Replacing $\Gamma_{22}{}^e$ and $\Gamma_{22}{}^o$ by $\overline{\Gamma}_{22}$ in (14), the following expression for C is obtained:

$$C = \frac{Y^o - Y^e}{Y^o + Y^e} = \left[\frac{32}{\pi^3 \sinh\left(\frac{\pi 1}{a}\right)} \right] \left[\frac{\Gamma_{12}{}^2}{\overline{\Gamma}_{22}(\Gamma_{11}\overline{\Gamma}_{22} - \Gamma_{12}{}^2)} \right]. \quad (15)$$

Results

Calculations for a ridged guide having the dimensions given in Table I were made. The characteristic impedance of either wire is given by $Z_C = \sqrt{Z^o Z^e}$.[1,2] Since Z^o and Z^e are very near, Z_C was calculated from (12c), replacing Γ_{22} by $\overline{\Gamma}_{22}$. For most dielectrics, the permeability is near that of space, and the dielectric constant is given by

$$\epsilon = \epsilon' \epsilon_0,$$

where

ϵ' = relative dielectric constant,
ϵ_0 = dielectric constant of free space.

Thus, η given by (1c) becomes $1/\sqrt{\epsilon'}\ 120\pi$ ohms. The quantity $Z_C\sqrt{\epsilon'}$ is given by

$$Z_C\sqrt{\epsilon'} = 120\pi \left(\Gamma_{11} - \frac{\Gamma_{12}{}^2}{\overline{\Gamma}_{22}} \right) \text{ohms}. \quad (16)$$

The coupling coefficient was calculated using (15).

TABLE I
Dimensions of Type DR-19 Double Ridge Waveguide Manufactured by Technicraft Laboratories of Thomaston, Conn.

Dimension	Length in Inches
a	0.191
h	0.475
d	0.3845
l	0.256

Since we are considering the TEM mode, the impedance given by (3) will be proportional to the dc resistance of a two-dimensional configuration having dimensions proportional to those of the actual ridged guide.[6] This is to be expected since the potential for this two-dimensional configuration satisfies the same Laplacian equation and same boundary conditions as $\phi(x, y)$. The even and odd mode impedances were found and their average taken as $Z_C\sqrt{\epsilon'}$. These values are shown in Fig. 3 along with the values of $Z_C\sqrt{\epsilon'}$ calculated from (16).

[6] J. D. Kraus, "Electromagnetic," McGraw-Hill Book Co., Inc., New York, N. Y.; 1953. See especially Sec. 11.5.

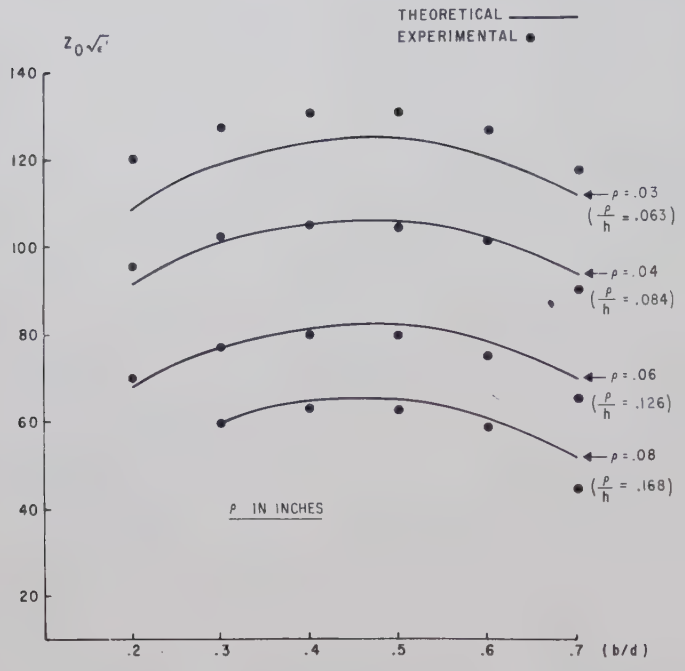

Fig. 3—Experimental and theoretical results for a double ridge guide having the dimensions given in Table 1.

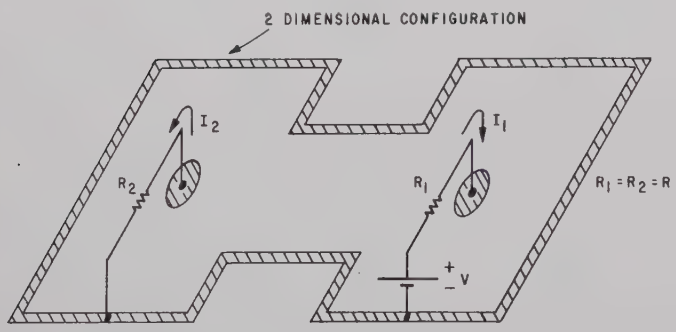

Fig. 4—Two-dimensional configuration used in finding the experimental results. The cross-hatched regions denote a highly conducting region. The experimental results shown in Figs. 3 and 5 were found with an electrolytic tank set-up based on the above.

Also the coupling coefficient, given by (4), can be found experimentally in a similar manner. It can be shown that

$$C = \frac{Z^e - Z^o}{Z^e + Z^o} = \frac{I_2}{I_1 - \frac{R}{V}(I_1^2 - I_2^2)},$$

where I_1, I_2, and V are shown in Fig. 4 for the case when $R_1 = R_2 = R$. The coupling coefficient found experimentally by this method is shown in Fig. 5 along with the theoretical calculated using (15).

As can be seen from Fig. 3 and 5, there is reasonable agreement between the theoretical and experimental results. Both the theoretical and experimental results indicate that this sort of system could be used as system for transmitting three messages inside a single closed guide.

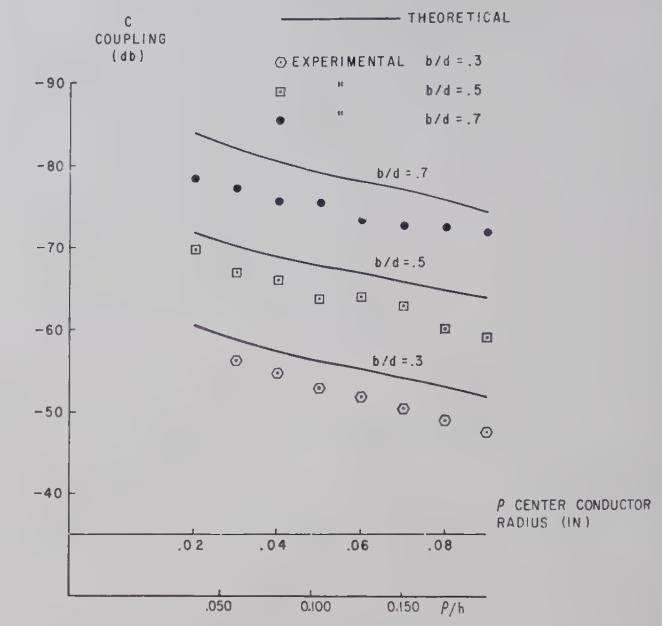

Fig. 5—Experimental and theoretical results for a double ridge guide having the dimensions given in Table I.

The characteristic impedances are reasonable and the coupling data indicates that for all practical purposes, the only cross talk between channels would result from mode conversion due to discontinuities.

Appendix

Evaluation of Γ_{11}

For the uniform current distribution, Γ_{11} given by (11c) becomes

$$\Gamma_{11} = \frac{1}{4\pi^2}\int_0^{2\pi}\int_0^{2\pi}\left[(G_1)_{C_1}\right]_{x_0,y_0\to C_1} d\theta d\theta_0. \tag{17}$$

The average of G_1 over the surface C_1 is the value of G_1 at $(b, 0)$. Thus, Γ_{11} becomes

$$\Gamma_{11} = \frac{1}{2\pi}\int_0^{2\pi}\left[(G_1)_{x=b,y=0}\right]_{x_0,y_0\to C_1} d\theta_0. \tag{18}$$

The Green's function in the above integral can be considered as the sum of free space Green's functions for the charge at x_0, y_0 and all of the images of the charge. The free space Green's function for a charge located at x_0, y_0 is

$$G_{fs} = -\frac{1}{2\pi}\ln\left[(x - x_0)^2 + (y - y_0)^2\right]^{1/2}. \tag{19}$$

Thus, G_1 becomes

$$G_1(x, x_0, y, y_0) = -\frac{1}{2\pi}\ln\left[(x - x_0)^2 + (y - y_0)^2\right]^{1/2} + \sum_{\text{all images of } x_0,y_0} G_{fs}. \tag{20}$$

Substituting the above in (18),

$$\Gamma_{11} = \frac{1}{2\pi}\int_0^{2\pi} \frac{-1}{2\pi} \ln\left[\rho^2 \cos^2\theta + \rho^2 \sin^2\theta\right]^{1/2} d\theta + \frac{1}{2\pi}\int_0^{2\pi}\left[\sum_{\text{all images of } b,0} G_{fs}\right] d\theta. \tag{21}$$

The first term is readily available. The second term is evaluated by replacing the integral by the field at the center. Thus,

$$\Gamma_{11} = \frac{-1}{2\pi}\ln\rho + \sum_{\text{all images of } b,0} (G_{fs})_{\substack{x\to b \\ y\to 0}}. \tag{22}$$

The second term in the above is evaluated using (20) where $x = b + \epsilon$ and limit is taken as ϵ approaches zero.

Therefore,

$$\Gamma_{11} = \frac{-1}{2\pi}\ln\rho + \lim_{\epsilon\to 0}\left[G_1(b+\epsilon, b, 0, 0) + \frac{1}{2\pi}\ln\epsilon\right].$$

G_1 is given by (7c). Thus,

$$\Gamma_{11} = \frac{-1}{2\pi}\ln\rho + \lim_{\epsilon\to 0}\left[2\sum_{n=0}^{\infty} \frac{\sinh\left(a_n \frac{b}{h}\right)\sinh\left(a_n \frac{d-b-\epsilon}{h}\right)}{a_n \sinh\left(a_n \frac{d}{h}\right)} + \frac{1}{2\pi}\ln\epsilon\right]$$

$$= \frac{-1}{2\pi}\ln\rho + \sum_{n=0}^{\infty} \frac{e^{-a_n(d/h)} - \cosh\left(a_n \frac{d-b}{h}\right)}{a_n \sinh\left(a_n \frac{d}{h}\right)}$$

$$+ \lim_{\epsilon\to 0}\left[\sum_{n=0}^{\infty} \frac{e^{-a_n(\epsilon/h)}}{a_n} + \frac{1}{2\pi}\ln\epsilon\right] = \frac{-1}{2\pi}\left[\ln\left(\frac{\pi\rho}{2h}\right)\right] + \sum_{n=0}^{\infty} \frac{e^{-a_n(d/h)} - \cosh\left(a_n \frac{d-2b}{h}\right)}{a_n \sinh\left(a_n \frac{d}{h}\right)}.$$

Design of a Coaxial Hybrid Junction*

L. STARK†, SENIOR MEMBER, IRE

Summary—The design of a coaxial hybrid junction is discussed. The hybrid consists of a shunt junction and a series junction. The shunt junction is a broad-band stub compensated tee, and the series junction is basically a balun of the type used to excite a slotted dipole. There is inherent isolation between the shunt and series terminals. The useful bandwidth of the hybrid is at least 10 per cent, while the bandwidth of the shunt junction alone exceeds this by a factor of four.

Design data are presented for frequency bands centered at 425 Mc and 220 Mc. Many of these hybrids have been manufactured for application, and the performance repeats very well. Performance data are given for VSWR, isolation, and peak power capacity.

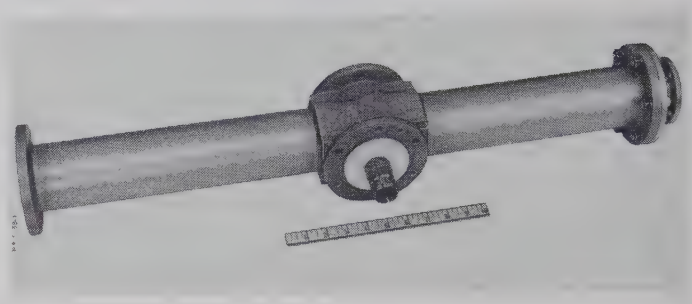

Fig. 1—Photo of 220-Mc hybrid junction.

Introduction

A COAXIAL hybrid junction has been developed which is suitable for VHF and UHF. The development was motivated by high-power antenna feed system applications including monopulse circuits and power dividers for antenna arrays.[1] A simple analysis of the device will be given and sufficient detailed design information will be furnished to allow construction of the hybrid.

Previous analysis and design of hybrids has been given by Alford and Watts,[2] Jones,[3] and others, of which a comprehensive listing can be found in Jones' paper.

The present design is similar to one reported by Alford and Watts.[2] It was developed before the results of this excellent reference were available. The Alford and Watts design appears to have more bandwidth capability, but the design reported here is simpler and should satisfy many requirements where bandwidth is of the order of 10 per cent.

Two designs were developed for application. The first junction which evolved was for operation over the band 400–450 Mc. The shunt arm and side arms were in $3\frac{1}{8}$ inch coaxial line (RG-154/U) and the series arm was in $1\frac{5}{8}$ inch coaxial line (RG-153/U). Following this, a junction was developed for another application for operation centered at 220 Mc. The shunt and side arms were again fabricated in $3\frac{1}{8}$ inch line and the series arm in $1\frac{5}{8}$ inch line. A photograph of the 220-Mc hybrid is shown in Fig. 1. The mechanical features of these hybrids show that the hybrids are rugged, easy to manufacture, and they give repeatable high quality performance, as evidenced in production of over 300 units for various applications.

Analysis of Shunt and Series Junctions

A drawing of the hybrid is shown in Fig. 2. It consists of a shunt junction and a series junction; the series excitation is brought out from the inside of the shunt junction. The shunt junction is basically a stub supported tee where the inner conductor is slotted down its length for a distance of approximately $\lambda/4$ each side of the junction point with the side arms. When the shunt arm is excited, a wave passes to the side arms and there is no potential difference across the slots in the inner conductor. The difference excitation of the side arms is provided by exciting a voltage difference across the slots at the junction point. This is accomplished with a balun of the type used to excite a slotted dipole.[4] An inner conductor is placed inside the slotted conductor and is connected to one segment of it at the junction point. The inner conductor runs an additional quarter wavelength beyond the junction point to provide a rigid stub support. The balun provides an out-of-phase excitation to the side arms which is independent of frequency. Likewise, the shunt junction provides an in-phase excitation which is independent of frequency. There is, therefore, an inherent isolation between shunt and series arms provided by the geometry of the junction, as in the case of the waveguide magic tee. This is superior to the ring-type of hybrid, which is frequency sensitive.

An ideal hybrid has no cross coupling between the shunt and series arms and is matched looking into the shunt arm and the series arm when matched loads are placed on all other arms. It can be proved from the scat-

* Received by the PGMTT, July 26, 1960; revised manuscript received, October 17, 1960.

† Ground Systems Group, Hughes Aircraft Co., Fullerton, Calif.

[1] L. Stark, "A helical line scanner for beam steering a linear array," IRE TRANS. ON ANTENNAS AND PROPAGATION, vol. AP-5, pp. 211–216; April, 1957.

[2] A. Alford and C. B. Watts, "A wide-band coaxial hybrid," 1956 IRE NATIONAL CONVENTION RECORD, pt. I, pp. 171–179.

[3] E. M. T. Jones, "Wide-band strip-line magic-T," IRE TRANS. ON MICROWAVE THEORY AND TECHNIQUES, vol. MTT-8, pp. 160–168; March, 1960.

[4] H. J. Riblet, "Slotted Dipole Impedance Theory," M.I.T. Rad. Lab., Cambridge, Mass., Rept. No. 772; November 1945.

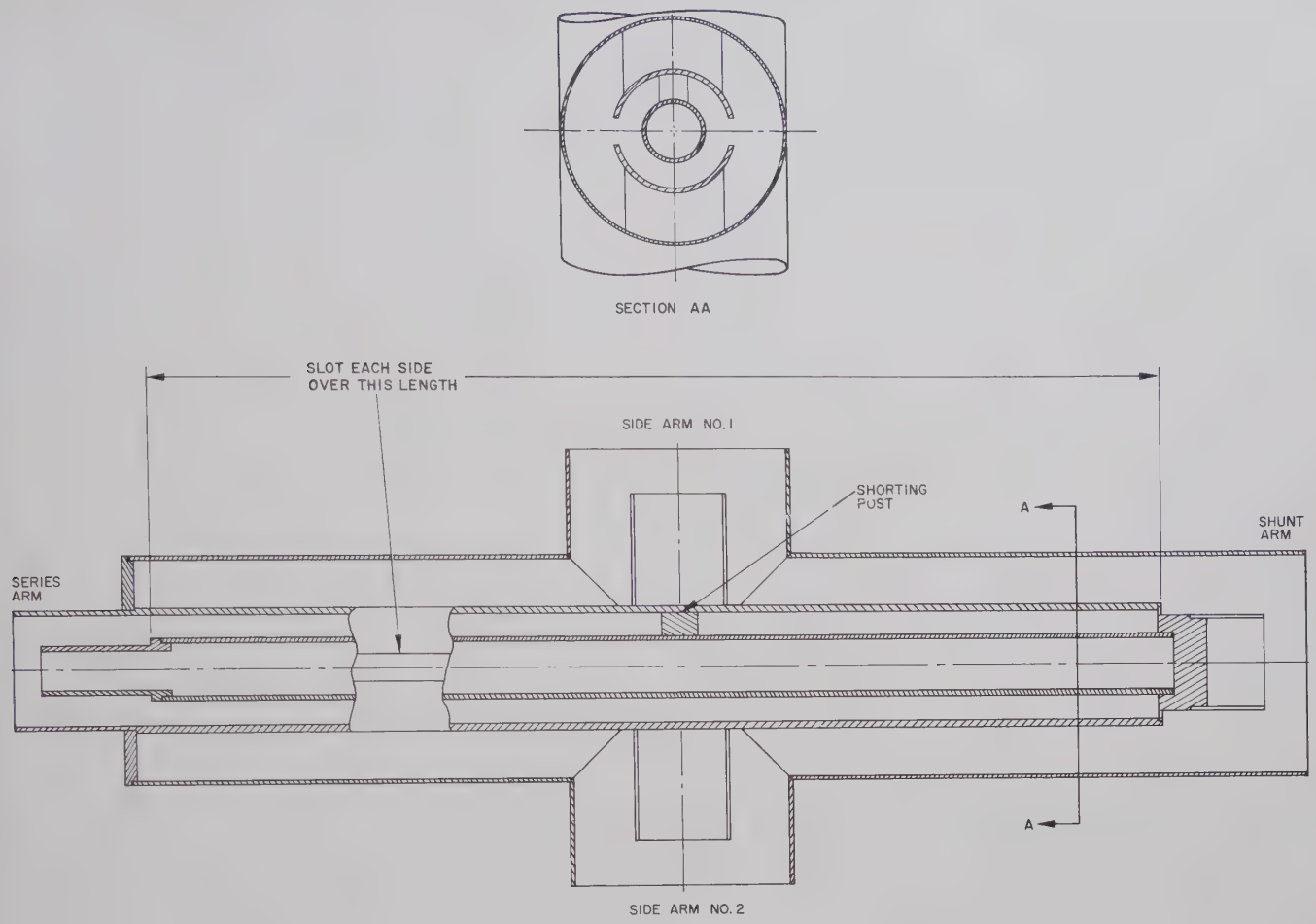

Fig. 2—Drawing of coaxial hybrid junction.

tering matrix of the junction[5] that it will then follow that the side arms will be matched and isolated from each other. A study of the series and shunt junctions will show the steps necessary to provide the matched condition in each of these junctions and thus approach the ideal performance.

Shunt Junction

The shunt junction is a stub-supported tee as shown in Fig. 3. The broad-band design of this type of junction has been studied extensively.[6–8] A simple and effective method having ample bandwidth is to design the quarter-wave transformer and the stub support so that characteristic impedances of these line sections are the same

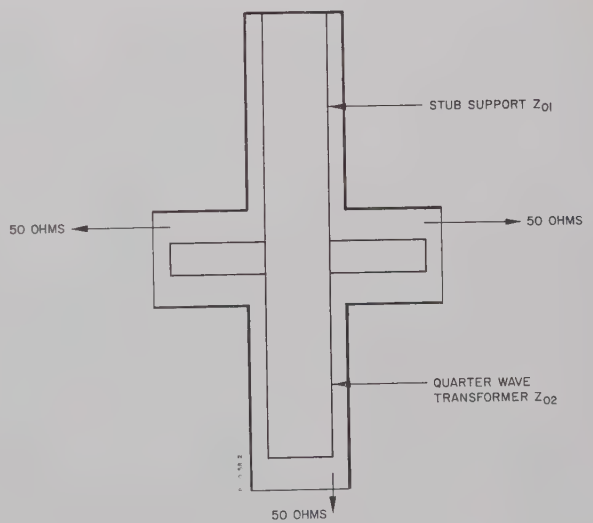

Fig. 3—Schematic drawing of stub-supported tee junction.

[5] C. G. Montgomery, "Technique of Microwave Measurements," M.I.T. Rad. Lab. Ser. vol. 11, McGraw-Hill Book Co., Inc., New York, N. Y., pp. 518–519; 1947.

[6] V. H. Rumsy, "Design of Frequency Compensating Matching Sections," Combined Res. Group, Naval Res. Lab., Washington, D. C., Rept. No. 89; September 1945.

[7] J. Reed and G. Wheeler, "A broadband fixed coaxial power divider," 1957 IRE National Convention Record, pt. I, pp. 177–181.

[8] G. L. Ragan, "Microwave Transmission Circuits," M.I.T. Rad. Lab. Ser., vol. 9, McGraw-Hill Book Co., Inc., New York, N. Y., pp. 516–519; 1948.

and equal to $R_0/\sqrt{2}$, where R_0 is the common impedance value to which all arms are to be matched, in this case 50 ohms. The frequency sensitivity of the stub support then cancels the frequency sensitivity of the quarter-wave transformer to a first order and the junction is much broader band than without the stub. The theoretical bandwidth is 33 per cent for a VSWR less than 1.07.[7] The characteristic impedance of the line sections with the slotted conductor is changed by a negligible amount by the presence of the slots, even though the slots are rather wide. That this should be so was predicted on the basis of calculated results for a slotted *outer* conductor where the slot subtended the same angle,[9,10] and this assumption was verified by measurement. The lengths of the nominal quarter-wave transformer and stub support sections were determined by experiment so as to include the junction effect. Design data were taken in the 425 Mc band for $3\frac{1}{8}$ inch line and $1\frac{5}{8}$ inch line. By scaling, the latter data served for the design of a 220 Mc-junction in $3\frac{1}{8}$ inch line. The data are summarized in Table I. The characteristic impedance of these line sections is 35.35 ohms, which is obtained with a diameter ratio of 1.805.

TABLE I

TRANSFORMER AND STUB LENGTHS FOR OPTIMUM PERFORMANCE OF SHUNT JUNCTION

	425 Mc		220 Mc	
	$L_{\text{Trans.}}$	L_{Stub}	$L_{\text{Trans.}}$	L_{Stub}
$1\frac{5}{8}$ inch line	7.000 inches	7.445 inches		
$3\frac{1}{8}$ inch line	6.750	7.500	13.500 inches	14.350 inches

Series Junction

In the design of the series junction, the side arms are energized in series by means of a balun. The balun is fed at the input by a 50-ohm coaxial transmission line. Across the output of the balun is a stub support for the inner conductor. The voltage and current transformations which occur along the balun have been investigated by Riblet.[4] He analyzed the balun as a three conductor system on which two TEM modes can propagate. One mode has the configuration shown in Fig. 4(a), and the second mode has the configuration shown in Fig. 4(b). For the first mode, the potential difference between the two halves of the outer conductor is zero. This is a perturbed ordinary mode of coax.

For the second mode, the potential of the inner conductor is half way between the potential between the split outer conductors and the net current on the center conductor is zero. The amplitudes of the mode currents are related to the voltages by the characteristic impedances of the modes, which are calculated in reference 10.

[9] "Reference Data for Radio Engineers," IT&T Corp., New York, N. Y., 4th ed., p. 594; 1957.

[10] J. Smolarska, "Characteristic impedance of the slotted coaxial line," IRE TRANS. ON MICROWAVE THEORY AND TECHNIQUES, vol. MTT-6, pp. 161–166; April, 1958.

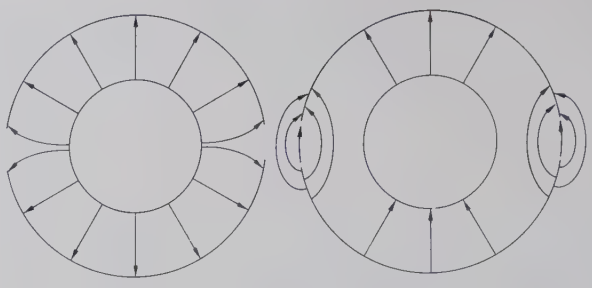

Fig. 4—Field patterns of coaxial modes. (a) First. (b) Second.

By applying the following appropriate end conditions to the three-wire system,

1) voltage between outer conductors is zero at input end,
2) voltage between inner conductor and one half of outer conductor is zero at output end,
3) load impedance Z_L is connected between inner conductor and the other half of outer conductor,

an equivalent circuit is derived which is shown in Fig. 5. The balun has the property of dividing the load impedance by four in transforming it from the terminals to the ordinary coaxial line mode. In shunt with the load are two parallel stubs, one due to the stub support and the other due to the slotted outer conductor extending towards the input from the junction. The Z_0 of the stubs is the characteristic impedance of the mode shown in Fig. 4(b), and the shunt impedance presented by the stubs is divided by 4. The length of each stub is the length of the corresponding slot measured from the junction.

The characteristic impedance of the input line section is the Z_0 of Fig. 4(a), and is negligibly different from the impedance of ordinary coax with slot widths that have been used.

The impedance presented to the balun by the side arms is 100 ohms. Since the balun divides the impedance by four, a 35.35-ohm quarter-wave transformer is used in the feeding coaxial section to bring the impedance to 50 ohms. The diameter ratio of outer to inner conductor is thus 1.805, as in the case of the shunt junction. An optimum broad-band stub support for this transformer can be calculated as in the case of the shunt junction but the required value of characteristic impedance places an impractical value on the slot width. The equivalent stub should have a characteristic impedance of 35.35 ohms, as seen by the ordinary coaxial line mode. This would require that each of the parallel stubs across the balun have a Z_0 of $4\times2\times35.35=283$ ohms, which is too high to be achieved with this configuration. The hybrids which have been developed in $3\frac{1}{8}$ inch line have used a slotted conductor which is 1.60 inches mean diameter with slots which were 0.375 inch wide. These parameters gave a characteristic impedance of approximately 75 ohms.[10] The bandwidth of the series arm is thus more restricted than that of the shunt arm, for which an

optimum broad-band stub is practical. In the design of the series junction, the lengths of the slots and the quarter-wave transformer were made equal to a quarter wavelength at the center frequency. The junction effect proved to be small and therefore the impedance match at band center was quite favorable.

Measured Performance Data

Two hybrid junctions have been designed, one for the frequency band 400–450 Mc and the second for a band centered around 220 Mc. A large number of these hybrids have been produced for antenna feed applications. The electrical features of the design are essentially as discussed above. One additional modification has been introduced to lengthen electrically the stub support for the balun. As shown in Fig. 6, a block of teflon has been placed at the input end of the stub support. The physical length of the stub is less than $\lambda/4$ because the slot is milled in the conductor which provides the quarter-wave transformer for the shunt junction (*cf.*, Table I). The stub support is teflon filled for a length of 1.0 inch for each of the designs.

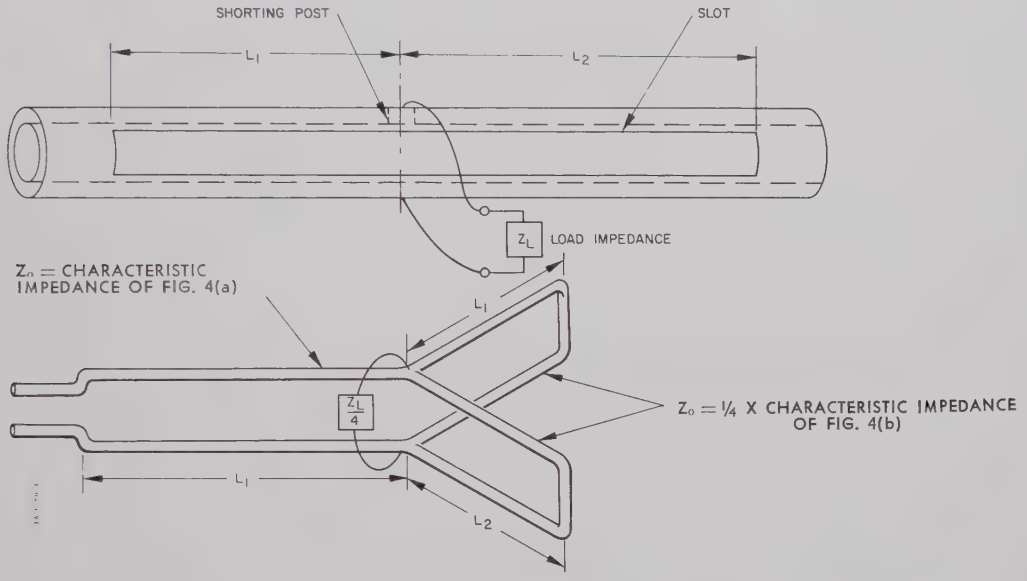

Fig. 5—Equivalent circuit of series junction.

Fig. 6—Photo showing teflon loading in series junction.

Measurements of VSWR and isolation are shown in Figs. 7, 8, 9 and 10 for the two designs. The frequency independence of isolation between the shunt and series arms is noted. The shunt junction is very broad band and the series junction has a VSWR less than 1.40 over a 10 per cent band. The side-arm VSWR is intermediate between the shunt and series-arm VSWR's. The isolation between side arms is dependent upon the match of the shunt and series arms and is thus frequency dependent. The isolation is greater than 20 db over a 10 per cent band.

The hybrids have been tested and operated under high peak power conditions. The shunt junctions have been tested with 2.5 Mw of peak power with no arcing. The 220 Mc hybrid was tested at a reduced pressure of 0.33 atmosphere and no arcing was observed at 0.5 Mw of power. This indicates a power capacity of 4.5 Mw at one atmosphere. The shunt junction appears to be able to handle as much power as a uniform length of 50 ohm $3\frac{1}{8}$ inch line. A contributing factor to the high power capacity is the 35-ohm characteristic impedance of the line sections, which is nearly optimum for voltage breakdown considerations.

The series junction of the 220-Mc hybrid was high

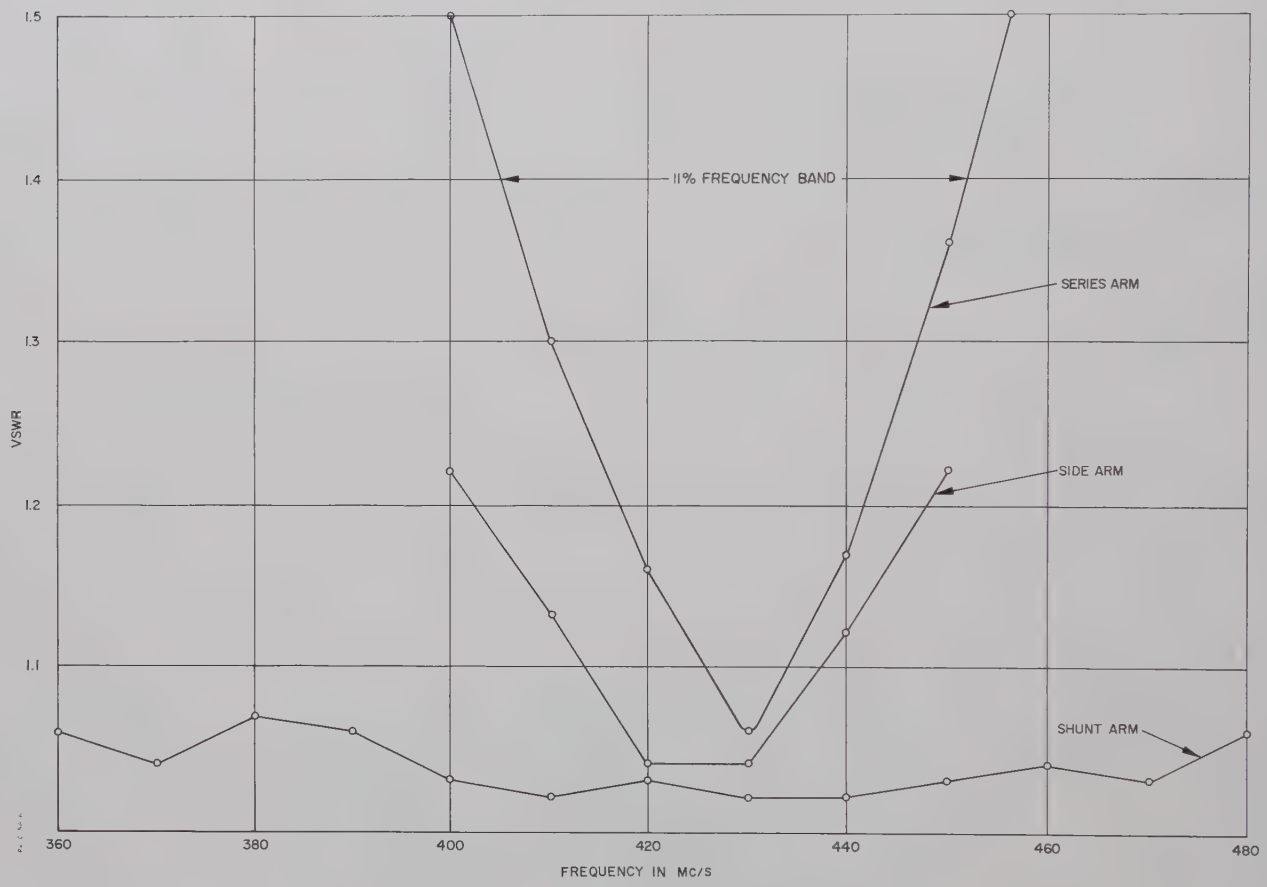

Fig. 7—VSWR of 425-Mc hybrid.

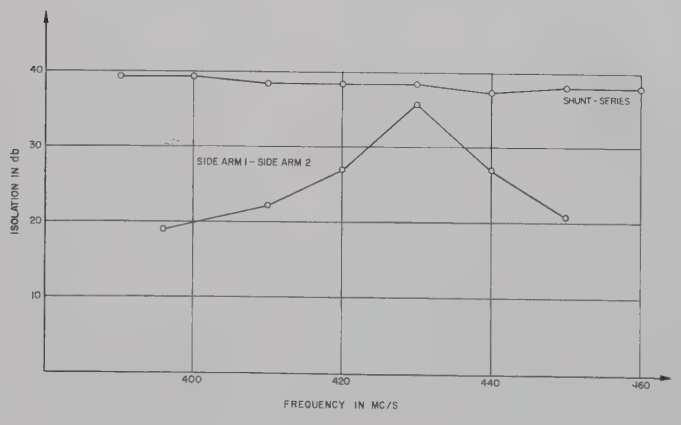

Fig. 8—Isolation between arms of 425-Mc hybrid.

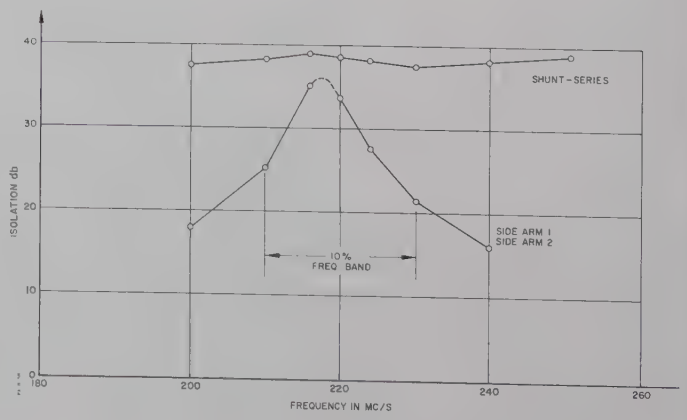

Fig. 9—Isolation between arms of 220-Mc hybrid.

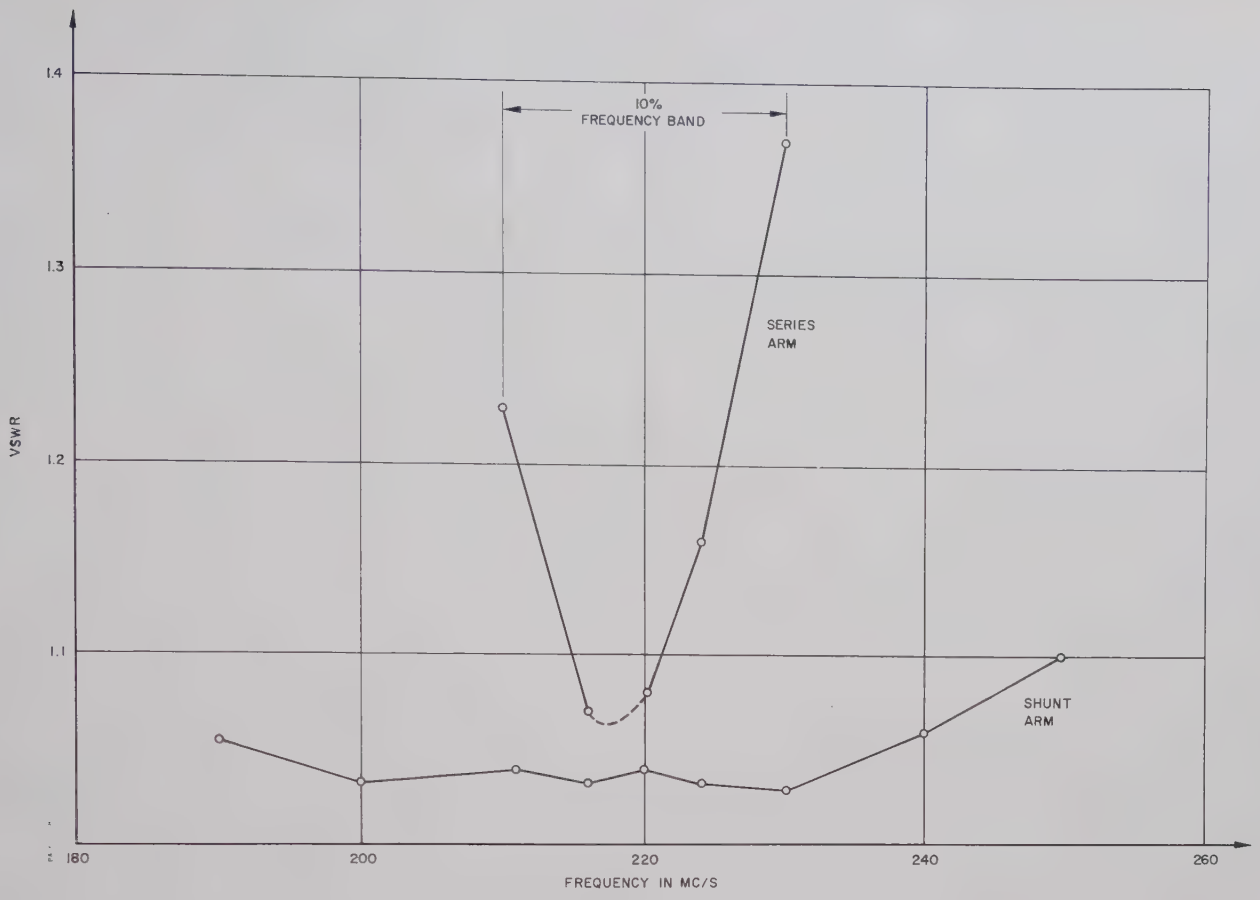

Fig. 10—VSWR of 220 Mc hybrid.

power tested at 1 atmosphere pressure and arcing occurred at 200 kw. The position of arcing was across the slot at the teflon filler for the stub support. The power capacity could be increased substantially, if required, by grooving the teflon piece and rounding the corners of the slot in the conductor.

Conclusions

The theory and design of a coaxial hybrid junction has been presented. The hybrid has inherent isolation between the shunt and series arms. The shunt arm has a nearly optimum broad-band impedance match by virtue of stub compensation. The series arm cannot be compensated in an optimum manner; however, the VSWR is less than 1.4 over a 10 per cent frequency band. Hybrid designs were given for bands centered at 425 Mc and 220 Mc. Many hybrids have been produced with repeatable results. Typical performance data have been given.

Acknowledgment

The author would like to acknowledge the assistance of R. Tang in carrying out a detailed set of high-power measurements for the 220-Mc hybrid and the assistance of W. E. Bullen, Jr. in obtaining VSWR and isolation measurements.

Step-Twist-Junction Waveguide Filters*

B. C. DeLOACH, Jr.†, MEMBER, IRE

Summary—**The properties of step-twist-junction discontinuities in rectangular waveguide are considered. Methods are presented whereby these step-twist-junctions may be used in filter design and, in particular, in the design of variable bandwidth constant-resonant frequency filters.**

Introduction

IN MANY laboratories work is often concentrated in some particular frequency band and, in such cases, a series of filters of different bandwidths tuned in this band are often a necessity as well as a great convenience.

This paper presents the results of design work on filters utilizing step-twist-junction discontinuities[1] and on filters utilizing modified step-twist-junction discontinuities. The former presents a particularly simple structure which can be easily fabricated, while the latter presents the useful property of variable bandwidth with fixed resonant frequency. This property allows one to adjust one filter for a wide range of bandwidths and thus avoid the tedious design of many separate filters.

Design Theory

A step-twist-junction will be defined to be a rectangular-to-rectangular waveguide junction of the type that would be produced by electroforming on the mandrel as illustrated in Fig. 1 and then removing the mandrel.

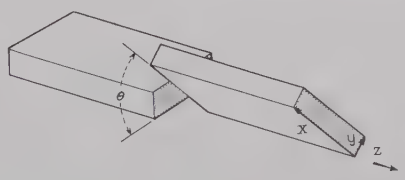

Fig. 1—Mandrel for a step-twist-junction.

The longitudinal axes of the two blocks will be assumed colinear and their cross-sectional dimensions identical. Thus, only one parameter θ will be needed to specify the junction completely. θ will be defined as the angular twist of the junction as illustrated in Fig. 1. In this paper the right-or-left-handedness of θ is irrelevant and, hence, we will specify $0 \leq \theta \leq \pi/2$, *i.e.*, θ will always be positive and will be the acute angle between the x, z faces of the two rectangular blocks.

If a guided wave of frequency 11.178 kMc is introduced on one side of a step-twist-junction in 0.400 inch $\times$0.900 inch guide and the guide on the other side of the junction is terminated with the characteristic impedance of the guide, an examination of the admittance of the step-twist-junction plus termination by means of a standing-wave detector produces the plot presented in Fig. 2 as θ is varied.

The information contained in Fig. 2 is enough to design a filter using two step-twist-junctions provided that use is made of further information obtainable from Wheeler and Schwiebert.[1]

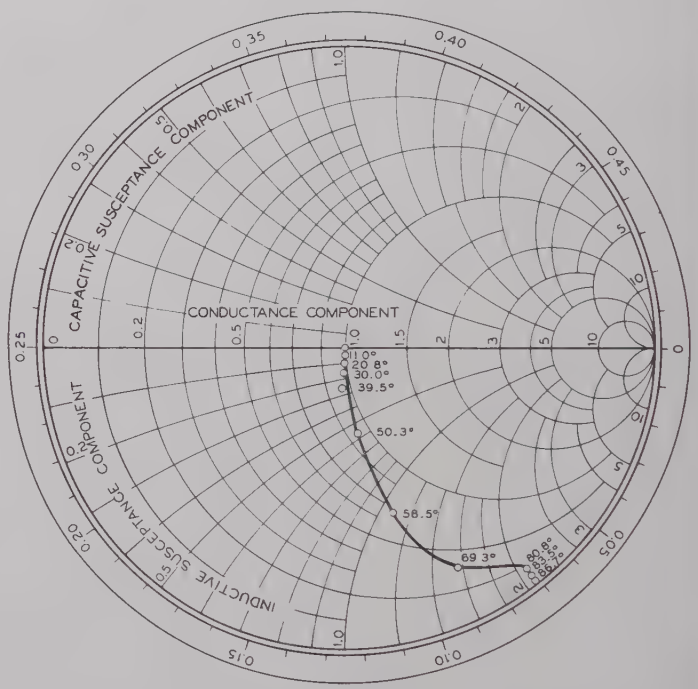

Fig. 2—The range of admittance of a step-twist-junction at 11.178 kMc for $0° \leq \theta \leq 90°$.

The following observation can be made. Any two-port passive symmetrical lossless microwave network may be represented at one frequency by a pure shunt susceptance with two equal lengths of transmission line on either side, as illustrated in Fig. 3(a). If this simple type of equivalent circuit is assumed for a step-twist-junction, it might be expected, in general, that the functional relation of length, susceptance, and frequency would assume some complicated form. Actually one finds, experimentally (see Appendix), that for a considerable range of frequencies in the vicinity of 11.178 kMc, the lengths of line may be accurately expressed as $L = a\lambda_g$ with a some constant, and the susceptance B as a con-

* Received by the PGMTT, August 22, 1960, revised manuscript received, October 25, 1961.

† Bell Telephone Labs., Inc., Holmdel, N. J.

[1] H. A. Wheeler and H. Schwiebert, "Step-twist waveguide components," IRE Trans. on Microwave Theory and Techniques, vol. MTT-3, pp. 44–52; October, 1955.

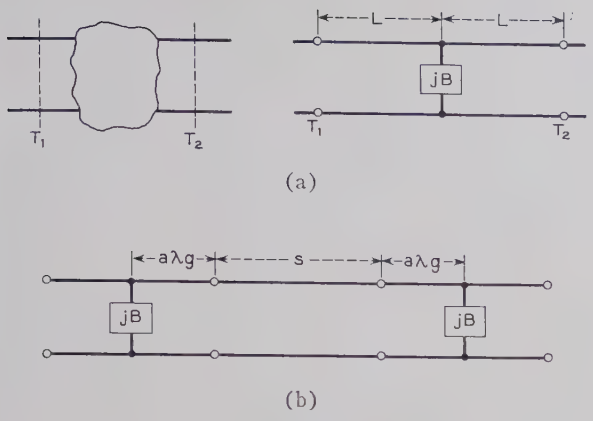

Fig. 3—(a) A two-port (symmetrical) microwave network and a transmission-line equivalent circuit. Planes T_1 and T_2 are assumed to be out of the area of fringing fields. (b) Transmission-line equivalent circuit for a step-twist-junction waveguide filter.

stant. This approximation will be made in all the succeeding work.

The lengths of line and the value of the susceptance for the equivalent circuit may be found graphically or analytically. The graphical method consists of drawing a constant standing-wave ratio circle (towards the load) from the point on the admittance chart (Fig. 2) representing the twist for the particular value of θ and λ_g, to an intersection point with the unit conductance circle. The magnitude of the equivalent pure shunt susceptance is read directly from this intersection, while the lengths of line are such as to have a equal the fractional wavelength separation of the unit circle intersection and the starting point above. (The shunt susceptance will turn out inductive if the minimum length of line is used.) These values can be equivalently calculated directly from the measurements of standing-wave ratio and minima positions from which Fig. 2 was obtained, and they are presented in Figs. 4 and 5.

Having obtained the equivalent circuit parameters, we will now proceed to develop expressions for the design of step-twist-junction waveguide filters in terms of resonant frequency wavelength and loaded Q.

For the usual type of filter, *i.e.*, two frequency independent pure shunt susceptances jB' separated by a distance l, the design formulas are obtained from Mumford[2] as

$$\tan \frac{2\pi l}{\lambda_{g0}} = \frac{2}{B'}, \tag{1}$$

$$Q = \left(\frac{\lambda_{g0}}{\lambda_0}\right)^2 \frac{\dfrac{2\pi l}{\lambda_{g0}}}{2 \sin^{-1} \dfrac{2}{\sqrt{(B')^4 + 4(B')^2}}}, \tag{2a}$$

[2] W. W. Mumford, "Maximally flat filters in waveguide," *Bell Sys. Tech. J.*, vol. 27, pp. 684–713; October, 1948.

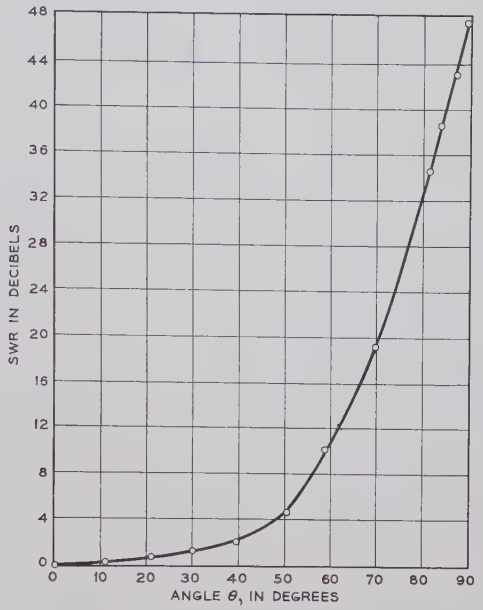

Fig. 4—SWR vs θ for a step-twist-junction with $f=11.178$ kMc.

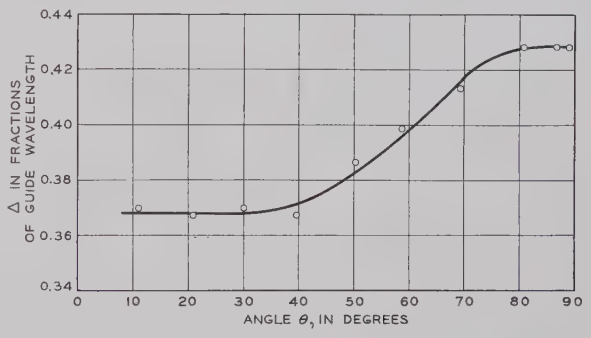

Fig. 5—Fractional wavelength separation of the step-twist-junction and the nearest minimum (toward the generator) of the standing-wave pattern of Fig. 2.

or

$$Q = \left(\frac{\lambda_{g0}}{\lambda_0}\right) \frac{\tan^{-1} \dfrac{2}{B'}}{2 \sin^{-1} \dfrac{2}{\sqrt{(B')^4 + 4(B')^2}}}, \tag{2b}$$

where

$Q \equiv$ the loaded $Q \equiv f_0/f_1 - f_2$ with f_0, f_1, and f_2 being the resonant frequency and the upper and lower half-power frequencies, respectively,[3]

$\lambda_{g0} \equiv$ the resonant frequency wavelength in the guide,

[3] Mumford's formulas are actually written in terms of a so-called wavelength Q defined by

$$Q = \frac{\dfrac{1}{\lambda_0}}{\dfrac{1}{\lambda_{g2}} - \dfrac{1}{\lambda_{g1}}},$$

where λ_0, λ_{g1}, and λ_{g2} are the resonant frequency-guide wavelength and the upper and lower half-power guide wavelengths, respectively. In (2a) and (2b) Mumford's equations have been rewritten in the more conventional loaded Q defined in terms of frequencies.

$\lambda_0 \equiv$ the resonant frequency wavelength in free space.
B' is positive or negative when the susceptance is capacitive or inductive, respectively,

These formulas will now be adapted to a twist filter. The necessity for this modification arises because the effective separation of our susceptances (the pure ones of our equivalent circuit) may be written [see Fig. 3(b)]

$$d = 2a\lambda_g + s, \tag{3}$$

where s is the physical separation of the two twist-junctions and $2a\lambda_g$ is a length of line added by the equivalent circuits of the twist-junctions. Thus for a twist filter (1) becomes

$$\tan \frac{2\pi}{\lambda_{g0}} (2a\lambda_{g0} + s) = \frac{2}{B}, \tag{4}$$

where it must be remembered that B is negative.

The expression for the loaded Q of a filter may be obtained[2] from the equivalence of two shunt susceptances jB', separated by a distance l, to a parallel resonant circuit (and a length of line to adjust phases). The admittance of the tuned circuit jB_x can be written as[2]

$$jB_x = jB'(B' \sin \theta_1 - 2 \cos 2\theta_1), \tag{5}$$

where

$$\theta_1 = \frac{2\pi l}{\lambda_g}.$$

The half-power points may be shown to occur at $B_x = \pm 2$. For the twist filter, the use of (3) and (4) in (5), in combination with double angle formulas, yields for the half-power wavelengths λ_{g1} and λ_{g2}

$$\frac{1}{\lambda_{g1}} = \frac{1}{\lambda_{g0}} - \frac{1}{2\pi s} \sin^{-1} \frac{2}{\sqrt{B^4 + 4B^2}}$$

$$\frac{1}{\lambda_{g2}} = \frac{1}{\lambda_{g0}} + \frac{1}{2\pi s} \sin^{-1} \frac{2}{\sqrt{B^4 + 4B^2}}, \tag{6}$$

and writing

$$Q = \left(\frac{\lambda_{g0}}{\lambda_0}\right)^2 \frac{\dfrac{1}{\lambda_{g0}}}{\dfrac{1}{\lambda_{g2}} - \dfrac{1}{\lambda_{g1}}},$$

we have

$$Q = \left(\frac{\lambda_{g0}}{\lambda_0}\right)^2 \frac{\dfrac{2\pi s}{\lambda_{g0}}}{2 \sin^{-1} \dfrac{2}{\sqrt{B^4 + 4B^2}}}. \tag{7}$$

Note the similarity of (7) with (2a), but also observe that the next step [Eq. (8)]

$$Q = \left(\frac{\lambda_{g0}}{\lambda_0}\right)^2 \left[\frac{\tan^{-1} \dfrac{2}{B}}{2 \sin^{-1} \dfrac{2}{\sqrt{B^4 + 4B^2}}} - \frac{4\pi a}{2 \sin^{-1} \dfrac{2}{\sqrt{B^4 + 4B^2}}} \right] \tag{8}$$

is different from (2b). From (7) we observe that s, the physical separation of the step-twist-junctions, occurs in the expression for the loaded Q as does l in (2a) for pure susceptive irises. That this should be the case can be seen from the fact that the phase separation of the equivalent circuit susceptances, *i.e.*, $2\pi d/\lambda_g$ is $2\pi[2a + (s/\lambda_g)]$, and only the s/λ_g term is frequency sensitive.

Thus (4) and (8) are the design equations for a step-twist-junction waveguide filter corresponding to (1) and (2b) for the usual type of filter. The design procedure for a step-twist-junction waveguide filter is as follows. First a curve such as that in Fig. 2 must be obtained (by extrapolation or measurement). Then for a given Q and resonant frequency, the value of B (and the corresponding value of a determined from the Smith chart plot) must be found that will satisfy (8). These values of B and a must then be substituted into (4) to determine s, the physical separation of the two step-twist-junctions. The value of θ is obtained from the curve corresponding to Fig. 4 by finding that value of θ which corresponds to a standing-wave ratio, identical to the one obtained from the pure susceptance B backed by a termination. From (4) we observe that for a particular resonant frequency the twist filter will be shorter for a given loaded Q than one made with pure inductive irises. The magnitude of this shortening depends upon the frequency of operation and the desired loaded Q.

Step-twist-junction waveguide filters can be designed with a rotatable center section. If different types of thin irises are attached to a step-twist-junction, the admittance vs θ plot for this junction and thus the resonant frequency-bandwidth plot for a filter made from two of the junctions can be radically altered. Note in particular that if the admittance plot of Fig. 2 lay along a straight line passing through the center of the chart, then for a filter, the design separation s for a given resonant frequency would be the same for any bandwidth. An admittance plot at 11.178 kMc for a step-twist-junction with a 0.010-inch thick 0.400-inch diameter centered circular iris inserted in the plane of the junction is presented in Fig. 6. This particular combination is observed to trace out the desired straight line as θ is varied from

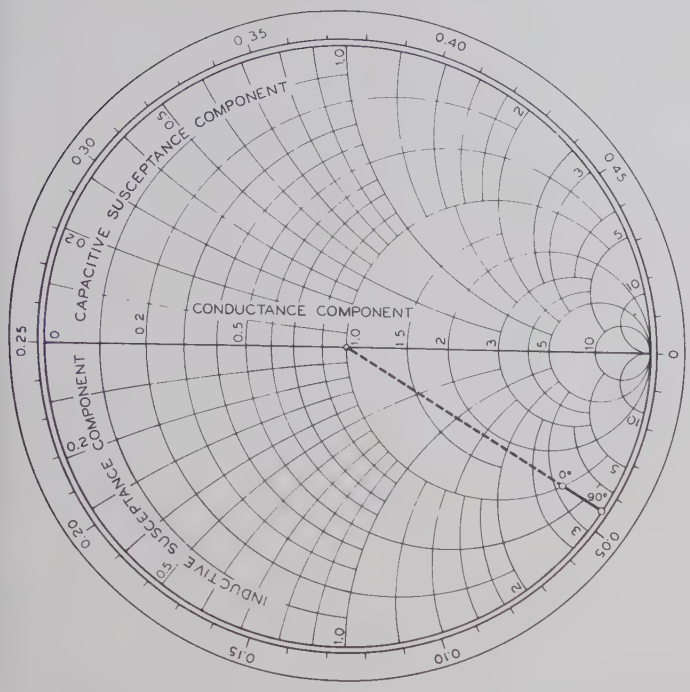

Fig. 6—The range of admittance of a step-twist-junction with centered 0.400-inch diameter iris at 11.178 kMc for $0° \leq \theta \leq 90°$.

90° (total reflection) to 0° (intersection with unit circle). Thus a filter composed of two such junctions should have the property of variable bandwidth and constant resonant frequency as θ is varied.

Experimental Results

A frequency vs transmission loss curve is presented in Fig. 7 for a singe-cavity step-twist filter. This cavity was designed for $f_0 = 11.72$ kMc and a 3-db bandwidth of 154 Mc. Experimentally we obtained $f_0 = 11.58$ kMc and a 3-db bandwidth of 147 Mc. The closeness of these results is a good check on the validity of our equivalent circuit. Dimensional tolerances place the experimental resonant frequency and 3-db bandwidth within the range of experimental error of the determination of the curve of Fig. 2.

Multiple cavity filters can, of course, be constructed either as direct coupled cavities or as "quarter"-wavelength coupled cavities. Fig. 8 presents the response of a three-cavity, three-quarter-wave coupled band-pass filter designed for a maximally-flat amplitude response. The design bandwidth was 500 Mc with the design resonant frequency 11.20 kMc. Experimental values of 525-Mc bandwidth and 11.14 kMc (midway between 3-db points) were obtained. The filter was electroformed from copper upon a series of rectangular blocks on a spindle which were later dissolved out. The curve of Fig. 8 was then obtained with no attempt being made to first tune the filter by means of tuning screws.

Photographs of two twist filters with rotatable center sections are shown in Fig. 9. The filter of Fig. 9(a) is a

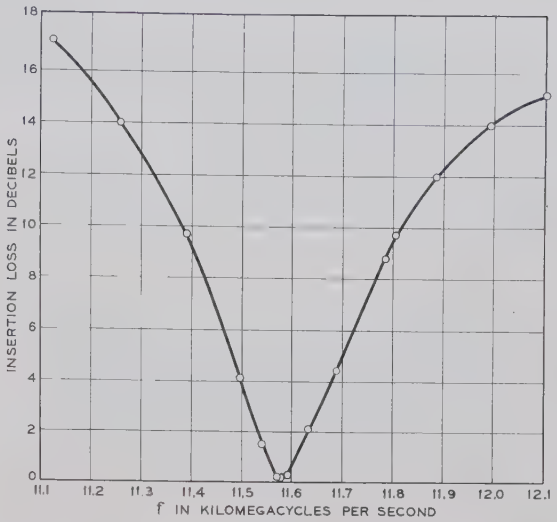

Fig. 7—Transmission characteristic of a single-cavity step-twist-filter.

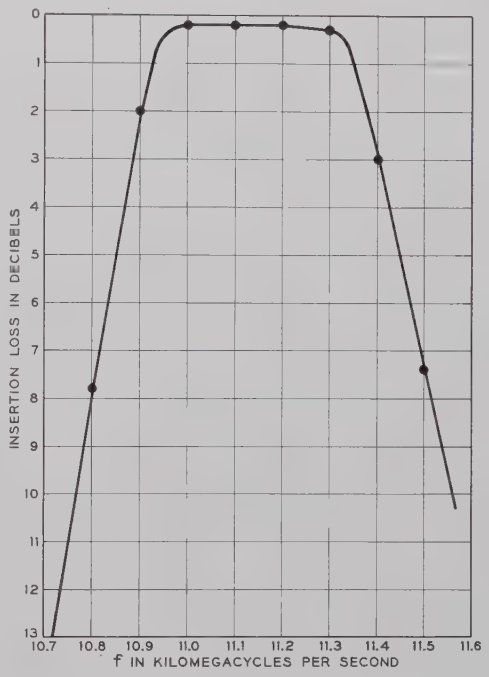

Fig. 8—Transmission characteristic of a three-cavity, three-quarter wavelength coupled, step-twist-junction filter.

pure step-twist-junction waveguide filter while that of Fig. 9(b) has 0.400-inch diameter centered circular irises attached to both ends of the rotatable center section. The resonant frequency transmission loss vs 3-db bandwidth curves for these two types are presented in Fig. 10. The resonant frequency vs bandwidth plots (as the center section is rotated) for these two types are presented in Fig. 11. As can be seen in Fig. 11, the resonant frequency of the cavity with circular irises (0.400-inch diameter) is constant out to 755-Mc bandwidth within experimental accuracy of ± 1 Mc at the narrow band-

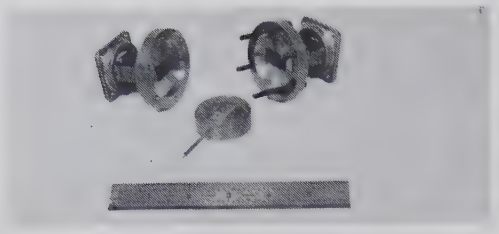

(a)

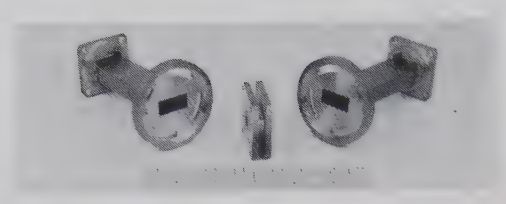

(b)

Fig. 9—(a) Step-twist-junction filter with rotatable center section with no corrective irises. (b) Step-twist-junction filter with rotatable center section with 0.400-inch diameter centered circular irises.

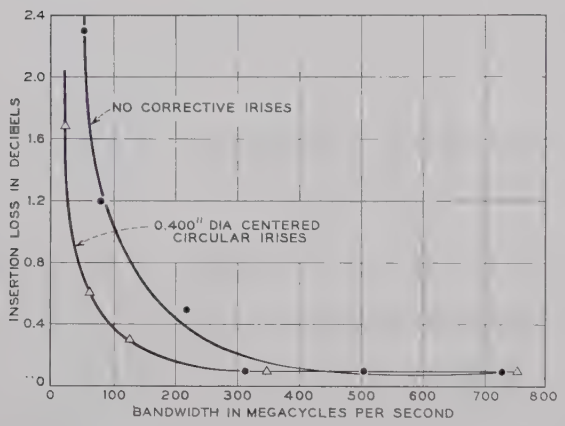

Fig. 10—Insertion loss vs bandwidth for two step-twist-junction filters with rotatable center sections at f_0.

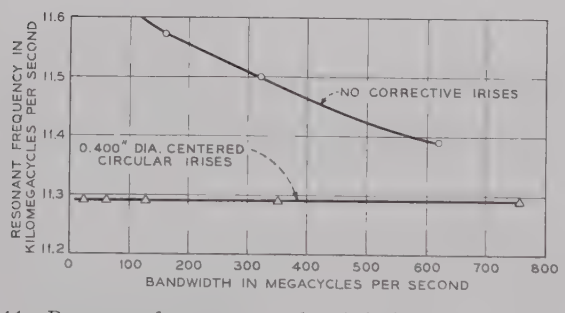

Fig. 11—Resonant frequency vs bandwidth for two step-twist-junction filters with rotatable center sections.

widths, to ±4 Mc at the 755-Mc bandwidth. The resonant frequency is here taken as the point of minimum transmission loss. This 755-Mc bandwidth is the maximum bandwidth that can be obtained with the cavity with circular (0.400-inch diameter) irises attached. The cavity with no irises on the ends of the center section will, of course, produce bandwidths limited only by the useful frequency range of the waveguide, at the expense of a changing resonant frequency with bandwidth and a slightly poorer resonant frequency transmission loss due to a more critical clamping problem for this model. The effects of rectangular and square irises on the resonant frequency vs bandwidth plot were also investigated but these proved inferior to the circular iris result presented in Fig. 11.

Conclusions

Design data has been presented for step-twist-filters in the vicinity of 11.178 kMc. Corrective irises have been described which will keep the resonant frequency of these filters constant (within experimental accuracy) as the bandwidth is varied from a few megacycles to 755 Mc. The addition of tuning screws in the appropriate place will, of course, allow variations of the center frequency of several hundred megacycles (depending upon the required Q of the cavity), and thus these variable bandwidth filters can be quickly and accurately adjusted to a given bandwidth and center frequency with the aid of an X-band sweeper. The design problem of obtaining a given bandwidth with practical tolerances (which in the usual type of filter is not readily adjustable) is thus alleviated.

At the expense of a slightly increased insertion loss, and with the irises attached to the holders rather than the rotatable center section, we may stock a few pieces of X-band guide of different lengths for filter cavities and with appropriate tuning screws we may cover the entire range of the guide in resonant frequency, and all but extremely narrow bandwidths at which the clamped junctions may become troublesome.

The constant frequency filters also allow the interesting possibility of cascading several sections and by adjusting the several θ's and resonant frequencies, actually obtaining any desired response by a direct experimental observation. The angle of rotation can also be servo controlled to provide one with electronically variable filter characteristics.

The inclusion of the first-order frequency sensitivity of step-twist-junctions in the filter design equations (4) and (8) allows one to accurately design broad-band waveguide filters utilizing these junctions.

Appendix

Tests were run on a 70° and an 80° step-twist junction to determine the range of application of (4) and (8). These two values of θ include bandwidths of approximately 1600 to 30 Mc. Values for the admittances of the two twists were obtained at 10.7, 11.2, and 11.7 kMc and were checked against our approximation of Fig. 3(b). For the 70° twist a was constant within experimental error, while B, instead of being a constant, actually varied ±0.3 about its 11.2 kMc value of 2.5 (+0.3 at 10.7 kMc and −0.3 at 11.7 kMc). For the 80° twist a varied ±0.010 about its 11.2 kMc value of 0.046 (−0.010 at 10.7 kMc and +0.010 at 11.7 kMc),

while B varied only ± 0.2 about its 11.2 kMc value of 5.8.

For twists of less than 70° a remains constant, while the approximation that B is a constant degenerates; for twists of more than 80° the approximation that a is a constant apparently degenerates, while the approximation that B is a constant improves.

At first glance the apparent 22 per cent error in assuming a equal to a constant for the 80° twist might appear alarming, but it should be remembered that this 22 per cent error is measured over a 1000-Mc range, whereas the 80° twist can be utilized in a filter cavity to produce no more than a 30-Mc bandwidth filter. Actually at the 3-db points, a differs from the 11.2 kMc value by less than 1 per cent. The approximation that a is a constant thus remains valid for twist angles greater than 80°, as well as for twist angles less than 70°.

The approximation that B is a constant, while being very good at twist angles of 80° and higher, is beginning to degenerate for a 70° twist. It is expected that, due to this variation, the design formulas will degenerate for bandwidths much in excess of 10 per cent.

Acknowledgment

The author would like to express his thanks to S. F. Jankowski and J. D. Deith for experimental assistance, and to D. H. Ring, E. A. Marcatili, and others at the Holmdel laboratory for many informative discussions.

Resonators for Millimeter and Submillimeter Wavelengths*

WILLIAM CULSHAW†, SENIOR MEMBER, IRE

Summary—**Further considerations on the mm-wave Fabry-Perot interferometer are presented. Computed Q values for parallel metal plate resonators indicate that at spacings around 2.5 cm, values ranging from 60,000 at 3 mm, to 300,000 at 0.1 mm wavelengths are possible. The plates must, however, be quite flat. These results are important for many investigations, and in particular for mm and sub-mm wave maser research. For the aperture per wavelength ratios possible here, diffraction effects should be small. Consideration is given to using curved reflectors or focused radiation in applications where the fields must be concentrated. For this purpose, re-entrant conical spherical resonators are treated in detail, as regards operation in the TEM mode at high orders of interference. Expressions for the Q and shunt impedance are given, and high values are possible at mm and sub-mm wavelengths. Quasi-optical methods of coupling into and out of such a resonator are proposed, and the higher modes possible in such a resonator are considered. Results indicate that it could have application to the mm-wave generation problem, and that it represents a good resonant cavity for solid-state research at mm and sub-mm wavelengths, and for maser applications in particular.**

Introduction

IN the region of wavelengths extending downwards from around 1 mm to the long infrared, much important research needs to be done, and many important applications arise. At these wavelengths, conventional cavity resonators become extremely minute, since their dimensions are around one-half wavelength. For some purposes, cavities of larger dimensions, capable of sustaining a number of higher order modes, are possible. This is a difficult procedure, and the difficulties increase with decreasing wavelength for a given size of cavity. Cavities much larger in terms of the wavelength, but which permit mode-free operation, are thus needed. In particular, the development of such a cavity with a suitable interaction gap and new methods of input and output coupling other than conventional waveguides would greatly assist in the development of a primary coherent electronic source for these wavelengths.

Referring to the reflex klystron, which for many purposes is still the most versatile and simplest of microwave tubes, such a cavity must be capable of bunching the electron stream, and hence must possess a suitable interaction gap of small dimensions compared to the wavelength. It also should have a large resonator volume for heat dissipation and a high shunt impedance for efficient electronic interaction. New methods for coupling into and out of the resonator are also necessary. There are other problems, as well, in the design of such tubes for very short wavelengths; another very important one being the provision of an adequate current density at these short wavelengths where the area of the electron beam for efficient interaction with the resonator steadily decreases. This difficulty would certainly be helped by providing larger, more efficient, and more suitable resonators. The required current densities in the resonator gap could possibly be approached with improved cathodes and by the use of suitable magnetic or

* Received by the PGMTT, July 8, 1960; revised manuscript received, October 31, 1960.
† Natl. Bur. of Standards, Boulder Labs., Boulder, Colo.

other focusing devices. In any event, such a resonator development would permit the extension of klystron techniques to shorter wavelengths, and could lead to easier construction techniques and higher powers from tubes presently available at wavelengths extending from 8 mm to around 2.5 mm.

Some progress in this general direction was effected by the development of the dielectric tube resonator.[1] This was used to produce interaction with highly bunched electron beams traveling at relativistic velocities.[2] Such cavities, however, are still not large enough in terms of the wavelength, they do not possess high enough Q values for many purposes, and their use would seem to be limited. Another possibility which seems to possess considerable potential for application in all areas of mm wave research is the mm-wave Fabry-Perot interferometer.[3,4] While this form of resonator is eminently suitable for many purposes, there are other applications, such as the electronic generation problem, or solid-state research, for which a smaller interaction space is desirable. Thus one might make the reflectors spherical and use focused radiation between them. Here diffraction problems arise,[5] and while such a system should resonate at infrared or shorter wavelengths, it may not do so at longer mm wavelengths, unless it is large. In any event, it is difficult to confine the field into linear dimensions even of the order of a wavelength in extent, and such a degree of confinement is not sufficient for the efficient bunching of electron streams as in a klystron. Thus, one must consider the provision of side walls round the interferometer, and a deformation of this into a cavity resonator bounded by two re-entrant cones and a sphere. Such a cavity was considered in the classical paper by Hansen and Richtmeyer[6] on resonators suitable for klystron oscillators, and it has also received considerable attention, particularly by Schelkunoff,[7,8] in the treatment of biconical antennas. At longer wavelengths, other types of resonators proved more suitable. However, at mm and sub-mm wavelengths, such conventional resonators become very small and serious problems arise in heat dissipation, low Q factors, low shunt impedance and in fabrication.

The paper presents a new appraisal of the biconical spherical resonator in the light of the new developments in the mm-wave Fabry-Perot interferometer and the possibility of operating such a biconical resonator at large orders of interference. This would provide a suitable resonator for the purposes discussed above. Features which help this approach considerably are that the coupling into the large biconical resonator is possible by a whole series of regularly spaced coupling holes as in the mm-wave interferometer, and optical methods such as focusing may be used to get the radiation into and out of such a resonator. Such methods seem highly desirable in this wavelength region.

Planar Millimeter Wave Interferometer or Resonator

Fig. 1 shows the mm-wave interferometer as used in transmission measurements.[4] The reflector system may be regarded as a resonant cavity formed by the parallel metal plates and the multiple reflections of plane waves between them. The holes are then exactly analogous to the coupling holes or irises used in microwave cavity resonators, and they provide the means for coupling into and out of the resonance region between the plates, while preserving the large Q value of the metal plate region. For small holes, the loading on the interferometer due to the generator and load impedances is small and can be adjusted by the hole diameter. Side wall losses are essentially absent except for diffraction effects, which can be kept small, and which decrease with decreasing wavelength. This results in a Q for the interferometer which increases directly as the order of interference. Referring to Fig. 1, the field at resonance due to plane waves between the plates with the origin as shown is given by

$$E_y = -2jE_0 \sin (n\pi z/d),$$
$$\eta H_x = 2E_0 \cos (n\pi z/d), \tag{1}$$

where d is the distance between the plates, E_0 is a constant, and $\eta = (\mu/\epsilon)^{1/2}$ is the intrinsic impedance of the medium between the plates in mks units. The energy stored and the mean power lost per unit area of the plates may be deduced from (1), and hence the unloaded Q determined, *viz.*,

$$Q_0 = \lambda/\Delta\lambda = n\pi/(1 - R), \tag{2}$$

where $R = 1 - (8\epsilon\omega/\sigma)^{1/2}$ is the power-reflection coefficient of the metal, ϵ and μ are its permittivity and permeability, usually equal to those of free space, σ is the conductivity, and ω is the angular frequency. In terms of the fringe width Δd between half power points we may write, using the equation $2d = n\lambda$,

$$Q_d = \lambda/\Delta d = 2\pi/(1 - R). \tag{3}$$

[1] R. C. Becker and P. D. Coleman, "The dielectric tube resonator: a device for the generation and measurement of millimeter and submillimeter waves," *Proc. Symp. on Millimeter Waves*, Polytechnic Inst. of Brooklyn, Brooklyn, N. Y., pp. 191–222; March, 1959.

[2] M. D. Sirkis and P. D. Coleman, "The harmodotron—a megavolt electronics millimeter wave generator," *J. Appl. Phys.*, vol. 28, pp. 944–950; September, 1957.

[3] W. Culshaw, "Reflectors for a microwave Fabry-Perot interferometer," IRE Trans. on Microwave Theory and Techniques, vol. MTT-7, pp. 221–228; April, 1959.

[4] W. Culshaw, "High resolution millimeter wave Fabry-Perot interferometer," IRE Trans. on Microwave Theory and Techniques, vol. MTT-8, pp. 182–189; March, 1960.

[5] G. W. Farnell, "Measured phase distribution in the image space of a microwave lens," *Canad. J. Phys.*, vol. 36, pp. 935–943; July, 1958.

[6] W. W. Hansen and R. D. Richtmeyer, "On resonators suitable for klystron oscillators," *J. Appl. Phys.*, vol. 10, pp. 189–199; March, 1939.

[7] S. A. Schelkunoff, "Electromagnetic Waves," D. Van Nostrand Book Co., Inc., New York, N. Y., pp. 285–290; 1943.

[8] S. A. Schelkunoff, "Advanced Antenna Theory," John Wiley and Sons, Inc., New York, N. Y., pp. 32–71; 1952.

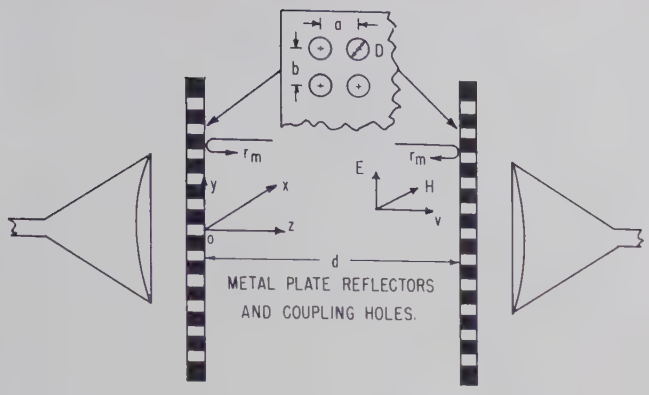

Fig. 1—Millimeter wave Fabry-Perot interferometer.

Since R will be around 0.999 for a metal at these frequencies, (3) shows that the metal plates must be quite flat, within 1/1000 of the operating wavelength.

Table I gives values of Q_0 for wavelengths extending into the submillimeter region and illustrates the great advantages of the Fabry-Perot interferometer, since it would be very difficult, if not impossible, to make conventional cavity resonators for these wavelengths. In contrast to these results, ideally an unloaded Q value of some 9000 would be obtained at 1 mm wavelength with a cylindrical cavity of diameter 0.060 inch operating in the $TE_{01,50}$ mode. This interferometer is thus ideal for many purposes, permitting the use of relatively large structures at these very short wavelengths with freedom from most higher order modes.

TABLE I

Computed unloaded Q Values for Silver Plates Spaced 2.5 CM Apart in a MM-Wave Interferometer (Conductivity σ Taken as 6.139×10^7 Mhos/M).

λ_{mm}	n	R	Q_0
3.125	16	0.99917	60,300
2.0	25	0.99896	75,300
1.0	50	0.99852	106,500
0.5	100	0.99792	150,000
0.1	500	0.99533	333,900

At suitable terminals, the holes may be regarded as perfect transformers, which enable us to couple into the metal plate resonator, in a uniform and efficient manner. Equivalent circuits for the mm-wave Fabry-Perot interferometer may now be drawn, and are shown in Fig. 2(a) and 2(b) for the transmission and reaction types respectively. The hole size may now be fixed by equating the reflectivity of the bulk metal to that deduced by regarding the hole as a reactive structure on a transmission line.[3] Smaller and larger hole sizes than those given by this criterion correspond respectively to lower and higher values of loading on the interferometer than those given by the matched condition. Such reflectors will have adequate bandwidth for mm-maser and spectroscopy applications, and designs can be optimized for any given wavelength region. The application of the

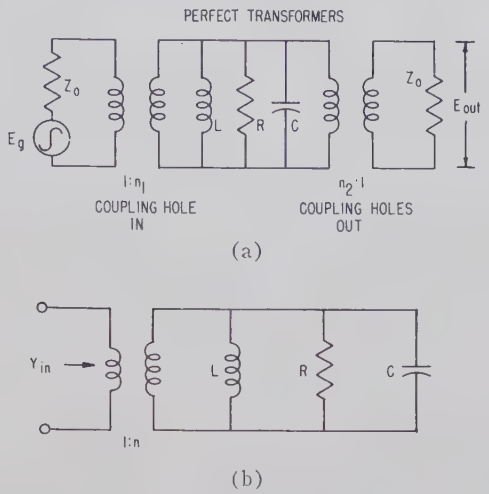

Fig. 2—Equivalent circuits for interferometer. (a) Transmission type. (b) Reaction type.

Fabry-Perot interferometer to the problem of mm-wave masers and spectroscopy is under active development.

Curved or Focused Fabry-Perot Resonators

For some experiments and applications, the planar type of interferometer or resonator is not suitable. Examples of this occur in solid-state research, optical-maser work, and electronic interaction with electric fields. Here, the resonator fields must be concentrated into a smaller volume, and it is natural to consider the use of cylindrical or spherical Fabry-Perot plates and focused radiation to produce concentrated fields in the vicinity of a focus. Such an arrangement might resonate in an analogous way to the plane reflector geometry, and coupling again be effected by a whole series of coupling holes. Fig. 3 shows a possible arrangement for a transmission interferometer employing curved reflectors. Either cylindrical or spherical reflectors could be used with appropriate lenses. The lines showing the concentration of the field and the constant-phase fronts are purely qualitative, but indicate approximately the field distribution between such plates.

The field distribution near the focus of a converging spherical wave has received extensive theoretical study.[9] With the coherent microwave sources and techniques now available, the field distribution in such regions can be experimentally determined. Such work has substantiated the results obtained by applying scalar diffraction theory to this problem when the aperture dimensions are some twenty wavelengths or more in extent,[5] and the regions of interest are close to the axis and somewhat distant from the lens. The literature on this subject is quite extensive, and we shall limit our remarks to those closely connected with the idea of using curved Fabry-Perot resonators.

[9] M. Born and E. Wolf, "Principles of Optics," Pergamon Press, London, Eng. pp. 434–448; 1959.

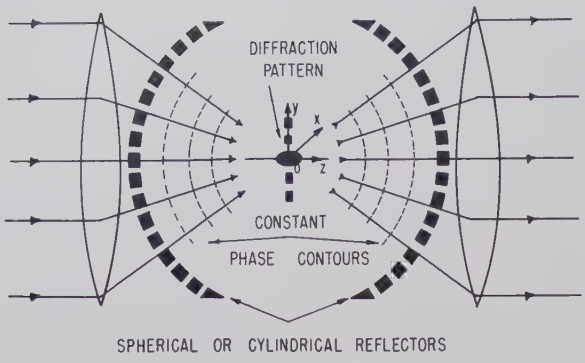

Fig. 3—Focused Fabry-Perot interferometer.

A full treatment of the problem for optics is given in reference 9, and general expressions are derived for the field in the focal region. Referring to Fig. 3, isophotes, or contour lines of intensity $I(p, q)$ near the focus of a converging spherical wave, as well as contours of equal phase, are given. Here $p=\beta z(a/f)^2$, and $q=\beta\rho(a/f)$, where $2a$ is the aperture diameter, f is the focal length, $\beta=2\pi/\lambda$, and $\rho=(x^2+y^2)^{1/2}$ is the radial distance in the focal plane $z=0$. In optics, the intensity distribution is symmetrical about the geometrical focal plane and also about the z axis. Also, the surfaces of constant phase are surfaces of revolution about the z axis. At a distance from the focus, the constant phase surfaces coincide with the spherical wave fronts of geometrical optics but become gradually deformed near the focal region. In the immediate region of the focus, the constant phase surfaces are plane, and on passing through this region, they gradually deform and again become spherical, but with opposite curvature.

In the focal plane $z=0$, the intensity is given by[9]

$$I(0, q) = \left[\frac{2J_1(q)}{q}\right]^2 I_0, \tag{4}$$

where J_1 is the usual Bessel function. This distribution is characteristic of the Airy-ring diffraction pattern in the image plane of an optical lens.[10] Along the z axis, the field intensity is given by

$$I(p, 0) = \left[\frac{\sin p/4}{p/4}\right]^2 I_0. \tag{5}$$

Eqs. (4) and (5) indicate the degree of confinement of the field possible in the focal region for given ratios of f/a. The first zero of $J_1(q)$ is at $q=3.83$; and for $f/a=4$, the radius to the zero of the central ring is 2.5λ. Along the z axis, the first zeros occur for $z=\pm f^2\lambda/2a^2$, and for $f/a=4$, we obtain $z=\pm 8\lambda$.

Farnell[5] discusses the field in the image space of a microwave lens, the main differences from optics arising because of the much smaller aperture to wavelength ratios possible with microwaves. With an optical lens, the field in the focal region is concentrated into smaller volumes and approximations can be used which are not necessarily valid for microwaves. Fig. 4 shows measured contours of constant phase in the image space of a microwave lens. This had a diameter of 50 cm, a focal length around 60 cm, and the wavelength used was 3.22 cm. Contours of constant intensity are also given in reference 5. The same general features discussed above for light optics are evident; there are, however, differences in the shape of the contours. Here the constant phase surfaces and the Airy pattern in the focal plane are slightly curved, the center of curvature being at the lens center as shown. Also the center of curvature of the wave diverging from the focus is at the position of maximum intensity which is not at the focus, but at a point some 2 wavelengths nearer the lens. The center of curvature of the converging wave, however, is at the geometrical image or focus. The deviations are due to the larger angular patterns which occur with microwave lenses, and at shorter mm and sub-mm wavelengths with similar aperture sizes, the optics distribution discussed above would be approached.

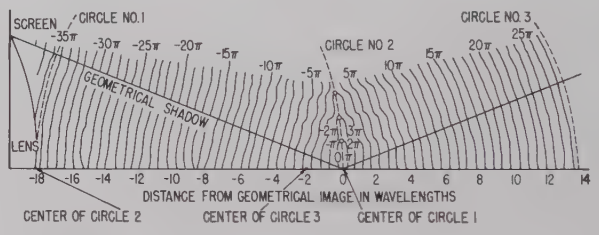

Fig. 4—Measure contours of constant phase in image space of a microwave lens with $R=63$ cm, $a=25$ cm, and $\lambda=3.22$ cm. Phase at geometrical image taken as $\pi/2$ radians. (After G. W. Farnell, *Canad. J. Phys.*, vol. 36, p. 935; 1958.)

Matthews and Cullen[11] have investigated at microwaves a converging spherical wave limited by a rectangular aperture. The approximations used in their analysis correspond to those used in optics, and are therefore valid when the diffraction pattern in the focal region is of small extent. Their deductions and measurements, however, give an interesting physical picture of what happens in the focal region and indicate that there are variations in axial wavelength in the focal region as compared to the free space wavelength. Results in the regions investigated indicated an increase in axial wavelength, or a decrease in the axial propagation constant at small distances either side of the focus. Linfoot and Wolf[12] also deduce that in optics there are regions very near the focus where the nearly plane constant phase surfaces are spaced closer together by a factor $1-a^2/4f^2$ than those in a parallel beam of light of the same wave-

[10] *Ibid.*, pp. 394–397.

[11] P. A. Matthews and A. L. Cullen, "A study of the field distribution at an axial focus of a square microwave lens," *Proc. IEE*, Pt. C., vol. 103, pp. 449–456; July, 1956.

[12] E. H. Linfoot and E. Wolf, "Phase distribution near focus in an aberration-free diffrasion image," *Proc. Phys. Soc. (London)*, vol. 69, pp. 823–832; November, 1956.

length. There are also regions of rapid phase variation at the nulls of the Airy pattern and along the axis.

We may sum up the possible use of curved reflectors for the mm and sub-mm resonator problem as follows. A spherical or cylindrical converging wavefront limited by an aperture gives a region near the focus where the field is concentrated within distances of a few wavelengths. At optical wavelengths, spherical or cylindrical reflectors placed along appropriate phase contours on either side of the focus should resonate at the appropriate wavelength. As indicated by the work at wavelengths of 3.2 cm, there may be departures from ideal conditions at mm and sub-mm wavelengths, and no such resonance may be possible. The problem in this respect needs further investigation. Such resonator types could thus be useful in optical masers and possibly at very short mm wavelengths, although close attention to the preservation of phase shapes in the focal region when obstacles are inserted would be necessary. Since the field in the focal region is still some wavelengths in extent, such a resonator is not suitable for electron bunching or for harmonic extraction from bunched electron beams.

Biconical Spherical Resonators

A. Dimensions, Q Values and Shunt Impedance

The cavity resonator bounded by two re-entrant cones and a sphere, as shown in Fig. 5, was considered in the early phases of klystron resonator development and has also been considered by Schelkunoff.[7] These investigations were concerned with such spherical resonators of radius equal to $\lambda/4$ or with orders of interference of unity. The feature which makes a new appraisal worthwhile is that such resonators can be operated at higher orders of interference provided facilities exist for coupling into and out of such a resonator in a uniform way and no serious difficulties from higher order modes are encountered. Such a method is that of a whole series of coupling holes as used in the planar Fabry-Perot interferometer. Useful features of such a biconical resonator, especially at mm and sub-mm wavelengths, are that the resonator becomes larger, the Q increases with order of interference, and shunt impedance remains high.

Referring to Fig. 5, if an RF voltage is impressed between the apices of the cones, the principal or TEM mode on such a structure is generated. This has the electric lines coinciding with meridians and the magnetic lines along circles coaxial with the axis as shown. Such a system is equivalent to a transmission line of characteristic impedance given by

$$Z_c = 120 \log \cot (\psi/2), \tag{6}$$

and expressions for the electric and magnetic fields may be obtained.[7] Resonances occur when the radius lq of the spherical boundary is equal to $n\lambda/4$, where n is an integer referred to as the order of interference. Here we consider odd values of n or the case of parallel resonance.

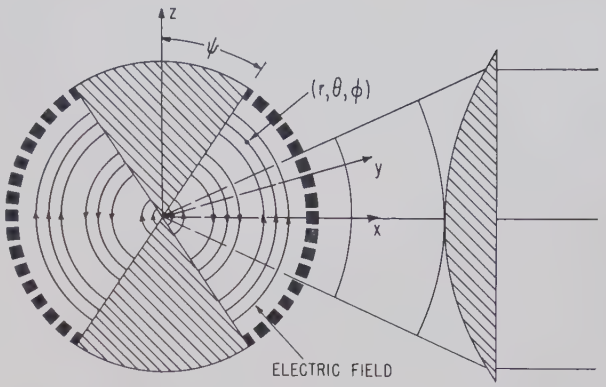

Fig. 5—Biconical spherical resonator and principal TEM mode.

Standing waves then exist in the resonator, and the Q value may be determined for any order n of interference. For equal and opposite cones in the sphere we thus obtain

$$Q_0 = \frac{30\pi^2 n \log \cot (\psi/2)}{R_m[\log \cot (\psi/2) + P \operatorname{cosec} \psi]}, \tag{7}$$

where ψ is the cone angle in Fig. 5 and R_m is the resistive part of the intrinsic impedance of the metal. The parameter P is given by

$$P = \tfrac{1}{2}[C + \log n\pi - Ci(n\pi)], \tag{8}$$

where C is Euler's constant, equal to 0.5772, and the function

$$Ci(x) = \int_{\infty}^{x} \frac{\cos t}{t}\, dt, \qquad x > 0. \tag{9}$$

Similarly, the shunt impedance at resonance is given by

$$Z_i = \frac{14400\pi[\log \cot (\psi/2)]^2}{R_m[\log \cot (\psi/2) + P \operatorname{cosec} \psi]}. \tag{10}$$

Apart from changes due to the increased order of interference n, (7) and (10) are similar to those given by Schelkunoff.[7]

For $n=1$, Q_0 is a maximum when $\psi=33.5°$, and is equal to $132/R_m$; hence $Q_0=924$ for such a copper resonator at $\lambda=1$ mm. Also, for $n=1$, Z_i is optimum when $\psi=9.2°$ and equal to $3.74\times10^4/R_m$ ohms; hence for copper $Z_i=2.6\times10^5$ ohms at $\lambda=1$ mm. It is evident that such a resonator has a high shunt impedance even at short wavelengths, which is a desirable feature for a klystron resonator. However, for $n=1$, the diameter is around 0.020 inch and thus is not very practical. The Q is also low at short wavelengths for this small order of interference.

Fig. 6 shows curves of Q_0 and shunt impedance Z_i for a copper resonator at a wavelength of 1 mm and order of interference $n=41$. As for $n=1$, Q_0 is a maximum when $\psi=33.5°$. The optimum angle for Z_i depends on n, and is given by

$$P \cot \psi - (2P \operatorname{cosec} \psi)/[\log \cot (\psi/2)] = 1. \tag{11}$$

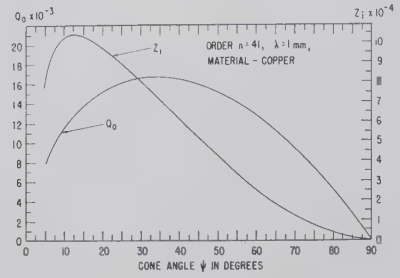

Fig. 6—Unloaded Q values and shunt impedance Z_i of biconical spherical resonator.

Values of Z_i ranging from 75,000 to 100,000 Ω are thus obtained for $n=41$, the diameter of the resonator at $\lambda=1$ mm then being 2 cm. The Q values are also relatively high for this wavelength, ranging up to 16,000. For a klystron resonator, Z_i is the important parameter and must be as high as possible. For other applications a higher Q may be required, and can be obtained by increasing n. Thus for $n=101$ and $\psi=22.5°$, we obtain $Q_0=34{,}200$ and $Z_i=83{,}500$ ohms, with a resonator diameter of 5 cm. The DX 151 Philips klystron for 4 mm wavelengths uses a conventional resonator of diameter 1.6 mm, and height 0.7 mm with a value of Z_i around 77,000 ohms.[13] Such a resonator would thus be extremely small at $\lambda=1$ mm, and Z_i would be reduced to around 38,000 ohms. The advantages of the biconical resonator are thus apparent.

Further computations for $\lambda=0.1$ mm, and $n=401$ are shown in Table II; here the increase in Q should be noted, values of 39,000 now being possible. Due to the increase in R_m at higher frequencies, Z_i decreases but even at $\lambda=0.1$ mm values around 24,000 ohms seem possible. The diameter of this resonator would again be around 2 cm at a sub-mm wavelength of 0.1 mm, an extremely important consideration for many areas of work.

TABLE II

VARIATION OF Q VALUES AND SHUNT IMPEDANCE Z_i FOR BICONICAL RESONATORS AT $\lambda=0.1$ MM AND ORDER OF INTERFERENCE $n=401$

ψ_0	10	13	22.5	33.5
Q_0	26,500	30,200	37,000	39,370
Z_i	24,100	24,400	22,300	17,600

For some purposes the resonator formed by a single re-entrant cone inside a hemisphere, as in Fig. 7, might be useful. Similar considerations apply to this type, and general expressions for Q_0 and Z_i are then

$$Q_0 = \frac{30\pi^2 n \log \cot(\psi/2)}{R_m[\log \cot(\psi/2) + P(\operatorname{cosec}\psi + 1)]}, \qquad (12)$$

and

$$Z_i = \frac{7200\pi[\log \cot(\psi/2)]^2}{R_m[\log \cot(\psi/2) + P(1 + \operatorname{cosec}\psi)]}. \qquad (13)$$

Both Q_0 and Z_i are thus smaller for this resonator, Z_i having around half the value for two re-entrant cones. However, such a resonator could be useful in applications where a number of closely spaced cavities are required.

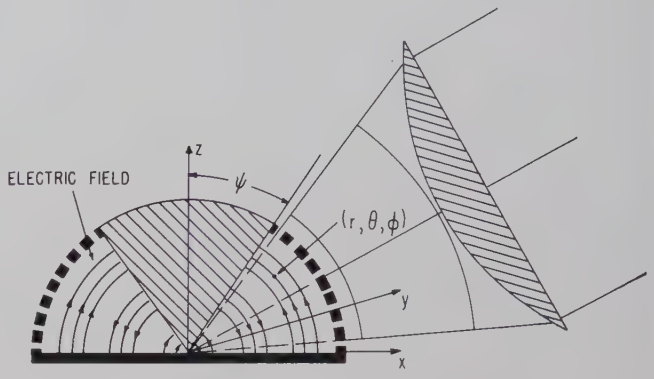

Fig. 7—Hemispherical conical resonator.

B. Coupling Considerations

Ideas on possible forms of coupling into such a resonator arise when it is considered as a distortion of the planar Fabry-Perot interferometer. Hence the design of the whole array of coupling holes will be similar, except now they will be on the surface of the spherical portion and focused radiation must be used as indicated in the figures. The intrinsic impedance of the principal mode is that of free space, *viz*, $E_\theta/H_\phi=\eta$, and the characteristic impedance Z_c may thus be regarded as derived from series and parallel combinations of elemental parallel-plate transmission lines, the number of which are determined by the hole spacings on the spherical surface. Since the number of such holes at fixed spacings around the circle $\theta=$ constant on the sphere varies as $\sin\theta$, a resultant Z_c of the form given by (6) is obtained.

From such general considerations, we deduce that the impedance transformations through the equally spaced holes on the spherical surface are identical, since the electric and magnetic walls into which the cavity can be divided give rise to a system of equal parallel-plate transmission lines with intrinsic impedance η. The amplitude transmission coefficients are also identical for all such holes, and since the number of holes around a given latitude varies as $\sin\theta$, and the fields vary as $1/\sin\theta$, the total power transmission from the cavity is the same along each line of latitude. The holes can thus be equally spaced along circles of latitude; some adjustment of the final hole along such a circle will, however, be necessary in general. The same spacings in the θ direction may also be used, but the lines of hole centers need not coincide with lines of longitude.

[13] B. B. Van Iperen, "Reflex klystrons for millimeter waves," *Proc. Symp. on Millimeter Waves*, Polytechnic Inst. of Brooklyn, Brooklyn, N. Y., pp. 249–250; March, 1959.

The biconical resonator may be regarded as a transmission line of length $n\lambda/4$, and of characteristic impedance Z_c given by (6). The impedance across the cone apices for any uniform impedance Z_t over the spherical boundary is then given by

$$Z = Z_c \frac{Z_t + jZ_c \tan \beta l}{Z_c + jZ_t \tan \beta l}. \tag{14}$$

and for $l = n\lambda/4$, $Z = Z_c^2/Z_t$. For a coupling hole system extending over the complete spherical surface, Z_t will be uniform over the surface and may be deduced from the equivalent circuit for such a coupling hole. Thus, the load impedance at the apices can be determined, and hence the degree of loading as compared with the shunt impedance Z_i of the resonator can be deduced.

Another approach which is useful when only a part of the spherical surface has coupling holes, and also in the previous case, is to use the general formulas[7] to determine the Q factor and the shunt impedance Z_i. The impedances transformed from free space through such holes give rise to increased losses over that portion of the spherical boundary concerned, and the external Q values and load impedances can be determined. Thus the result for the increased power loss due to the load coupling will be given by

$$W_L = \tfrac{1}{2} R \int H_\phi H_\phi^* dA, \tag{15}$$

where the limits of integration for ϕ and θ extend over the coupling region on the sphere, and R is the resistive part of the load impedance at the spherical boundary. In this way the effect of various degrees of coupling can be considered and loaded Q values and load impedances determined. A number of coupling holes are thus required, and this approach should be reasonably valid if the area over which energy is coupled into or out of the resonator is large compared with the wavelength; otherwise diffraction effects will be serious. Since such reconators are intended for very short wavelengths this condition can be satisfied.

The coupling may thus be deduced from the equivalent circuit for a single coupling hole in a metal plate, which is shown in Fig. 8. Values of the susceptances are given by the following equations.[14]

$$B_a = \frac{B}{2Y_0} + \frac{|Y_0'|}{Y_0} \tanh\left(\frac{\pi t}{|\lambda_g'|}\right),$$

$$B_b = \frac{|Y_0'|}{Y_0} \operatorname{csch}\left(\frac{2\pi t}{|\lambda_g'|}\right), \tag{16}$$

where in our case $B/2Y_0 = (3a^2\lambda)/(2\pi D^3)$, and

$$\frac{|Y_0'|}{Y_0} = \frac{0.284 a_g^2 \lambda}{D^3}\left[1 - \left(\frac{1.706D}{\lambda}\right)^2\right]^{1/2}, \tag{17}$$

[14] N. Marcuvitz, "Waveguide Handbook," M.I.T. Rad. Lab. Ser., McGraw-Hill Book Co., Inc., New York, N. Y., pp. 408–412; 1951.

approximately. Here a_g refers to the large dimension of a rectangular waveguide propagating only the dominant mode, and $|\lambda_g'|$ is given in reference 14. For matched conditions in free space, the transformed normalized impedance at the inside wall of the sphere is then given by

$$Z = \frac{B_b^2 + j(B_a + B_b)(B_a^2 + 2B_aB_b + 1)}{(B_a^2 + 2B_aB_b)^2 + (B_a + B_b)^2}. \tag{18}$$

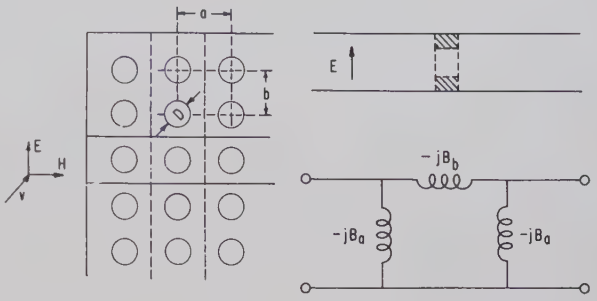

Fig. 8—Perforated metal plate and equivalent transmission line circuit electric wall ——, magnetic wall - - -.

The phase angle of the reflection coefficient at the spherical boundary may thus be determined, and the effect of transformed reactances on the resonance condition investigated for various hole configurations and wall thicknesses. This is important since the resonance condition demands a uniform phase shift over the spherical surface, and the phase changes occurring in regions where there are coupling holes differ from those at a metal wall. However, the phase change for holes in thick walls is not very different from that due to holes in the thinner walls where coupling is effected. This occurs because all holes are circular waveguides excited beyond cut-off, and the reactive contribution to the transformed impedance is close to that due to the hole at the inner surface of the sphere.

Thus, areas other than those used for energy transfer could possibly have thicker walls with holes similar to those in coupling areas. It may also be possible by suitable impedance transformations to have holes only in such coupling regions, with the remaining parts of the metallic spherical surface undisturbed. This would be a more satisfactory arrangement, and while the problem of coupling requires experimental evaluation, it seems clear that it can be done along the lines described.

Higher-Order Modes

So far, we have tacitly assumed the existence of only the principal mode in the biconical resonator, and we must now consider whether difficulties can arise from the higher-order modes which can also exist in it. The problem has been extensively treated by Schelkunoff in his work on antennas.[8] With an impressed RF voltage between the apices of the cones, the modes in question are the transverse magnetic spherical ones with $H_r = 0$.

As we have seen, in the biconical region a principal TEM wave exists with the electric field lines terminating normally to the conical surfaces. A continuation of this mode into free space is not possible, and in the case of the biconical antenna, other modes are generated at the spherical boundary between free space and the ends of the cone. The boundary conditions at the spherical boundary between the fields in the antenna region and the fields of spherical TM waves in free space may then be satisfied. Fig. 9 shows the electric field configuration for the first-order TM spherical wave in free space and in the biconical region respectively. The field patterns are quite similar, the difference being the presence of the small loops near the conical conductors which satisfy the boundary conditions for the electric field. The patterns for modes of higher-order are quite similar, except that the number of loops increases. Such field configurations are directly analogous to the electric field patterns of higher-order TM_{0n} modes between parallel plates and arise from appropriate distortions of such plates. If b is the spacing between the plates, the cut-off wavelengths for these modes are given by $2b/n$.

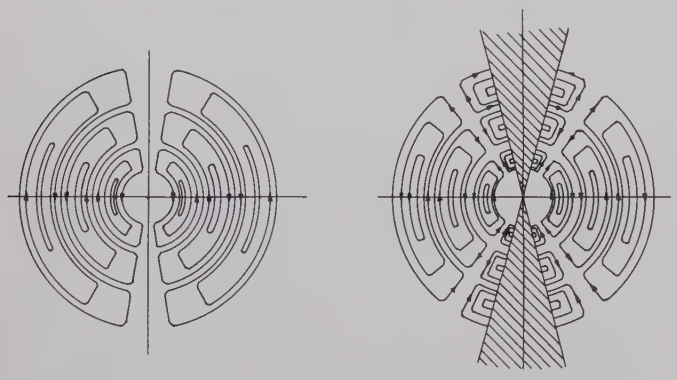

(a) (b)

Fig. 9—Electric field of first order TM spherical wave. (a) In free space. (b) With conical conductors. Magnetic lines circles coaxial with cones.

In the proposed biconical resonator, the fields are enclosed by a metallic spherical boundary on which the boundary conditions on the field may be satisfied by the fields of the dominant TEM wave, the electric field of which is given by

$$E_\theta = j\eta \frac{I_0 \sin \beta(l - r)}{2\pi r \sin \theta}, \tag{19}$$

where I_0 is the maximum current at $r = l$, and l is the radius of the sphere.[8] Thus, no higher-order modes arise at such a boundary, and this is still true when the coupling holes are present since these are spaced less than $\lambda/2$ apart. The fringing fields at the holes then correspond to non-propagating modes between parallel plates and represent a localized impedance at the spherical boundary. It follows then that no higher-order modes should exist in the resonator when the radius of the input region r_i is very small, or when the cones are pointed. Such higher-order modes may be generated in the input region around the apices of the cones if this is finite in extent, and this must be considered.

Expressions for such fields are given by Schelkunoff[8] and are independent of the angle ϕ. We shall be concerned with θ component of the electric field, which is given by

$$rE_\theta = \frac{\eta V(r)}{2\pi Z_c \sin \theta} + j\frac{\eta}{2\pi} \sum_n \frac{1}{n(n+1)} \frac{d}{d\theta} M_n(\cos \theta) S_n'(\beta r). \tag{20}$$

Here $M_n(\cos \theta) = \frac{1}{2}[P_n(\cos \theta) - P_n(-\cos \theta)]$, P_n being the Legendre function of order n, and

$$S_n(\beta_r) = A_n Jn_n(\beta r) + B_n Nn_n(\beta r), \tag{21}$$

where $Jn_n(\beta r)$ and $Nn_n(\beta r)$ are the normalized Bessel functions of the first and second kind, and A_n and B_n are constants determined from the boundary conditions. Values of n over which the summation in (20) is made are determined by the relation

$$M_n(\cos \psi) = 0, \tag{22}$$

which corresponds to the condition $E_r = 0$ on the conical surfaces. Generally, the values of n are not integral and may be determined from the formula[8]

$$n_m(\psi) = \left[\left(\frac{2m\pi}{\pi - 2\psi}\right)^2 - \frac{1}{4}\right]^{1/2} - \frac{1}{2}, \tag{23}$$

where $m = 1, 2, 3, \cdots$.

The component E_θ of the electric field must vanish at the spherical boundary for all values of θ, and hence from (20) we must have

$$S_n'(\beta l) = 0, \tag{24}$$

expressing the resonance condition for any higher-order mode. For perturbations of the input region around the cone apices, the field at a specific input radius r_i may be expanded in terms of the orthogonal properties of Legendre functions and their derivatives; to obtain

$$E_n = \frac{\int_\psi^{\pi-\psi} r_i E_\theta(r_i) \sin \theta \frac{d}{d\theta}(M_n \cos \theta) d\theta}{\int_\psi^{\pi-\psi} \sin \theta \left[\frac{d}{d\theta} M_n(\cos \theta)\right]^2 d\theta}, \tag{25}$$

where

$$[j\eta S_n'(\beta r_i)]/[2\pi n(n+1)] = E_n. \tag{26}$$

The values of the constants A_n and B_n in (21) are now determined from (24) and (26) and will be small if the radius r_i is small. Hence for pointed cones in close proximity at the center, operation in the TEM mode without serious excitation of unwanted modes is feasible. This

also follows, because $Nn_n(\beta r_i)$ becomes infinite when $r_i \to 0$, and hence B_n must be zero in this case.

As an approximation to the resonance condition we may assume that $E_n = 0$ for small input regions or values of r_i. Then we find from (26) that

$$B_n/A_n = -J'n_n(\beta r_i)/N'n_n(\beta r_i), \tag{27}$$

and hence (24) becomes

$$J'n_n(\beta l)N'n_n(\beta r_i) - N'n_n(\beta l)J'n_n(\beta r_i) = 0. \tag{28}$$

But it follows from (27) that B_n/A_n tends to zero for small values of βr_i, particularly for large values of n. Hence for small perturbations of the input region, the resonance condition for higher modes is given by

$$J'n_n(\beta l) = 0, \tag{29}$$

and we have already noted that the amplitudes of such modes will also be small in this case. Such higher modes would also not exist if $r_i E_\theta(r_i) = 0$ for all θ, which occurs when the apices are joined by a metallic sphere in the input region. Other perturbations can be considered for specific cases, such as for a klystron type resonator, and would have to be investigated. The prime criterion is that the transition of the spherical fields of the TEM mode to those in the input region should be smooth and the field patterns matched as far as is possible. This can be approached by suitable shaping in such regions, and hence mode generation kept small.

Eq. (29) represents the condition for resonance in a higher-order mode, and for the large values of βl applicable here, we may write

$$Jn_n(\beta l) \simeq \sin(\beta l - n\pi/2),$$

and hence

$$J'n_n(\beta l \simeq \cos(\beta l - n\pi/2), \tag{30}$$

which gives the condition for resonance as

$$l = (2m + 1 + n)\lambda/4. \quad m = 1, 2, 3, \cdots. \tag{31}$$

Here n is not an integer in general, and this resonance condition can differ from that required for the principal mode. Thus even though higher-order modes are possible, depending on the shape of the input region between the cones, it may be possible to differentiate against them as regards resonance. We remark again that for small input regions, or perturbations, the amplitudes of such modes will be small and, in general, may be kept small by suitable transitions between the field regions in the resonator.

Conclusions

The basic ideas presented here appear to have considerable promise and significance for future work at mm and sub-mm wavelengths. Some results on a planar type of Fabry-Perot interferometer with high resolution may have already been given.[4] This interferometer represents the solution to the wavemeter problem for this wavelength region. The very high Q values already obtained at 6 mm wavelengths and the increases possible at very short wavelengths indicate its great potential use in all phases of millimeter-wave spectroscopy and maser research. A gaseous maser at a wavelength of 3.4 mm, using such an interferometer as the resonator, is under active development. Applications of this interferometer to solid state masers at sub-mm wavelengths are also feasible. As indicated, the curved reflector or focused type of Fabry-Perot interferometer may find similar applications at very short sub-mm or infrared wavelengths, and it represents an interesting problem for future investigation.

The new developments on the biconical spherical resonator which stem from the Fabry-Perot interferometer investigations appear quite significant. Suitable resonators are needed for electronic generation at mm wavelengths, for solid state masers at mm and sub-mm wavelengths, and for many other areas of research in this important wavelength region. The biconical resonator is a possible solution to this problem. The development of such a klystron resonator at reasonable orders of interference would materially help in the major problems of small size, circuit losses and heat dissipation in conventional resonators at these short wavelengths. There remains the problem of obtaining the required current densities from cathodes presently available, since the efficiency of electronic interaction with the resonator depends on the gap diameter as well as on the transit time across the gap.[13] However, the use of such a resonator would certainly assist in the generation of still shorter mm wavelengths, and would possibly permit greater ease in fabrication and greater power outputs to be obtained at wavelengths now possible. Higher-order modes in such a resonator have been discussed, and relatively mode-free operation should be possible. Further work must be done on the investigation of these, and on mechanical tuning methods.

In solid-state maser research this cavity represents a possible solution to the difficult problem of a resonator for a two-level, solid-state maser. This may well represent one method of obtaining relatively high-pulsed powers at mm and sub-mm wavelengths.[15] One of the major problems, that of obtaining a high Q cavity, appears to be adequately met by the biconical resonator, and for ideal conical geometries inside the sphere, mode troubles should not arise. Specimen shapes would conform to the field geometry at the cone apices or completely fill the cavity with the dc magnetic field suitably oriented along the axes of the cones, or along any other preferred direction. The proposed method of coupling would be extremely desirable in all such areas, since it would eliminate the necessity for long lengths of small waveguide into the low temperature bath. The Q of the cavity would also increase at low temperatures. Similar

[15] J. R. Singer, "Masers," John Wiley and Sons, Inc., New York, N. Y., pp. 71–87; 1959.

remarks apply to the three-level, solid-state maser.

Although further development of these resonators is required, such developments appear feasible in contrast to the present difficulties in applying conventional resonators to mm and sub-mm wavelengths. Such difficulties are very severe and most probably conventional resonators are impractical. There appears to be no reason why the ideas presented here should not be intensively pursued, as the rewards and knowledge to be gained from this virtually unexplored region of the electromagnetic spectrum are very great.

Note added in proof: The biconical spherical resonator has now been operated very satisfactorily by Dr. R. W. Zimmerer at wavelengths around 8 mm. The diameter of the sphere used was 4 inches, and the cone angle Ψ was 45°. Coupling holes after the manner described were used only in areas illuminated by the focused radiation. Both quarter-wavelength and half-wavelength resonances were observed and were the dominant ones. The Q value approaches the theoretical one, and higher mode effects are small.

Acknowledgment

The author would like to acknowledge the assistance and encouragement derived from discussions with his colleagues, and in particular, with Dr. R. C. Mockler.

A Recording Microwave Spectrograph*

D. ILIAS†, MEMBER, IRE, AND G. BOUDOURIS‡, SENIOR MEMBER IRE

Summary—**The principle of operation and the fundamentals of realization of a recording microwave spectrograph designed for use in the study of the absorption and the index of refraction of gases under medium pressures (1 mm Hg to 1 atm) are presented. The apparatus results from a similar spectrograph with synchroscope, in which the responses of the cavity resonators are interpreted by means of a pulse method. The high performances of the apparatus render its use advantageous, not only as a spectrograph, but also as an accurate recording refractometer, as well as a direct-reading *Q*-meter.**

I. Introduction

THE IDEA of the application of the pulse technique to microwave spectrographs with cavity resonators [12] was originally suggested in 1953 by Professor A. Gozzini of the University of Pisa (Italy) and his coworkers [2d]. Spectrographs of this type, although subject to continuous improvements, have been constructed in Pisa (Istituto di Fisica), in Paris (Laboratoire de Physique de l'Atmosphère) and in Amsterdam (Natuurkundig Laboratorium Universiteit). The new experimental setup has already been used successfully in various investigations [3]–[7].

The electronic indicator of this apparatus is an oscillograph used as a synchroscope. The result of the measurement is given by the relative positions of the pulses which appear on the screen of the synchroscope. In the following, we will refer to this apparatus as the "spectrograph with synchroscope."

The work described here makes use of this spectrograph to function as a recording instrument. As an output indicator, the synchroscope is replaced by an automatic recorder. The absorption coefficient or the index of refraction is recorded as a function of the pressure of the gas. The apparatus works, as does the previously mentioned spectrograph with synchroscope, in the centimetric (as well as in the millimetric) region of radio waves and is used in the study of gases under medium pressures (from about 1 mm Hg to 1 atm).

This function has been obtained through suitable modifications of the electronic parts of the instrument, especially those of the pulsers. The resulting recording spectrograph extends the possibilities of research in the field of microwave spectroscopy since it can also be used as a refractometer and as a *Q*-meter.

II. The Principle of the Spectrograph with Synchroscope

The original spectrograph with synchroscope has been the subject of previous papers [2a], [5]. Briefly its principle is as follows.

The block diagram is shown in Fig. 1. The energy of the microwave source (a klystron) is frequency modulated by means of an isosceles triangular signal. The modulated energy is guided both to the channel of meas-

* Received by the PGMTT, August 4, 1960; revised manuscript received October 31, 1960.

† Laboratoire de Physique de l'Atmosphère, Faculty of Sciences, the Sorbonne Paris, France.

‡ Laboratoire de Spectroscopie Hertzienne, Faculty of Sciences, Sorbonne University, Paris, France. Formerly with Laboratoire de Physique de l'Atmosphère.

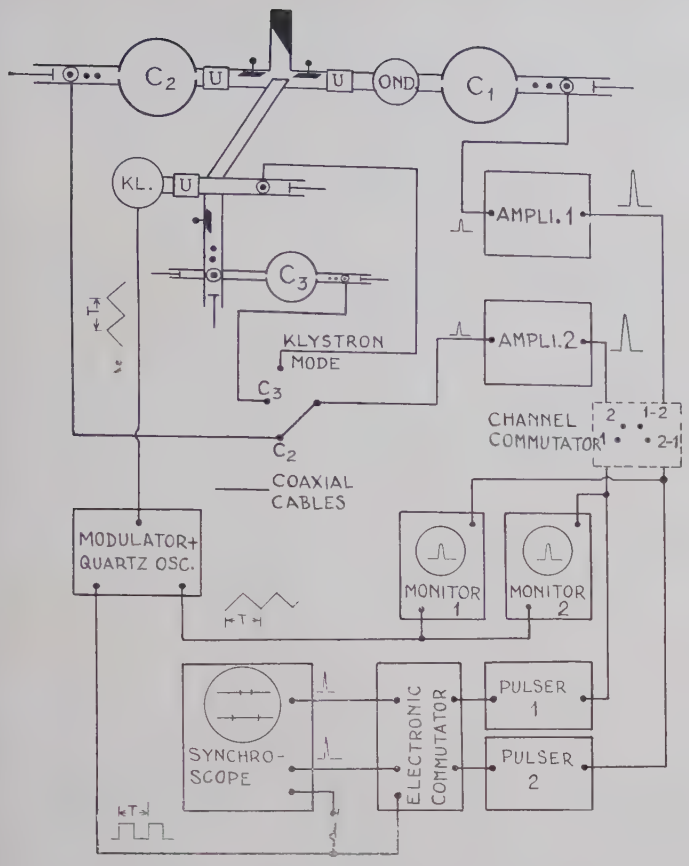

Fig. 1—Block diagram of the spectrograph with synchroscope.

urement and to the channel of reference of the apparatus. The resonance signals (responses) given by the cavity resonators are coupled to the inputs of the pulsers, after detection and amplification.

The pulse technique is used in order to mark, with the best possible accuracy and sensitivity, the relative position and the form of the response of the channel of measurement with respect to that of the channel of reference. This is achieved by the production of very narrow pulses in predetermined points of the response curves. This method is much more advantageous than any of the older methods of direct comparison.

The theory of the apparatus proves that the distances of the pulses appearing on the synchroscope are related, by simple relations, to the index of refraction and the absorption coefficient of the gas placed into the cavity of measurement. In fact, it is known that the introduction of a gas to a cavity resonator causes a displacement of the resonance frequency (effect of the index of refraction) and, at the same time, the resonance signal is broadened and weakened (absorption effect) (Fig. 4).

Although the recording spectrograph is based on the same theoretical considerations, its principle presents some quite essential differences, as will be shown. (See also a brief report in [1].)

III. The Principle of the Recording Spectrograph

Suppose the klystron is doubly modulated in frequency: 1) by the signal of a triangular modulator, and 2) by means of another sinusoidal modulator operating at a frequency of 1 Mc. The response signals received on the crystal detectors now show two secondary maxima due to the sidebands $\nu_0 \pm 1$ (Mc), apart from the central curve of the principal resonance ν_0 of the cavity (Fig. 2). The shape of the principal resonance is practically not disturbed by the presence of its lateral images, because the degree of modulation is adjusted so as to be weak enough, and because the frequency of 1 Mc is quite high with respect to the width of the principal resonance of the cavity.

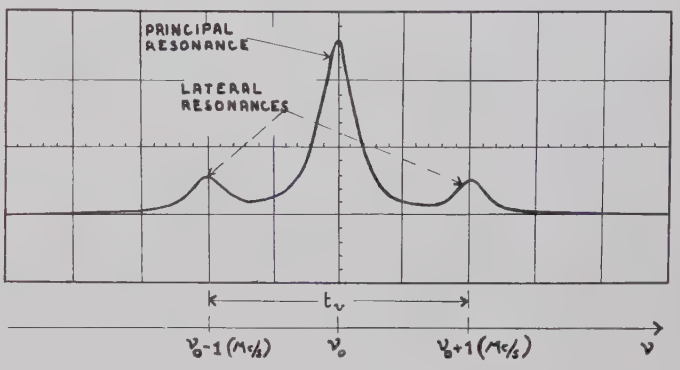

Fig. 2—Response of one cavity when swept by the doubly modulated klystron.

Also, suppose that the power falling on the crystal detector is weak enough so that the detection is quadratic (P_{max} <about 10μW). Furthermore, given that the quality coefficient Q of the cavity is high enough (the special construction of the over-dimensioned cavities provides a quality of the order of 30,000 within the X-band) [2a], [5], we will have for the detected voltage [9], [10]:

$$V = \frac{V_{max}}{1 + 4Q^2\left(\frac{\nu - \nu_0}{\nu_0}\right)^2}, \qquad (1)$$

where V_{max} is the voltage corresponding to the resonance frequency ν_0. The second derivative of this expression with respect to the frequency ν becomes zero at two points around the resonance frequency. The frequency distance of these points is finally given by the relation (Fig. 3):

$$\nu_a = \frac{\nu_0}{Q\sqrt{3}}. \qquad (2)$$

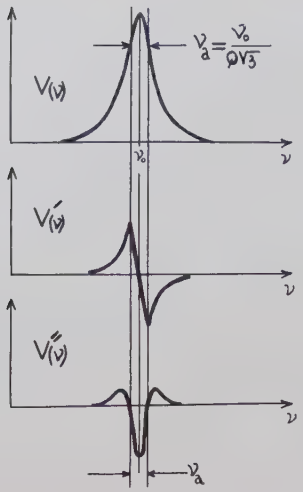

Fig. 3—Cavity principal response and its first and second derivatives.

However, owing to the triangular modulation of the klystron, its frequency is changed according to the equations:

$$\left.\begin{aligned} \nu &= \bar{\nu} + vt && \text{during one half-period} \\ \nu &= \bar{\nu} + v(T - t) && \text{during the next half-period} \end{aligned}\right\}, \quad (3)$$

where T is the sweep period of the klystron (1/50 sec, in our case) and v the velocity of modulation. Taking into account these equations, the above-mentioned frequency distance ν_a corresponds to a time distance t_a:

$$t_a = \frac{\nu_0}{vQ\sqrt{3}}, \quad \left(\text{from which } Q = \frac{\nu_0}{\sqrt{3}\, vt_a}\right). \quad (4)$$

Now let the two cavities of the apparatus be empty and in resonance (both at the same frequency ν_0) at the beginning of an experiment. Suppose we introduce to the cavity of measurement a gas under a certain pressure p, while keeping the reference cavity empty. Then (Fig. 4) the resonance frequency of the cavity of measurement is displaced to a new value, $\nu = \nu_0/n$, where n is the index of refraction of the gas under the pressure p and the temperature of the experiment, while, at the same time, in the case of an absorbing gas, the response curve is broadened.

The frequency displacement of the resonance $\nu_0 - \nu = \nu_0 - (\nu_0/n)$ corresponds to a time difference Δt_n [see (3)]:

$$\Delta t_n = \frac{\nu_0}{v}\left(1 - \frac{1}{n}\right), \quad (5)$$

from which

$$n - 1 = (v/\nu_0) \cdot \Delta t_n, \quad (6)$$

the index of refraction being near enough to unity.

On the other hand, the broadening of the response curves indicates a relative lowering of the quality coefficient of the measurement cavity. Thus, we have (4):

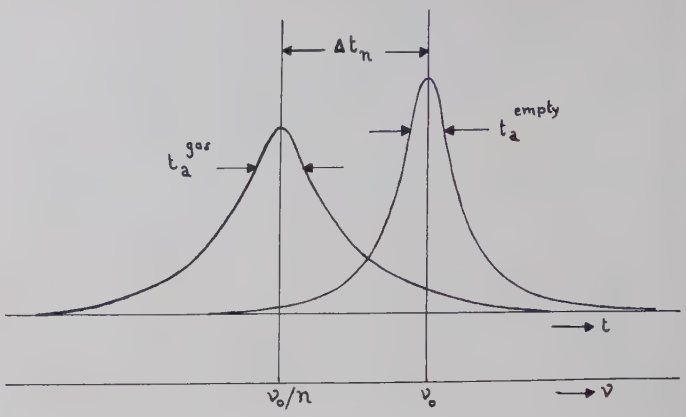

Fig. 4—Effect of the gas refractive index and of the absorption on the response of measurement cavity.

$$\Delta t_a = \frac{\nu_0}{v\sqrt{3}}\left(\frac{1}{Q} - \frac{1}{Q_0}\right). \quad (7)$$

Furthermore, since, as it is known,

$$(1/Q) - (1/Q_0) = \epsilon_r'' = \alpha c/2\pi\nu,$$

where $\epsilon_r = \epsilon_r' - i\epsilon_r''$ is the complex dielectric constant of the gas, α its absorption coefficient (small as compared to unity), and $c \approx 3 \cdot 10^8$ msec (the magnetic permeability of the gas is taken as $\mu_r = 1$), it follows that:

$$\alpha = \frac{2\pi\sqrt{3}\, v}{c} \cdot \Delta t_a, \text{ (neper/m)}. \quad (8)$$

Finally, the relations (6), (8) and (4) take the following practical form if the sweep velocity v is replaced in them by the expression $v = 2(\text{Mc/s})/t_v$, where t_v is the time distance between the two side maxima of the response signal (Fig. 2):

$$N = (n - 1) \cdot 10^6 = \frac{2 \cdot 10^6}{\nu_0} \cdot \frac{\Delta t_n}{t_v} = C_n \frac{\Delta t_n}{t_v}, \quad (9)$$

$$\alpha = \frac{4\pi \cdot 10^6\sqrt{3}}{c} \cdot \frac{\Delta t_a}{t_v} = C_a \frac{\Delta t_a}{t_v}, \quad (10)$$

$$Q = \frac{\nu_0}{2\sqrt{3}} \cdot \frac{t_v}{t_a} = C_Q \frac{t_v}{t_a}, \quad (11)$$

where ν_0 is measured in megacycles, α in neper/m, the time t in microseconds, $c = 3 \cdot 10^8$ m/sec, and C_n, C_a and C_Q are constants.

The measurement of the index of refraction of the gas, its absorption and the quality coefficient of the cavity of measurement, is thus reduced to the measurement of the times t_n, t_a and t_v. This is achieved by so designing the time circuits of the apparatus that a direct current is produced at their output, which is proportional to the intervals being measured; the proportionality factor is constant for every sort of measurement. This direct cur-

rent is used to drive an autographic voltmeter destined to record continuously, on a paper tape, the curves of variation of the measured quantities as a function of the gas pressure.

IV. Operation of the Apparatus

The block diagram of the recording spectrograph is shown in Fig. 5. The different stages of the electronic part can be distinguished, from the operation point of view, into two discrete sets:

1) The block "amplifier—derivation and clipping—electronic windows—pulsers" (one block for each channel of the apparatus) provides at every half-period of the sweep one pair of suitable pulses separated by the time interval t_a, t_n or t_v.

2) The other block which includes the "scale of two," the integrator and the output recorder, and which is connected to the preceding block by means of a relay, receives the above mentioned pairs of pulses and produces a direct current proportional to their distance.

A. Measurement of the Interval t_a

During the measurement of the time t_a (measurement of the absorption, position II of the commutator), a first derivative of the response of the measurement cavity is realized by a resistance-capacity circuit at the output of the preamplifier (oscillogram $1a$ of Fig. 5). After amplification, a second derivation, followed by a clipping deep and symmetrical with respect to the zero level, makes the interval t_a appear in the form of a rectangular signal (central part of oscillogram $2a$). However, this useful signal appears among other parasitic signals with which it is confused. The discrimination is obtained by means of electronic windows $3a$ and $4a$) properly synchronized, which allow the pulser to work only when the desired signal is initiated or interrupted. The leading edges of the pulses given by the pulsers thus constitute very accurate marks which repeat the distance t_a.

The next stage, a bistable multivibrator (scale of two), driven by these pulses, restores the original rectangular signal, but this time free of parasites (oscillogram $6a$). Finally, an integrator produces a direct current:

$$i_a = 2 \cdot 50 \cdot I_{\max} \cdot t_a$$

($T = 1/50$ sec the period of the principal modulation of the klystron) by means of which the recorder is driven. The integrator is a constant current pentode ($I_{\max}$) which conducts only during the intervals t_a and the current of which passes through a rectifying filter.

B. Measurement of the Interval t_n

A similar process is applied for the measurement of the time t_n (measurement of the refractive index, position I of the commutator). The difference is that the two pulses ($5n$ and $5'r$) which determine the interval t_n, now originate from the channel of measurement and from the channel of reference, respectively, and they correspond to the maxima of the principal resonances of the response curves of the cavities.

To produce these pulses, the signals of response are applied, after amplification, directly to the circuits of derivation and clipping. Their first derivatives undergo a strong clipping and they appear in the oscillograms $2n$ and $2r$. The leading edges corresponding to the maxima of the principal resonances of the cavities excite the pulsers, while the effect of any other pulse is eliminated by means of electronic windows.

C. Measurement of the Interval t_v

The pair of pulses used for this measurement corresponds to the maxima of the two side resonances of the cavity of reference (oscillogram $5r$ in Fig. 5).

To pass to this sort of measurement, the triggering of the previously mentioned relay is required. The resistance R, which is then connected at the output of the integrator, protects the microammeter from an excessive direct current. The same resistance, if it has been designed to be variable and calibrated, serves also the measurement of the ratio t_a/t_v when the apparatus is used as a Q-meter.

D. Pressure Marker

The records are obtained during the slow evacuation of the cavity of measurement. A special barometric setup (Fig. 5) allows the calibration of the time axis of the record in pressure units.

The barometric setup consists of a glass tube (internal diameter of the order of 10 mm) provided with metallic contacts 10 mm apart from one another (this distance is suitably corrected so that the effect of the vessel containing the mercury can be taken into account). The metallic contacts consist of tungsten wires sealed along the side of the glass tube so that they penetrate it.

Every contact is connected outside of the barometric tube to a small capacity (100 pF). The free ends of these condensers are short-circuited and brought together, through a resistance of a few tenths of ohms, to a positive potential (90 volts) with respect to the mass of the mercury.

The slow rising of the mercury during the evacuation of the cavity of measurement establishes one contact at every 10 mmHg of pressure. The pulses produced at every new contact because of the charging of the corresponding condenser, after amplification, trigger the monovibrator which acts on the relay. The relay remains triggered for a certain time adjustable from 1 to 20 seconds. During this period, the block "scale-of-two

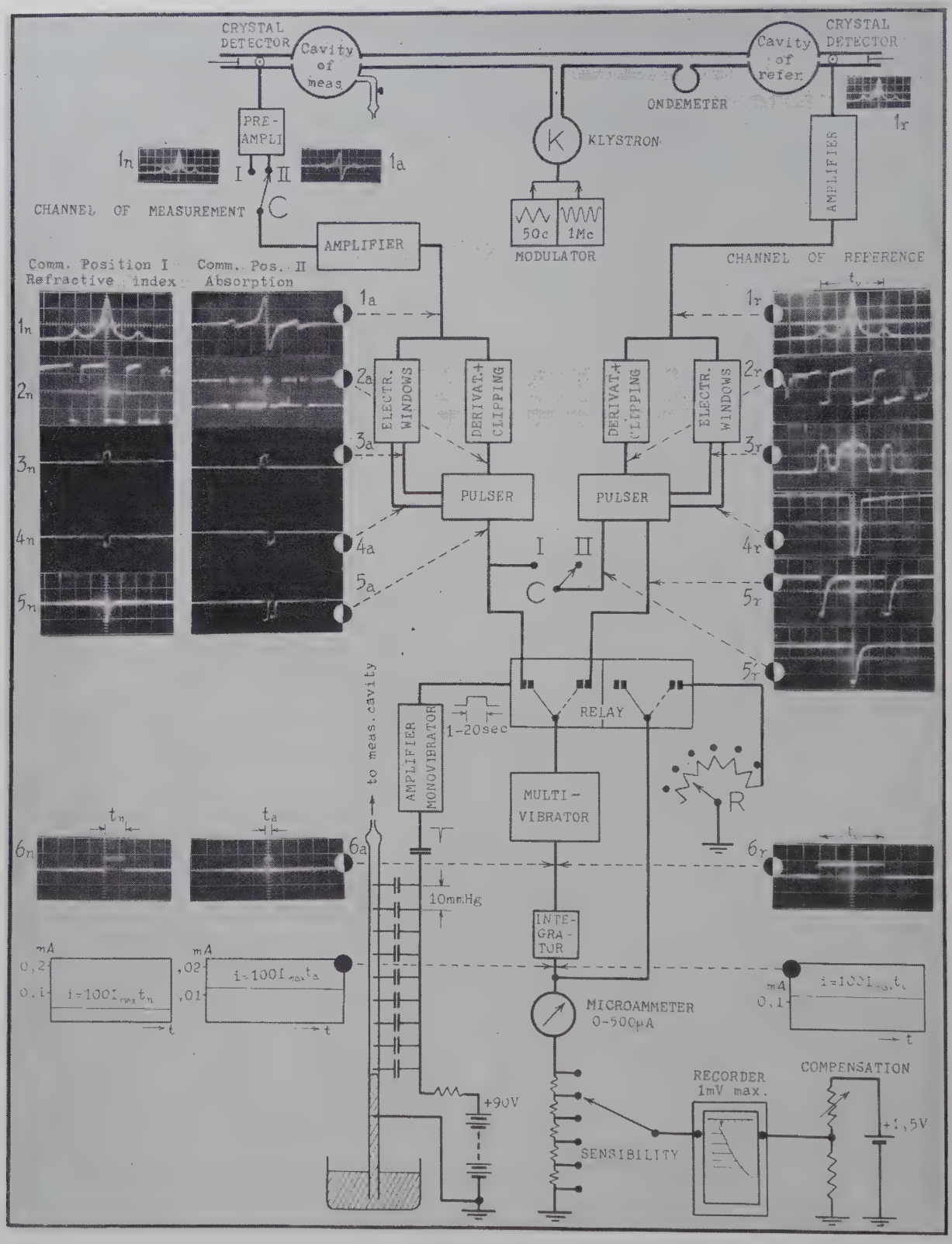

Fig. 5—Block diagram and oscillograms (400 μsec/cm horizontal sweep) illustrating the operation of the recording spectrograph.

recorder" is connected to the circuits which correspond to the measurement of the interval t_v. The traces of the resulting displacements of the recording pen constitute the marks of the pressure for every 10 mm Hg. In order to prepare the apparatus for the next measurement, the capacities of 100 pF are shunted by high resistances (20 MΩ) which provide a rapid discharge during the next filling of the cavity.

If the sweep velocity of the klystron (which is proportional to t_v) is stable enough, the ends of the pressure traces should lie on a straight line corresponding to one and the same value measured by the recorder. This value can be used as zero-reference provided that the resistance R is adjusted so that the recorder will show the same value when the cavity of measurement is empty. It is evident that any change of the sweep velocity disturbs the straightness of the line formed by the ends of the pressure traces. This permits one to control and, if necessary, to correct the stability of the sweep velocity and thus to ensure a sort of permanent calibration of the spectrograph.

V. Design

We give here in brief some information on the design of the recording spectrograph and in particular on those parts which are essentially different or absent in the previous spectrograph with synchroscope. Since the microwave block remains as in Fig. 1, we will not deal with it (see [2a], [5]). The electronic block can be divided into the following parts (Fig. 5):

A. Double Modulator of the Klystron

This includes a generator of an isosceles triangular signal synchronized to the power line (frequency of 50 cps, variable amplitude for the adjustment of the sensitivity of the apparatus), as well as a sinusoidal crystal generator (frequency of 1 Mc). The design of the triangular modulator should provide high linearity and symmetry.

B. Low-Frequency Amplifiers

These amplify the response signals of the cavities and have been designed to present low noise level, sufficient frequency pass band and high gain (of the order of 60 db). The peak value of the amplified signal is of the order of 100 or 200 volts.

The two amplifiers, corresponding to the two channels of the apparatus, are identical except in the following respect: The first tube (preamplifier) of the channel of measurement is connected to the rest of the amplifier by means of a double coupling circuit RC. One of these circuits is identical with the corresponding circuit of the amplifier of reference. The other one has a time constant of far less (of the order of 0.5 microsecond) and provides the first preliminary derivation of the response of the channel of measurement in the case of the absorption measurement.

C. Derivation and Clipping, Electronic Windows, Pulsers (Channel of Measurement) (Fig. 6)

Suppose that one is dealing with the measurement of the absorption. The input signal immediately undergoes a second derivation by means of the circuit $R=5000$ ohms, $C=100$ pF. If the signal of the second derivative were directly applied to the dc amplifier (12AT7), a displacement of the zero-level as a function of the amplitude of the signal might result. To avoid this, one connects, at the input of the 12AT7 and in parallel with the resistance R, a set of two crystal diodes with opposing polarities. This set provides a preliminary clipping and keeps the amplitude of the input signal at low levels. Furthermore, since the two diodes have been selected to be identical, the zero level can no longer be displaced for any amplitude of the input signal.

The dc amplifier is thus used mainly for the amplification of a signal which has already undergone a preliminary clipping; this is facilitated by the presence of a weak positive feedback.

The pulsers (two thyratrons 2D21) are fed by the amplified signal through a decoupling stage ($\frac{1}{2}$12AU7). However, since the clipping is deep and the amplification high, the system could be activated not only by the useful signal but also by any disturbance in the input voltage (noise, secondary resonances). This possibility is eliminated by means of electronic windows (one for each thyratron). The windows are synchronized on the input signal (the first derivative of the response of the measurement cavity for the absorption measurement). This signal is doubled by means of a phase inverter ($\frac{1}{2}$12AU7) and it feeds two detection circuits. The current flows only near the maximum and minimum of the input signal. The corresponding pulses are amplified and they constitute the suitably synchronized electronic windows.

In the case of measurement of the refractive index, one obtains in the same way two electronic windows, but this time the windows appear both in the same position, that corresponding to the principal resonance of the cavity of measurement. However, the two thyratrons do not work together at the same time, since one of them works during the rising part of the clipped signal and the other one during the falling part. Therefore, one will receive at the output only one pulse.

D. Respective Circuits of the Channel of Reference (Fig. 7)

The input signal consists here of the response signal itself of the cavity of reference (amplified to about 200 volts, peak value). The output is double: The two pulses received from the output S_1 correspond to the two side maxima of the input signal (measurement of the sweep velocity of the klystron). Only one pulse, placed at the

maximum of the principal resonance of the reference cavity, comes out of the output S_2 (measurement of the refractive index).

The derivation and the clipping are produced by exactly the same procedure as in the channel of measurement. The fronts of the triple rectangular signal thus produced, as well as the fronts of the parasite signals (Fig. 5, oscillogram $2r$), feed the mutually short-circuited grids of the two thyratrons (V_{16} and V_{19}). On the other hand, these grids receive the signal of a triple electronic window, the apertures of which are synchronized to the three maxima of the reference response. Thus, the potential level of the three "useful" wave fronts is raised relatively to any other wave front. This, however, does not result in the triggering of the two thyratrons at the positions of the three useful fronts. The polarizations of the thyratrons are, in fact, adjusted so that the conditions of ignition are then satisfied only for the output S_1, and not for the output S_2.

Under such a situation, one should receive three pulses at the output S_1. However, the screen of the corresponding thyratron (V_{16}) receives a negative signal which is also produced by the circuits of the electronic windows and which is synchronized with the maximum of the principal resonance of the input signal (Fig. 5, oscillogram $4r$). Thus, at the output S_1, two pulses only are obtained, by means of which the two side maxima are pointed out.

The same pulse of selection (oscillogram $4r$) is also applied to the cathode of the other thyratron (V_{19}). Its action consists of rendering this thyratron, which otherwise is kept off, able to select the sole pulse corresponding to the maximum of the principal resonance of the input signal.

The single (negative) electronic window is produced by the method of detection, as in the case of the channel of measurement. To obtain the triple window, the response signal of the cavity of reference is forced to pass through a crystal diode (OA5) polarized by a cell of 1.5 volts. The clipping performed by the diode reduces the three maxima of the response curve to the same height. The remainder of the process is quite evident.

E. Scale of Two, Integrator and Recorder (Fig. 8)

The pairs of pulses, obtained as outlined above, correspond to the time intervals t_a, t_n or t_v. They are re-

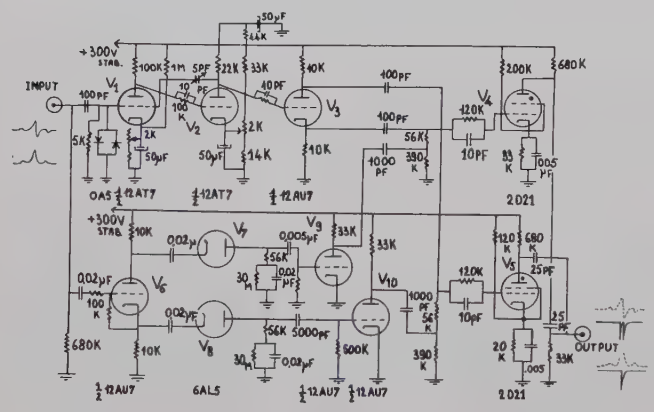

Fig. 6—Pulse circuits (channel of measurement).

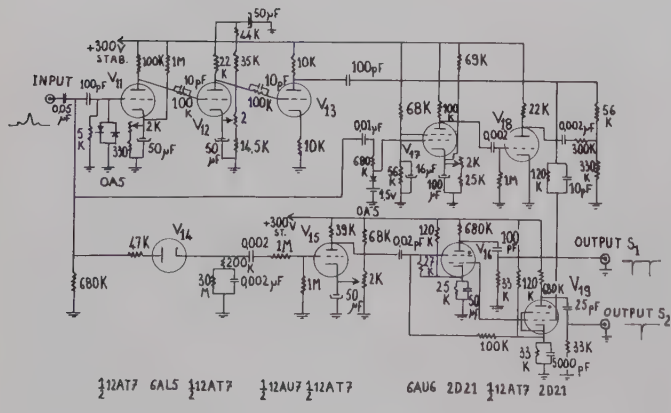

Fig. 7—Pulse circuits (channel of reference).

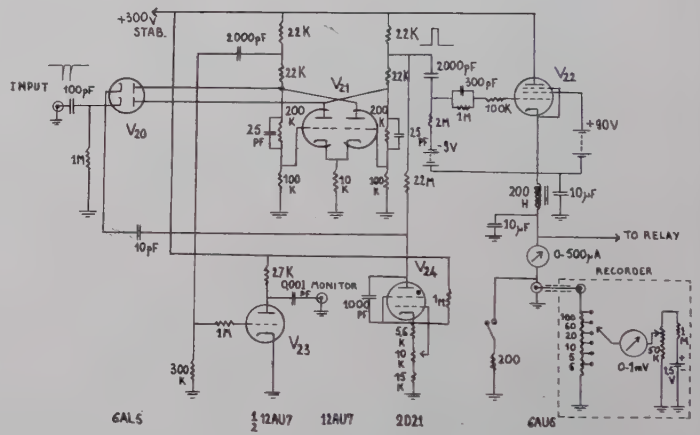

Fig. 8—Scale of two, integrator and recorder.

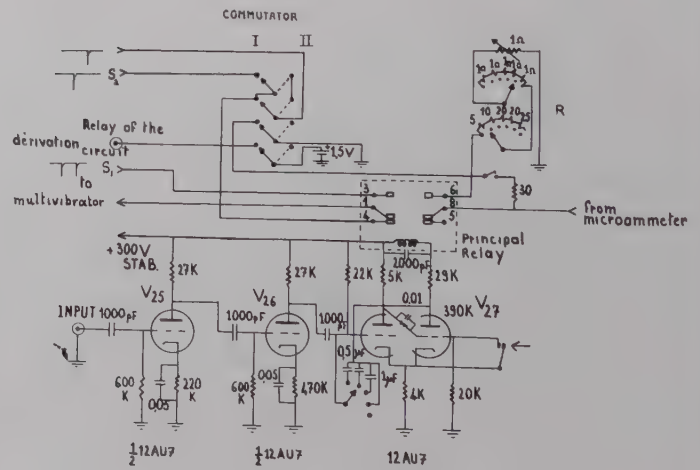

Fig. 9—Pressure circuits.

peated at the rate of 100 per second and couple, through a double diode (V_{20}), to the two plates of a bistable multivibrator (V_{21}). The width of the rectangular signal provided with this "scale of two" represents the time distance separating the two pulses of the respective pair.

The rectangular signal received by one of the plates of the multivibrator is used, after decoupling (V_{23}), for the control of the operation of the scale by means of the monitor.

The rectangular signal from the other plate is applied to the grid of an integrating pentode (V_{22}). This tube becomes conductive and supplies a constant current, only during the time periods defined by the rectangular signal of the scale. The action of the rectifying filter (LC), placed at the cathode load of the tube, permits one to obtain at the output a direct current proportional to the width of the rectangular signal. The proportionality factor (of the order of 1 μa/μsec) is very stable.

Finally, since it might be possible for the polarity of the rectangular signal of the scale to be inverted because of some disturbance, whatever it may be, which would put in danger the operation of the apparatus, a set for automatic re-establishment of the polarity has been foreseen (V_{24}).

F. Pressure Circuits (Fig. 9)

The pulses for the identification of the gas pressure (see Section IV-D) are amplified and they feed a monostable multivibrator. The plate current of its one part controls the main relay of the apparatus: the appearance of a pulse at the input causes the activation of the relay which passes, for an adjustable time, from the position "measurement" over to the position "pressure marker." The same result, and for any time, can also be obtained by means of a press-button (use of the instrument as a Q meter).

G. Monitors

The operation of the apparatus is controlled by means of two monitors (one for each channel of the instrument). The response signals obtained at the outputs of the low-frequency amplifiers appear on the screens of the respective cathode ray tubes.

VI. Results and Conclusions

The photograph in Fig. 10 shows a general view of the recording spectrograph. Its performance is comparable with that of the spectrograph with synchroscope [2a], [5]. The sensitivity remains at the order of 10^{-6} neper/m for the absorption and of 10^{-8} for the index of refraction. The precision evidently depends on the type of measurement (the error can be of the order of 1 per cent for the absorption, even less for the refractive index). The stability of measurements seems to favor the use of a recorder instead of a synchroscope, where the calibration is subjected to a permanent control. The reproducibility of the measurements is also highly satisfactory.

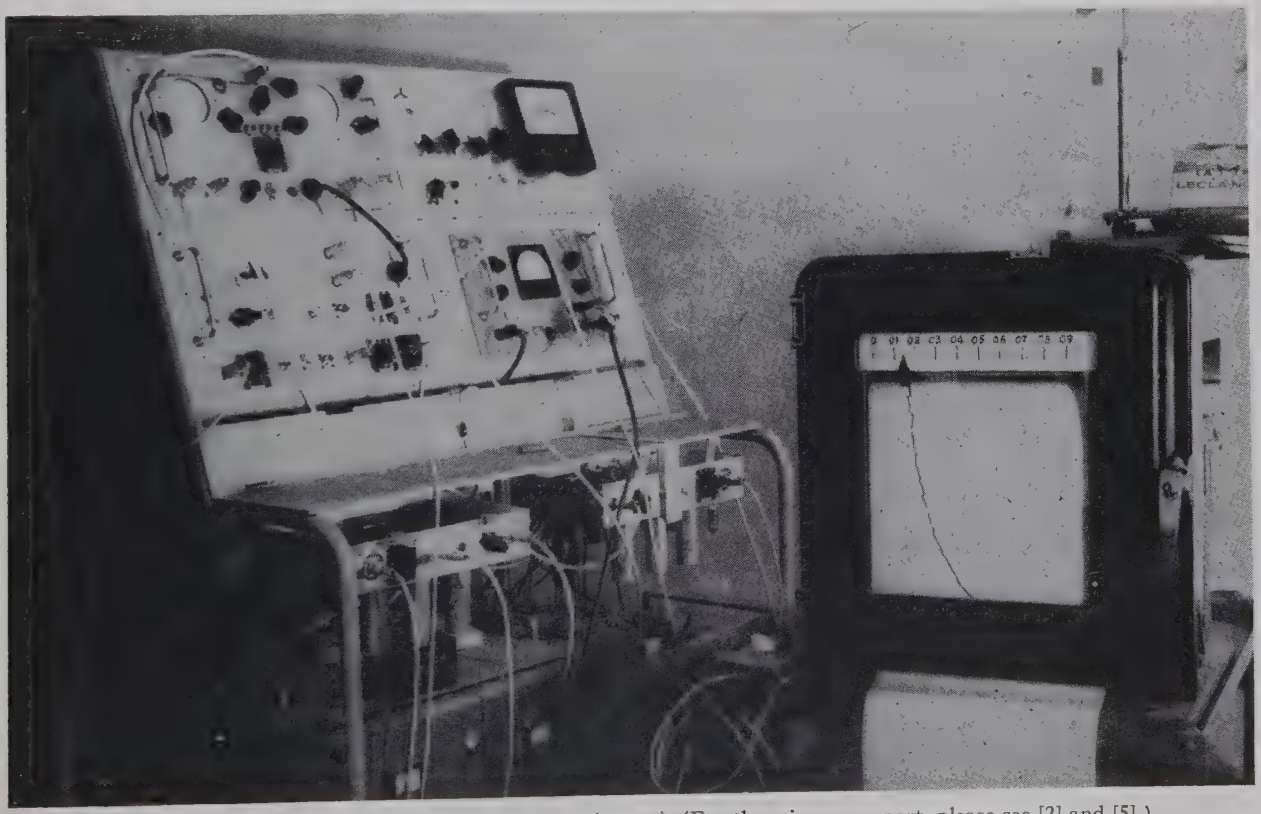

Fig. 10—Photograph of the apparatus (electronic part). (For the microwave part, please see [2] and [5].)

Figs. 11 and 12 illustrate an example of measurement of the absorption by ammonia. The apparatus is now ready and is being used in carrying out some original research work.

In conclusion, we remind the reader of the principal features of this recording spectrograph:

1) Convenient measurements through the use of an automatic recorder.
2) Possibility of use, after modifications to reduce size and weight, as a light, accurate airborne refractometer (like the existing Crain's refractometer [8]).
3) Possibility of use as a direct-reading Q meter.
4) High general performance, due to the application of the pulse method to the interpretation of the cavity responses.

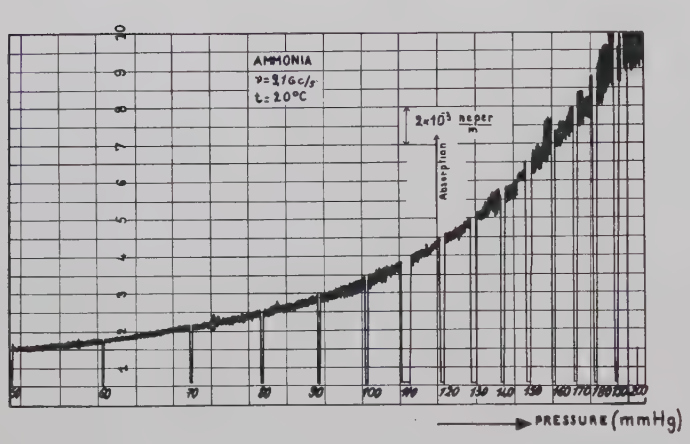

Fig. 11—Microwave absorption (ν=9100 Mc) by ammonia at 20°C.

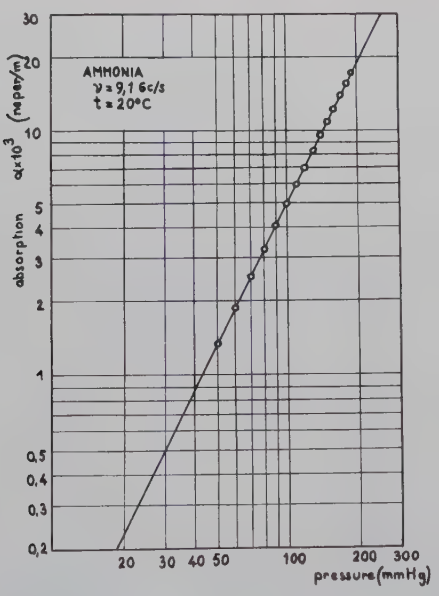

Fig. 12—The recorded curve (Fig. 11) transferred in log-log scales (straight line with a slope equal to 1.97: $\alpha=(\mathrm{Cte})p^{1.97}$).

Acknowledgment

The authors wish to express their thanks to Prof. A. Gozzini of the University of Pisa, pioneer of the application of the pulse method to microwave spectrographs, for his permanent interest in carrying out the present work.

References

[1] D. Ilias, "Un spectromētre microonde enregistreur pour l'étude des gaz-pressions moyennes," *J. Phys. Rad.*, vol. 20, pp. 653–655; June, 1959.
[2] a) A. Battaglia, G. Boudouris, F. Bruin, A. Gozzini, and D. Ilias, "Un spectromētre en microonde utilisant la technique des cavités et des impulsions," *Onde Electrique*, 2, special suppl., pp. 430–440, August, 1958.
b) A. Battaglia, F. Bruin, and A. Gozzini, "Microwave apparatus for the measurement of the refraction, dispersion and absorption of gases at relatively high pressure," *Nuovo Cimento*, ser. 10, vol. 7, pp. 1–9; January, 1958.
c) A. Battaglia and A. Gozzini, "Un appareil pour l'étude de la dispersion des gaz et des vapeurs dans la bande des hyperfréquences," *Onde Electrique*, vol. 35, pp. 500–502; May, 1955.
d) A. Gozzini and E. Polacco, "Méthods pour la mesure de la constante diélectrique des gaz dans la bande des hyperfréquences," *Compt. Rend. Acad. Sci.*, vol. 237, pp. 1497–1499; December, 1953; "Complement á la méthode de mesure de la constante diélectrique des gaz dans la bande des hyperfréquences," pp. 1652–1654; December, 1953.
[3] A. Battaglia, G. Boudouris, and A. Gozzini, "Sur l'indice de réfraction de l'air humide en microondes," *Ann. Télécommun.*, vol. 12, pp. 181–184; May, 1957.
[4] A. Battaglia, F. Bruin, and A. Gozzini, "Absorption and refraction of some polar gases as a function of pressure at microwave frequencies," *Nuovo Cimento*, ser. 10, vol. 7, pp. 87–94; January, 1958.
[5] G. Boudouris, "Sur l'indice de refraction de l'air, l'absorption et la dispersion des ondes centimetriques par les gaz," Sci.D. dissertation, University of Paris, Paris, France; November 15, 1958.
[6] G. Boudouris and D. Ilias, "Sur l'absorption en microondes de quelques mélanges gazeux," *Compt. Rend. Acad. Sci., France*, vol. 246, pp. 730–733, February, 1958; "Mesures d'absorption des microondes par des mélanges gazeux binaires," pp. 1407–1410; March, 1958; "Spectre d'absorption de la trimethylamine en ondes centrimétriques—pressions moyennes, vol. 250, pp. 1833–1836, March, 1960.
[7] F. Bruin, "The line shape of collision broadened spectral absorption lines," Ph.D. dissertation, University of Amsterdam, The Netherlands; July, 1956.
[8] a) C. M. Crain, "The dielectric constant of several gases at a wave-length of 3.2 cm," *Phys. Rev.*, vol. 74, pp. 691–693; September, 1948.
b) ———, "Apparatus for recording fluctuations in the refractive index of the atmosphere at 3.2 centimeters wave-length," *Rev. Sci. Instr.*, vol. 21, pp. 456–457; May, 1950.
[9] G. Goudet and P. Chavance, "Ondes Centimetriques," Chiron, Paris, France; 1955.
[10] C. G. Montgomery, "Technique of Microwave Measurements," M.I.T. Rad. Lab. Ser., No. 11, McGraw-Hill Book Co., Inc., New York, N. Y.; 1947.
[11] C. H. Townes and A. L. Schalow, "Microwave Spectroscopy," McGraw-Hill Book Co., Inc., New York, N. Y.; 1955.

A Cavity-Type Parametric Circuit as a Phase-Distortionless Limiter*

F. A. OLSON†, MEMBER, IRE, AND G. WADE‡, SENIOR MEMBER, IRE

Summary—This paper is a study of the properties of a diode parametric frequency converter (negative-conductance type) when used to perform microwave limiting. Unlike the parametric amplifier, the output power of a converter cannot exceed a certain level, regardless of the amplitude of the input signal. Thus, the ability to limit is a fundamental property of regenerative parametric frequency converters. An experimental limiter circuit, consisting of two stages of parametric frequency conversion, provided an output which was constant to within ±1 db over a range of input of 50 db, and had 10-db small-signal gain. The phase variation was less than seven degrees over the entire range of input power.

Introduction

FROM simple energy-conservation considerations, saturation is known to occur both in parametric amplifiers and in parametric frequency converters.[1] Since the only energy available to provide amplification is that delivered from the pump source, the gain of any parametric circuit must decrease as the level of the input signal approaches the level of the maximum available pump power. For the case of a parametric circuit used as an amplifier, the gain may decrease to the extent that the circuit appears passive. A typical experimental saturation curve for an amplifier is shown in Fig. 1.

When used as a frequency converter (the output is at the idler frequency), the parametric circuit has a markedly different saturation characteristic, because the idler-frequency power exists only as a result of parametric excitation. The nature of the saturation characteristic can be predicted from considering the general energy relations formulated by Manley and Rowe.[2] The equation relating the power at the idler frequency to the power at the pump frequency is

$$\frac{P(\omega_2)}{P(\omega_p)} = \frac{\omega_2}{\omega_p} . \qquad (1)$$

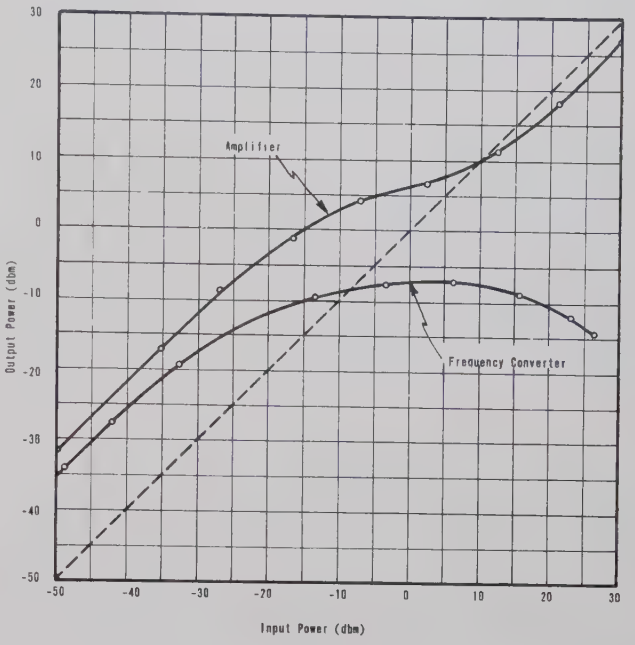

Fig. 1—Typical saturation characteristics of parametric circuits.

This relation establishes an upper bound on the idler-frequency power. That is, the output of the frequency converter cannot exceed the level of the pump power delivered to the variable element, regardless of the amplitude of the input signal. Thus, the ability to limit is an inherent property of regenerative parametric frequency converters.[3] A typical large-signal response of a converter is compared with the response of an amplifier in Fig. 1.

It should be noted here that parametric circuits employing semiconductor diodes are not envisioned as limiters in high power applications, for obvious reasons. However, these circuits may be suitable for other applications. A need exists, for example, for phase-distortionless limiting at moderate power levels in microwave systems that utilize phase detection, since the phase detectors presently employed are amplitude sensitive. Furthermore, the capabilities of parametric limiters may be extended into other power ranges through the use of variable reactance elements other than semiconductor diodes.

* Received by the PGMTT, July 11, 1960; revised manuscript received, November 10, 1960. This study was performed at the Stanford Electronics Lab., Stanford University, Stanford, Calif., under Contract AF33(616)-6207.

† Electronics Res. Directorate, Air Force Res. Div. (ARDC), Laurence G. Hanscom Field, Bedford, Mass.

‡ Raytheon Manufacturing Co., Spencer Lab., Burlington, Mass.

[1] The term frequency converter is used throughout this paper to describe the parametric circuit when the output is at the idler frequency (the difference between the pump frequency and the frequency of the input signal). Parametric up-converters, in which the frequency is the sum of the pump and input frequencies, are not considered in this study.

[2] J. M. Manley and H. E. Rowe, "Some general properties of nonlinear elements—part I, general energy relations," PROC. IRE, vol. 44, pp. 904–913; July, 1956.

[3] F. A. Olson, C. P. Wang and G. Wade, "Parametric devices tested for phase-distortionless limiting," PROC. IRE, vol. 47, pp. 587–588; April, 1959.

Theory of Saturation

The mechanism of saturation in a parametric circuit can be found from a first-order analysis of the model circuit shown in Fig. 2. The circuit is made up of three tuned tanks and the parametric diode. It is assumed that the loaded Q's are sufficiently high for each resonant tank so that voltage components exist at only three specified frequencies $\cdots \omega_1$, ω_2 and ω_p. These frequencies are related by

$$\omega_1 + \omega_2 = \omega_p, \tag{2}$$

and are termed the signal, idler and pump frequencies, respectively.

The diode is considered to consist of a conductance, a steady capacitance, and a voltage dependent capacitance. To simplify the notation, the conductance and the steady capacitance are included in the elements making up each resonant circuit. The voltage dependent part of the capacitance is assumed to be of the series form

$$C = K_1 v + K_2 v^2 + \cdots. \tag{3}$$

However, for a first-order analysis, it is sufficient to consider the variable capacitance to be a linear function of the voltage ($C = K_1 v$).

The gain of the circuit shall be defined as the transducer gain: that is, the ratio of the power dissipated in the load conductance P_L to the power available from the source P_{avs}.

From an analysis of the form used by Heffner and Wade[4] and others, one finds the gain of the circuit, when used as an amplifier operating on resonance, to be

$$g = \frac{4G_{g1}G_{L1}}{\left[G_{t1} - \dfrac{\omega_1\omega_2 K_1{}^2 4G_{gp}P_{avp}}{G_{t2}\left(G_{tp} + \dfrac{\omega_p\omega_2 K_1{}^2 V_1 V_1{}^*}{G_{t2}}\right)^2}\right]^2}, \tag{4}$$

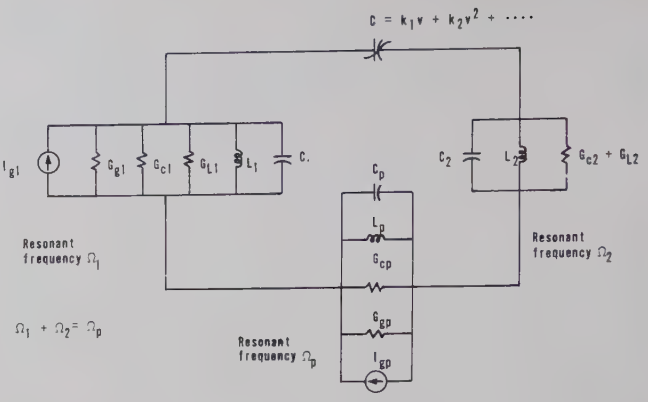

Fig. 2—Model for the parametric circuit.

I_{g1} = signal-source current generator
G_{g1} = signal-source conductance
G_{cn} = conductance due to circuit and diode losses
G_{L1} = load conductance
L_n = inductance of tuned circuit
C_n = capacitance of tuned circuit including the steady capacitance C_0 of the diode
I_{gp} = pump-source current generator
G_{gp} = pump-source conductance
C = the voltage-dependent part of the diode capacitance
$n = 1, 2, p$

Thus, when the input level is large, the relation for the output power of the amplifier becomes

$$P_L(\omega_1) \simeq \left(\frac{4G_{g1}G_{L1}}{G_{t1}{}^2}\right) P_{avs}(\omega_1), \tag{6}$$

which is just the passive response of the circuit when no pump power is applied. A decrease in pump power delivered to the circuit is, in fact, just what occurs when the input signal at frequency ω_1 becomes large, since large signals produce a mismatch in the pump circuit.

The gain of the parametric circuit when used as a frequency converter (the output is at the idler frequency) is defined as the ratio of the idler-frequency power dissipated in the load, $P_L(\omega_2)$, to the power available from the source at the signal frequency, $P_{avs}(\omega_1)$. This is a conversion gain

$$g_c = \frac{\omega_2{}^2 K_1{}^2 4^2 G_{g1}G_{gp}G_{L2}P_{avp}}{G_{t2}{}^2\left(G_{tp} + \dfrac{\omega_p\omega_2 K_1{}^2 V_1 V_1{}^*}{G_{t2}}\right)^2\left[G_{t1} - \dfrac{\omega_1\omega_2 K_1{}^2 4G_{gp}P_{avp}}{G_{t2}\left(G_{tp} + \dfrac{\omega_p\omega_2 K_1{}^2 V_1 V_1{}^*}{G_{t2}}\right)^2}\right]^2}, \tag{7}$$

where G_{t1}, G_{t2}, and G_{tp} represent the sum of the conductances of the respective circuits. The value of this expression for large signal levels (for large V_1) is approximately

$$g \simeq \frac{4G_{g1}G_{L1}}{G_{t1}{}^2}. \tag{5}$$

which, at large signal levels, can be approximated as

$$g_c \simeq (\text{Constant})\left(\frac{1}{V_1 V_1{}^*}\right)^2. \tag{8}$$

Thus, unlike the amplifier, where the gain approaches a constant as the signal level increases, the gain of the frequency converter continues to decrease with increasing input power. For large input levels, then, the relation for the output power of the converter becomes

[4] H. Heffner and G. Wade, "Gain, bandwidth and noise characteristics of the variable-parameter amplifier," *J. Appl. Phys.*, vol. 29, pp. 1321–1331; September, 1958.

$$P_L(\omega_2) \simeq (\text{Constant})\left(\frac{1}{P_{avs}(\omega_1)}\right). \quad (9)$$

Remembering the fact that large signals produce a mismatch in the pump circuit, and hence, less pump power, we note from (1) that this decrease in pump power corresponds to a decrease in the maximum value of the power at the idler frequency. Thus, the large-signal relation of (9) is consistent.

Calculated saturation characteristics for both the amplifier and the converter are shown in Fig. 3. It is apparent from the nature of the saturation curves that the frequency converter is considerably more suitable than the amplifier for performing microwave limiting.

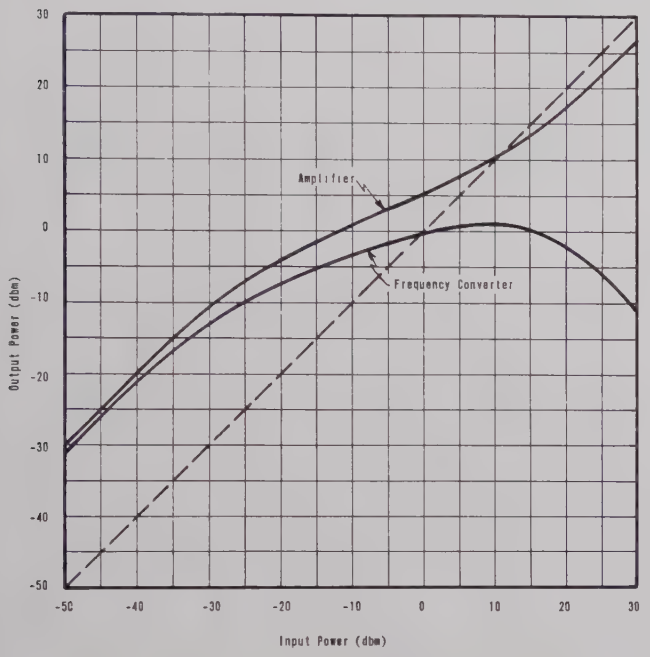

Fig. 3—Calculated saturation characteristics of parametric circuits.

Large-Signal Pulse Response

It is appropriate to consider the pulse response of the parametric frequency converter since many limiters allow an undesired spike to be transmitted at the leading edge of a pulse. In ferrite limiters, for example, the mechanism producing the attenuation of large microwave signals has a build-up time associated with it, during which time the RF signal is not attenuated, and a transmitted spike of large amplitude results.[5] For high-power operation, this spike is very detrimental, and hence, of major importance. For low-power applications, where diode parametric circuits are useful, a spike is bothersome but of less practical importance. However, since the power handling capabilities of parametric circuits may be extended through the use of variable reactance elements other than semiconductor diodes, the pulse response of these devices is worthy of consideration.

For the case of a limiter employing parametric frequency conversion, one can reason without a detailed analysis that the pulse response cannot result in a transmitted spike. First, note that the operation of other limiters depends upon some energy-absorbing mechanism being triggered by a large amplitude signal. Because there is a build-up time associated with the occurrence of this mechanism, there is a short time during which the large signal is allowed to pass through unattenuated; hence, a transmitted spike results. In contrast to this, the basic mechanism of the limiter being considered here is the conversion of energy to another frequency, with the efficiency of conversion being amplitude dependent. Because the frequency of the output is different from that of the input, any delay or build-up time associated with the conversion mechanism will result in a delayed output rather than a large amplitude spike. That is, there is no output without the conversion process, since the input signal cannot be simply transmitted through the circuit.

What then, can one predict for the pulse response of a parametric frequency converter? Consider a large amplitude input pulse at frequency ω_1. During the initial portion of the pulse, when the fields at ω_1 are building up in the circuit, the interaction of these small-signal fields and the pump produces idler-frequency fields of essentially the same build-up time, since the idler power is proportional to small-signal input power. As the fields at ω_1 build up to large amplitude, saturation takes place in the circuit, *i.e.*, large amplitude signals create a mismatch in the pump circuit which reduces the pump power, and hence, the conversion gain decreases. Although it has not been checked experimentally, one can expect the change in pump power to occur as rapidly as the build-up of the large amplitude input signal. Thus, the saturation of the circuit should take place smoothly, and the output pulse should be a slightly-rounded, reduced-amplitude replica of the input pulse.

Large-Signal Phase Response

We now need to consider the phase response of the parametric frequency converter under large-signal conditions, since phase-distortionless limiting is our objective. From the first-order analysis, which approximates the capacitance as a linear function of the voltage, one can find that the phase response of the circuit is independent of the signal level for operation on resonance. However, from the typical diode capacitance curve shown in Fig. 4, it is apparent that the linear approximation is not generally valid except at large values of bias voltage. At large bias, the slope of the capacitance curve is decreased (the gain of the circuit is reduced), so one must make a compromise between the value of gain desired and the amount of nonlinearity tolerable. Generally, after such a compromise, the amount of nonlinearity is appreciable, and thus, it is necessary to include

[5] G. S. Uebele, "Characteristics of ferrite microwave limiters," IRE Trans. on Microwave Theory and Techniques, vol. MTT-7, pp. 18–23; January, 1959.

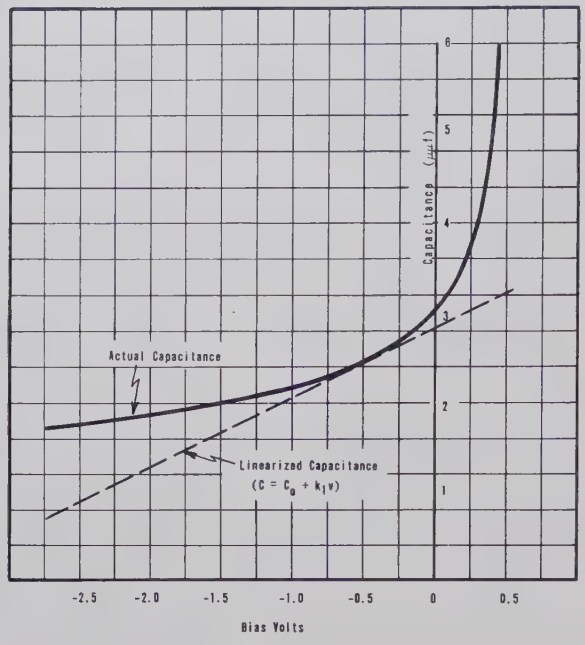

Fig. 4—Diode capacitance vs bias voltage.

the second-order term in the expression for the capacitance, (3), in order to determine the phase behavior of a parametric circuit.

From an analysis that includes the second-order term in the capacitance expression, one finds little change in the saturation characteristic of the parametric circuit, but considerable phase variation at large-signal levels.[6] The inclusion of the second-order term has the effect of introducing an additional capacitance in the circuit. This additional capacitance has a second-order dependence on the voltages; hence, it produces considerable variation in the phase response at large-signal levels. Phase distortionless performance, then, requires a diode with a linear capacitance-voltage curve or a method of compensating for the phase variations. Because diodes with the desired characteristic are not presently available, a phase compensation technique must be employed.

A Parametric Limiter Circuit

In order to increase the range of limiting and to provide a means of compensating for the phase distortion resulting from the nonlinear capacitance-voltage curve, a two-stage limiter circuit was devised, as shown in Fig. 5.

This limiter circuit consists of two parametric frequency converters connected in series. Each of the two stages of the circuit is considered to consist of a nonlinear capacitor and three resonant circuits, much like the model circuit of Fig. 2. The circles represent the resonant circuits, tuned to the indicated frequency. The input signal at frequency ω_1 is converted in the first stage to an output signal at ω_2. This signal at frequency ω_2 is sent to the second stage, where it is converted into an output signal at frequency ω_1. One characteristic of this limiter circuit is already apparent: the frequency of the output signal is the same as the frequency of the input signal.

An increased range of limiting results from the use of more than one stage of frequency conversion. That is, the saturation characteristic of the two-stage parametric limiter is a combination of the saturation characteristics of the individual converters, assuming that there is adequate isolation between the stages so that each frequency converter is unaffected by the other.

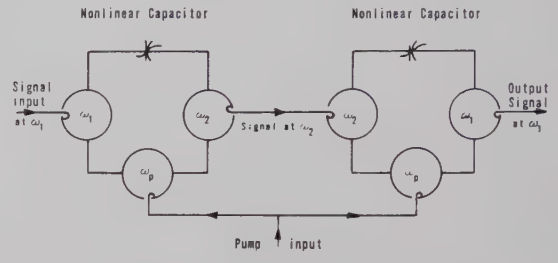

Fig. 5—Diagram of a parametric limiter circuit.

In a two-stage circuit, there is also the possibility of adjusting the phase responses of the individual stages so that the over-all phase response is nearly independent of signal level. That is, the phase behavior of a converter is dependent on the nature of the bias (self bias or fixed bias), the value of the bias voltage and the level of the pump power, the characteristics of the particular diode used, and the elements of the resonant circuits. By proper selection of these parameters, it is theoretically possible to tailor the phase response of each converter so that the sum of the individual phase variations is nearly zero. Experimentally, one can presumably measure the phase vs power characteristic of each converter, make suitable adjustments, and superimpose the characteristics to achieve phase distortionless performance. In our experiment, however, it was more expedient to monitor the phase behavior of the entire limiter circuit and adjust the parameters until the resultant phase response was suitably independent of power level.

Experimental Results

Measurements were made of the properties of an experimental limiter circuit of the form shown in Fig. 5. An input signal at 3720 Mc was converted in the first stage to a signal at 1780 Mc, which was then converted in the second stage to an output signal at 3720 Mc.

The best measured phase and limiting characteristics are shown in Fig. 6. The power output of the circuit

[6] F. Olson, "The Large-Signal Properties of Microwave Cavity-Type Parametric Circuits," Stanford Electronics Lab., Stanford University, Stanford, Calif., Tech. Rept. No. 315-1; 1960.

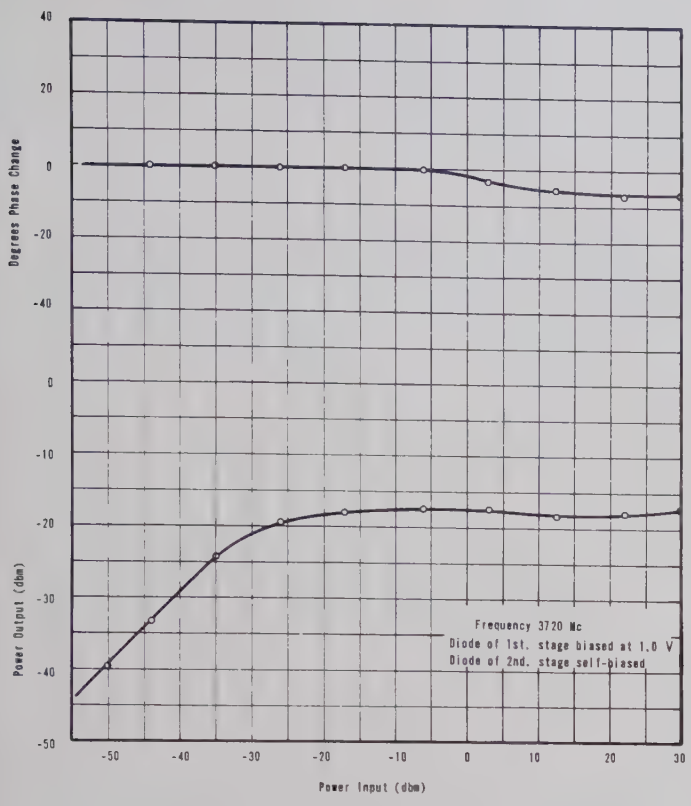

Fig. 6—Best measured phase and saturation characteristics of the parametric limiter.

remained at -18 dbm ± 1 db for input levels from -20 to $+30$ dbm, and the circuit had about 10-db small-signal gain. Although there was phase variation present in each of the converter stages, the over-all phase variation was slight, since a proper selection of bias conditions (fixed bias for the first stage, self bias for the second stage) provided adequate phase compensation. When properly tuned for on-resonance operation, there was an over-all phase change of less than seven degrees over the entire range of input power.

The frequency range of the limiter, for phase distortionless performance, was found to be small, since the phase distortion increased rapidly for operation slightly off resonance. The individual frequency converters must be composed of circuits having more bandwidth than simple tuned circuits if phase-distortionless performance is to be achieved over a range of frequencies. Wide-band circuits, such as those described by Matthaei,[7] would be helpful in extending the bandwidth of the limiter.

Conclusion

Saturation occurs in parametric circuits when the input signal level approaches the level of the pump power. A first-order theory is adequate to describe the mechanism of saturation. However, a higher-order analysis is required if information is to be obtained about the phase behavior at large signal levels. Second-order effects, which occur if the capacitance-voltage curve of the diode is not linear, cause the phase response of any parametric circuit to be a function of the signal level.

A combination of parametric frequency converters can be used to perform good microwave limiting, and, under certain conditions, limiting without phase distortion. In addition, no spike can be present in the pulse response of limiters of this type. However, for phase-distortionless performance to be achieved over a range of frequencies, the individual frequency converters must be composed of circuits having more bandwidth than simple tuned circuits. Also, a substantial improvement in the operation will result if diodes with linear capacitance-voltage curves are developed, since this would eliminate the source of the phase variations, and hence, the need for a phase compensation technique.

[7] G. L. Matthaei, "A Study of the Optimum Design of Wideband Parametric Amplifiers and Up-Converters," presented at the Microwaves Theory and Techniques Symp., Coronado, Calif.; May, 1960.

A Stripline Frequency Translator*

ELISABETH M. RUTZ†, SENIOR MEMBER, IRE

Summary—**A frequency translator is discussed which operates at *C*-band frequencies. The modulators in the frequency translator are crystal diodes, and modulation is obtained by periodic variation of the reflection characteristic of the crystal modulators. The conversion loss of the frequency translator is 6.5 db at 8-mw input power. The unwanted sidebands are at least 25 db below the translated signal.**

I. Introduction

A FREQUENCY translator in stripline technique operating at *C*-band frequencies was developed in a program of miniaturizing microwave components. In the frequency translator, crystal modulators are connected to the symmetrical ports of a hybrid junction. The arms to which the modulators are connected differ in length by an eighth of a wavelength. The modulating voltages which drive the crystal diodes are in phase quadrature. The modulation characteristic of the crystal diodes is such that each diode effectively operates as a balanced modulator. The frequency translator is similar in principle to the continuous phase modulator which has been described before.[1]

II. Analysis

The performance of the frequency translator can be analyzed by correlating the transmission and reflection characteristics of the individual circuit elements. An RF signal entering port 1 of the hybrid junction in Fig. 1 is divided and directed into the symmetrical arms of the hybrid, which differ in length by an eighth of a wavelength. Semiconductor diodes are placed at ports 2 and 3 of the hybrid.

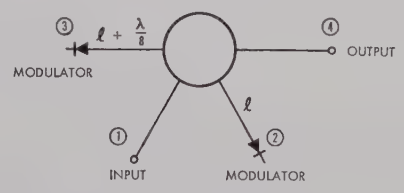

Fig. 1—Schematic of frequency translator.

The impedance of the crystal modulators is varied periodically with the phase of the modulation voltage. The reflection characteristic of the crystal diodes when operated as modulators is such that a microwave signal which is reflected by each of the crystal diodes has the characteristics of the output of a balanced modulator. The variation of the reflection coefficient of the crystal diode with the phase of the modulation voltage, $A \cos \omega_1 t$, which results in the balanced modulator characteristic, is sinusoidal; it can be represented by:

$$\Gamma = \Gamma_0 \cos \omega_1 t \tag{1}$$

where Γ_0 is a constant and $\omega_1/2\pi$ is the modulation frequency. The modulation voltages which are applied to the diodes in port 2 and port 3 are in phase quadrature.

A scattering matrix presentation describes the performance of the frequency translator. A scattering matrix of hybrid junction is given by

$$\begin{vmatrix} 0 & \frac{\sqrt{2}}{2} e^{-j\beta L} & \frac{\sqrt{2}}{2} e^{-j(\beta L+\pi/4)} & 0 \\ \frac{\sqrt{2}}{2} e^{-j\beta L} & 0 & 0 & \frac{\sqrt{2}}{2} e^{-j\beta L} \\ \frac{\sqrt{2}}{2} e^{-j(\beta L+\pi/4)} & 0 & 0 & \frac{\sqrt{2}}{2} e^{-j(\beta L+5\pi/4)} \\ 0 & \frac{\sqrt{2}}{2} e^{-j\beta L} & \frac{\sqrt{2}}{2} e^{-j(\beta L+5\pi/4)} & 0 \end{vmatrix}.$$

Input signals are given by

$$\begin{vmatrix} \Re(e^{j\omega_0 t}) \\ \frac{\sqrt{2}}{2} \Gamma_0 \cos \omega_1 t \, \Re(e^{j(\omega_0 t-\beta L)}) \\ \frac{\sqrt{2}}{2} \Gamma_0 \cos\left(\omega_1 t + \frac{\pi}{2}\right) \Re(e^{j(\omega_0 t-\beta L-\pi/4)}) \\ 0 \end{vmatrix}$$

where $\Re(e^{j\omega_0 t})$ is the real component of the complex rotating vector representing the incident wave at port 1.

Outgoing signals are given by

$$b_1 = \frac{1}{2} \Gamma_0 \cos (\omega_0 t + \omega_1 t - 2\beta L)$$

$$b_2 = \frac{\sqrt{2}}{2} \Re(e^{j(\omega_0 t-\beta L)})$$

$$b_3 = \frac{\sqrt{2}}{2} \Re(e^{j(\omega_0 t-\beta L-\pi/4)})$$

$$b_4 = \frac{1}{2} \Gamma_0 \cos (\omega_0 t - \omega_1 t - 2\beta L).$$

* Received by the PGMTT, September 8, 1960; revised manuscript received November 16, 1960.

† Emerson Research Laboratory, Silver Spring, Md.

[1] E. M. Rutz and J. E. Dye, "Frequency translation by phase modulation," 1957 IRE WESCON Convention Record, pt. II; pp. 201–207.

The outgoing microwave signal at port 4 is translated in frequency by the modulation frequency. Dependent on the relative phasing, the signal is translated either to the lower or higher sideband. In the scattering matrix presentation, the phase of the modulating voltage which drives the crystal diode in the shorter arm of the hybrid is lagging. It follows from the RF and ac phase relation that the output signal is translated to the lower sideband. The opposite result is obtained by reversing the relative phase of the modulating voltages. Because of the geometry of the hybrid junction and the length of its arms, half of the modulated energy is coupled into port 1 of the frequency translator. The signals at port 1 and port 4 are translated to opposite sidebands, since there is an inherent difference in RF phase of 180° between port 1 and port 4 of a hybrid junction.

The amplitude of the translated signal is proportional to Γ_0 in (1), and the conversion efficiency of the frequency translator is optimized when Γ_0 becomes one.

III. Modulation Characteristic of the Crystal Diodes

The crystal modulators in the frequency translator are p-type silicon diodes, and are series elements terminating the symmetrical ports of the stripline hybrid junction. The modulation characteristic represented by (1) requires that the amplitude of the microwave signal reflected by the diode vary with the cosine of the phase of the modulating voltage, while the RF phase of the signal changes suddenly by 180° whenever the amplitude becomes zero. In Fig. 2 the variation of the reflection coefficient is given, which is obtained with the crystal modulators in the frequency translator for different bias voltages. The absolute value of the voltage reflection coefficient is approximately 0.85 at −1 volt, which decreases with decreasing negative voltage and becomes very small for zero volt. With increasing positive voltage, the absolute value of the voltage reflection coefficient increases, its phase changes by 180°, and for a positive voltage of approximately 0.6 volt, $|\Gamma|$ becomes 0.85.

A close approximation of the modulation characteristic represented by (1) can be obtained with the crystal diodes by shaping the modulation voltage such that the peak voltage is 1 volt when driving the crystal in the nonconducting state and 0.6 volt when driving it in conduction. For comparison, the variation of the voltage reflection coefficient as represented in (1) for the asymmetrical modulation voltage is shown in Fig. 2.

The modulation characteristic of the crystal diode can be derived from the equivalent circuit of the diode, as given in Fig. 3.[2]

The equivalent circuit elements of the diode cartridge are the whisker inductance L and cartridge capacitance C_c. The equivalent circuit elements of the metal-to-semiconductor junction are the nonlinear resistance R, which is shunted by the nonlinear capacitance C. The two are in series with the linear spreading resistance r.

The variation of the nonlinear resistance and the nonlinear capacitance with bias voltage is given in Fig. 4, and shows the rapid decrease of the nonlinear resistance and the increase of the nonlinear capacitance with forward bias. The spreading resistance was found to be comparatively small.

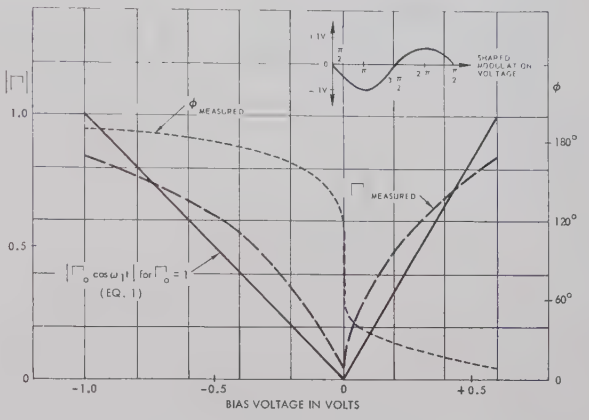

Fig. 2—Variation of voltage rection coefficient of the crystal modulator with bias voltage.

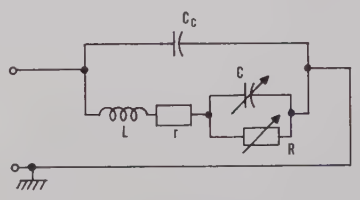

Fig. 3—Equivalent circuit of crystal diode.

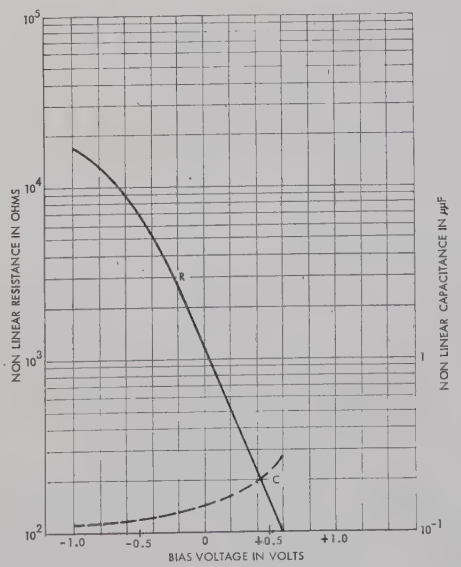

Fig. 4—Equivalent circuit elements of the metal-to-semiconductor junction of a C-band silicon diode as a function of bias voltage.

[2] R. V. Garver and J. A. Rosado, "Microwave diode cartridge impedance," IRE Trans. on Microwave Theory and Techniques, vol. MTT-8, pp. 104–107; January, 1960.

For large negative bias, the barrier reactance $1/\omega C$ approximates at C-band frequencies the conjugate of the whisker inductance ωL. The equivalent circuit of the diode for large negative bias can be simplified, and effectively becomes a series resonant circuit formed by the whisker inductance and barrier capacitance operating closely below resonance, in series with the inversed value of the nonlinear resistance. The cartridge reactance $1/\omega C_c$ is large compared to these values and can be neglected. The normalized RF impedance which the diode represents for large reverse bias is very small.

At positive bias the nonlinear resistance R and the nonlinear capacitive reactance $1/\omega C$ are small. The RF impedance of the diode is determined primarily by the cartridge capacitance and the whisker inductance which form a shunt resonance circuit. At C-band frequencies this resonant circuit operates below resonance. The real and imaginary parts of the normalized RF impedance for positive bias are comparatively large. The real part is the nonlinear resistance of the junction, which is stepped up by the ratio of operating frequency to resonant frequency of the resonant circuit, and is in series with an inductive reactance resulting from operation of the shunt resonant circuit below resonance.

At zero bias no resonance phenomena occur; the equivalent circuit elements in Fig. 3 are all of about the same magnitude. The normalized RF impedance of the diode is close to one.

The modulation characteristic of the crystal diodes follows from the behavior of series and shunt circuits when operated close to resonance. The absolute value of the impedance of a series resonant circuit is small. The absolute value of the impedance of a shunt resonant circuit is large. When operated below resonance, the phase angle of the impedance of the series resonant circuit is negative, and the phase angle of the shunt resonant circuit is positive. The absolute value of the voltage reflection coefficient for series and shunt resonant circuits is close to one. The phase angle of the respective voltage reflection coefficients differs by approximately 180°. The absolute value of the voltage reflection coefficient and the phase relation between series and shunt resonant circuits is preserved over a comparatively wide range of frequencies if both circuits operate on the same side of the resonance curve.

With decreasing bias voltages, the nonlinear resistance and the nonlinear capacitance change in magnitude, and the resonance phenomena no longer are preserved. The absolute value of the voltage reflection coefficient decreases, and the difference in the phase angle of the voltage reflection coefficient between positive and negative bias voltages becomes smaller.

In the frequency translator, modulation is obtained by variation of the reflection characteristics of the crystal modulators which reflect primarily the RF power and absorb only a comparatively small amount of the power. In conventional modulators, the entire RF power is absorbed by the nonlinear elements in order to convert it into power at different frequencies. Because of the difference in operation, the crystal diodes in the frequency translator can be operated at a higher power level than when used in conventional modulator circuits.

It seems to be of interest to mention that variable capacitance diodes were considered as modulators in the frequency translator; however, they do not perform satisfactorily at the present time in this application. The reasons for this are: 1) variation of the phase of the voltage reflection coefficient of 180° with bias voltage as required by the balanced modulator characteristic cannot be obtained with the varactors; 2) the range of phase variation is less than 150° at C-band frequencies at the present time; 3) the range is limited for large reverse bias by voltage breakdown and for forward bias by a resistance in series with the variable capacitance. However, development of varactors is directed towards increasing the breakdown voltage and decreasing the series resistance, thus widening the range of phase variation.

IV. Stripline Frequency Translator

The stripline frequency translator is shown in Fig. 5. At the comparatively high operating frequencies an air-dielectric transmission line is used, which combines the advantage of a strip transmission line and a coaxial line.

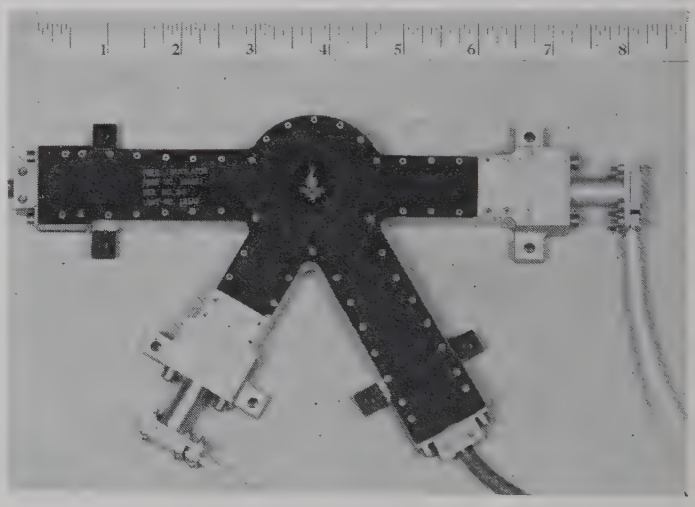

Fig. 5—Stripline frequency translator.

The transmission line is similar to the conventional strip transmission line with one exception: the spacers which support the inner conductor board are of metal, where top and bottom spacers are kept at the same electrical potential. The spacers are moved comparatively close to the inner conductor, and are placed in a region in which the electrical field strength is approximately 10 db below the field strength in the center of the transmission line. The transmission line rejects all propagation modes except the TEM mode.

The hybrid junction is of the conventional type. To obtain isolation between input port and output port, the length of one transmission path of the ring differs by a half wavelength from the symmetrical path. At *C*-band frequencies the dimensions of the transmission lines which form the ports of the hybrid ring are no longer very small compared to the wavelength. To decrease their dimension, the characteristic impedance of these lines was increased. Mechanical considerations set a limit to the highest characteristic impedance of the stripline, which is approximately 100 ohms.

To dimension the hybrid ring correctly, the phase velocity in the stripline has to be known. The phase velocity in stripline deviates slightly from its value in air because part of the fringing electrical field penetrates the dielectric which supports the inner conductor. The percentage of fringing field increases with decreasing strip width. Consequently, the phase velocity decreases with increasing characteristic impedance.

The crystal modulators are placed in series with the symmetrical port lines of the hybrid junction. The design of the crystal mount is shown in Fig. 6. A stripline-to-coaxial-line transition is the receptacle for one terminal of the crystal. In order to match the crystal impedance to the 70-ohm port line, the crystal diode is placed in a small cavity which is obtained by shaping the ground planes of the port line. The height and width of the crystal mount hardly exceed the height and width of the stripline.

The spectrum of the frequency translator output, given in Fig. 7, was measured at 8-mw input power where the measured conversion loss was 6.5 db. The undesired sidebands are at least 25 db below the translated signal.

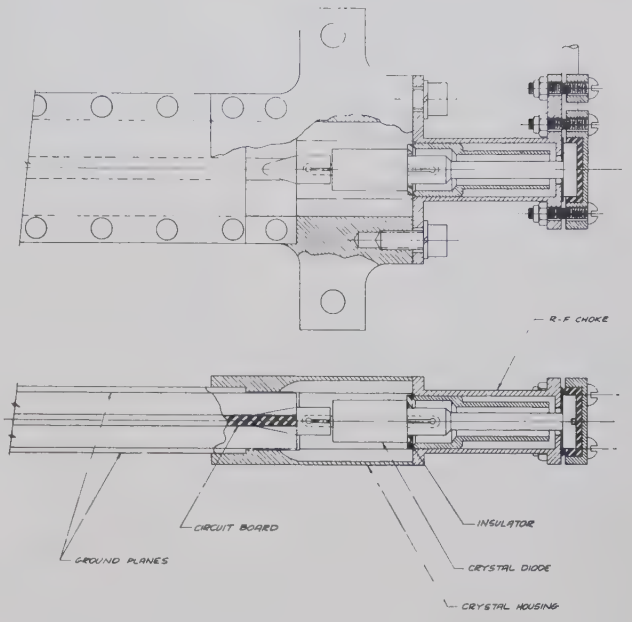

Fig. 6—Crystal holder.

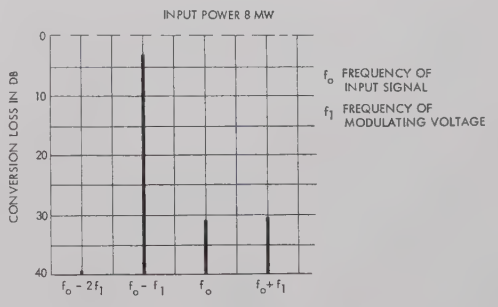

Fig. 7—Spectrum of frequency translator output.

An Approximate Solution to Some Ferrite Filled Waveguide Problems with Longitudinal Magnetization*

SHELDON S. SANDLER†

Summary—**An approximate solution for the field structure and propagating modes in parallel plane, circular, and coaxial ferrite filled waveguide is presented. Bundles of plane waves are assumed to propagate in these structures which bounce back and forth along the guide. The solutions are classified into two types depending on the negative or positive equality of the incident and reflected waves. In the case of the circular guide the waves form a cone, and in the coaxial guide they form a frustum of a cone about the axis. The elemental plane waves are also assumed to satisfy Polder's relation and the boundary conditions at the guide walls. Simple relations are obtained with this equivalence for the propagation constant and the field. Comparison to rigorous theory is made in the case of the parallel plane and circular guide. Some experimental verification is presented for the completely filled coaxial waveguide.**

Introduction

THE solution of the propagating modes in a general cylindrical guide has been given by Kales [1] and Suhl and Walker [2]. With these formulations the researcher is faced with an almost insurmountable computational problem for the propagation constants and the field configurations in practical waveguide structures. It is not the purpose of this paper to reformulate the problem, but rather to present an approximate method which will lend insight into the phenomenon and ease some of the computational difficulties.

The method is based on a well-known result in isotropically filled waveguide. The result shows that the solution to the rigorous boundary value problem in parallel-plate guide may be visualized as a set of plane waves bouncing back and forth along the guide. The results of using the plane wave picture are identical to the rigorous results. For example, in the cutoff condition the plane waves move at right angles to the longitudinal axis of the guide. It will be demonstrated that the same picture may be applied to a parallel-plate ferrite filled waveguide. Furthermore, the same method may be extended to the completely filled circular and coaxial waveguide.

The results of the approximate method will be compared to the rigorous results for the completely filled parallel-plate guide given by Brodwin [3] and the completely filled circular guide given by Gamo [4]. Since no results have been published on the completely-filled coaxial line, these results will be presented with some verification from experimental measurements.

* Received by the PGMTT, September 15, 1960; revised manuscript received, November 28, 1960. The research reported herein was supported in part by the AF Cambridge Res. Ctr., Air Res. and Dev. Command, under Contract AF 19(604)-5234 and in part by the Naval Bureau of Ships under Contract NObsr 77602.

† Electronic Communications Inc., Timonium, Md.

The Method

An explanation of the approximate method might best begin from a crude discussion of the most elementary isotropic waveguide, the parallel-plate guide. It has been shown by many authors that the rigorous solution is equivalent to a set of plane waves bouncing back and forth along the guide. Consider a plane wave impinging on a semi-infinite perfect conductor as shown in Fig. 1.

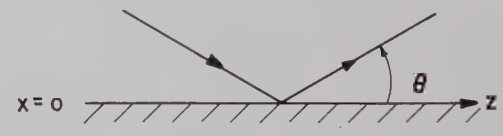

Fig. 1—Plane wave impinging on perfect conductor.

From geometrical considerations, the phase factors of the tangential incident and reflected waves of Fig. 1 are given by

$$E_i \sim \mathcal{E}_i e^{-j\beta \cos\theta z - j\beta \sin\theta x}$$

$$E_r \sim E_r e^{-j\beta \cos\theta z + j\beta \sin\theta x}. \tag{1}$$

Since the tangential components of the electric field must be zero at $x=0$ for all z, then $\mathcal{E}_i = -\mathcal{E}_r$ and

$$E_{\text{tang}} \sim \sin(\beta x \sin\theta) e^{-j\beta \cos\theta z}. \tag{2}$$

Eq. (2) represents a standing wave in the x direction and a traveling wave in the z direction. Note that another plate may be inserted at $x=a$ if

$$\beta a \sin\theta = v_m, \tag{3}$$

where

$$v_m = m\pi \qquad m = 1, 2, 3, \cdots.$$

(TM TYPE, "TMT")

Eq. (3) may be shown to be identical to the rigorous expression for β derived from the boundary value problem. Similarly, for a TE type (TET) solution the phase factors of the incident and reflected H waves are given in the same form as (1). The boundary condition is then

placed on the normal component of H with the result

$$H_{\text{norm}} \sim \cos(\beta x \sin\theta) e^{-j\beta \cos\theta z}. \tag{4}$$

The above result was obtained by representing the incident and reflected H field in the form given by (1). In this case, the origin must be shifted to the center of the guide and the walls placed at $x = \pm a$ such that

$$\beta a \sin\theta = vl \tag{5}$$

where

$$vl = l\pi/2, \qquad l = 1, 3, 5$$

(TE TYPE, "TET").

The preceding discussion has been given purposely in a nonrigorous manner as an introducton to a more involved treatment. The general vector form of the incident and reflected waves of Fig. 1 is given by

$$\begin{aligned} \boldsymbol{E}_i &= (\boldsymbol{E}_{xi} + \boldsymbol{E}_{yi} + \boldsymbol{E}_{zi}) e^{-j\beta \cos\theta z - j\beta \sin\theta x} \\ \boldsymbol{E}_r &= (\boldsymbol{E}_{xr} + \boldsymbol{E}_{yr} + E_{zr}) e^{-j\beta \cos\theta z + j\beta \sin\theta x}. \end{aligned} \tag{6}$$

Two different types of solutions will be considered. For the first type the magnitude of the reflected components tangential to the metal guide walls will be equal in magnitude and sign to the incident tangential components. The second type has reflected components which are equal in magnitude and opposite in sign to the incident tangential components. These results are summarized below for the parallel-plate guide

$$\left.\begin{aligned} \boldsymbol{E}_{yi} &= \boldsymbol{E}_{yr} \\ \boldsymbol{E}_{zi} &= \boldsymbol{E}_{zr} \end{aligned}\right\} \text{TET} \tag{7}$$

$$\left.\begin{aligned} \boldsymbol{E}_{yi} &= -\boldsymbol{E}_{yr} \\ \boldsymbol{E}_{zi} &= -\boldsymbol{E}_{zr} \end{aligned}\right\} \text{TMT}. \tag{8}$$

Note that (7) corresponds to a boundary condition (b.c.) of type (5) and similarly (8) corresponds to (3).

Now consider the same waveguide completely filled with a ferrite characterized by a tensor permeability of the following form

$$\underline{\mu} = \mu_0 \begin{bmatrix} \mu & -j\mu' & 0 \\ j\mu' & \mu & 0 \\ 0 & 0 & 1 \end{bmatrix}. \tag{9}$$

The particular solutions presented in this paper will consist of bundles of plane waves, satisfying boundary conditions of type (3) or (5) at the guide walls. The angle of propagation θ given by (3) or (5) must also be the angle θ for propagation of a plane wave in an infinite medium. The well-known result for the propagation of a plane wave in an infinite ferrite medium is due to Polder [5] and is summarized below for convenience.

Let $\hat{s}$ be the direction of the wave (see Fig. 2) and

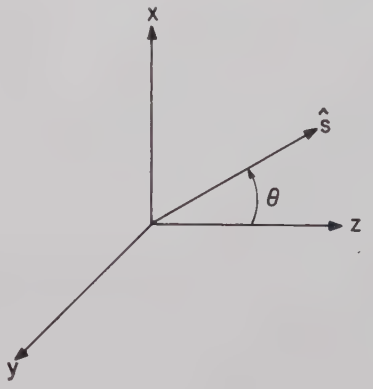

Fig. 2—Coordinate system for Polder's relation.

$\gamma = j\beta$, the corresponding propagation constant. Then Maxwell's equations reduce to

$$\gamma \hat{s} \times \boldsymbol{E} = -j\omega \underline{\mu} \boldsymbol{h} \tag{10}$$

$$\gamma \hat{s} \times \boldsymbol{h} = j\omega\epsilon \boldsymbol{E}. \tag{11}$$

Eqs. (10) and (11) may be combined to give the following wave equation

$$\gamma^2[\hat{s}(\hat{s}\cdot\boldsymbol{h}) - \boldsymbol{h}] - \omega^2 \underline{\mu}\epsilon \boldsymbol{h} = 0. \tag{12}$$

With the assumption $\boldsymbol{h} \neq 0$, (12) may be solved for γ^2, or

$$\gamma^2 = -\omega^2\mu_0\epsilon \frac{(\mu^2 - \mu - \mu'^2)\sin^2\theta + 2\mu \pm [(\mu^2 - \mu - \mu'^2)^2 \sin^4\theta + 4\mu'^2\cos^2\theta]^{1/2}}{2[(\mu - 1)\sin^2\theta + 1]}. \tag{13}$$

Since the assumption is that plane waves are propagated, the value of θ in (13) must be identical to the value of θ in (3) or (5) or

$$\beta_r{}^2\mu = \frac{(\mu^2 - \mu - \mu'^2)\left(\frac{v_m}{\beta_r a_r}\right)^2 + 2\mu \pm \left[(\mu^2 - \mu - \mu'^2)^2\left(\frac{v_m}{\beta_r a_r}\right)^4 + 4\mu'^2\left(1 - \frac{v_m{}^2}{\beta_r{}^2 a_r{}^2}\right)\right]^{1/2}}{2\left[(\mu - 1)\left(\frac{v_m}{\beta_r a_r}\right)^2 + 1\right]} \tag{14}$$

where

$$\beta_r^2 = \beta^2/\omega^2\mu\mu_0\epsilon$$
$$a_r = a\omega\sqrt{\mu\mu_0\epsilon}.$$

Eq. (14) may be solved directly for β^2 in terms of μ, μ', v_m, and a. Note that the solution for β (13) is a function of the on-diagonal permeability μ. The results computed in this paper will assume a value of $\mu=1$, which is known to be a fairly good approximation for small anisotropies. It is important to note the simplicity of the expressions for the field and propagation constants compared with the classical results for the general case.

For $\mu=1$, (14) reduces to

$$2\beta_r^2 = -\left(\frac{\mu'}{\mu}\right)^2 \frac{v_m^2}{\beta_r^2 a_r^2} + 2 \pm \left[\left(\frac{\mu'}{\mu}\right)^4 \left(\frac{v_m}{\beta_r a_r}\right)^4 + 4\left(\frac{\mu'}{\mu}\right)^2 \left(1 - \frac{v_m^2}{\beta_r^2 a_r^2}\right)\right]^{1/2}. \quad (15)$$

The individual plane wave components satisfying (12) must be investigated to see which are TMT or TET. These actual plane wave components may be computed from (12) arranged in the matrix form given by

$$\begin{bmatrix} \gamma^2\cos^2\theta+\omega^2\mu\mu_0\epsilon & -j\omega^2\mu'\mu_0\epsilon & -\gamma^2\sin\theta\cos\theta \\ j\omega^2\mu'\mu_0\epsilon & \gamma^2+\omega^2\mu\mu_0\epsilon & 0 \\ -\gamma^2\sin\theta\cos\theta & 0 & \gamma^2\sin^2\theta+\omega^2\mu_0\epsilon \end{bmatrix} \begin{Bmatrix} h_x \\ h_y \\ h_z \end{Bmatrix} = 0. \quad (16)$$

The result (13) was found by noting that with $h\neq 0$ the determinant of the coefficients must be zero. The result gave two possible values of γ^2, γ_+^2 and γ_-^2. In general the determinant of (16) is of rank two, which is one less than the number of unknowns. The values of the h's in (16) are proportional to the cofactors of the coefficients in any row of the matrix (16).

The following three sets of polarization vectors represent three possible solutions

$$\begin{aligned} h_x &= C_1(\gamma^2+\omega^2\mu\mu_0\epsilon)(\gamma^2\sin^2\theta+\omega^2\mu_0\epsilon) \\ h_y &= C_1(j\omega^2\mu'\mu_0\epsilon)(\gamma^2\sin^2\theta+\omega^2\mu_0\epsilon) \\ h_z &= C_1(\gamma^2+\omega^2\mu\mu_0\epsilon)(\gamma^2\sin\theta\cos\theta), \end{aligned} \quad (17)$$

$$\begin{aligned} h_x &= C_2(-j\omega^2\mu'\mu_0\epsilon)(\gamma^2\sin^2\theta+\omega^2\mu_0\epsilon) \\ h_y &= C_2\{(\gamma^2\cos^2\theta+\omega^2\mu\mu_0\epsilon)(\gamma^2\sin^2\theta+\omega^2\mu_0\epsilon) \\ &\qquad -\gamma^4\sin^2\theta\cos^2\theta\} \\ h_z &= C_2(\gamma^2+\omega^2\mu\mu_0\epsilon)(\gamma^2\sin\theta\cos\theta), \end{aligned} \quad (18)$$

$$\begin{aligned} h_x &= C_3(\gamma^2+\omega^2\mu\mu_0\epsilon)(\gamma^2\sin\theta\cos\theta) \\ h_y &= C_3(j\omega^2\mu'\mu_0\epsilon)(\gamma^2\sin\theta\cos\theta) \\ h_z &= C_3\{(\gamma^2+\omega^2\mu\mu_0\epsilon)(\gamma^2\cos\theta+\omega^2\mu\mu_0\epsilon) \\ &\qquad -(\omega^2\mu'\mu_0\epsilon)^2\}. \end{aligned} \quad (19)$$

Kales[1] has shown that at the cutoff condition (*i.e.*, $\theta=\pi/2$) the classical hybrid solution reduces to the normal TE and TM waves. The plane wave solutions (17)–(19) will be examined near cutoff. For the case $\theta=\pi/2$, $\gamma^2=-\omega^2\mu_0\epsilon$ and the only nonzero solution is (19). The E and H components of this wave are shown in Fig. 3. This wave reduces to the TE-type wave at cutoff. On the other hand, if $\theta=\pi/2$ and $\gamma_+^2=-\omega^2\mu_0\epsilon(\mu^2-\mu'^2)/\mu$ then (17) and (18) reduce to the TMT wave shown in Fig. 4.

With $\theta<\pi/2$ both the γ_+^2 and γ_-^2 waves may be shown to satisfy TMT or TET b.c. with some degree of approximation. The degree of satisfaction of the b.c. of the correct type is found by noting the phase and

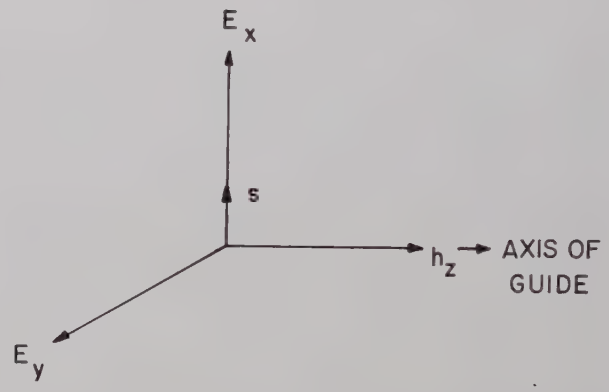

Fig. 3—Components of γ^2 wave at cutoff.

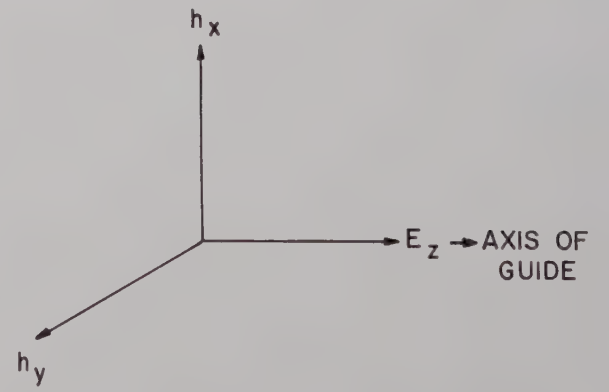

Fig. 4—Components of γ_+ wave at cutoff.

[1] Kales [1], *op. cit.*, p. 605.

magnitude of the incident and reflected tangential waves. All TMT waves must satisfy (8) and TET waves must satisfy (7). The electric field is easily found from (11) or

$$\boldsymbol{E} = \frac{\gamma}{j\omega\epsilon}\,\hat{s} \times \boldsymbol{h}$$

$$\boldsymbol{E} = \frac{\gamma}{j\omega\epsilon}\,[-\cos\theta h_x\hat{x} + (h_x\cos\theta - h_z\sin\theta)\hat{y} + h_y\sin\theta\hat{z}]. \quad (20)$$

The problem of satisfying (7) or (8) reduces to the determination of the evenness or oddness of the tangential E field of a particular solution. For example the TET solution (19) has the following properties for $\theta < \pi/2$

$$E_{yi} = -E_{yr}$$
$$E_{zi} = +E_{zr}. \quad (21)$$

Note that the E_z components satisfy TET b.c. for all values of θ while the E_y components do not satisfy the b.c. Consider now the TMT particular solution (18) where

$$E_{yi} = +E_{yr}$$
$$E_{zi} = -E_{zr}. \quad (22)$$

Note that in this case the E_z component satisfies the TMT b.c., and the E_y component does not satisfy the b.c. The behavior of the E_y component at the boundary must be investigated further by finding the ratio of E_y to E_z. This ratio may be computed from (20) with (17)–(19). The results for some representative values shown in Figs. 5 and 6 yield the ratio $(E_y/E_z) \leq 0.07$. For each solution it is necessary to check this ratio as a basis for estimating the accuracy of the results.

Brodwin has shown that there are certain critical spacings for each mode. From (3) and (5) it is really seen that for each mode

$$\beta_r x_r \geq (2m-1)\pi/2 \qquad m = 1, 2, 3 \cdots \text{TET} \quad (23)$$
$$\beta_r x_r \geq m\pi \qquad m = 1, 2, 3 \cdots \text{TMT} \quad (24)$$

where

$$\beta_z = \beta_r \cos\theta.$$

The critical spacings are given by the equalities in (23) and (24), since at cutoff

$$\sin\theta = 1 = v_m/\beta_r x_r. \quad (25)$$

Substitution of (25) in (13) gives, for the critical spacing,

$$x_r^{\text{crit}} = \frac{v_m}{\left[1 - \dfrac{\mu'^2}{\mu^2}\right]^{1/2}} \quad \text{TMT}. \quad (26)$$

Eq. (26) was derived with the plus sign in (13); application of the negative sign shows that

$$x_r^{\text{crit}} = v_m \quad \text{TET}. \quad (27)$$

Eq. (26) agrees exactly with Brodwin's equation (9). The critical spacing given by (27) is identical to the critical spacing in an isotropic waveguide. Note also that for the lowest-order plane wave modes to propagate in this type of structure β_r and X_r must satisfy

$$\beta_r x_r \geq \pi/2 \quad \text{TET}$$
$$\beta_r x_r \geq \pi \quad \text{TMT}.$$

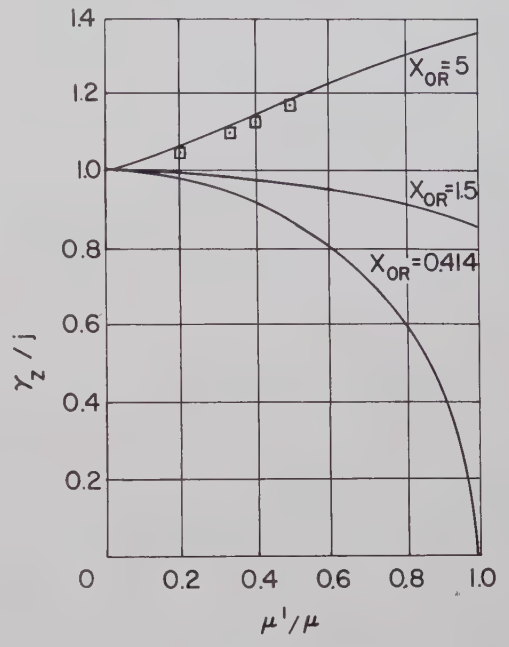

Fig. 5—Propagation constants of parallel-plane guide as a function of the anisotropy.

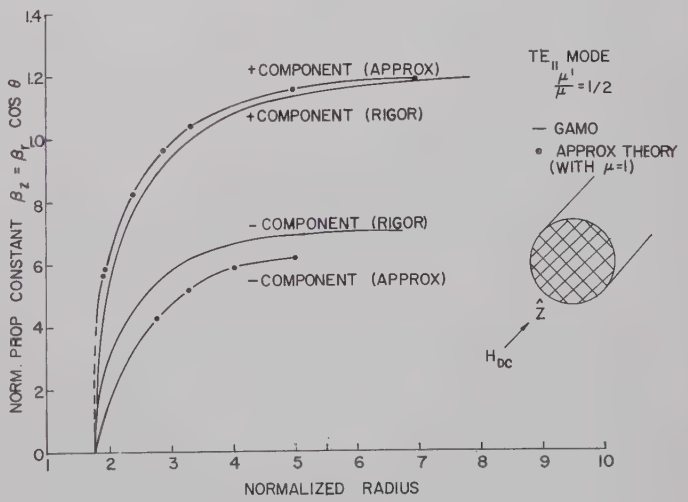

Fig. 6—Propagation constant of circular guide as a function of the radius ($\mu'/\mu = \frac{1}{2}$).

The above picture of a bundle of plane waves bouncing back and forth along the ferrite filled guide may be extended to circular structures. As a second application of the method, consider the circular guide in Fig. 7.

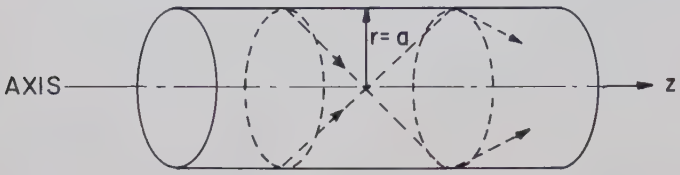

Fig. 7—Plane waves in circular guide.

In the case of the circular guide the bundle of plane waves forms a cone about the guide axis. For isotropically filled guide Schelkunoff [7] has shown that it is possible to express guided waves above cutoff as bundles of plane waves repeatedly reflected from the cylindrical boundary. A somewhat similar approach will be taken in this paper. Let the amplitude of the element incident tangential wave be $\mathcal{E}_{ti}(\alpha)d\alpha$ and reflected wave $\mathcal{E}_{tr}(\alpha)d\alpha$, then the total tangential field, E_t, is given by

$$E_t \sim e^{-j\beta z\cos\theta}\left\{\int_0^{2\pi}\mathcal{E}_{ti}(\alpha)e^{-j\beta(x\cos\alpha+y\sin\alpha)\sin\theta}d\alpha + \int_0^{2\pi}\mathcal{E}_{tr}(\alpha)e^{+j\beta(x\cos\alpha+y\sin\alpha)\sin\theta}d\alpha\right\}. \quad (28)$$

The first type of solution under consideration will have an elemental wave variation given by

$$\mathcal{E}_{ti} = E_0 e^{in\alpha} = \mathcal{E}_{tr}(\alpha) \quad \text{TMT} \quad (29)$$

where n is an integer. With (29) in (28) it follows that

$$E_t \sim E_0 e^{-j\beta z\cos\theta}\int_0^{2\pi}\cos\left[\beta\rho\sin\theta\cdot\cos(\phi-\alpha)-n\alpha\right]d\alpha, \quad (30)$$

where

$$\rho\cos(\phi-\alpha) = x\cos\alpha + y\sin\alpha.$$

The integration of (30) is readily performed with the result

$$E_t \sim 2E_0 e^{-j\beta z\cos\theta}\begin{Bmatrix}\sin n\phi\\ \cos n\phi\end{Bmatrix}J_n(\beta\rho\sin\theta). \quad (31)$$

The b.c. is that (31) be zero at the surface of a perfectly conducting cylinder of radius a, or

$$J_n(\beta a\sin\theta) = 0,$$

or

$$\beta a\sin\theta = v_m, \quad \text{where} \quad v_1 = 383,\ v_2 = 7.02, \text{ etc.} \quad (32)$$

The TET solution is constructed by considering elemental waves given by

$$\mathcal{E}_{ti}(\alpha) = E_0\cos(\phi-\alpha)e^{in\alpha} = -\mathcal{E}_{tr}(\alpha) \quad \text{TET.} \quad (33)$$

The odd symmetry of the incident and reflected waves in (33) result in a total tangential field given by (28) or

$$E_t \sim E_0 e^{-j\beta z\cos\theta}\int_0^{2\pi}\cos(\phi-\alpha)\cdot\sin\left[\beta\rho\sin\theta\cos(\phi-\alpha)-n\alpha\right]d\alpha$$

$$E_t \sim 2E_0 e^{-j\beta z\cos\theta}\begin{Bmatrix}\sin n\phi\\ \cos n\phi\end{Bmatrix}J_n'(\beta\rho\sin\theta). \quad (34)$$

Again, the b.c. is that (34) be zero at the surface of a perfectly conducting cylinder of radius a, or

$$J_n'(\beta a\sin\theta) = 0 \quad (35)$$

or

$$\beta a\sin\theta = v_m$$

where

$$v_1 = 1.84 \qquad v_2 = 5.34, \text{ etc.}$$

Note that the definition of the wave types has been changed for the round guide in order to preserve internal consistency. As in the case of the parallel-plane guide the assumed TET and TMT polarizations do not agree exactly with (33) or (29). The TET solution in the circular guide has E_z satisfied identically and E not satisfied. Similarly an examination of (18), (20) and (29) shows that for the TMT solution E_z is satisfied and E_ϕ is not. As in the case of the parallel-plate guide the ratio of the unsatisfied to the satisfied component must be negligible for a valid solution.

Since each plane wave in the bundle must satisfy Polder's relation, then (15) applies in this case with v_m given by (32) or (34). For each value of v_m, two values of β_r are obtained, and the critical radii are given by

$$a^{\text{crit}} = \frac{v_m}{\left[1-(\mu'^2/\mu^2)\right]^{1/2}} \quad \text{TMT} \quad (36)$$

$$a^{\text{crit}} = v_m \quad \text{TET.} \quad (37)$$

As a further application of the method, consider the coaxial line shown in Fig. 8. In this case one set of plane waves of the type (28) is not able to satisfy the boundary condition at $r=a$ and $r=b$.

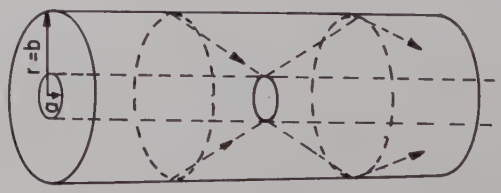

Fig. 8—Plane waves in coaxial guide.

In order to generate a second independent solution for the coaxial region, a new set of plane wave components must be found. These plane wave components will differ in amplitude from the plane wave components in (29) and (33). The second independent Bessel solution is well known (*i.e.*, the Neuman function solution). Here the problem is to represent the second bundle of waves as a Neuman function. The physical interpretation of the method in this paper is best preserved by working in the real domain. Consider the following representation of the Neuman function:

$$N_n(z) = \lim_{\nu \to n} \left\{ \frac{\partial J_\nu(z)}{\partial \nu} - (-1)^n \frac{\partial J_{-\nu}(z)}{\partial \nu} \right\}. \quad (38)$$

Now, from the integral representation

$$J_{\pm n}(z) = \frac{j^{\pm n}}{2\pi} \int_0^{2\pi} e^{\pm jn\psi} e^{+jz \cos \psi} d\psi \quad (39)$$

it follows

$$\frac{\partial J_{\pm \nu}(\partial)}{\partial \nu} = \frac{j^{\pm \nu}}{2\pi} \int_0^{2\pi} \pm j\psi e^{\pm j\nu\psi} e^{+jz \cos \psi} d\psi. \quad (40)$$

With (40) in (38) the Neuman function may be given in the form

$$N_n(z) = \lim_{\nu \to n} \frac{1}{2\pi} \left\{ \int_0^{2\pi} [j^{(1-n)} e^{jn\psi} - (-1)^n j^{-(1-n)} e^{-j\nu\psi}] \cdot e^{jz \cos \psi} d\psi \right.$$

$$N_n(z) = \frac{j^{3n+1}}{2\pi} \int_0^{2\pi} \psi \cos n\psi e^{jz \cos \psi} d\psi. \quad (41)$$

In other words, to obtain the second independent Bessel solution in a circular region the elemental plane waves must have amplitudes which vary as

$$\psi \cos \psi. \quad (42)$$

Returning to the TMT solution, the elemental incident and reflected waves have amplitudes given by

$$\mathcal{E}_{ti} = E_1(\phi - \alpha) \cos n\phi e^{jn(\phi - \alpha)} = \mathcal{E}_{tr} \quad \text{TMT}. \quad (43)$$

Substituting (43) in (28) and performing the integration, it follows that

$$E_t \sim \cos n\phi \{ E_0 J_n/\beta\rho \sin \theta) + E_1 N_n(\beta\rho \sin \theta) \}. \quad (44)$$

The b.c. are applied at $r = a$ and $r = b$, and noting that E_0 and E_1 are not identical zero it follows that

$$J_n(\beta a \sin \theta) N_n(\beta b \sin \theta) - J_n(\beta b \sin \theta) N_n(\beta a \sin \theta) = 0. \quad (45)$$

Without belaboring the point, the TET solution is generated by finding the elemental plane-wave components which integrate to form the derivative of the Neuman function. The propagation constant β is then given as a solution of the determinantal equation

$$J_n'(\beta a \sin \theta) N_n'(\beta b \sin \theta) - J_n'(\beta b \sin \theta) N_n'(\beta a \sin \theta) = 0. \quad \text{TET}. \quad (46)$$

Again as in the case of the circular guide, (45) and (46) are used in conjunction with Polder's relation (15) to determine the permissible values of β. Fortunately, all of the determinantal equations for β are identical to the isotropic case and have been solved for a wide variety of cases.

Theoretical and Experimental Results

Parallel-Plate Guide

Brodwin [3] has made some computations of the propagation constant and critical spacings of ferrite-filled parallel-plate guide. These results are given as a function of the anisotropy (μ'/μ) and were computed from the classical formulation. Brodwin's computation of β_z as a function of (μ'/μ) for different values of normalized spacing X_{0r} is shown in Fig. 5. The results apply to the odd quasi-TE, even quasi-TM and quasi-TEM modes. As a comparison the variation of β_z was calculated as a function of (μ'/μ) for a normalized spacing of $X_{0r} = 5$ from (15) and (23). Eq. (15) was solved by separating the equality into two parts, y_1 and y_2, where

$$y_1 = 2\beta_r^2 + \left(\frac{\mu'}{\mu}\right) \frac{v_n^2}{\beta_r^2 x_{0r}^2} - 2$$

$$y_2 = \left[\left(\frac{\mu'}{\mu}\right)^4 \frac{v_m^4}{\beta_r^4 x_{0n}^4} + 4\left(\frac{\mu'}{\mu}\right)^2 \left(1 - \frac{v_m^2}{\beta_r^2 x_{0r}^2}\right) \right]^{1/2}. \quad (47)$$

The value of β_z is found by multiplying the value of β_r by $\cos \theta = [1 - (v_m/\beta_r X_{0r})^2]^{1/2}$. The correct value of β_r was determined graphically from the equality $y_1 = y_2$. The quantitative agreement in Fig. 5 is excellent. The equation for the critical spacing (26) agrees exactly with Brodwin's (9) and was not plotted for comparison.

Circular Waveguide

Gamo investigated the propagation constant of ferrite filled circular guide for specific values of anisotropy. For a value of $(\mu'/\mu) = 1/2$, the propagation constant is plotted as a function of the radius in Fig. 6. Gamo's quasi-TE_{11} mode corresponds to the TET_{11} mode. Note that the behavior of the approximate solution is very close to the rigorous solution. Note that the TET_{11} cutoff may be defined for the minus component only. However, the plus component has the correct behavior near cutoff.

Coaxial Waveguide

No classical theoretical results were available to compare the approximate theory. An experimental model was constructed to test the theory and is shown in Figs. 9 and 10. A length of ferrite[2] 0.500 inch O.D. $\times$ 0.040 inch ID $\times$ 0.810 inch was placed between two stycast ($\varepsilon = 12$) pieces. The center conductor extended through

[2] Trans-Tech TT1-105.

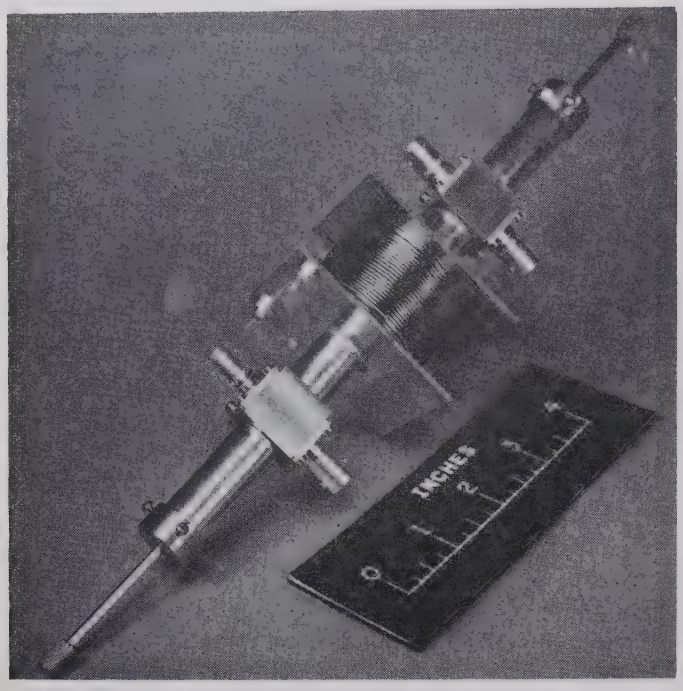

Fig. 9—Experimental device for measuring Faraday rotation in coaxial waveguide.

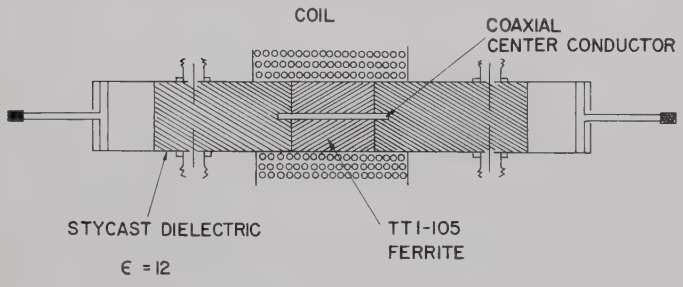

Fig. 10—Cross section of experimental coaxial rotator shown in Fig. 9

the ferrite and a short distance into the stycast pieces. Two probes were driven 180 electrical degrees out of phase to excite the TE_{11} mode in the completely stycast filled section of the guide. The guide was constructed so as to pass the TE_{11} mode and reject the next highest mode. Hopefully, the comparable TE_{11} mode was excited in the ferrite. Two other probes were mechanically fixed at the receiver end of the guide structure and lined up to the driven probes. The receiver probes were tuned for maximum output at 6000 Mc input with no applied field. The longitudinal magnetic field was then increased until the receiver output was a minimum. Filmohm resistance cards were placed at both ends of the unit in the dielectric pieces. These cards absorb the cross component of the RF energy when the magnetic field is applied. This value of field corresponded to 90° of Faraday rotation or

$$(1/2)(\beta_+ - \beta_-)l = \pi/2$$

or

$$(\beta_+ - \beta_-) = 0.206\beta_0. \tag{48}$$

Values of β_+ and β_- were computed from (15) as a function of (μ'/μ). It was found that for the size of coaxial ferrite insert (*i.e.*, $D/d = 12.5$) a value of $(\mu'/\mu) = 0.20$ corresponded to $(\beta_+ - \beta_-) = 0.206\beta_0$.

In order to gain some check on the above value of (μ'/μ) the experimental value of applied field was substituted in Kittel's theoretical expressions to find the actual value of (μ'/μ). The following physical constants were used

$$\chi = 0.558^{(8)}$$

$$N_l = 2.51 \qquad N_t = 5.03^{(9)}$$

$$H_a = 215 \text{ oersteds}$$

$$\bar{\gamma} = 1.76 \times 10^7 \text{ raa/sec/oersted.} \tag{49}$$

The demagnetization factor N was calculated by assuming the center hole in the ferrite had a negligible effect.

The value of (μ'/μ) corresponding to the above constants was calculated from the following formula given by Hogan [10]

$$\frac{\mu'}{\mu} = \frac{(4\pi - N_l)M\bar{\gamma}\omega}{\omega_0^2 + (4\pi - N_l)\bar{\gamma}M\omega - \omega^2} \tag{50}$$

$$\frac{\mu'}{\mu} = 0.20 \tag{51}$$

The above value represents an excellent agreement with approximate theory considering the variation of H_a (*i.e.*, 5 per cent) and the value of N.

Acknowledgment

The author would like to acknowledge the helpful suggestions and encouragement given by Dr. M. L. Kales of the Naval Research Laboratory. He also wishes to express his appreciation to Dr. J. Wiltse of Electronic Communications Inc., for his assistance on the experimental aspects of the problem.

Bibliography

[1] M. L. Kales, "Modes in waveguide containing ferrites," *J. Appl. Phys.*, vol. 24, pp. 604–608; May, 1953.
[2] H. Suhl and L. R. Walker, "Topics in guided wave propagation through gyromagnetic media," *Bell Sys. Tech. J.*, vol. 33, pp. 575–659; May, 1954.
[3] M. E. Brodwin, "Propagation in ferrite-filled microstrip," IRE Trans. on Microwave Theory and Techniques, vol. MTT-6, pp. 150–155; April, 1958.
[4] H. J. Gamo, "The Faraday rotation of waves in a circular waveguide," *J. Phys. Soc. Japan*, vol. 8, pp. 176–182; March–April, 1953.
[5] D. Polder, "On the Theory of Ferromagnetic Research," *Phil. Mag.*, vol. 40, pp. 99–115; 1949.
[6] F. B. Hildebrand, "Methods of Applied Mathematics," Prentice-Hall Inc., New York, N. Y. p. 23; 1952.
[7] S. A. Schelkunoff, "Electromagnetic Waves," D. Van Nostrand Co., Inc., Princeton, N. J., pp. 410–412; 1943.
[8] Data supplied by Trans-Tech, Rockville, Md. (A. C. Blankenship, private communication), August 23, 1960.
[9] G. R. Jones, "Calculated Magnetic Fields of Ferrite, Rods, Discs, and Slabs," U. S. Dept. of Commerce, O.T.S. No. PB 131938; 1959.
[10] C. L. Hogan, "The elements of nonreciprocal microwave devices," Proc. IRE, vol. 44, pp. 1345–1368; October, 1956.

Synthesis of Low-Reflection Waveguide Joint Systems*

P. FOLDES†, MEMBER, IRE, AND N. GOTHARD†

Summary—**Some characteristics of flat-flange type joints are analyzed. Experimental evidence is given proving that it is possible to reproduce, in practice, waveguide joints which have identical complex-reflection coefficients. Such joints can be combined to form large joint systems by means of a synthesis method, which keeps the over-all reflection coefficient to a minimum. Both theory and experimental data are presented.**

I. Introduction

In high-quality, wide-band, frequency-modulated microwave communication systems the ultimate distortion level is quite often determined by the end and internal reflections of the transmission line.[1–4] In and above the *S* band (2000 Mc) the transmission loss in a coaxial line becomes high and the required tolerances for a coaxial branching system are extremely tight. It is difficult to obtain a low input reflection coefficient with a coaxial antenna input in a wide frequency band.

Thus it becomes mandatory to use waveguide components in high-quality transmission systems. Such a system assures low resistive loss and low end reflections; however, it introduces new types of reflection sources at the waveguide joints. From communication-system distortion standpoint two parameters characterize these internal reflections; the reflection coefficient of one joint, and the so-called "ripple factor," which is the ratio of the maximum and the average reflection coefficient in the operational frequency band at the input of the waveguide system.

The first parameter depends on the construction of the joint, while the ripple factor is determined by the positions of the joints along the line. By means of a simple synthesis method it is possible to calculate: 1) the allowable number of joints and their position for a given maximum reflection coefficient, and 2) frequency band and total length of transmission line.

II. Characteristics of the Individual Waveguide Joint

A. General Behavior

The complex reflection coefficient of the flat-flange type joint depends on three factors:[5–9]

1) Size difference between two joining waveguides.
2) Misalignment between the two waveguides.
3) Surface geometry and electrical conductivity along the flange surface.

The surface geometry depends on the surface roughness, the connecting bolt pressure, and the elasticity of the flange material close to the mating surface. The electrical conductivity depends on the quality and purity of the material and is also affected by the long-term corrosion processes.

According to the experimental data it is possible by careful manufacturing to obtain a joint which can be represented by approximately the series impedance

$$Z = R(f) + \frac{1}{j2\pi fC} + jX(f), \tag{1}$$

where $R(f)$ represents the frequency-dependent loss resistance along the contact surface, C is the series capacity between the two mating flanges, and $X(f)$ represents the effect of step and misalignment, which can be either inductive or capacitive. However, it can be found, experimentally that

$$\left| R(f) + \frac{1}{j2\pi fC} \right| \gg | X(f) | , \tag{2}$$

if the manufacturing tolerances are within small, but practically possible, limits. Two important facts follow from (1) and (2):

1) The magnitude of the reflection coefficient can be relatively constant in ±15 per cent frequency band if the resistive and capacitive components of (1) are comparable.
2) It is possible to obtain approximately identical complex reflection coefficients for each joint along the waveguide system, if the surface quality and flange pressure on the flanges are nearly equal.

The utilization of these facts leads to the application of the synthesis method to obtain an optimally located waveguide joint system.

Table I summarizes the practically possible tolerances and their corresponding theoretical reflection coefficients

* Received by the PGMTT, July 18, 1960; revised manuscript received, December 5, 1960.

† Tech. Products Div., RCA Victor Co., Ltd., Montreal, Can.

[1] L. Lewin, "Interference in multichannel circuits," *Wireless Engr.*, vol. 27, pp. 294–304; January, 1950.

[2] L. Lewin, "Multiple reflections in long feeders," *Wireless Engr.*, vol. 29, pp. 189–193; July, 1952.

[3] L. Lewin, "Aerial feeders for multi-channel links," *Electronic Engrg.*, vol. 30, pp. 414–419; July, 1958.

[4] R. G. Medhurst, "Echo-distortion in frequency modulation," *Electronic and Radio Engr.*, vol. 36, pp. 253–259; July, 1959.

[5] F. Bolinder, "Fourier transforms in the theory of inhomogeneous transmission lines," Proc. IRE, vol. 38, (Correspondence), p. 1354; November, 1950.

[6] N. Marcuwitz, "Waveguide Handbook," M.I.T. Rad. Lab. Ser., McGraw-Hill Book Co., Inc., New York, N. Y., vol. 10, p. 62; 1951.

[7] L. Virgile, "Waveguide flange design for better microwave performance," *Electronic Design*, vol. 7, pp. 28–30; October, 1959.

[8] D. Wray and R. A. Hastie, "Waveguide bend," *Electronic Tech.*, vol. 37, pp. 76–82; February, 1960.

[9] H. A. Wheeler and H. Schwiebert, "Step-twist waveguide components," IRE Trans. on Microwave Theory and Techniques, vol. MTT-3, pp. 44–51; October, 1955.

for S-band waveguides (4.300×2.150 inch inside dimensions). The sum of these individual reflections gives an indication of the upper limit of the reflection coefficient caused by the size and misalignment tolerances.

With the tolerances indicated in Table I the theoretical maximum value of the reflection coefficient is 0.071 per cent. However, the measured reflection coefficient on such a system is five to ten times larger, depending on the surface roughness, flatness and contact pressure on the flanges. The difference can be obviously interpreted as the effect of the gap between the flanges, and the order of this difference shows that the approximation indicated in (2) is reasonable.

Fig. 1 shows three typical measured flange surface qualities: Curve A represents the measured roughness of a cast brass flange; B shows the surface roughess after precision milling; C after lapping. From these samples, it is clear that the actual conducting flange surface can be several times larger than the nominal surface. This results in a larger resistive loss.

Besides the loss, RF energy is stored in the microscopic voids between the flanges. This energy storage can be represented by an equivalent series-capacitive reactance.

The effective conductivity between two flanges depends on the material and the surface roughness. No detectable difference can be measured in the reflection coefficient of silverplated or aluminum flanges maintaining the same surface roughness. However, large deterioration in the conductivity considerably affects the reflection coefficient. For example, when the surface quality was achieved by means of a lapping process, it was found that the reflection coefficient was considerably higher than the expected value. After the highly resistive lapping compound was partly removed, the reflection coefficient was improved slightly in spite of the fact that the chemical cleaning process resulted in a somewhat rougher surface.

From the assumed equivalent series impedance of the joint (1) it can be seen that, as the frequency increases, the capacitive reactance decreases more rapidly than the series resistance increases. (The first term in (1) increases approximately with the square root of frequency, while the second term decreases inversely with the frequency.) Therefore the reflection coefficient should decrease slightly with the frequency. The experimental data proved this assumption.

In practice, the gap size can be reduced by

1) Decreasing the surface roughness.
2) Adding a thin, soft metallic layer on top of the finished mating surfaces.
3) Applying a large uniform pressure on the contact area.

B. *Methods Reducing the "Gap Effect"*

Improvement in the Surface Roughness: Tables II and III show some measured reflection coefficient values

TABLE I

Effects of Geometrical Imperfections

Type of Error	Tolerance	Reflection Coefficient (per cent)
Step	±0.0015 inch	0.050
Transversal Misalignment	±0.0005 inch	0.010
Polar Misalignment	±0.1°	0.001
Total		0.071

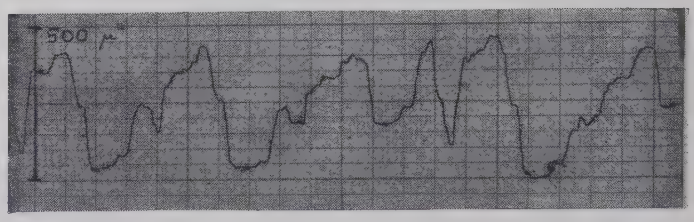

(a)

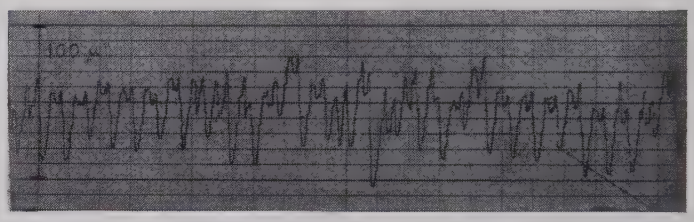

(b)

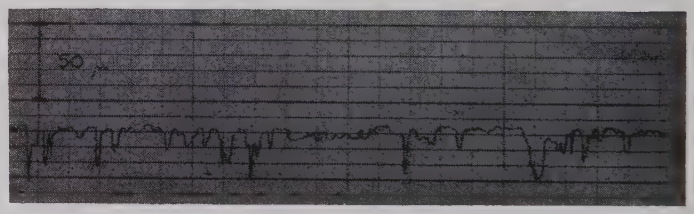

(c)

Fig. 1—Typical flange surface qualities.

for different flange surface qualities in the 1800–2300-Mc frequency band. The first of these tables offers simple proof of the gap effect. The input reflection coefficients were measured on a waveguide run which consisted of 10 sections, each 20 feet long. (The "average of the maxima" is defined in the following way: The 500-Mc-wide operational frequency band is divided into 10 50-Mc-wide sub-bands. The largest value of a reflection coefficient is taken from each of the sub-bands and then the 10 values are averaged.) The effect of the size and misalignment tolerances was negligible, relative to the effect of the flange surface. A peak-to-peak surface roughness of 100 μ inch was measured on the surfaces.

In arrangement A, $\frac{1}{8}$-inch-long spacers were placed between the two flanges, while in arrangement B these spacers were eliminated. Physically the lossy, reactive air-gap was reduced by a factor of 2 in the second arrangement. It can be seen that both the peak and the average reflections were reduced in the second arrangement approximately by a factor of two.

Table III shows the reflection coefficients of wave-

TABLE II
EFFECT OF VARYING THE NUMBER OF AIRGAPS

Arrangement	Maximum Input Reflection Coefficient (per cent)	Average of the Maxima in the Input Reflection Coefficient (per cent)	Average of the Maxima per Joint (per cent)
A. Waveguide Run with Elementary Spacers in the Joints	18.2	11.6	1.05
B. Waveguide Run without Elementary Spacers	9.2	6.2	0.56

TABLE III
EFFECT OF SURFACE ROUGHNESS

Surface Roughness in μ inch			Average of the Maxima in the Input Reflection Coefficient per Joint (per cent)	Note
Case	Peak to Peak	rms		
1	500	62	0.49	Flanges Cut from Extruded Material
2	100	12	0.38	The same as Case 1 with Standard Milling
3	60	8	0.33	The Same as Case 1 with Precision Milling
4	60	8	0.30	The Same as Case 3 with Gold Interconnecting Layer

TABLE IV
THE EFFECT OF THE QUARTER-WAVE SPACER

Condition	Maximum Input Reflection Coefficient (per cent)	Average Input Reflection Coefficient (per cent)	Average Reflection Coefficient per Joint (per cent)	Average of the Maximum Reflection Coefficient per Joint (per cent)
5 Sections without Spacers, 500-μ Inch Peak-to-Peak Surface Roughness.	6.5	2.0	0.33	0.81
5 Sections with Spacers, 500-μ Inch Peak-to-Peak Surface Roughness.	4.0	1.19	0.20	0.50

guide joints which have different surface roughness. These data were measured with quarter-wave spacers between the waveguide flanges. Table III also shows that the reflection coefficient varies considerably with the surface roughness. However there is a practical limit (probably 8 μ inch rms) beyond which there is no economical return.

Application of a Soft Interconnecting Layer: The idea of using some soft interconnecting metallic layer (indium, gold, etc.) between the two mating flanges is one solution to decrease the air-gap in the joint, or to ease the surface roughness requirement for the same electrical quality. The utilization of gold plating was tried in case 4 in Table III where the reflection coefficient decreased by an additional 10 per cent.

Optimum Contact Pressure on the Flanges: It is obvious from the construction of a flange that the air-gap between two flanges has a minimum value which is a function of the connecting bolt tension. At low tension the gap is not closed completely, while at high tension levels the flange warps and the air gap increases again.

Ten $\frac{1}{4}$-inch-diameter standard stainless-steel bolts were used to maintain the connecting pressure on the flanges. The reflection coefficient was recorded as a function of the torque applied on the individual bolts. The effect of pressure was investigated in the 5–30 foot-pound torque range and it was found that the optimum value was between 10–15 foot-pounds.

Quarter-Wave Spacer Compensated Joint: The previous results indicated that under certain conditions the reflection of a joint is limited by the gap effect, which may be approximately equal for each joint. If the spacing between two identical joints is a quarter wavelength, then their net reflection is zero. In a frequency band the compensation can be only partial, but as Fig. 2 shows, the improvement is theoretically more than 6 db in the useful band of the RG-104 waveguide. Fig. 3(a) shows a photograph of such a quarter-wave spacer and Fig. 3(b) shows the reflection coefficient of a 5-section waveguide run with and without quarter wave spacers. During this test relatively rough flange surfaces were used with a 500 μ inch surface finish. Table IV summarizes the conclusions which can be drawn from the two curves on Fig. 3(b). It indicates that the quarter wave spacer resulted in a 4.6-db improvement in the average reflection coefficient, which is quite close to the theoretically estimated value.

III. Determination of a Low-Reflection Joint System Along a Waveguide Run

A. Uniformly Distributed Joints

Fig. 4 shows an L-long waveguide run which is divided by n joints. If the higher-order internal reflections are negligible, then the input reflection coefficient

$$\Gamma_{in} = \Gamma_0 + \Gamma_1 e^{j2\beta_g l_{01}} + \cdots + \Gamma_{n-1} e^{j\beta_g l_{0,n-1}}, \quad (3)$$

where β_g is the propagation constant of the guide and l_{0k} is the length between the first and kth joint. When

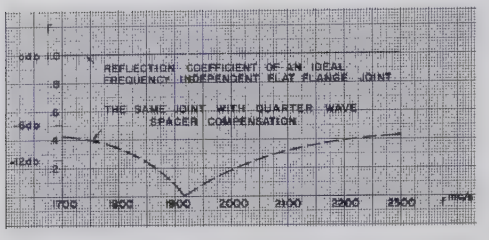

Fig. 2—Theoretical reflection coefficient of a quarter-wave spacer compensated joint.

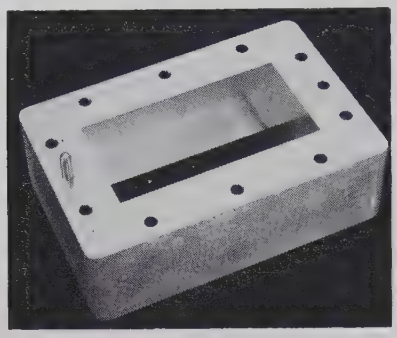

(a)

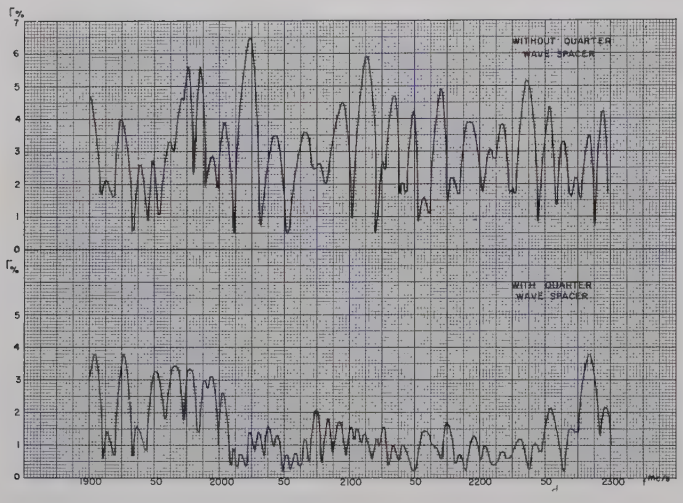

(b)

Fig. 3—(a) Quarter-wave waveguide spacer. (b) Reflection coefficient of a five-section waveguide run with and without quarter-wave spacer.

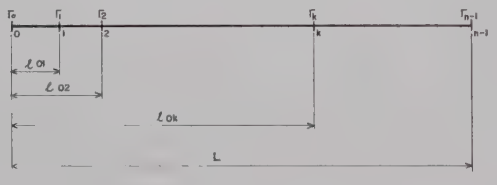

Fig. 4—Geometrical arrangement of a joint system.

all the individual joint reflections are equal in magnitude and phase ($\Gamma_k = \Gamma_i = \Gamma$) and the sections are equal in length, then the normalized input reflection coefficient

$$\Gamma_N = \frac{\Gamma_{in}}{\Gamma} = e^{j(n-1)} \frac{w}{2} \frac{\sin \frac{nw}{2}}{\sin \frac{w}{2}}, \tag{4}$$

and

$$|\Gamma_N| = \left| \frac{\sin \frac{nw}{2}}{\sin \frac{w}{2}} \right|, \tag{5}$$

where

$$w = 2\beta_g l = 4\pi \frac{l}{\lambda_g}.$$

Some important characteristics of this simple function are:

1) $|\Gamma_N|$ is periodic as a function of w,

$$w = 4\pi l \frac{1}{\lambda_g} = \frac{4\pi}{c}\left[1 - \left(\frac{c}{2af}\right)^2\right]^{1/2} clf. \tag{6}$$

where c is the velocity of light.
In a narrow frequency band the factor under the square root is approximately constant, *i.e.*, $|\Gamma_N|$ is approximately periodic with frequency.

2) The mth maximum of $|\Gamma_N|$ occurs at a point where

$$2\pi \frac{l}{\lambda_{gm}} = m\pi, \quad \text{and here} \quad |\Gamma_N|_M = n. \tag{7}$$

The ratio of two adjacent resonant wavelengths is

$$\frac{\lambda_{gm+1}}{\lambda_{gm}} = \frac{m}{m+1}. \tag{8}$$

For example if $l = 20$ feet $= 609.6$ cm and $f_0 = 1997$ Mc, then $\lambda_{gm} = 20.68$ cm and $m = 59$. The difference between two adjacent resonant frequencies is approximately 1.7 per cent.

3) From a practical standpoint not only $|\Gamma_N|_M$ is interesting, but also the average of $|\Gamma_N|$ throughout the operational frequency band. This average can be defined as

$$\Gamma_{av} = \frac{1}{w_2 - w_1} \int_{w_1}^{w_2} |\Gamma_N| \, dw, \tag{9}$$

where w_1 and w_2 correspond to the two limits of the frequency band. Furthermore, the input reflection coefficient can also be characterized by

$$R = \frac{|\Gamma_N|_M}{\Gamma_{av}}. \tag{10}$$

R will be called the ripple factor in this paper. Fig. 5 shows the variation of the ripple factor and $|\Gamma_N|_M$ as a function of the number of joints. It can be seen that both R and $|\Gamma_N|$ increase rapidly with the number of joints if the waveguide sections are equal in length.

B. Synthesis of a Smoother Input Reflection Coefficient

A simple synthesis method is now given which results in a joint distribution with a low $|\Gamma_N|_M$ and a low ripple

factor. It is assumed that the absolute value of the input reflection coefficient $|\Gamma_{in}|$ can be represented by the following function:

$$F_n = |\Gamma_{in}|_n = \left| \prod_{k=1}^{n/2} (1 + e^{j(\lambda_{g0}/\lambda_g)} e^{jkw}) \right|$$

$$\left[2^n \prod_{1}^{n/2} (1 - \cos kw) \right]^{1/2} \equiv \left[2^n \prod_{1}^{n/2} G(k) \right]^{1/2}$$

$$\text{if } \lambda_g = \lambda_{g0}$$

$$= \left[2^n \prod_{1}^{n/2} (G(k) + \pi\Delta \sin kw) \right]^{1/2}$$

$$\text{if } \lambda_g = (1 + \Delta)\lambda_{g0}. \quad (11)$$

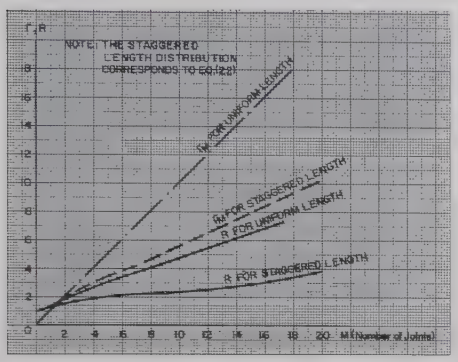

Fig. 5—The maximum reflection coefficient and ripple factor of the uniform and staggered joint distribution vs number of joints.

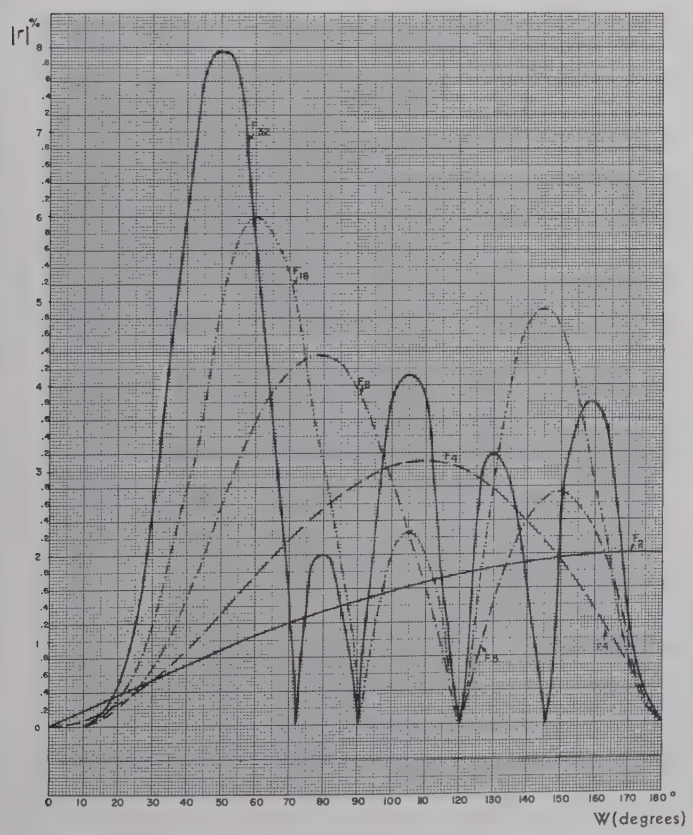

Fig. 6—The F_n functions at the center of the frequency band.

The F_n functions are given in Figs. 6 and 7 for various n as a function of w in the center and at the end of a ± 12.5 per cent frequency band. As can be seen from the curves, the F_n functions have very desirable characteristics as input reflection coefficients, *viz.*, they increase relatively slowly as n increases.

If (11) is selected as the input reflection coefficient of the waveguide system, then it is easy to generate the

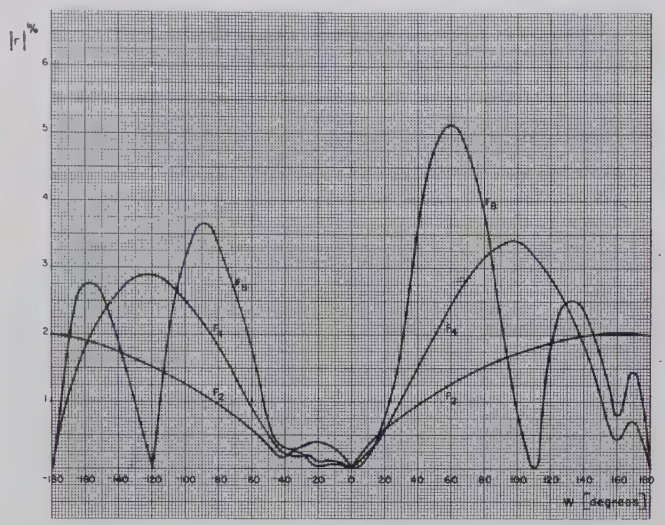

(a)

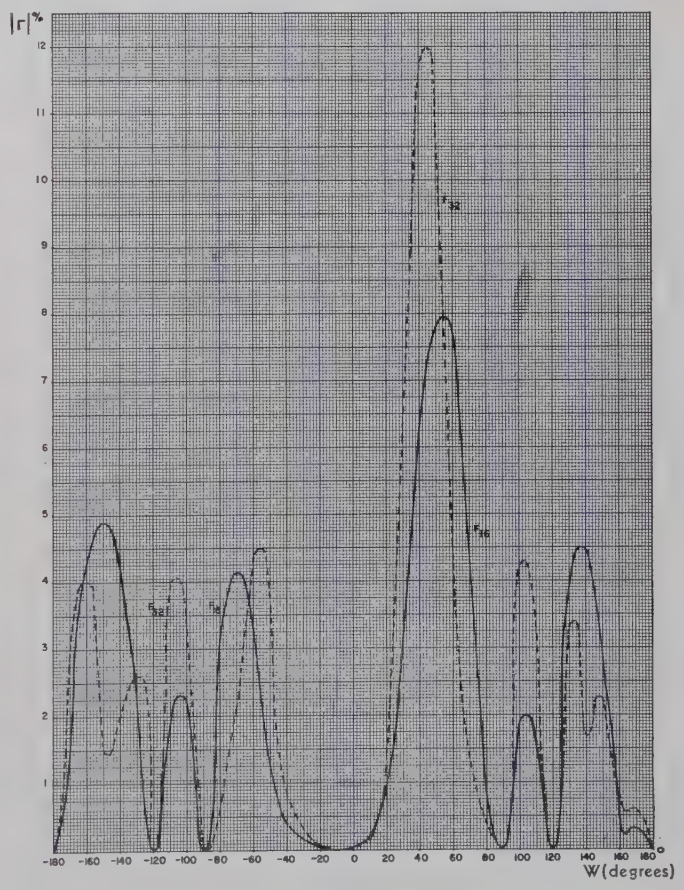

(b)

Fig. 7—The F_n functions at the limits of a ± 12.5 per cent frequency band.

corresponding joint distribution. For this purpose it is sufficient to analyze the form of (11) in the center of the frequency band ($\lambda_g = \lambda_{g0}$). The reflection coefficient for the A_2 joint distribution in Fig. 8 is

$$\begin{aligned} |\Gamma_2| &= |1 + e^{j2\beta_g(4l-\lambda_{g0}/4)}| \\ &= |1 - e^{j4w}| = \sqrt{2}[1 - \cos 4w]^{\frac{1}{2}}. \end{aligned} \quad (12)$$

In this distribution a $4l-\lambda_{g0}/4$ separation is assumed between the two joints. If an identical second joint system will be added to the first in such a way that its position will be shifted relative to the first by $3l-\lambda_{g0}/4$ toward the end of the line, then the resultant input reflection coefficient

$$\begin{aligned} |\Gamma_4| &= |\,|\Gamma_2| + |\Gamma_2| e^{j2\beta_g(3l-\lambda_{g0}/4)}| = |\Gamma_2|\,|1 - e^{j3w}| \\ &= 2[(1 - \cos 4w)(1 - \cos 3w)]^{1/2}. \end{aligned} \quad (13)$$

This is the A_4 joint distribution in Fig. 8. Repeating the process similarly, the end result is

$$\begin{aligned} |\Gamma_{1b}| = 4[&(1 - \cos w)(1 - \cos 2w)(1 - \cos 3w) \\ &\cdot(1 - \cos 4w)]^{1/2}, \end{aligned} \quad (14)$$

which is (11) in the center of the band for $n=8$. Fig. 8 shows the whole process graphically. In the end results (A_{16} joint distribution) the lines are almost equal, but simple joints as well as quarter-wave spacer separated joints should be employed. There are practical cases when from manufacturing standpoint it is not desirable to use different line lengths, or larger than one unit reflection at one joint. In such cases it is possible to obtain an approximation of the theoretical requirements by the use of quarter-wave spacers. For instance, a good equivalent of the A_{16} distribution is A_{16}' and A_{16}'' (see Fig. 9). In Table V some measured data are shown. From it a comparison can be made between the system with uniform length and spacers, and the A_{16}' distribution. The sensitivity of the synthetized reflection coefficient to the length tolerances of the individual sections was measured on three manufactured A_{16}'-type waveguide run. Table VI indicates the manner in which the input reflection coefficient varied as a function of the rms line length variations. According to the table the maximum value of the reflection coefficient shows more tolerance sensitivity than the average value.

IV. Method of Measurement

There are two type of difficulties in the measurement technique of low-reflection waveguide joints or joint systems.[10–12]

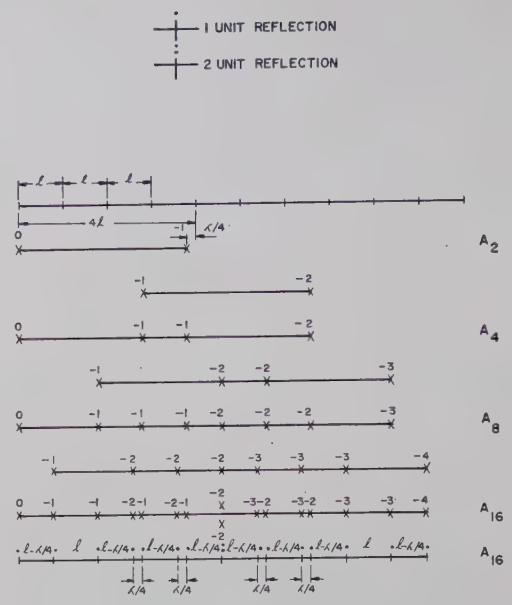

Fig. 8—Determination of the joint distribution, which corresponds to the F_{16} function.

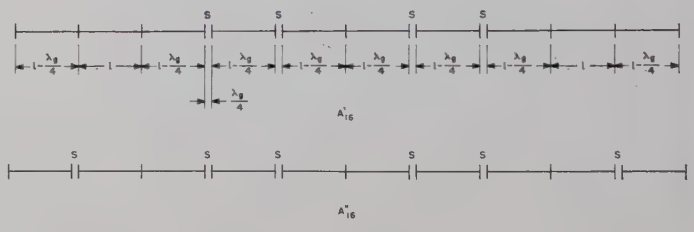

Fig. 9—Two approximate equivalents of the A_{16} distribution. S=quarter-wave spacer. All lengths are $1'=1-\lambda g/4$.

TABLE V

Comparison Between the Uniform Length and the A_{16}' Distribution

Distribution	Number of Joints	Input Reflection Coefficient Theoretical*		Input Reflection Coefficient Experimental	
		Γ_M per cent	Γ_{av} per cent	Γ_M per cent	Γ_{av} per cent
Uniform Length	11	4.94	0.99	5.07	1.2
A_{16}'	11	2.70	0.77	2.50	0.76

* 0.45 per cent reflection coefficient was assumed for one joint and for calculation purpose, the actual A_{16}' was replaced by A_{16}.

TABLE VI

Effect of the Length Tolerances

RMS Deviation from the Nominal Length (in inches)	Γ_M per cent	Γ_{av} per cent
0.041	4.56	1.12
0.033	3.57	1.15
0.016	2.50	0.76

[10] W. A. Rawlinson, J. Hooper, and R. Branch, "A Swept-Frequency Method of Locating Faults in Waveguide Aerial Feeders," Post Office Res. Sta., Dollis Hill, London, N.W. 2, Res. Rept. No. 20209; June, 1959.

[11] A. C. MacPherson and D. M. Kerns, "A new technique for the measurement of microwave standing-wave ratios," Proc. IRE, vol. 44, (Correspondence), p. 1024; August, 1956.

[12] A. C. Beck, "Microwave testing wilh millimicrosecond pulses," IRE Trans. on Microwave Theory and Techniques, vol. MTT-1, pp. 93–99; April, 1953.

1) If the reflection coefficient of one waveguide joint is in the order of less than 1 per cent, it is not convenient to measure accurately such a low-reflection coefficient with the slotted line technique.
2) It is relatively easy to use a sweep method and a high directivity directional coupler if the reflection coefficient is larger than 1 per cent, *i.e.*, in the case of joint systems. This method, however, is very time consuming because every change in the physical arrangement must be carried out along the full waveguide run.

For time saving, some of the preliminary measurements were carried out on systems which contained few joints. For this purpose an intermediate-power (lw) sweep generator and high-quality waveguide directional coupler were developed (7-db coupling, more then 50-db directivity). The high-power level and high directivity extended the absolute measuring limit down to reflection coefficients of 0.5 per cent, while a 0.05 per cent relative change was still detectable.

The effects of the various parameters (steps at the joints, surface finish, flange pressure, etc.) were studied on a relative basis, while the final numerical data were recorded using point-by-point measurements on larger joint systems.

Fig. 10 shows the test set-up which was used for the individual-joint reflection study, as well as the various length modulation experiments. Fig. 11 shows a typical scope presentation of the reflection coefficient. The line under test was the A_{16}' distribution. The peak value on the scope is equivalent to a 2.5 per cent reflection coefficient (3.5 unit). Within the represented frequency range (1780–2300 Mc), the total output power variation of the sweep generator and the coupling variation of the coupler was less than 1 db/100 Mc.

From an applicational standpoint the most important datum is the value of the peak and average reflection coefficient as a function of the line length (joints). Fig. 12 shows the theoretical maximum and average reflection coefficients and the points indicate some measured data. The calculations and measured data correspond to quarter-wave spacer compensated joints, and the length modulation is based on (11). It can be seen that there is significant agreement between the theoretical and experimental results.

V. Conclusions

With precise manufacturing processes, it is possible to produce waveguide joints which have identical electrical characteristics. Such joints can be very useful building blocks in a system with specially located flanges. In the resulting network both the maximum and the average input reflection coefficients may have unusually low values.

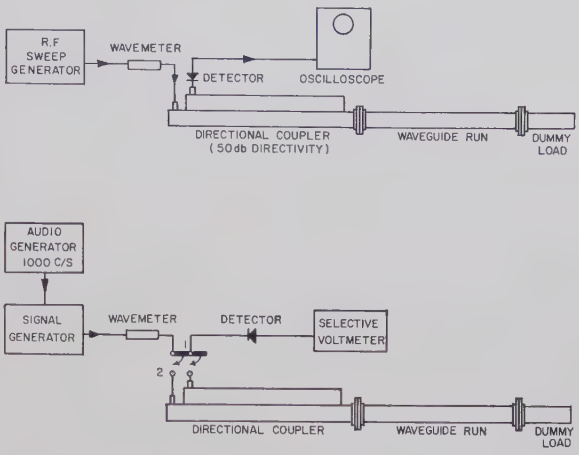

Fig. 10—Test setup for the reflection coefficient measurement.

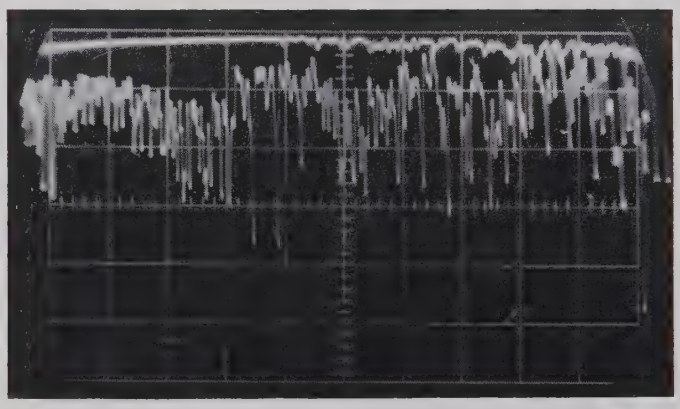

Fig. 11—Scope presentation of the reflection coefficient for the A_{16} distribution.
F=1780–2300 Mc.
Γ=2.5 per cent.

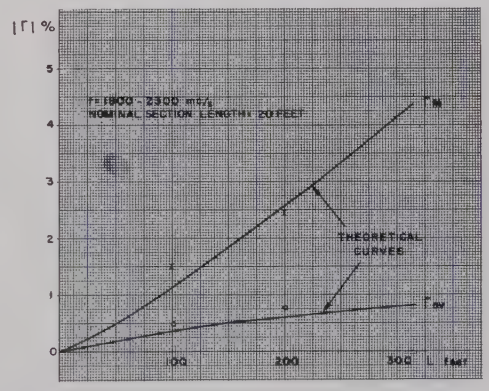

Fig. 12—Reflection coefficient of straight waveguide run vs length. Joints are quarter-wave spacer compensated. Length modulation corresponds to (11).

VI. Acknowledgment

The authors wish to express their thanks to T. B. Thompson who contributed to the early experimental work, and to R. Desrochers who helped to carry out the time-consuming measurements.

A Channel-Dropping Filter in the Millimeter Region Using Circular Electric Modes*

E. A. J. MARCATILI†, MEMBER, IRE

Summary—**A channel-dropping filter in the millimeter region that transfers TE°_{01} to $TE^{\square}_{10}$ is described and analyzed. The important features are the use of $TE^{\circledcirc}_{011}$ mode in the resonant cavities combined with a mode-selective coupling between circular symmetric and rectangular waveguides which make both heat loss and mode conversion low. Design formulas and experimental results on a model filter centered at 56 kMc are included. Finally, several possible mode transducers and filters based on the idea of mode-selective coupling are described.**

Introduction

THE long-distance waveguide communication system[1] will require the separation of many bands, each several hundred Mc wide, in the region of 35 to 75 kMc. The transmission from repeater to repeater will be made using the low-loss circular electric mode TE°_{01}, but the microwave circuitry at each repeater station will use the $TE^{\square}_{10}$ mode. Consequently, it is convenient to combine the filtering and transducing of modes in a single low-loss operation.

Insertion loss has three sources: mode conversion, heat loss and reflection.

Mode conversion must be kept very low not only because of the insertion loss but also because of possible unwanted resonances of spurious modes.

Heat losses can be minimized using cavities that resonate with high intrinsic Q; this demands the use of circular electric modes in the cavities and a structure that does not require soldering.

Finally, the filters have to be of the constant resistance type in order to permit stacking tens of them, without impairing through multiple reflections the channels to be dropped last.

This paper describes a filter that satisfies all the above conditions and also has the advantages of compactness and convenient spatial orientation of the ports.

The derivations were made having in mind a single pole branching filter, but they are also applicable to the design of maximally flat filters.[2]

As by-products of the filter, several possible transducers from single-mode rectangular waveguide to round waveguide are described. These transducers may be useful for measuring purposes.

* Received by the PGMTT, October 3, 1960; revised manuscript received, December 13, 1960.

† Bell Telephone Labs., Inc., Holmdel, N. J.

[1] S. E. Miller, "Waveguide as a communication medium," *Bell Sys. Tech. J.*, vol. 33, pp. 1209–1265; November, 1954.

[2] G. Goubau, "Electromagnetische Wellenleiter und Hohlraume," Wissenschaftliche Verlagsgesellschaft M.B.H., Stuttgart, Ger.; 1955.

Description of the Filter

In order to understand the behavior of the filter and the reasoning by which the final structure was adopted, consider the schematic circuit in Fig. 1. Because of the proper selection of normalized reactances, the impedance seen towards the right of the plane AA is 1 at all frequencies. At midband frequency the maximum power available goes to R_a and far from resonance it goes to R_b.

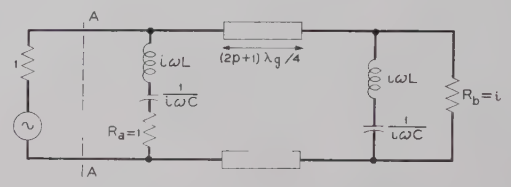

Fig. 1—Low-frequency channel-dropping filter.

The passage from the low-frequency circuit to a microwave circuit is not unique, but an obvious way appears in Fig. 2. The resonators in Fig. 1 have been replaced with the cavities that resonate with the coaxial circular electric mode TE°_{011}.

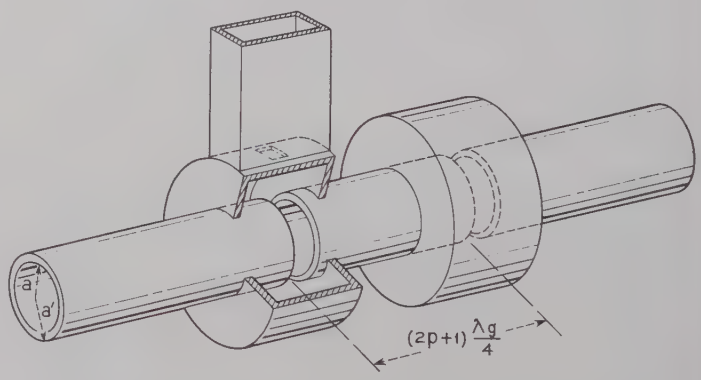

Fig. 2—Microwave channel-dropping filter.

The coupling from the first cavity to an outgoing rectangular waveguide is provided by a hole. This introduces a substantial asymmetry in the otherwise circular symmetric structure, and the first cavity resonates with unwanted spurious modes at frequencies below and above the wanted TE°_{011} mode.

The spurious resonances can be avoided by distributing the coupling from the coaxial cavity to the rectangular waveguide as indicated in Figs. 3(a) and 3(b). An

E-plane T junction in rectangular waveguide has been wrapped around the coaxial cavity. Imagine for the time being that there is no coupling between the rectangular waveguide and the coaxial cavity and that a wave enters the T junction. The standing electric field is antisymmetric with respect to the plane BB and consequently at point 1 has to be zero. This implies that the magnetic field parallel to the axis of the cavity is maximum. At points 2, 3, and 4 located at distances 1, 2 and 3 guided wavelengths from point 1 and measured in the rectangular waveguide, the magnetic fields are also maxima and in phase with that in 1. If now coupling holes are opened in those points, excitation for $TE^{\circledcirc}_{0mn}$, $TE^{\circledcirc}_{7mn}$, $TE^{\circledcirc}_{14mn}$, etc. is provided. By proper selection of the dimensions, the cavity may be made to support only TE_{011} for frequencies smaller than those dropped, and the multimode resonances are avoided.

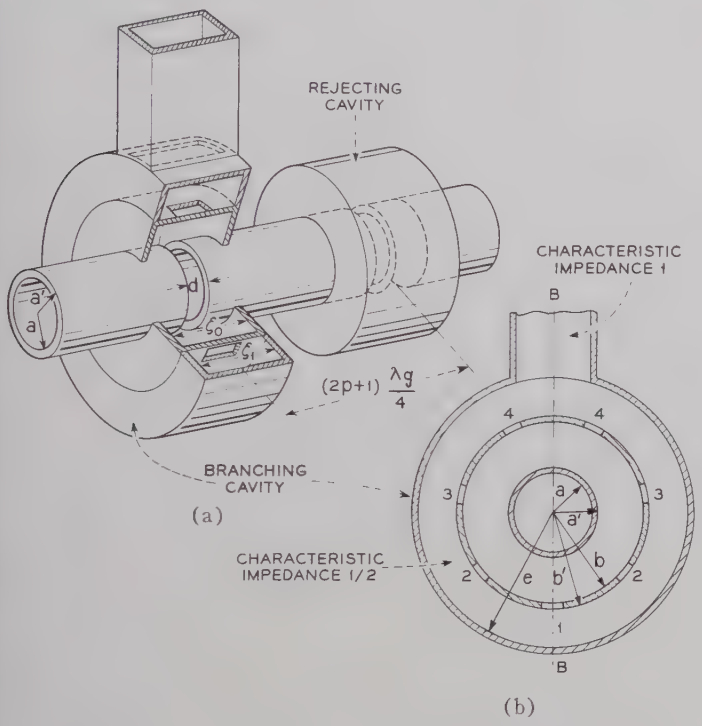

Fig. 3—Mode conversion-free channel-dropping filter.

Another way of looking at the problem of multimode resonances consists in calculating the amount of coupling between the exciting $TE^{\circledcirc}_{011}$ mode and the other coaxial spurious modes. That coupling is proportional to

$$\int_s \overline{H^{\circledcirc}_{011}} \cdot \overline{H^{\circledcirc}_{sp}}\, ds$$

where the vectors $\overline{H^{\circledcirc}_{011}}$ and $\overline{H^{\circledcirc}_{sp}}$ are the magnetic fields of the unperturbed exciting and coupled modes and the integration is extended over the coupling aperture S.[3] In the structure of Fig. 2 the integral is finite, but in that of Fig. 3 the integral tends to zero either because $\overline{H^{\circledcirc}_{sp}}$ is periodic or because the scalar product is null.

[3] H. A. Bethe, "Theory of diffraction by small holes," *Phys. Rev.*, vol. 66, pp. 163–182; October, 1944.

Resume of Design Formulas

In this section, we specify the design formulas. Their derivation is detailed in the Appendix.

In general, the requirements for a filter specify the midband frequency and bandwidth. Alternatively, the requirements may be expressed in terms of λ, midband free space wavelength and Q_L, loaded Q.

The dimensions a, a', b, b', d, e, ζ_0, and ζ_1 in Fig. 3, and c in Fig. 4, are the unknowns.

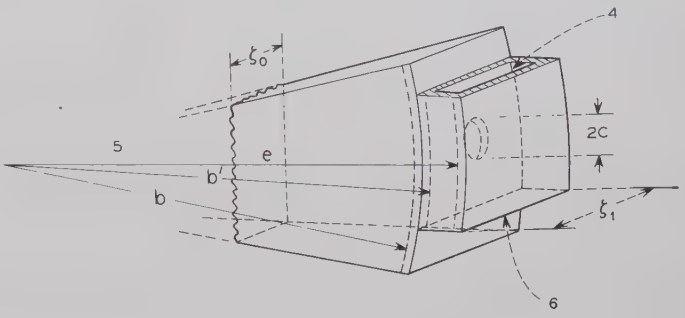

Fig. 4—Elemental outer junction.

Selecting $e-b'/\zeta_1=\frac{1}{2}$, which is the usual aspect ratio of rectangular waveguides, and calling ξ the aspect ratio $b-a'/\zeta_0$ of the coaxial cavity, it follows from (1), (2), (4), (5), (7), (13), (14), and (18), that

$$\frac{\zeta_0}{\lambda} = \frac{1}{2\xi}\sqrt{1+\xi^2}\,(1+\Delta)$$

in which

$$\Delta = \frac{3}{8\pi^2}\frac{\left(\frac{\lambda}{2a}\right)^2}{K} + 3.832\left(\frac{\lambda}{4\pi a}\right)^{3/2}\frac{1}{\left[1-\left(\frac{3.832\lambda}{2\pi a}\right)\right]^{1/4} Q_L^{1/2}} + \sqrt{1-\left(\frac{n\lambda}{2\pi aK}\right)^2}\left(\frac{n}{\pi\xi Q_L}\right)^{1/2}$$

$$K = 1 + \frac{\lambda}{2a}\sqrt{1+\xi^2}$$

and n is the number of coupling holes between coaxial cavity and rectangular waveguide. From (4), (5) and (18),

$$\frac{d}{a} = \left[\frac{16}{3.832^2\pi}\frac{\lambda}{a}\sqrt{1-\left(\frac{3.832\lambda}{2\pi a}\right)^2}\,\frac{(1+\xi^2)^2}{\xi}\,\frac{1}{Q_L}\right]^{1/4} \cdot\left[1-\frac{\Delta}{2}(1-\xi^2)\right]+\pi\frac{a'-a}{2a}\cdot$$

From (2), (4), (5), (7), (11) and (13),

$$\frac{2c}{a} = \left[\frac{9\pi}{16n^3}\left(\frac{\lambda}{a}\right)^4\,\frac{K^2}{1-\left(\frac{n\lambda}{2\pi aK}\right)^2}\,\frac{(1+\xi^2)^2}{\xi Q_L}\right]^{1/6} \cdot\left\{1+\frac{\Delta}{3}(1-\xi^2)+\frac{\gamma}{3}\left[2-\left(\frac{2\pi aK}{n\lambda}\right)^2\right]\right\} + 1.841\,\frac{2}{3}\,\frac{b'-b}{a}$$

where

$$\gamma = \frac{\dfrac{\lambda}{8aK\sqrt{1-\left(\frac{\lambda n}{2\pi aK}\right)^2}} + (1+\xi^2)\sqrt{1-\left(\frac{n\lambda}{2\pi aK}\right)^2}\,\frac{1}{(n\pi\xi Q_L)^{1/2}} + \frac{\lambda}{2a}\,\frac{(1+\xi^2)^{1/2}\Delta}{K}}{\left(\frac{2\pi aK}{n\lambda}\right)^2-1}.$$

In the expressions for d/a and $2c/a$, the corrections due to wall thickness are given by the last terms.

From (6) and (11),

$$\frac{\zeta_1}{\lambda} = \frac{1-\gamma}{2\sqrt{1-\left(\frac{\lambda n}{2\pi aK}\right)^2}}.$$

Finally, from (19), the intrinsic Q of the coaxial cavity results in

$$Q_i = \frac{\pi}{4}\sqrt{120\lambda g}\,\frac{(1+\xi^2)^{3/2}}{1+\xi^3}$$

where g, the conductivity of the metal, and λ are given in mks units. The intrinsic Q passes through a maximum for $\xi=1$, that is, when the cross section of the coaxial cavity is a square.

Experimental Results

A model filter made of silver has been constructed for operation at 56 kMc [Figs. 5(a) and 5(b)]. The performance is shown in Fig. 6. The 3-db bandwidth of the dropped channel is 185 Mc, the insertion loss at midband is 1.4 db and the return loss, measured from 50 to 60 kMc, is larger than 19 db.

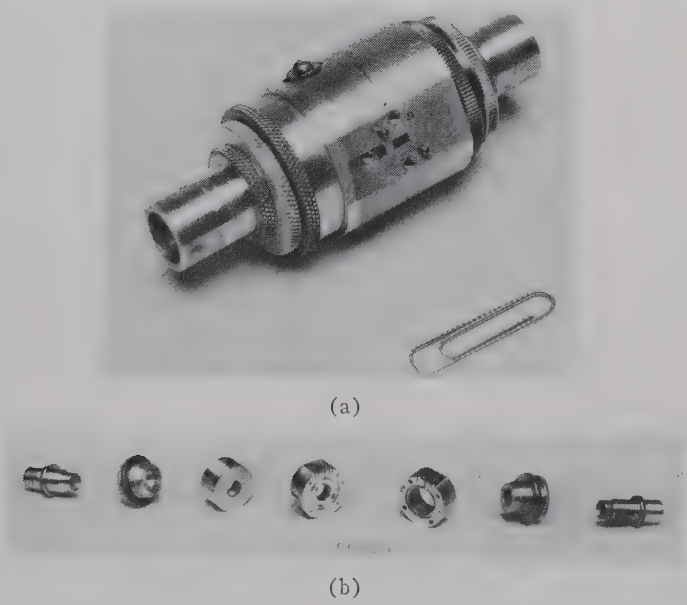

Fig. 5—(a) Channel-dropping filter. (b) Exploded view of channel-dropping filter.

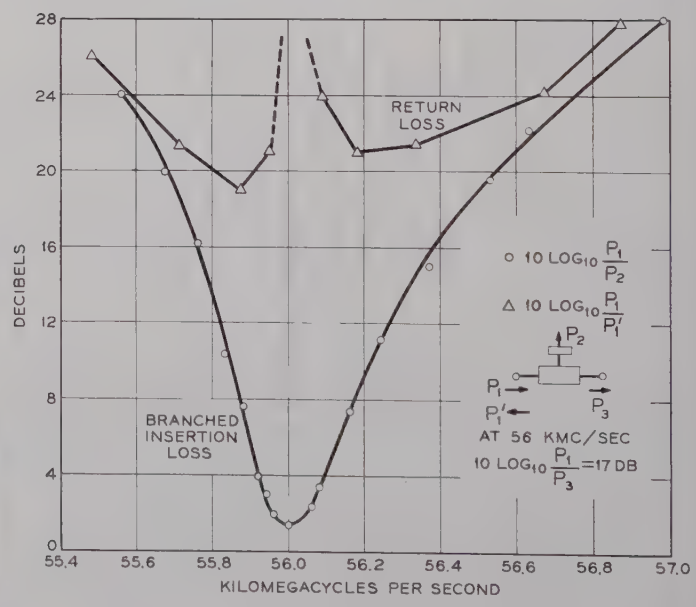

Fig. 6—Experimental results obtained with the channel-dropping filter.

From the measured Q_L and the midband insertion losses in the dropped channel and through waveguide, the intrinsic Q's of the cavities turn out to be

Q_i branching cavity = 2420
Q_i rejecting cavity = 4090.

The theoretical value for both cavities is 6400. The larger loss of the branching cavity is due to the heat dissipation in the multiple coupling holes and in the wrapped rectangular waveguide.

For comparison purposes, it is interesting to know that the measured intrinsic Q of a silver cavity made with 98U waveguide resonating in the $TE^{\square}_{101}$ mode at 5.4 mm is 1000.

Because of the narrow gap providing the coupling between the circular waveguide and the cavities, the return loss of the filter is small, particularly out of resonance. This characteristic makes this filter very attractive when many of them must be stacked together.

Other Transducers

Following the idea of mode-selecting coupling, it is possible to devise many transducers. For example, if in Fig. 3(b) the coupling holes are displaced $\lambda_g/4$, Fig. 7 is obtained. Now the mode excited is circular magnetic and the filter transduces $TE^{\square}_{10}$ to TM°_{01}.

Another example. Using only two holes diametrically opposed coupling electrically in opposite phases, the filter transduces $TE^{\square}_{10}$ to TE°_{11}.

If the resonant cavities are eliminated, Figs. 8 and 9 are obtained. In general, they no longer represent matched narrow-band devices; they become broad-band mismatched mode transducers.

The wrapped-around rectangular waveguide may be located at the end of a round pipe and the holes may be in the broad wall side as in Fig. 10. Circular magnetic modes are excited. The cavity limits the bandwidth but decreases the insertion loss.

The reader can image many more combinations.

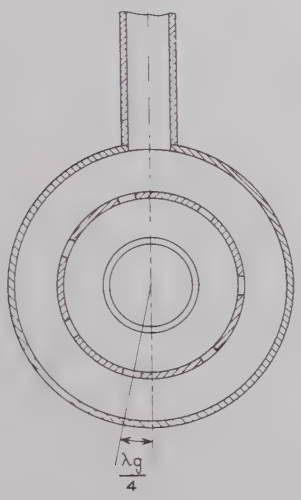

Fig. 7—Matched $TE^{\square}_{10}$ to TM°_{01} transducer.

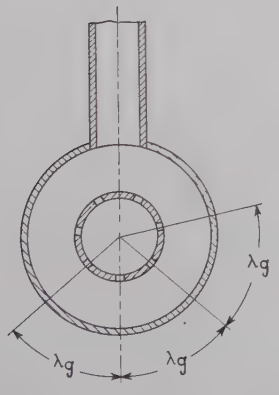

Fig. 8—Mismatched $TE^{\square}_{10}$ to TE°_{01} transducer.

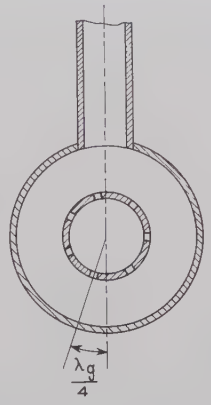

Fig. 9—Mismatched $TE^{\square}_{10}$ to TM°_{01} transducer.

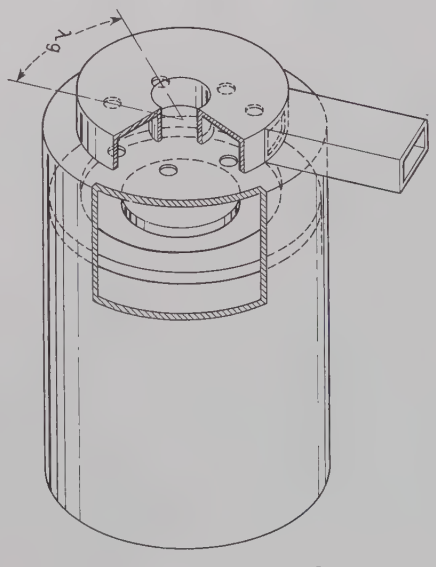

Fig. 10—Matched $TE^{\square}_{10}$ to TM°_{0n} transducer.

Conclusions

A channel-dropping filter capable of transducing TE_{01}° into $TE_{10}^{\square}$ has been described and analyzed. Circular electric modes in the resonant cavities combined with a mode-selective coupling between circular symmetric and rectangular waveguides make both heat loss and mode conversion low. Design formulas and experimental results on a model centered at 56 kMc are included. Because of the narrow gap providing the coupling between the circular waveguide and the cavities, the return loss of the filter is very small, particularly out of resonance. This property, together with the low insertion loss, makes the filter attractive when many of them must be stacked together.

Appendix

Design Formulas

We start analyzing each of the elementary structures that constitute the branching cavity of Fig. 3 and the conditions they must satisfy in order to resonate and to provide the proper bandwidth. Throughout all the following calculations, the arguments of the Bessel functions are large enough to justify asymptotic expansions.

A. Inner Junction, Fig. 11

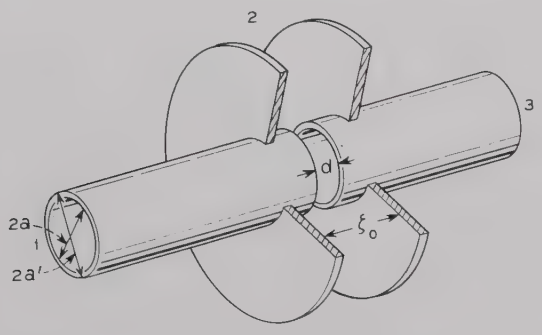

Fig. 11—Inner junction.

This consists of a circular waveguide carrying TE_{01}° and cutoff for TE_{02}°, coupled through a gap to a radial waveguide. Because of symmetry, reciprocity and small coupling, the scattering matrix for this three-port junction is

$$\begin{vmatrix} S_{11} & S_{12} & 1+S_{11} \\ S_{12} & S_{22} & S_{12} \\ 1+S_{11} & S_{12} & S_{11} \end{vmatrix}.$$

The reference surfaces are the plane of symmetry and the cylindrical surface defined by $r=a$.

S_{11} and S_{12}, calculated from small hole theory[3] have moduli small compared to 1. Neglecting powers of S_{11} and S_{12} bigger than 2, S_{22} is obtained from the relations of conservation of energy,[4]

$$S_{11} = i\frac{X_1^2}{32}\frac{d^2\lambda_g}{a^3} \tag{1}$$

$$S_{12} = -\frac{\pi^{1/2}X_1X_2^{1/2}}{8\sqrt{2}}\left(\frac{\lambda_g}{\zeta_0}\right)^{1/2}\left(\frac{d}{a}\right)^2 \tag{2}$$

$$S_{22} = (-1 + |S_{12}|^2)e^{-2S_{11}} \tag{3}$$

where $X_1=3.832$ is the first root of $J_1(x)$.

$$\lambda_g = \frac{\lambda}{\sqrt{1-\left(\frac{3.832\lambda}{2\pi a}\right)^2}} \tag{4}$$

is the midband wavelength in the round waveguide

$$X_2 = \frac{2\pi}{\lambda}a'\sqrt{1-\left(\frac{\lambda}{2\zeta_0}\right)^2}. \tag{5}$$

λ is the midband free space wavelength.

B. Outer Junction, Fig. 12

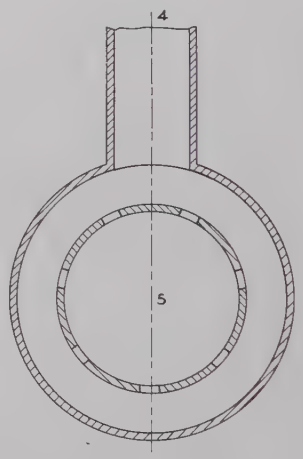

Fig. 12—Outer junction.

This is made out of a radial waveguide carrying a circular symmetric mode coupled through discrete holes to a rectangular waveguide carrying $TE_{10}^{\square}$.

In the description of the filter, it was shown that the holes couple only magnetically. This consideration plus the fact that circular electric modes are unaffected by radial metallic infinitely thin sheets allows one to imagine the junction in Fig. 12 made of n symmetrical three-port structures such as those indicated in Fig. 4.

[4] N. Marcuwitz, "Waveguide Handbook," M.I.T. Rad. Lab. Ser., McGraw-Hill Book Co., Inc., New York, N. Y., vol. 10, pp. 106–108; 1951.

Again using small hole theory, symmetry, reciprocity and conservation of energy, we obtain the elements of the scattering matrix of the junction in Fig. 4. The reference surfaces are the plane of symmetry that contains the round waveguide axis and the cylindrical surface defined by $r=b$.

$$S_{44} = i\frac{16\pi}{3}\frac{c^3}{\lambda_{g1}b'\zeta_1\left[\left(\frac{e}{b'}\right)^2-1\right]} \tag{6}$$

$$S_{45} = -\frac{16\pi}{3}\frac{c^3\left[1-\left(\frac{\lambda}{2\zeta_0}\right)^2\right]^{1/4}}{[(e-b')\zeta_1\zeta_0\lambda]^{1/2}\lambda_{g1}} \tag{7}$$

$$S_{55} = (-1+|S_{45}|^2)e^{-2S_{44}} \tag{8}$$

where ζ_1 is the width of the rectangular waveguide, λ_{g1} the midband wavelength measured along the curved axis of the guide, and $4c^3/3$ the polarizability of the circular coupling hole. If the hole is rectangular, and elongated in the direction of the magnetic field, its polarizability can be found in the literature.[5]

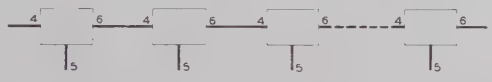

Fig. 13—Equivalent outer junction.

Connecting n such structures together (Fig. 13) and considering that all terminals 5 form a single port in which power adds and that end terminals 4 and 6 form a single port in which power also adds, it is possible to ascertain the scattering matrix elements of the two-port junction in Fig. 12.

$$\Gamma_{45} = (2n)^{1/2}|S_{45}| \tag{9}$$

$$\Gamma_{55} = (-1+n|S_{45}|^2)e^{-2nS_{44}}. \tag{10}$$

The wrapped waveguide must maintain the coincidence of zero electric field with each hole. Therefore, the number of holes, n, is equal to the number of guided wavelengths in the wrapped waveguide. Accordingly,

$$e = \frac{n\lambda\left(1+i\frac{S_{44}}{\pi}\right)}{\pi\sqrt{1-\left(\frac{\lambda}{2\zeta_1}\right)^2}} - b'. \tag{11}$$

The small correction $i(S_{44}/\pi)$ accounts for the lumped reactances introduced by the coupling holes.

[5] S. B. Cohn, "Determination of aperture parameters by electrolytic-tank measurements," Proc. IRE, vol. 39, pp. 1416–1421; November, 1951.

C. Resonance Conditions

At midband the rejecting cavity provides an open circuit at the input of the branching cavity. In order to have complete transfer of power through the branching cavity, the reflection coefficients seen looking away from each side of a reference surface must be complex conjugates. If that reference is the cylinder of radius $r=a'$ (Fig. 3), the following condition is obtained,

$$S_{22}^* = (-1+2|S_{12}|^2)e^{+2S_{11}}$$

$$= \left[\frac{H_1^{(1)}(X_2)}{H_1^{(1)}\left(X_2\frac{b}{a}\right)}\left|\frac{H_1^{(1)}\left(X_2\frac{b}{a}\right)}{H_1^{(1)}(X_2)}\right|\right]\Gamma_{55}, \tag{12}$$

where the asterisk means complex conjugate of. The Hankel functions $H_1^{(1)}$ appear because of the radial line of length $b-a'$ connecting the junctions in Figs. 11 and 12. Replacing the value of Γ_{55} with the one obtained in (10), equating moduli and arguments, and using asymptotic expansions for the Hankel functions, the following expressions are found

$$|S_{12}| = \left(\frac{n}{2}\right)^{1/2}|S_{45}| \tag{13}$$

$$\frac{b}{a'} = 1+\frac{\pi}{X_2}+\frac{3\pi}{8X_2^3}\frac{1}{1+\frac{\pi}{X_2}}-\frac{S_{11}+nS_{44}}{iX_2}. \tag{14}$$

For the rejecting cavity, the condition of resonance is fulfilled when the arguments of the two reflection coefficients are equal and of opposite sign. Consequently, from (14),

$$\frac{\bar{b}}{a'} = 1+\frac{\pi}{\bar{X}_2}+\frac{3\pi}{8\bar{X}_2^3}\frac{1}{1+\frac{\pi}{\bar{X}_2}}-\frac{\bar{S}_{11}}{i\bar{X}_2} \tag{15}$$

where the dashed letters refer to dimensions in the rejecting cavity.

D. Q of the Cavities

We start considering the different loaded Q's that can be found in the circuit shown in Fig. 1. The voltage at AA is frequency independent and therefore the prescribed dropped channel's Q is $Q_L=\sqrt{L/C}$.

For measuring purposes, it is important to realize what are the loaded Q's of the two cavities when they are considered separately. In Fig. 1, if the branching cavity doesn't exist, the loaded Q of the rejecting cavity is $2Q_L$. On the other hand, if the rejecting cavity doesn't

exist, the branching cavity has a loaded Q equal to $\frac{2}{3}Q_L$ and it is not matched. At midband, entering in any port, the normalized reflected power is 1/9 and the normalized transmitted power to each of the other two ports is 4/9.

By definition, the Q of a cavity is

$$Q = \frac{w\omega}{P} \tag{16}$$

where w is the energy stored in the cavity, ω is the angular frequency and P is the power leaving the cavity.

The loaded Q of either cavity when they are operating together, that is, the Q measured in the dropped channel is

$$Q_L = \frac{w\omega}{4\left|S_{12}\right|^2 P_i} \tag{17}$$

where P_i is the power carried by either of the two radially propagating waves that build the standing wave in each cavity. The calculation is straightforward and

$$Q_L = \frac{256\pi}{X_1^2 X_2^2}\,\frac{\zeta_0}{\lambda_g}\,\frac{a'^2}{\lambda^2}\left(\frac{b}{a'}-1\right)\left(\frac{a'}{d}\right)^4. \tag{18}$$

The intrinsic Q of a cavity is obtained from (16) when P is the power dissipated in the walls, and the result is

$$Q_i = \frac{2(b-a')^3}{\delta\lambda^2}\,\frac{1}{1+\left(\dfrac{b-a'}{\zeta_0}\right)^3}\,\frac{}{}. \tag{19}$$

$\delta = \sqrt{2/\omega\mu g}$ is the skin depth, ω is the angular frequency, μ the permeability and g the conductivity of the metal.

Eqs. (18) and (19) may be applied to either of the cavities by choosing the appropriate dimensions given in (14) and (15).

Coupled-Mode Description of Crossed-Field Interaction*

J. E. ROWE†, MEMBER, IRE, AND R. Y. LEE†

Summary—**The coupled-mode theory is developed for two-dimensional *M*-type flow, and a system of five coupled-mode equations is obtained. A fifth degree secular equation is found for the perturbed propagation constants of the system. Under weak space-charge field conditions, both the forward-wave and backward-wave interactions may be described in terms of only two coupled modes. The two-mode theory is applied to the calculation of starting conditions for the M-BWO, and to the M-FWA. The conditions for beating-wave amplification are determined, and the variation of the mode amplitudes with distance is given.**

Introduction

THE coupled-mode theory has been used extensively to describe the operation of the traveling-wave amplifier and backward-wave oscillator.[1–3] In these analyses, the four mode equations refer to the two beam space-charge waves and the two circuit waves. In both the *O*-type amplifier and the backward-wave oscillator, the best interaction occurs near synchronism between the slow space-charge wave and the circuit wave, and three waves are sufficient to describe the interaction, the fourth being far out of synchronism with the electron beam. Under large space-charge conditions in *O*-type devices, the interaction is accurately described by utilizing only the slow space-charge wave and the forward circuit wave. The coupled-mode analysis has great utility in obtaining a clear understanding of the detailed interaction mechanism.

Heretofore, the *M*-type interaction has not been studied with the coupled-mode theory. The general analysis is somewhat more complicated than that for the *O*-type, since there are five waves involved, which leads to a fifth-degree secular equation. When the RF structure is matched at its output, and the device is operated near synchronism between the electron beam and the foward circuit wave, the interaction is principally due to two waves. This two-wave interaction occurs for low space-charge conditions, unlike the corresponding conditions in the *O*-type tube. It is the purpose of this paper to develop the coupled-mode description for planar *M*-type amplifiers and oscillators and to show how this description may be used to investigate growing-wave gain, beating-wave gain and start-oscillation phenomena.

* Received by the PGMTT, November 29, 1960.

† Electron Physics Lab., Dept. of Elec. Engrg., The University of Michigan, Ann Arbor, Mich. This work was supported by the U. S. Signal Corps under Contract No. DA 36-039 sc-78260.

[1] J. R. Pierce, "Coupling of modes of propagation," *J. Appl. Phys.*, vol. 25, pp. 179–183; February, 1954.

[2] J. R. Pierce, "The wave picture of microwave tubes," *Bell Sys. Tech. J.*, vol. 33, pp. 1343–1372; November, 1954.

[3] R. W. Gould, "A coupled mode description of the backward-wave oscillator and the Kompfner dip condition," IRE TRANS. ON ELECTRON DEVICES, vol. ED-2, pp. 37–42; October, 1955.

Circuit and Ballistic Equations

It is convenient to formulate the circuit and ballistic equations using the equivalent circuit analysis, and following the methods of Pierce.[4] The geometry envisaged is that of a relatively thin planar strip beam flowing in orthogonal electrostatic and magnetostatic fields between planar electrodes as illustrated in Fig. 1.

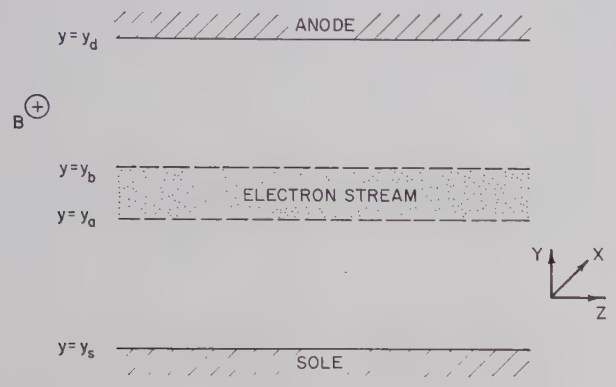

Fig. 1—M-type interaction configuration.

It is assumed that the space-charge conditions satisfy Brillouin flow requirements. It is well known that this is a problem in two-dimensional space-charge flow, and hence, the fields vary in the transverse dimension.

The circuit, ballistic, and continuity equations are expressed as shown below for both the M-FWA and the M-BWO.

$$\frac{\partial V_c}{\partial z} \pm j\beta_0 K_c I_c = 0 \tag{1}$$

$$\frac{\partial I_c}{\partial z} \pm j\beta_0 \frac{1}{K_c} V_c = -\frac{\partial i_b}{\partial z} \tag{2}$$

$$\ddot{y} = \eta\left[\frac{\partial(\Phi V_c)}{\partial y} - B\dot{z}\right] \tag{3}$$

$$\ddot{z} = \eta\left[\frac{\partial(\Phi V_c)}{dz} + B\dot{y}\right] \tag{4}$$

$$\frac{\partial i_b}{\partial z} + \frac{\partial \rho_E}{\partial t} = 0 \tag{5}$$

where

$$i_b = \Phi(y)(\rho u_0 + \rho_0 \dot{z})$$

and

$$\rho_E = \rho\Phi(y) + \rho_0\Phi'(y)y. \tag{6}$$

The quantities introduced in the above equations are defined as follows:

V_c = RF voltage on the circuit
I_c = RF current along the circuit
K_c = circuit impedance
β_0 = unperturbed circuit phase constant
ρ = beam space-charge density
ρ_E = total effective space-charge density
i_b = effective electron beam convection current density
$\Phi(y)$ = transverse potential dependence, and
B = magnetic induction.

In the case of the double signs, the upper one refers to the M-FWA and the lower to the M-BWO. It is convenient to introduce the following new variables into (3) and (4), the ballistics equations:

$$V_{1b} \triangleq -\frac{u_0\dot{z}}{\eta\Phi}$$

$$V_{2b} \triangleq -\frac{u_0\dot{y}}{\eta\Phi}$$

$$\beta_e \triangleq \eta B/u_0. \tag{7}$$

The result is

$$\frac{\partial V_{1b}}{\partial z} + j\beta_e V_{1b} = \beta_e V_{2b} - \frac{\partial V_c}{\partial z} \tag{8}$$

and

$$\frac{\partial V_{2b}}{\partial z} + j\beta_e V_{2b} = -\beta_e V_{1b} - V_c\frac{\Phi'(y)}{\Phi(y)}. \tag{9}$$

Eq. (5), the continuity equation, is written in terms of the new variables, using (6), as

$$i_b - \frac{j}{\beta_e}\frac{\partial i_b}{\partial z} = \frac{2C^3}{K_c}(V_{1b} - j\alpha V_{2b}), \tag{10}$$

where

$$\alpha \triangleq \frac{-\Phi'(y)}{\beta_e\Phi(y)} = \frac{\Phi'(y)}{j\Gamma_0\Phi(y)}$$

$$C^3 \triangleq \frac{\eta\Phi^2 K_c I_0}{2u_0^2}$$

Γ_0 = unperturbed circuit spatial propagation constant for the z-direction,

and

$$\Phi'(y) = \frac{d\Phi(y)}{dy}.$$

A beam impedance K_b is defined by $1/K_b = 2C^3\beta_e/K_c\beta_c$. Eq. (10) is now written as

$$\frac{\partial i_b}{\partial z} + j\beta_e i_b - \frac{\beta_c}{K_b}(jV_{1b} + \alpha V_{2b}) = 0. \tag{11}$$

[4] J. R. Pierce, "Traveling-Wave Tubes," D. Van Nostrand Co., Inc., New York, N. Y., ch. 15; 1950.

Eqs. (8) and (9) are transformed, using (1) and the definitions of α and C:

$$\frac{\partial V_{1b}}{\partial z} + j\beta_e V_{1b} - \beta_c V_{2b} \mp j\beta_0 K_c I_c = 0 \tag{12}$$

and

$$\frac{\partial V_{2b}}{\partial z} + j\beta_e V_{2b} + \beta_c V_{1b} \pm \alpha\beta_0 K_c I_c = 0. \tag{13}$$

Mode Formalism

The coupled-mode formalism is now conveniently introduced into the circuit, ballistics and continuity equations with the aid of the following definitions. These definitions are made to simplify the final equations, and they give the wave amplitudes as being proportional to square root power.

Circuit Modes:

$$P_c \triangleq \frac{1}{2}\left(\frac{V_c}{\sqrt{K_c}} + \sqrt{K_c} I_c\right) \tag{14}$$

$$Q_c \triangleq \frac{1}{2}\left(\frac{V_c}{\sqrt{K_c}} - \sqrt{K_c} I_c\right). \tag{15}$$

Beam Modes:

$$P_{1b} \triangleq \frac{1}{2\sqrt{K_b}} (V_{1b} + jV_{2b}) \tag{16}$$

$$P_{2b} \triangleq \frac{1}{2\sqrt{K_b}} (V_{1b} - jV_{2b}) \tag{17}$$

$$Q_b = \frac{1}{2}\left(\frac{\sqrt{\alpha}\, V_{1b}}{\sqrt{K_b}} - j\frac{V_{2b}}{\sqrt{\alpha K_b}} \quad \sqrt{\frac{K_b}{\alpha}}\, i_b\right). \tag{18}$$

After introduction of the definitions contained in (14)–(18), the circuit and beam coupled-mode equations are expressed as follows:

$$\frac{\partial P_{1b}}{\partial z} + j(\beta_e + \beta_c) P_{1b} \mp j\frac{(1-\alpha)}{2}\beta_0\left(\frac{K_c}{K_b}\right)^{1/2}(P_c - Q_c) = 0 \tag{19}$$

$$\frac{\partial P_{2b}}{\partial z} + j(\beta_e - \beta_c) P_{2b} \mp j\frac{(1+\alpha)}{2}\beta_0\left(\frac{K_c}{K_b}\right)^{1/2}(P_c - Q_c) = 0 \tag{20}$$

$$\frac{\partial Q_b}{\partial z} + j\beta_e Q_b \mp j\beta_0\left(\frac{\alpha K_c}{K_b}\right)^{1/2}(P_c - Q_c) = 0 \tag{21}$$

$$\frac{\partial P_c}{\partial z} \pm j\beta_0 P_c + j\frac{(1-\alpha)}{2}\left(\frac{K_c}{K_b}\right)^{1/2}(\beta_e + \beta_c) P_{1b} - j\frac{(1+\alpha)}{2}\cdot\left(\frac{K_c}{K_b}\right)^{1/2}(\beta_e - \beta_c) P_{2b} + j\beta_e\left(\frac{\alpha K_c}{K_b}\right)^{1/2} Q_b = 0 \tag{22}$$

and

$$\frac{\partial Q_c}{\partial z} \mp j\beta_0 Q_c - j\frac{(1-\alpha)}{2}\left(\frac{K_c}{K_b}\right)^{1/2}(\beta_e + \beta_c) P_{1b} + j\frac{(1+\alpha)}{2}\cdot\left(\frac{K_c}{K_b}\right)^{1/2}(\beta_e - \beta_c) P_{2b} - j\beta_e\left(\frac{\alpha K_c}{K_b}\right)^{1/2} Q_b = 0. \tag{23}$$

Eqs. (19)–(23) constitute the five coupled-mode equations for M-type interactions. These equations are written in terms of the unperturbed wave propagation constants; the next step is to develop the secular equation from their simultaneous solution. The uncoupled phase constants will be perturbed as the coupling between the individual modes is increased.

The roots of the determinant formed from the coefficients of the modes P_c, Q_c, Q_b, P_{1b}, and P_{2b} give the following secular equation. It is assumed that all modes vary as $\exp(j\omega t - \Gamma z)$.

$$[(j\beta_e - \Gamma)^2 + \beta_c^2](-\Gamma + j\beta_0)(\Gamma^2 + \beta_0^2) = \beta_e\beta_0\Gamma^2 H^2\left((j\beta_e - \Gamma) + 2j\beta_c\frac{\alpha}{1+\alpha^2}\right), \tag{24}$$

where

$$H^2 \triangleq 2C^3(1+\alpha^2).$$

This dispersion equation agrees with that obtained by Pierce.[4] It is worthwhile to proceed one step further and verify the possibility of amplification in such a system. Under the condition that $\beta_e + \beta_c \approx \beta_0$, approximately only the modes P_{1b} and P_c are coupled (cyclotron-wave interaction); hence, the determinant becomes

$$\begin{vmatrix} -\Gamma + j(\beta_e + \beta_c) & -j\dfrac{(1-\alpha)}{2}\beta_0\left(\dfrac{K_c}{K_b}\right)^{1/2} \\ j\left(\dfrac{K_c}{K_b}\right)^{1/2}\dfrac{(1-\alpha)}{2}(\beta_e + \beta_c) & -\Gamma + j\beta_0 \end{vmatrix} = 0. \tag{25}$$

For cyclotron-wave interaction, the electron motion is essentially circular, with equal y-directed and z-directed energies, and the modes Q_c, Q_b, and P_{2b} are excited to a negligible extent due primarily to weak coupling to the circuit. Expanding the determinant and defining $\Gamma = j\beta_0(1+p)$ yields

$$p = \pm\frac{j}{2}\frac{(1-\alpha)}{(1+\alpha^2)^{1/2}}\left(\frac{\beta_e}{\beta_c}\right)^{1/2} H, \tag{26}$$

which agrees with Pierce. Gain occurs for all values of α, and is a maximum for $\alpha = -1$.

Forward-Wave Amplifier

Under low space-charge conditions, the M-FWA may be described in terms of two coupled modes, P_c and P_{1b}. This is counter to the O-type FWA, which may be described in terms of two coupled modes only for high

space-charge conditions. It is convenient to write the solution as

$$P_c = Ae^{-\Gamma_1 z} + Be^{-\Gamma_2 z}, \tag{27}$$

and then P_{1b} may be expressed as

$$P_{1b} = -(j\beta_0 - \Gamma_2)Ae^{-\Gamma_1 z} - (j\beta_0 - \Gamma_1)Be^{-\Gamma_2 z}. \tag{28}$$

The boundary conditions for the forward-wave amplifier are expressed as follows for an initially unmodulated stream:

$$\begin{aligned} P_c &= 1 \\ P_{1b} &= 0 \quad \text{at} \quad z = 0. \end{aligned} \tag{29}$$

It is convenient to assume approximate synchronism between the slow space-charge wave and the forward circuit wave ($\beta_e \approx \beta_0$), and write the propagation constants in the following form:

$$\Gamma_{1,2} = j\beta_e + \beta_e D\delta_{1,2}.$$

Under the above condition for maximum excitation of the near-synchronous waves, the cyclotron waves are negligibly excited, and hence, their effect is neglected. Using the above form for Γ_n yields

$$A = \frac{1}{1 - \delta_2/\delta_1} \quad \text{and} \quad B = \frac{1}{1 - \delta_1/\delta_2};$$

then

$$P_c = e^{-j\beta_e}\left[\frac{\delta_1}{\delta_1 - \delta_2}e^{-\theta\delta_1} - \frac{\delta_2}{\delta_1 - \delta_2}e^{-\theta\delta_2}\right], \tag{30}$$

where

$$\theta \triangleq \beta_e Dz = 2\pi DN_s.$$

For low space-charge conditions, the solution of the dispersion equation for the perturbed propagation constants yields

$$\delta_{1,2} = \pm\sqrt{1 - (b/2)^2} + j\frac{b}{2}, \tag{31}$$

where $b \triangleq (\beta_0 - \beta_e)/\beta_e D$.

For exact synchronism, the δ's are purely real and each wave is excited in equal amplitude, which indicates that the initial loss factor for the M-FWA is -6.02 db. It should be noted that the mode amplitudes are proportional to square-root power and hence, proportional to the RF voltage in a matched system. It is interesting to examine the first term of (31). For

$$\begin{aligned} 1 - (b/2)^2 > 0; &\quad \text{growing waves} \\ = 0; &\quad \text{transition region} \\ < 0; &\quad \text{beating waves.} \end{aligned}$$

The transition point occurs at $b = 2$; for larger values of b, both δ's are purely imaginary.

The growing-wave regime has been investigated, and excellent agreement has been obtained with the results of Muller.[5] The square of the mode amplitude in the beating-wave regime is readily expressed as

$$|P_c|^2 = A^2 + B^2 + 2AB\cos\theta(y_1 - y_2), \tag{32}$$

where y_1, y_2 are the imaginary parts of the propagation constants. At the input $\theta = 0$,

$$|P_c| = A + B = 1, \tag{33}$$

where B is a *negative* number. Under these conditions, there are two purely propagating waves on the circuit which are out of phase at the input and beat together, adding in phase at the output. Since $A > 0$ and $B < 0$, the maximum of (32) occurs at (in phase condition)

$$\theta = \frac{\pi}{(y_1 - y_2)} = \frac{\pi}{2\sqrt{(b/2)^2 - 1}}. \tag{34}$$

At the maximum point,

$$|P_c| = A - B. \tag{35}$$

It is seen that the position of maximum gain, and the maximum gain are solely functions of b. The gain and optimum length are given as a function of b in Table I.

The predictions made using the two-wave coupled-mode theory agree exactly with the general M-FWA theory. The gain as a function of θ and b is shown in Fig. 2.

TABLE I

Length and Gain for Beating-Wave Interaction

b	θ_{opt}	DN	Voltage Gain	G_{db}
2.02	11.11	1.77	7.15	17.10
2.05	7.05	1.12	4.6	13.25
2.1	4.97	0.79	3.32	10.40
2.2	3.45	0.55	2.41	7.60
2.3	2.78	0.44	2.04	6.16

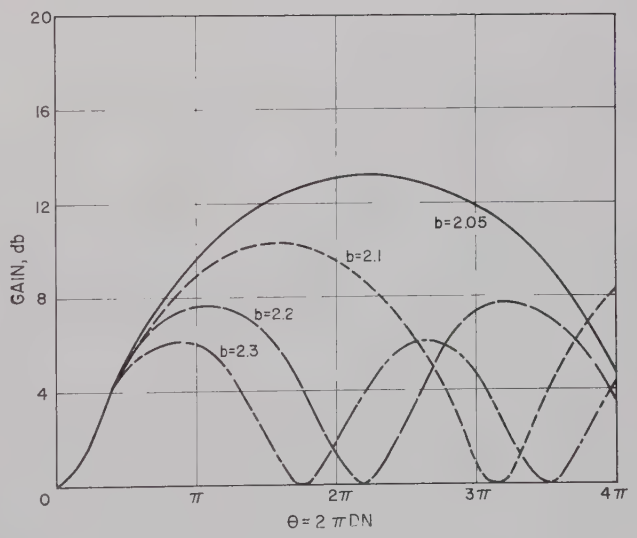

Fig. 2—Gain vs θ for zero space charge.

[5] M. Muller, "Traveling-wave amplifiers and backward-wave oscillators," Proc. IRE, vol. 42, pp. 1651–1659; November, 1954.

Backward-Wave Oscillator

The M-type backward-wave oscillator may also be described in terms of two coupled modes for low space-charge conditions. In this instance, we deal with the backward-circuit wave and the slow space-charge wave. For the condition that $\beta_e \approx \beta_0$, the coupled modes are Q_c and Q_b, and the mode equations are

$$\frac{\partial Q_c}{\partial z} + j\beta_0 Q_c - j\beta_e \left(\frac{\alpha K_c}{K_b}\right)^{1/2} Q_b = 0 \tag{36}$$

and

$$\frac{\partial Q_b}{\partial z} + j\beta_e Q_b - j\beta_0 \left(\frac{\alpha K_c}{K_b}\right)^{1/2} Q_c = 0. \tag{37}$$

The roots of the determinant of the coefficients of the above system give for the coupled propagation constants

$$\Gamma_{1,2} = \frac{j}{2}\left[(\beta_0 + \beta_e) \pm \sqrt{(\beta_0 - \beta_e)^2 + 4\beta_e\beta_0\alpha\frac{K_c}{K_b}}\right]. \tag{38}$$

Here again, it is convenient to write

$$Q_c = A_1 e^{-\Gamma_1 z} + B_1 e^{-\Gamma_2 z}, \tag{39}$$

and then

$$Q_b = (j\beta_0 - \Gamma_1) A_1 e^{-\Gamma_1 z} + (j\beta_0 - \Gamma_2) B_1 e^{-\Gamma_2 z}, \tag{40}$$

where A_1 and B_1 are yet undetermined. In the case of the backward-wave oscillator, it is desired to find the point along the structure $z>0$ where the energy in the circuit field has been completely transferred to a beam space-charge field. These boundary conditions on Q_c and Q_b are

$$\begin{aligned} Q_b &= 0 \quad \text{at} \quad z = 0 \\ Q_c &= 0 \quad \text{at} \quad z = L. \end{aligned} \tag{41}$$

The above conditions give

$$\frac{A_1}{B_1} = -\frac{j\beta_0 - \Gamma_2}{j\beta_0 - \Gamma_1} = -e^{-\Gamma_2 L}/e^{-\Gamma_1 L}. \tag{42}$$

Upon introduction of the propagation constants and the velocity parameter, (42) becomes

$$\frac{b + \sqrt{b^2 + \dfrac{4\alpha}{D_i^2}\dfrac{K_c}{K_b}}}{b - \sqrt{b^2 + \dfrac{4\alpha}{D_i^2}\dfrac{K_c}{K_b}}} = \exp\left\{j\theta\sqrt{b^2 + \frac{4\alpha}{D_i^2}\frac{K_c}{K_b}}\right\}. \tag{43}$$

The radicals in (43) may be considerably simplified by using the definitions of interaction parameter and transverse field variation suggested by Dombrowski:[6]

$$\begin{aligned} D_i^2 &= \frac{\omega}{\omega_c}\frac{K}{2}\frac{I_0}{V_0}G^2 \\ G^2 &= -\frac{1}{2}\frac{\sinh 2j\Gamma_0(\bar{y} - y_s)}{\sinh^2[j\Gamma_0(y_d - y_s)]}. \end{aligned} \tag{44}$$

The result is

$$\frac{b + \sqrt{b^2 + 4}}{b - \sqrt{b^2 + 4}} = e^{j\theta\sqrt{b^2+4}}. \tag{45}$$

Eq. (45) is satisfied, and an oscillation condition exists for

$$\begin{aligned} b &= 0 \\ D_i N_s &= \frac{\theta}{2\pi} = 0.25. \end{aligned} \tag{46}$$

These are exactly the start-oscillation conditions for a M-BWO when the space-charge fields are weak as compared to the circuit fields, independent of the beam position between the anode and sole plates. This result indicates that the energy is completely transferred between the beam and the circuit every 90 degrees.

Conclusions

The general interaction between wave and beam for two-dimensional M-type flow has been described in terms of coupled modes, resulting in five mode equations. They are written in terms of the uncoupled mode propagation constants and arise out of the ballistic, circuit, and continuity equations. Under the conditions of weak space-charge fields, both the forward-wave and the backward-wave interactions may be described satisfactorily in terms of two coupled modes. In the forward-wave case, the mode equations were used to calculate the optimum length and gain of a beating-wave amplifier; for backward-wave interaction, starting conditions were determined.

The development of a satisfactory coupled-mode theory for a device hinges on the separate determination of the wave coupling parameter in terms of device parameters. Based on the above results, it is felt worthwhile to apply this coupled-mode approach to a study of cyclotron-wave interaction in crossed fields, in order to obtain a physical picture of the interaction phenomena. This technique could also be applied to a study of cyclotron-wave parametric devices.

[6] G. E. Dombrowski, "A Small-Signal Theory of Electron-Wave Interaction in Crossed Electric and Magnetic Fields," Electron Tube Lab., The University of Michigan, Ann Arbor, Mich. Tech. Rept. No. 22; October, 1957.

Broad-Band Cavity-Type Parametric Amplifier Design*

KENNETH M. JOHNSON†

Summary—This paper tells how maximum bandwidth can be obtained from a nondegenerate parametric amplifier which utilizes a circulator. Expressions are derived for the gain bandwidth product and maximum possible gain bandwidth product. It is then shown how the Q of the cavities used for the signal and idler circuits may be kept at a minimum without degrading the noise performance of the amplifier. It is shown that best performance results when the TEM mode is used in coax, or, if waveguide is used, when the operating frequency is far away from the waveguide cutoff frequency. The diode used should have as high a self-resonant frequency as possible and the line admittance should be approximately the diode susceptance. Using a diode with a self-resonant frequency at the idler frequency will be seen to give optimum performance.

This paper also discusses double tuning the signal circuit to achieve broader bandwidths. In this case, the addition of the second tuned circuit will be seen to give much broader bandwidths than one would expect from conventional filter theory.

Two sample amplifiers are considered and their bandwidths calculated. The effect of double tuning one of the amplifiers is then considered.

Introduction

THE PROBLEM of achieving optimum bandwidth is encountered in cavity-type parametric amplifiers designed to operate in the microwave region. Because the reactance diode has a finite Q and because of its lead inductance, there is a maximum theoretical bandwidth. Usually, however, the main difficulty in achieving maximum bandwidth is caused by the many frequency-dependent effects encountered in waveguide-type circuits.

This paper tells how maximum bandwith can be achieved by presenting an analysis of a nondegenerate parametric amplifier that utilizes a circulator. Expressions for the gain-bandwidth product and the maximum gain-bandwidth product are obtained. It is then shown how the microwave circuit may be adjusted to approach this gain-bandwidth product; that is, it is shown how the Q of the cavity used for signal and idler circuits may be kept at a minimum without degrading the noise performance of the amplifier. It is shown that best performance results when the TEM mode is used in coax, or, if waveguide is used, when the operating frequency is far away from the waveguide cutoff frequency. The diode used should have as high a self-resonant frequency as possible and the line susceptance should be approximately the diode susceptance. If a diode is chosen with a self-resonant frequency at the idler frequency, much broader bandwidths can be achieved in many cases because of the simple lumped-constant nature of the circuit.

This paper also discusses double tuning of the signal circuit to achieve broader bandwidths. In this, the addition of the second tuned circuit will be seen to give much broader bandwidths than one would expect from conventional filter theory. The reason for this is that the second tuned circuit alters the rate at which the idler reactance reduces the negative resistance. Two sample amplifiers will be considered and their theoretical bandwidth calculated. By careful application of the principles set forth in this paper, the bandwidth of almost any single-tuned parametric amplifier can be predicted quite closely, and an amplifier that approaches the maximum theoretical bandwidth can be designed.

Theoretical Bandwidth

The only amplifier considered is a reflection-type parametric amplifier using a circulator. The equivalent circuit for this amplifier is shown in Fig. 1, where the arrow indicates direction of energy flow. This type of amplifier is the most commonly used and provides low noise figures and stable operation.[1]

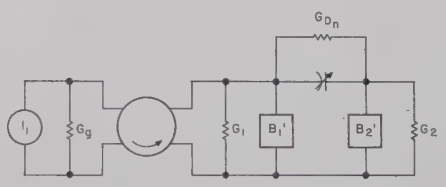

Fig. 1—Parametric amplifier equivalent circuit.

In deriving the expression for the gain-bandwith product, the general circuit relations derived by Bloom and Chang,[2] or Heffner and Wade,[3] will be used; the expression for the input admittance is the same as theirs except that it includes a diode loss conductance G_{D_n}. Throughout this paper the subscript n will always refer

* Received by the PGMTT, June 28, 1960; revised manuscript received, December 9, 1960.

† Texas Instruments, Inc., Dallas, Tex.

[1] R. C. Knechtli and R. D. Weglein, "Low-noise parametric amplifier," PROC. IRE, vol. 48, pp. 1218–1227; June, 1960.

[2] S. Bloom and K. K. N. Chang, "Theory of parametric amplifiers using nonlinear reactances," *RCA Rev.*, vol. 18, pp. 578–593; December, 1957.

[3] H. Heffner and G. Wade, "Gain, bandwidth, and noise characteristics of the variable-parameter amplifier," *J. Appl. Phys.*, vol. 29, pp. 1323–1331; September, 1958.

to the nth frequency. Thus, G_{D_1} and G_{D_2} are the diode conductances at the signal and idler frequencies, respectively. Since in a real diode the spreading resistance r_s is in series with the operating point capacitance C_0 and the lead inductance L, then the diode loss conductance and effective capacitance C_n' are frequency dependent and, in fact, given as

$$G_{D_n} = \frac{1/r_s}{1 + Q_{D_n}^2\left(\frac{\omega_n^2}{\omega_D^2} - 1\right)^2}$$

$$C_n' = \frac{C_0 Q_{D_n}^2}{1 + Q_{D_n}^2\left(\frac{\omega_n^2}{\omega_D^2} - 1\right)^2}, \tag{1}$$

where

$\omega_D = \dfrac{1}{\sqrt{LC_0}}$ is the diode self-resonant frequency, and

$Q_{D_n} = \dfrac{1}{\omega_n C_0 r_s}$ is the diode Q at the frequency ω_n.

The normalized input admittance to the amplifier is then given as

$$y = \frac{G_c}{G_g} - \frac{G_N}{G_g}\left(1 + \frac{B_2^2}{G_{T_2}^2}\right)^{-1} + j\left[\frac{B_1}{G_g} - \frac{G_N B_2}{G_g G_{T_2}}\left(1 + \frac{B_2^2}{G_{T_2}^2}\right)^{-1}\right], \tag{2}$$

and the reflection voltage gain Γ by

$$\Gamma = \frac{1 - y}{1 + y}. \tag{3}$$

The following definitions are useful:

$G_c = G_1 + G_{D_1}$ = signal circuit admittance,
$G_{T_2} = G_2 + G_{D_2}$ = idler circuit admittance,
$G_N = \omega_1\omega_2 C_1' C_2' \gamma^2 / G_{T_2}$ = negative conductance,
$\gamma = C_1/2C_0$ = Fourier capacitance ratio,
$B_1 = B_1' + \omega C_0$ = total signal circuit susceptance,
$B_2 = B_2' + (\omega_c - \omega)C_0$ = total idler circuit susceptance,

$$\xi = \frac{G_N}{G_g} - \frac{G_c}{G_g},$$

$\Gamma_0 = \dfrac{1+\xi}{1-\xi}$ = resonance voltage gain,

$G_0 = \Gamma_0^2$ = resonance power gain.

$$\xi = \frac{\sqrt{G_0} - 1}{\sqrt{G_0} + 1},$$

where B_1' and B_2' consist of an ideal filter and the susceptance element necessary to resonate the signal and idler circuit, respectively.

In order to compute the gain-bandwidth product, we will make the following definitions and approximations:

$$\delta_1 = \frac{\omega}{\omega_1} - \frac{\omega_1}{\omega} \approx \frac{2(\omega - \omega_1)}{\omega_1},$$

$$\delta_2 = \frac{\omega_3 - \omega}{\omega_2} - \frac{\omega_2}{\omega_3 - \omega} \approx -\frac{\omega_1}{\omega_2}\delta_1,$$

Q_c = unloaded signal circuit tank Q,

Q_2 = idler tank Q,

$$Q_T = Q_c\frac{G_c}{G_g} + \frac{Q_2 G_N \omega_1}{G_g \omega_2},$$

$$B_1/G_c = Q_c\delta_1,$$

$$B_2/G_{T_2} = Q_2\delta_2 = -\left(\frac{\omega_1}{\omega_2}Q_2\delta_1\right).$$

The approximations are valid to within 10 per cent for bandwidths less than 40 per cent if it is assumed that the susceptance variation, as a function of frequency, is linear over the range of interest. We will assume this to be the case since, as will be shown later, it is not possible to obtain bandwidths much greater than about 2.5 per cent for a single-tuned circuit when operating at 20-db gain with good noise figure.

Under normal operation with good noise figures, the following may also be assumed:

$$\left(\frac{G_c}{G_g}Q_c + \frac{\omega_1 G_N}{\omega_2 G_g}Q_2\right) \gg \frac{G_c\omega_1^2}{G_g\omega_2^2}Q_c Q_2^2\delta_1^2$$

$$G_0 - 2 \approx G_0;$$

and that $\zeta \ll 1$, where

$$\zeta = \frac{4\omega_1^4 Q_2^4}{\omega_2^4(1+\xi)^2}\left[G_0\left(1 + \frac{G_c}{G_g}\right)^2 - 2\left(1 - \frac{G_c}{G_g}\right)^2\right] \cdot \left\{\frac{Q_T^2 G_0}{(1+\xi)^2} + \frac{2Q_2^2\omega_1^2}{(1+\xi)\omega_2^2}\left[\sqrt{G_0}\left(1 + \frac{G_c}{G_g}\right) - 2\left(1 - \frac{G_c}{G_g}\right)\right]\right\}^{-2}.$$

Let $\Delta\omega = 2(\omega - \omega_1)$ at the half-power points; the gain bandwidth product may now be written

$$\frac{\sqrt{G_0}\,\Delta\omega}{\omega_1} = \left[\frac{Q_T^2}{(1+\xi)^2} + \frac{2\omega_1^2 Q_2^2[\sqrt{G_0}\,(1 + G_c/G_g) - 2(1 - G_c/G_g)]}{\omega_2^2(1+\xi)G_0}\right]^{-1/2}. \tag{4}$$

Examination of (4) reveals that it consists of two parts: one contains the term Q_T^2, due only to the reactive part of the input admittance; the other part contains the term Q_2^2, due only to the drop in negative conductance of the input admittance. It is the latter term that is neglected by Heffner and Wade, and Bloom and Chang. This term can only be neglected for gains greater than 30 db. Usually, however, stable operation is nearer 20 db, and this term cannot be neglected.

At this point, it is desirable to determine the magnitude of G_c/G_g and G_N/G_g. The quantity G_N/G_g is related to the gain and G_c/G_g by

$$\frac{G_N}{G_g} = \frac{G_c}{G_g} + \frac{\sqrt{G_0} - 1}{\sqrt{G_0} + 1}. \tag{5}$$

Thus, it is only necessary to determine G_c/G_g. The determining factor on G_c/G_g is the noise figure of the parametric amplifier. At high gains, this is given as

$$F = \left(1 + \frac{\omega_1}{\omega_2}\right)\left(1 + \frac{G_c}{G_g}\right).^{4,5} \tag{6}$$

For good noise figures the generator is to be overcoupled as much as possible to the signal circuit. Overcoupling is limited by the diode, since more pump power is required to achieve gain as the generator conductance is increased. The limit on the over-coupling has already been discussed by Knechtli and Weglein[1] and will not be repeated here. This is given by

$$\left(\frac{G_g}{G_c}\right)_{\max} = \left(\left(\gamma^2 Q_{D_1}{}^2 \frac{\omega_1}{\omega_2}\right) - 1\right)\left(\frac{\sqrt{G_0} + 1}{\sqrt{G_0} - 1}\right), \tag{7}$$

in which it is assumed that all loss is in the diode conductance. Since both (6) and (7) contain G_c/G_g and ω_1/ω_2, there is an optimum frequency ratio and coupling ratio for minimum noise figure. These are[6]

$$\left(\frac{G_g}{G_c}\right)_{\text{opt}} = (\sqrt{1 + \gamma^2 Q_{D_1}{}^2})\left(\frac{\sqrt{G_0} + 1}{\sqrt{G_0} - 1}\right) \tag{8}$$

and

$$\left(\frac{\omega_1}{\omega_2}\right)_{\text{opt}} = (1 + \sqrt{1 + \gamma^2 Q_{D_1}{}^2})/\gamma^2 Q_{D_1}{}^2. \tag{9}$$

[4] The exact expression for a reflection-type amplifier which gives the gain variation is

$$F = 1 + \frac{(\sqrt{G_0} + 1)^2}{G_0}\left[\frac{G_c}{G_g} + \frac{\omega_1}{\omega_2}\left(\frac{\sqrt{G_0} - 1}{\sqrt{G_0} + 1} + \frac{G_c}{G_g}\right)\right].$$

[5] H. Heffner and G. Wade, "Minimum noise figure of a parametric amplifier," *J. Appl. Phys.*, vol. 29, p. 1262; August, 1958.

[6] K. Kotzebue, "Optimum noise performance of parametric amplifiers," PROC. IRE, vol. 48, pp. 1324–1325; June, 1960.

Usually, γ can be made about 0.29 as may be determined by solving the hypergeometric series for the capacitance coefficients.[7]

Notice here that to obtain a noise figure of less than 3 db, it is required that $\omega_1/\omega_2 = 1/2$, $G_c/G_g = 1/2$, and that the diode have a Q of at least 8.

Now let us determine the absolute maximum possible gain-bandwidth product for a single-tuned circuit. To achieve resonance, the simplest signal or idler circuit must have a diode and a reactive element. Such a circuit is shown in Fig. 2. The X indicates the reactance which must be added to achieve resonance. When $\omega_D < \omega_n$, the circuit Q may be written as $Q = Q_{D_n}(\omega_n{}^2/\omega_D{}^2)$; when $\omega_D > \omega$, it may be written as $Q = Q_{D_n}$. Thus the minimum obtainable Q is limited by the diode Q and self-resonant frequency. Obviously, a diode should be chosen with as high a self-resonant frequency as possible. It will be assumed that both signal and idler circuits are resonated independently through use of an ideal filter,[8] and that all the loss occurs in the diode conductance. Thus, when both signal and idler frequencies lie below the diode self-resonant frequency, the maximum gain-bandwidth product is

$$\frac{\sqrt{G_0}\Delta\omega}{\omega_1} = \left(\frac{Q_{D_1}}{1 + \xi}\right)^{-1}\left\{\frac{G_c}{G_g} + \frac{G_N\omega_1{}^2}{G_g\omega_2{}^2} + \frac{2\omega_1{}^4(1 + \xi)}{\omega_2{}^4 G_0} \cdot \left[\sqrt{G_0}\left(1 + \frac{G_c}{G_g}\right) - 2\left(1 - \frac{G_c}{G_g}\right)\right]\right\}^{-1/2}. \tag{10}$$

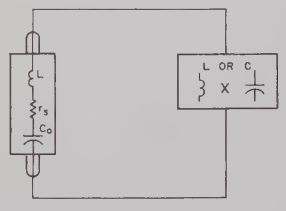

Fig. 2—Simplest parametric signal or idler resonant circuit.

In Fig. 3, the gain-bandwidth product normalized to diode Q is plotted against G_c/G_g for various idler-to-signal-frequency ratios to show the importance of the coupling factor, G_c/G_g, on bandwidth. Since the parameters in (10) all enter into the noise figure expression to maintain a noise figure less than 3 db, it is possible to obtain at best a 2.5 per cent bandwidth at 20-db gain for a single-tuned circuit. In addition, most double-tuned circuits will not have bandwidths much in excess of 2.5 per cent and certainly less than 25 per cent at 20-db gain. Thus, the approximations used in this paper will be valid.

[7] S. Sensiper and R. D. Weglein, "Capacitance and charge coefficients for parametric diode devices," *J. Appl. Phys.*, to be published.

[8] Usually it is not possible to build an amplifier whose filters are ideal and do not affect the bandwidth of an amplifier. However, if the idler frequency is much greater than the signal frequency, a filter can be built whose dimensions are sufficiently small at the signal frequency so that its performance approaches that of an ideal filter.

Achieving Optimum Q in a Microwave Circuit

It is now convenient to consider how Q_c and Q_2 may be determined for a diode mounted in a microwave circuit, and what can be done to achieve the minimum possible Q. The Q of any circuit for reasonable frequency changes can be expressed in differential form as[9]

$$Q = \frac{\omega}{2R}\frac{\partial X}{\partial \omega} \quad \text{or} \quad Q = \frac{\omega}{2G}\frac{\partial B}{\partial \omega}. \tag{11}$$

Thus,

$$Q_c = \frac{\omega_1}{2G_c}\frac{\partial B_1}{\partial \omega} \quad \text{and} \quad Q_2 = \frac{\omega_2}{2G_{T_2}}\frac{\partial B_2}{\partial \omega}. \tag{12}$$

There are two ways in which a diode may be mounted in a microwave circuit: in series or in parallel with a transmission line. Usually, a shorting plunger is used to achieve resonance; however, the Q we wish to consider is that seen from the terminals of the capacitance, since the susceptance transfer occurs across these terminals. Because of this, the equivalent circuit for either the series or parallel mount will be that shown in Fig. 4.

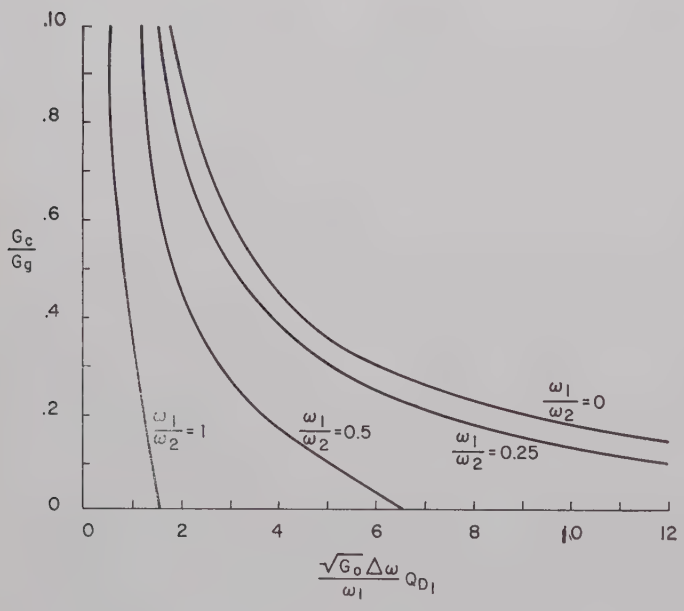

Fig. 3—Gain-bandwidth product vs input coupling for various signal-to-idler-frequency ratios. Both signal and idler frequencies are below the diode self-resonant frequency.

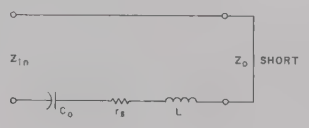

Fig. 4—Equivalent circuit of a diode mounted in series in a transmission line.

[9] C. G. Montgomery, R. H. Dicke, and E. M. Purcell, "Principles of Microwave Circuits," M.I.T. Rad. Lab. Ser., McGraw-Hill Book Co., Inc., New York, N. Y., vol. 8, p. 230; 1948.

The inductance shown is the lead inductance. Let us consider the series mount first.

The most common example of a series-mounted diode is that mounted in the center conductor of a coaxial line. In this, the characteristic line impedance Z_0 and the wavelength are not frequency-dependent in any special way as they would be in waveguide, unless the TEM mode is not used. It will be assumed that the series mount is in coaxial line and that the TEM mode is used. It will also be assumed that the losses in the circuit are all in the diode, and that other circuit losses, such as cavity-wall losses, are negligible. This is a good assumption if there are no lossy elements (*e.g.*, filters) present; however, if other lossy elements are present, their effective resistance must be added to the diode series resistance. The admittance of Fig. 4 for the series mount is given as

$$Y = j\omega C_0 + \frac{1}{r_s + j(\omega L + Z_0 \tan \theta\omega)}, \tag{13}$$

where $\theta = l/c$, and where l is the distance to the short. All discontinuity capacitances and inductances are assumed negligible. For a reasonably high-Q circuit ($Q > 3$) the admittance may be simplified as

$$Y = \frac{r_s}{[\omega L + Z_0 \tan \theta\omega]^2} + j\left[\omega C_0 - \frac{1}{\omega L + Z_0 \tan \theta\omega}\right]. \tag{14}$$

The Q of this circuit may then be expressed as

$$Q = \frac{\omega}{2G}\frac{\partial B}{\partial \omega}$$

$$= \frac{Q_{D_n}}{2}\left[1 + \frac{{\omega_n}^2}{{\omega_D}^2} + \frac{2\theta\omega_n}{\sin 2\theta\omega_n}\left(1 - \frac{{\omega_n}^2}{{\omega_D}^2}\right)\right]. \tag{15}$$

Upon examination of (15), the conditions imposed on $\theta\omega_n$ and, thereby, on Z_0 can be determined in order to achieve the smallest value for Q possible. In (15) these factors enter as $2\theta\omega_n/\sin 2\theta\omega_n$. The minimum values are solutions of the equation, $\tan 2\theta\omega_n = 2\theta\omega_n$. However, to resonate the circuit, $\theta\omega_n$ is restricted to certain ranges of values, depending on the value of ω_D; that is, for

$$\omega_D > \omega, \quad 0 < \theta\omega_n < \pi/2$$

and for

$$\omega_D < \omega, \quad \pi/2 < \theta\omega_n < \pi.$$

Now, the first two minimums occur for $2\theta\omega_n = 0$ and $2\theta\omega_n = 257.5°$. Successive minimums occur approximately for odd multiples of $\pi/2$. In the case of the first minimum, which occurs for $\omega_D > \omega$, the short is to be placed as close to the diode as possible. This corresponds to making Z_0 as large as possible. For $\omega_D < \omega$, the short is to be placed at $\theta\omega_n = 128.2°$, which corresponds to $\tan \theta\omega_n = 1.23$; or, Z_0 is to equal 0.81 times the diode reactance.

This corresponds to almost matching the diode reactance. The other minimum further down the line corresponds more closely to matching the diode reactance to Z_0. Of course, for the smallest Q the short should be placed at the minimum closest to the diode. When operating at the optimum values for $\theta\omega_n$, the circuit Q's for the following special cases are

$$\omega_D \gg \omega_n\colon\ Q = Q_D$$

$$\omega_n \gg \omega_D\colon\ Q = Q_D(\omega_n^2/\omega_D^2)2.8. \tag{16}$$

It is obvious from (15) and (16) that it is desirable to have ω_D as high as possible. Evidently, in this type of circuit unless $\omega_D > \omega_n$, the Q of the circuit does not equal the minimum obtainable Q. However, improvement in bandwidth can be realized by properly selecting Z_0.

The most common example of a diode mounted in parallel with a transmission line is one which is mounted across a waveguide. Here, it is necessary to consider the frequency variations of Z_0 and $\theta\omega_g$. Assuming again that we have a reasonably high-Q circuit, the admittance may be expressed as

$$Y = \frac{r_s}{(\omega L + Z_0 \tan\theta\omega_g)^2} + j\left[\omega C_0 - \frac{1}{\omega L + Z_0 \tan\theta\omega_g}\right]; \tag{17}$$

and for TE modes,

$$Z_0 \approx (2b/a)\sqrt{\mu/\epsilon}\,(1 - \omega_{cg}^2/\omega^2)^{-1/2}, \tag{18}$$

where a is the waveguide width, b its height, and

$$\omega_g = \omega(1 - \omega_{cg}^2/\omega^2)^{1/2}, \tag{19}$$

in which ω_{cg} is the waveguide cutoff frequency.

Although Z_0 is not clearly defined for waveguide, if the diode is mounted in the center of the waveguide, the three possible definitions for Z_0 will differ only a small amount. Also, the optimum value for Z_0 will be seen not to be critical, so that a variation of 30 per cent in Z_0 will not appreciably affect the determined value for bandwidth. Again it has been assumed that all other capacitance or inductances are negligible.

The Q of the circuit is

$$Q = \frac{Q_{D_n}}{2}\left\{\left(\frac{\omega_n^2}{\omega_D^2} + 1\right) + \frac{\left(1 - \frac{\omega_n^2}{\omega_D^2}\right)}{\left(\frac{\omega_n^2}{\omega_{cg}^2} - 1\right)}\left[\frac{2\theta\omega_g}{\sin 2\theta\omega_g}\left(\frac{\omega_n^2}{\omega_{cg}^2} - 1\right)^{1/2}\frac{\omega_n}{\omega_{cg}} - 1\right]\right\}. \tag{20}$$

Since Q_D, ω_D, and ω_n are fixed, the only variables are ω_{cg} and $2\theta\omega_g/\sin 2\theta\omega_g$. For minimum Q, $\omega_{cg} \ll \omega_n$ and $2\theta\omega_g/\sin 2\theta\omega_g$ are to be kept at a minimum. As before, in order to achieve resonance, limits are imposed on $\theta\omega_g$. These are the same as in the previous case; *i.e.*, for $\omega_D > \omega$: $0 < \theta\omega_g < \pi/2$, and for $\omega_D < \omega$: $\pi/2 < \theta\omega_g < \pi$. Thus, when $\omega_D > \omega$ the short is to be placed as close to the diode as possible and Z_0 is to be correspondingly large. When $\omega_D < \omega$, the short is to be placed at the next minimum, which occurs for $\theta\omega_g = 128.2°$; and Z_0 is to be made equal to 0.81 times the diode susceptance. In Fig. 5, Q/Q_{D_n} is plotted vs ω_{cg}/ω for $\omega_D = 2$ and for $\omega_D = 1/2$. It is assumed that Q_D is much greater than 1. Note that in some cases operation near the guide cutoff frequency raises the circuit Q considerably. Note also that this type of circuit only approaches the minimum theoretical Q when $\omega < \omega_D$, and when the operating frequency is far from the guide cutoff frequency. The only other way to lower the effective Q of the circuit is to double tune the signal circuit. Double tuning to increase gain-bandwidth product will be discussed in the next section.

When operating with $\omega = \omega_D$ at the diode self-resonant frequency, it may be observed that the Q of the circuit becomes merely the diode Q. A very broad-band amplifier can be built by using this fact. A particular example

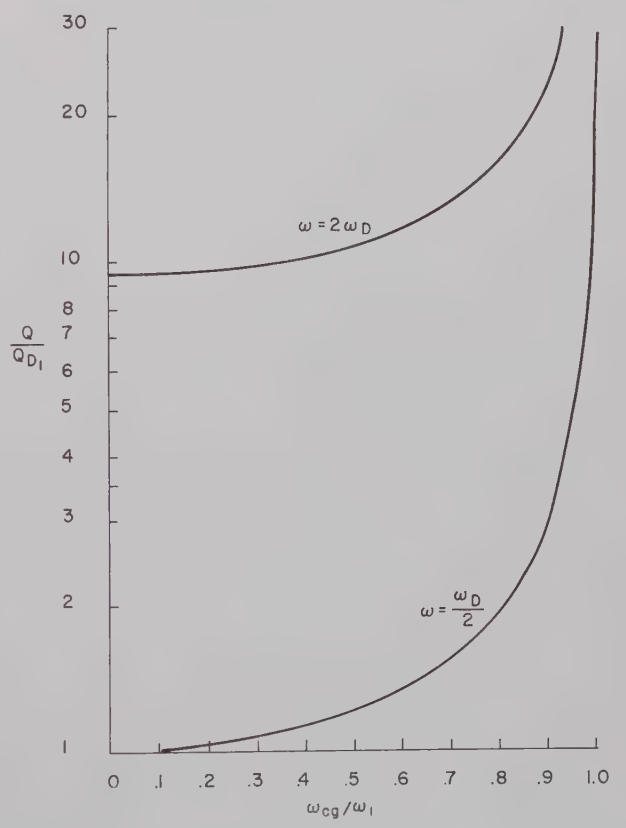

Fig. 5—Circuit Q normalized to diode Q vs ratio of guide cutoff frequency to signal frequency for TE modes in rectangular guide.

of this would be to have the diode used with its self-resonant frequency at the idler frequency, or in some cases, it may be desirable to add a small capacitance or capacitive discontinuity in series with the diode to raise its resonance frequency to the idler frequency. Examples of these applications are shown in Fig. 6. The idler frequency is suggested because its frequency most commonly limits the bandwidth, and the idler frequency could be adjusted to maximize bandwidth simply by changing the pump frequency. Also, by reducing the idler Q, the second term in (4) is considerably reduced. Operating with a diode which has a self-resonance at the idler could improve the bandwidth by a factor of 3 or more.

Double-Tuned Circuit Bandwidths

An alternate way to improve the bandwidth is to double tune the signal circuit. Briefly, to describe the theory:[10,11] Consider the signal circuit of a double-tuned amplifier such as shown in Fig. 7. The admittance at plane 1 is given by (2). With the same assumptions used

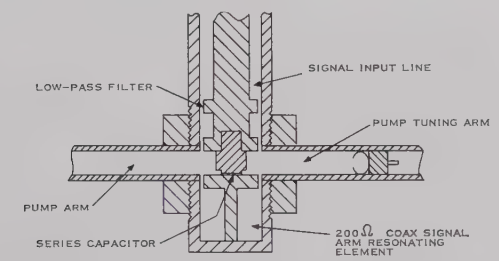

(a)

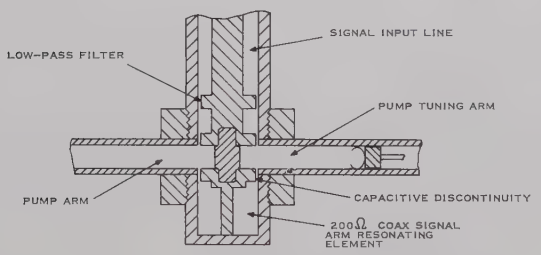

(b)

Fig. 6—Circuits with series idler resonance.

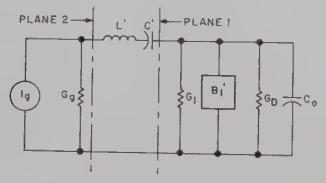

Fig. 7—Double-tuned signal circuit equivalent circuit.

to write (4); and assuming $G_c \ll G_g$, (2) may be rewritten as

$$y_1 = \frac{-\xi + jQ_T\delta}{1 + \epsilon^2\delta^2}, \tag{21}$$

where $\epsilon = (\omega_1/\omega_2)Q_2$.

The impedance at plane 2 is

$$z_1 = \frac{1 + \epsilon^2\delta^2 - Q_T\beta_\delta{}^2 - j\beta\xi\delta}{-\xi + jQ_T\delta}, \tag{22}$$

where $\beta = \omega_1 L' G_g = Q$ of the second cavity, loaded only by the generator. The power gain may now be calculated as

$$\frac{G(\omega)}{G_0} = \frac{\left[1 + \dfrac{(\epsilon^2 - Q_T\beta)_\delta{}^2}{1+\xi}\right]^2 + \dfrac{\delta^2}{(1+\xi)^2}(\beta\xi + Q_T)^2}{\left[1 + \dfrac{(\epsilon^2 - Q_T\beta)\sqrt{G_0}\,\delta^2}{1+\xi}\right]^2 + \dfrac{\delta^2 G_0}{(1+\xi)^2}(\beta\xi - Q_T)^2}.$$

The solution of an equation in δ^2 and δ^4 is obtained. For maximally flat response the coefficient of the δ^2 term is set equal to zero. This fixes the value for β. For reasonably high gains ($G_0 > 15$ db), the value for β is given approximately by

$$\beta \approx \frac{Q_T}{\xi}\left[1 + \frac{4}{G_0} + \frac{2(\sqrt{G_0} - 1)}{G_0}\right] \cdot \left[1 \pm \sqrt{1 - \frac{1 + \dfrac{4(\sqrt{G_0} - 3)\epsilon^2}{G_0 Q_T{}^2}}{\left[1 + \dfrac{4}{G_0} + \dfrac{2(\sqrt{G_0} - 1)}{G_0}\right]^2}}\right]. \tag{24}$$

The equation for the gain-bandwidth product is

$$\frac{\Delta\omega\sqrt{G_0}}{\omega_1} = \left[\frac{(1+\xi)^2 G_0{}^2}{(\epsilon^2 - Q_T\beta)^2}\right]^{\frac{1}{4}}, \tag{25}$$

which at high gains is

$$\frac{\sqrt{G_0}\,\Delta\omega}{\omega_1} = \frac{(4G_0)^{\frac{1}{4}}}{|\epsilon^2 - Q_T{}^2|^{\frac{1}{2}}}, \tag{26}$$

so that there is an improvement for a double-tuned signal circuit.

It is possible for the denominator of (25) to go to zero in some special cases. In any case there is considerable improvement in the gain-bandwidth product because β is approximately equal to Q_T and ϵ is just slightly smaller than Q_T. The factor ϵ differs from Q_T by just $G_c Q_c / G_g$. Thus, $G_c Q_c / G_g$ is to be made as small as possible. Of course it is not possible to achieve infinite gain-bandwidths since, among other assumptions, approximately linear frequency dependence is assumed for the reactance variation. However, (25) predicts a greater

[10] H. Seidel and G. F. Hermann, "Circuit aspects of parametric amplifiers," 1959 WESCON Convention Record, pt. 2, pp. 83–90.
[11] G. L. Matthaei, "A Study of the Optimum Design of Wide-band Parametric Amplifiers and Up Converters," presented at the PGMTT Natl. Symp., San Francisco, Calif.; May 9–11, 1960.

bandwidth improvement than would a conventional filter. Conventional filter theory usually assumes that the amplifier frequency response is determined by just the imaginary part of the input impedance. This is not a good assumption for a parametric amplifier unless the idler Q is less than the loaded signal circuit Q.

In the following section two amplifiers will be designed and their bandwidths computed.

Theoretical Broad-Band Amplifier Designs

The first amplifier to be designed is similar to the one shown in Fig. 6(b), though without the capacitive discontinuity. The diode available has a self-resonant frequency at 12.6 kMc. The amplifier then has the following characteristics:

$$f_1 = 5000 \text{ Mc},$$
$$f_2 = 12.6 \text{ kMc},$$
$$f_3 = 17.6 \text{ kMc},$$
$$f_1/f_2 = 0.396,$$
$$f_c/f_1 = 26.4,$$
$$\gamma = 0.29,$$
$$G_g/G_c = \text{(calculated) } 27.1.$$

The signal circuit is formed in a 200-ohm coax line. The line impedance is chosen large to obtain the minimum possible Q. Since the signal frequency is considerably below the diode self-resonant frequency, an inductive length is added to achieve resonance. A one-section filter one-fourth wavelength long at the idler frequency is employed to provide a short circuit to the idler, but to pass the signal. Assuming the impedance of the line at this filter section is 10 ohms, then the effective line impedance at the signal frequency would correspond approximately to a $\sqrt{150\times 10} = 44.7$-ohm line. The short for the signal frequency then is about $\pi/8$ away from the diode. The pump arm is formed in a waveguide which is beyond cutoff for the idler and signal frequencies. A band-pass filter in the signal arm places a short circuit at the waveguide wall at the idler frequency. The signal arm is tuned by placing the short behind the diode at the proper place.

Using this information, the circuit Q's and gain-bandwidth product may be computed as

$$Q_c = \frac{26.4}{2}\left[1 + \left(\frac{1}{13}\right)^2 + \frac{2\pi/4}{\sin 2\pi/4}\left(1 - \frac{1}{13}\right)^2\right]$$
$$= 33.8,$$
$$Q_2 = Q_{D_2} = 10.5,$$
$$Q_T = 4.80,$$
$$\sqrt{G_0}\Delta f = 1700 \text{ Mc},$$
$$\Delta f_{20\,\text{db}} = 170 \text{ Mc}.$$

This bandwidth is to be compared with a bandwidth of 12.8 Mc which would have been achieved had a diode with a self-resonance at 3 kMc been used with the idler circuit formed in waveguide. Some improvement over 12.8 Mc could be achieved by moving the signal-circuit filter up so that the idler resonated in the coax. In this case, however, the frequency dependence of the line must still be taken into account.

The second amplifier to be designed is shown in Fig. 8 and employs double tuning in the signal circuit to provide increased bandwidths. The amplifier has the following characteristics:

$$f_1 = 9000 \text{ Mc},$$
$$f_3 = 35 \text{ kMc},$$
$$f_1/f_2 = 0.375,$$
$$f_D/f_2 = 0.300,$$
$$f_{cg}/f_2 = 0.725,$$
$$f_{cg}/f_1 = 0.585,$$
$$\gamma = 0.29,$$
$$f_c/f_1 = 21.0,$$
$$G_g/G_c = 15.8.$$

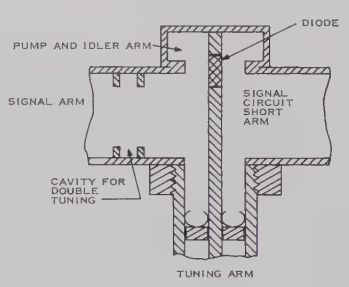

Fig. 8—Double-tuned signal circuit.

The signal arm is in reduced-height waveguide of about 50-ohm impedance to obtain a small circuit Q. The pump and idler occur in the same guide, reduced to have an impedance of 50 ohms, again to obtain a small circuit Q.

To determine the Q of the second cavity, it is necessary to compute the Q's of the single-tuned amplifier. These are

$$Q_c = 61.8,$$
$$Q_2 = 48.4,$$
$$Q_T = 19.93,$$
$$\epsilon = 18.1.$$

For a single-tuned circuit this would correspond to a bandwidth of 73 Mc at 20-db gain. For double tuning, the second-cavity Q is calculated from (24) to be 8.68. This then gives a bandwidth of 310 Mc, which is an improvement of a factor of 4.25.

Experimental Results

Calculations of the bandwidth of single-tuned L- and S-band parametric amplifiers constructed at Texas Instruments and elsewhere agree with the experimentally determined bandwidth. The amplifiers were all of the type shown in Fig. 8, except that the discontinuity capacitance was omitted. An S-band amplifier constructed at Texas Instruments which originally had 10-Mc bandwidth was made to have 70-Mc bandwidth at 16-db gain by operating with the diode self-resonance at the idler frequency. In this amplifier, both the signal and idler frequencies were below cutoff in the pump waveguide instead of using cutoff filters. A C-band amplifier constructed elsewhere was of the type shown in Fig. 6(b). This particular amplifier had as much as a 75-Mc bandwidth at 20-db gain, and gave 12- to 30-db gain over a 200-Mc bandwidth. The gain response was not maximally flat over the 200-Mc range, however.

In general, it may be said that broad bandwidths are achieved when a diode series resonance is achieved at the idler frequency. All resonant circuits should be formed as close to the diode as possible to avoid high-Q-type circuits. There is no exact method for achieving an idler resonance; ordinarily, this can be determined experimentally.

Design Comments

In some cases it may not be desirable to obtain the minimum circuit Q. In particular, if one seeks to obtain the minimum circuit Q, the series resistance or conductance may become so large that, to over-couple the generator to this resistance or conductance, it may be necessary to double-tune the signal circuit to achieve the proper coupling at resonance. In order to avoid this problem, since the signal circuit has such a broad bandwidth already, it may be desirable not to use the line impedance which corresponds to minimum Q.

Filters should be placed in a low-impedance line wherever possible, since a 0.4-db-loss filter in a 50-ohm line corresponds to an additional series resistance of 1.0 ohm, while the same loss in a 15-ohm line corresponds to only a series resistance of 0.3 ohm.

In many cases the shunt capacitance of a diode will raise its effective circuit Q, although the γQ_{D_n} product remains constant. This effect must be considered when computing bandwidth in a practical circuit. Therefore, for a diode with a shunt capacitance of C_s across the series resistance r_s and operating point capacitance C_0, the effective Q becomes

$$Q_{D_n\ \text{effective}} \approx Q_{D_n}\left(1 + \frac{C_s}{C_0}\right).$$

Thus, it is desirable to choose a diode with the lowest possible shunt capacitance.

Conclusions

Optimum gain-bandwidth product can be achieved if the characteristic line impedance is adjusted so as to obtain the minimum circuit Q. Substantial improvement can be achieved if the signal circuit is double tuned or if a diode series resonance is obtained at the idler frequency. When operating in waveguide, the operating frequency should be as far from the waveguide cutoff frequency as possible. By careful application of the principles set forth in this paper, one is able to predict bandwidth performance and design an amplifier with optimum gain-bandwidth product.

Acknowledgment

The author is indebted to Conrad Nelson of the Micromega Corporation for many of the ideas set forth in this paper, and to Thomas Straus and Jack Honda of the Hughes Aircraft Company Microwave Laboratory for their helpful comments.

Correspondence

Dependence of the Resonance Linewidth of Microwave Ferromagnetic Materials on Incident RF Power*

Introduction

The intrinsic resonance linewidth of ferromagnetic materials is a key parameter in delineating the characteristics of these materials. Most of the published data concerning the resonance linewidth of ferrites and garnets are valid for small-signal conditions. However, Suhl's theory has indicated that the linewidth is dependent upon the RF peak power to which the material is subjected.

Experiments performed by Damon[1] have shown that the magnetization vector of a ferromagnetic material fans out at an increasing angle from the direction of the applied dc field as the RF signal amplitude is increased, until some critical angle is reached. The material is then said to be saturated. A further increase in RF power will broaden the resonance absorption curve and decrease the resonance absorption peak value. Under certain conditions a subsidiary resonance absorption curve will appear on the low-field side of the main curve.

These nonlinear characteristics will affect the operation of many microwave devices to a considerable degree. Therefore, an experimental investigation was undertaken to determine the resonance absorption characteristics of several families of polycrystalline ferrite materials, a polycrystalline garnet material, and a single-crystal garnet material. Experiments were made over a wide range of incident power levels. The information obtained will be helpful in predicting the performance of these materials when used in such microwave devices as circulators, power limiters, harmonic generators, and parametric amplifiers.

Discussion

A. Nonlinear Effects

If a pulse of RF power impinges on a ferrite sample that is magnetized perpendicular to the signal field direction, the magnetization vector fans out, dissipates its energy, and relaxes to its equilibrium position. A long relaxation time indicates that a large amount of energy is stored in the spin system of the ferrite sample, analogous to a high-Q resonant circuit. A narrow-linewidth ferrite will have a high peak absorption per unit volume, indicating that a large amount of RF energy is stored in the spin system.

At high signal powers, the uniformity of the spin precessional motion is disturbed. This disturbance causes a time lag in the precessional motion of adjacent spins, and creates spin waves within the sample. Suhl[2] has shown that, as the RF power is increased, a critical RF field h_c is obtained because of these spin waves. The relationship for this critical RF field is given by

$$h_c = 2\Delta H \sqrt{\frac{2\Delta H_k}{4\pi M_s}},$$

where ΔH is the linewidth of the resonance as measured at low power, ΔH_k is the linewidth of the first unstable spin-wave mode, and $4\pi M_s$ is the saturation magnetization of the ferrite sample. After this critical field is reached, further increases in RF power cause the main resonance to decline and the resonance linewidth to increase.

TABLE I
Composition of Materials

Material	Chemical Composition					
	MgO (Per Cent)	Fe_2O_3 (Per Cent)	Al_2O_3 (Per Cent)	MnO_2 (Per Cent)	Y_2O_3 (Per Cent)	NiO (Per Cent)
Trans-Tech 414	41.19	48.83	5.42	4.56	—	—
General Electric 551-16	50.00	38.50	10.00	1.50	—	—
Trans-Tech Y1-8	—	62.50	—	—	37.5	—
General Ceramics R-1	58.00	36.00	—	6.00	—	—
Trans-Tech 189-1350	35.00	45.00	—	20.00	—	—
Trans-Tech 191-1300	25.00	45.00	—	30.00	—	—
Trans-Tech 447-1100	—	52.00	—	—	—	48

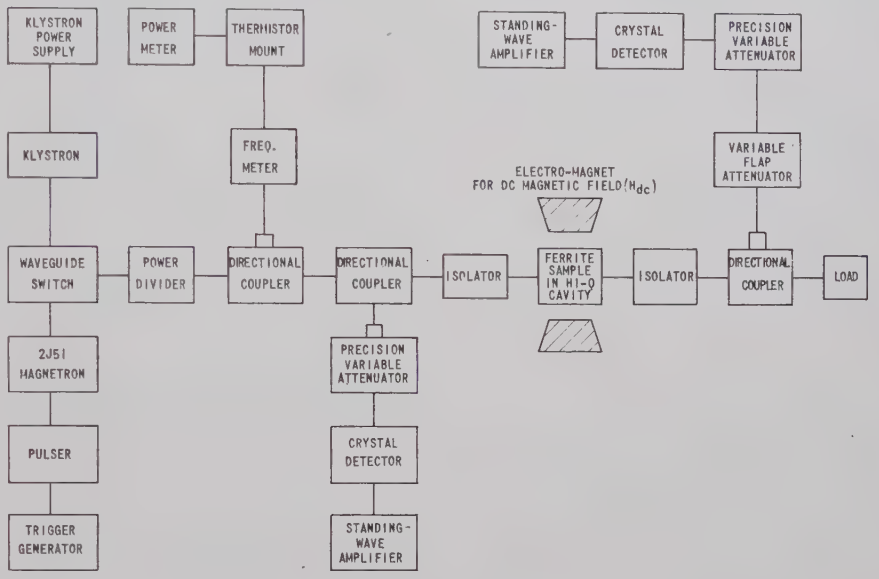

Fig. 1—Block diagram of test equipment setup, high-Q cavity technique.

B. Experimental Procedure

Ferrite linewidth measurements were made at both high- and low-power levels on a number of ferromagnetic materials as a function of incident power level (and thus RF magnetic field). The measurements were made with a high-Q, nondegenerate waveguide cavity. The samples used and their chemical compositions are listed in Table I.

A block diagram of the equipment used in making measurements by the high-Q cavity technique is shown in Fig. 1. A pulsed magnetron provided the high-power RF source. Measurements were made at a pulse repetition rate of 30 cps and a pulse length of one microsecond. This very low duty cycle was used in order to eliminate any spurious effects which might be caused by heating of the ferrite sample.

The ferrite samples were in the shape of small, accurately ground spheres varying in diameter from 0.015 inch to 0.090 inch.[3] The choice of dimension was determined by the dispersion effect of the sample in the cavity. A spherical form factor was used since, for a spherical geometry, the internal demagnetization factors are equal along each of the three mutually perpendicular axes of the sphere.

The power divider permitted the incident power level to be varied over a wide range. Ferrite isolators were used to isolate the cavity from the rest of the microwave circuitry and to insure matched conditions for stable magnetron operation.

Measurements were also made (with the same technique and experimental arrangement) using a low-power reflex klystron. A waveguide switch with high isolation

* Received by the PGMTT, July 26, 1960; revised manuscript received, November 18, 1960.

[1] R. W. Damon, "Relaxation effects in the ferromagnetic resonance," *Rev. Mod. Phys.*, vol. 25, pp. 239–245; January, 1953.

[2] H. Suhl, "The nonlinear behavior of ferrites at high microwave signal levels," Proc. IRE, vol. 44, pp. 1270–1284; October, 1956.

[3] J. L. Carter, E. V. Edwards, D. L. Fresh, and I. Reingold, "Ferrite sphere grinding technique," *Rev. Sci. Instr.*, vol. 30, pp. 946–947; October, 1959.

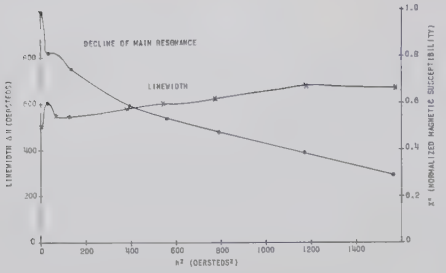

Fig. 2—Observed linewidth and decline of the main resonance as a function of incident power (square of RF field) for type-R-1 material.

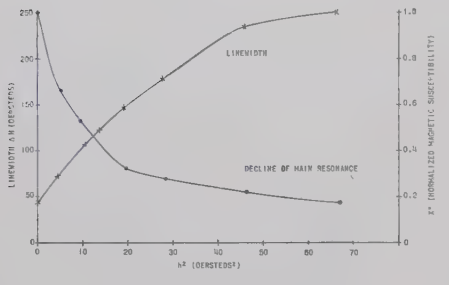

Fig. 3—Observed linewidth and decline of the main resonance as a function of incident power (square of RF field) for type-YIG material.

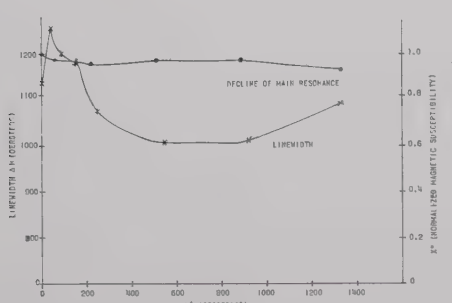

Fig. 4—Observed linewidth and decline of the main resonance as a function of incident power (square of RF field) for type 447-1100 material.

between ports permitted either the reflex klystron or the magnetron output power to be incident upon the cavity.

A rectangular, transmission-type cavity in 1.25 inch × 0.60 inch cross-section waveguide was used in these experiments. The cavity, which was coupled to the transmission line by means of asymmetric, inductive-type irises, operated in the TE_{102} mode at a resonance frequency of 8957 megacycles and a loaded Q of 2239. A sample holder, containing a polystyrene rod with the ferrite material cemented to its tip, was mounted on the narrow side of the waveguide cavity so that the specimen was located at the point of maximum RF field. The perturbation caused by the polystyrene rod was minimal.

The transmission-type cavity permits linewidth measurements to be made at a constant RF field. As the energy absorbed in the ferrite sample increased, the monitored power at the output termination of the cavity decreased. Increasing the input power until the output power level reached

TABLE II

FIGURE OF MERIT AS A FUNCTION OF INCIDENT POWER LEVEL FOR EIGHT POLYCRYSTALLINE FERROMAGNETIC MATERIALS

Material	h_s	p_t	ΔH	F_R	%	F_P	%
1) 414	0.02	50×10^{-3}	166	6000	100	38.7	100
	11.3	18×10^{3}	207	3844	64	31.0	80
	22.8	70×10^{3}	266	2300	38	24.0	62
	36.0	180×10^{3}	288	1980	33	22.2	57
2) 551-16	0.02	50×10^{-3}	143	8100	100	45.0	100
	12.5	21×10^{3}	283	2000	24	27.8	51
	21.6	65×10^{3}	431	885	11	15.0	33
	30.5	130×10^{3}	428	890	11	15.0	33
3) R1	0.02	50×10^{-3}	505	645	100	12.7	100
	10.8	15×10^{3}	550	545	85	11.9	92
	23.4	75×10^{3}	609	440	68	10.5	83
	34.2	160×10^{3}	676	360	56	9.5	75
4) 189-1350	0.02	50×10^{-3}	300	1840	100	21.5	100
	11.4	18×10^{3}	290	1980	108	22.0	102
	16.1	35×10^{3}	354	1350	73	18.7	85
	36.0	180×10^{3}	565	520	28	11.4	53
5) YIG	0.02	50×10^{-3}	44	86,000	100	136.5	100
	3.0	1.2×10^{3}	104	15,350	18	62.0	46
	5.2	3.5×10^{3}	172	5620	7	37.5	28
	8.2	9×10^{3}	250	2640	3	25.5	19
6) Y1-8	0.02	50×10^{-3}	56	57,120	100	119.5	100
	4.8	3×10^{3}	157	6700	12	41.0	34
	8.2	9×10^{3}	315	1680	3	20.5	17
	10.6	15×10^{3}	353	1360	2	18.2	15
7) 191-1300	0.02	50×10^{-3}	44	1400	100	18.7	100
	2.8	1×10^{3}	369	1200	86	17.3	93
	10.2	14×10^{3}	298	1850	132	21.5	116
	25.5	90×10^{3}	561	530	38	11.5	62
	36.0	180×10^{3}	670	370	265	9.6	52
8) 447-1100	0.02	50×10^{-3}	1130	128	100	5.7	100
	21.5	21×10^{3}	1182	119	93	5.4	96
	21.6	65×10^{3}	1006	147	115	6.0	107
	36.0	180×10^{3}	1094	141	110	5.9	105

h_s = RF field at sample, oersteds
P_t = peak transmitted power in waveguide, watts
ΔH = linewidth of sample, oersteds
F_R = figure of merit for resonance absorption device
F_P = figure of merit for phase-shift device

an appropriate reference level thus enabled maintenance of a constant RF field in the cavity over the complete range of measurements.

RESULTS

The change in the observed linewidth and the decline of the main resonance (decrease in magnetic susceptibility) as the incident RF power is increased are shown in several curves (Figs. 2–4) for some of the polycrystalline ferromagnetic samples evaluated. These two parameters are plotted as functions of the square of the RF field, and the decline of the main resonance is compared to the low power normalized value of the magnetic susceptibility, X''. Figs. 2 and 3 are representative of the common types of ferrite materials in which there is a substantial decline of the main resonance and a corresponding broadening of the linewidth as the incident power level is increased.

From the standpoint of practical application, it is probably more meaningful if variations in linewidth and resultant figures of merit[4] are presented as functions of the incident power rather than the microwave RF field. Therefore, the RF fields for the various samples were converted to the equivalent power in X-band waveguide, based upon the derivation of Stern and Mangiaracina,[5] and the calculated figures of merit and percentage change in figures of merit were compared to those at low-power-level conditions for the different incident peak-power levels.

The somewhat astronomical figures of merit achieved with the YIG and Y1-8 materials at low power levels [Table II, 5) and 6)] would ordinarily indicate the desirability of using narrow linewidth materials for high-power devices. However, because of line broadening, the figures of merit decrease rapidly with increased power, indicating that poor device performance will result at high power levels. Therefore, a narrow linewidth material must be chosen judiciously. It should also be noted that the use of narrow linewidth materials introduces the problem of maintaining a high degree of magnetic field stability, since a comparatively small shift in the magnetic field may result in a complete loss of the resonance condition.

The curve for type 447-1100 material (Fig. 4) is surprising, inasmuch as there is no appreciable decline of the main resonance and the linewidth becomes narrower with increasing RF field. A first explanation of this anomalous behavior is to attribute it to heating effects. Therefore, measurements were made over a range of duty cycles varying from 12.5×10^{-5} to 3×10^{-5} for constant peak power, and no change in the results were noted. No theory has been offered to explain the peculiar behavior noted for the type 447 material. The fact that this material is relatively porous and has small grain size may account, in part, for the observed results. The peculiar behavior of this

[4] B. Lax, "Frequency and loss characteristics of microwave ferrite devices," PROC. IRE, vol. 44, pp. 1368–1386; October, 1956.

[5] E. Stern and R. S. Mangiaracina, "Ferrite high power effects in waveguides," IRE TRANS. ON MICROWAVE THEORY AND TECHNIQUES, Vol. MTT-7, pp. 11–15; January, 1959.

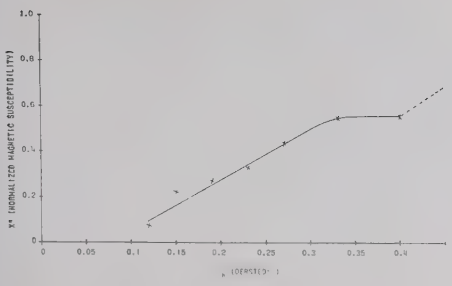

Fig. 5—Dependence of magnetic susceptibility on the reciprocal of the RF magnetic field at high power levels for type-YIG material.

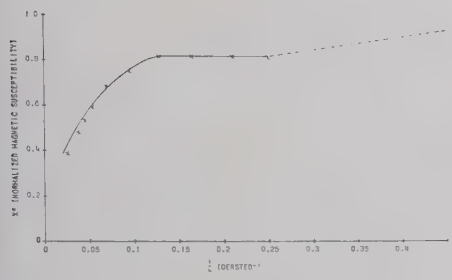

Fig. 6—Dependence of the magnetic susceptibility on the reciprocal of the RF field at high power levels for type R1 material.

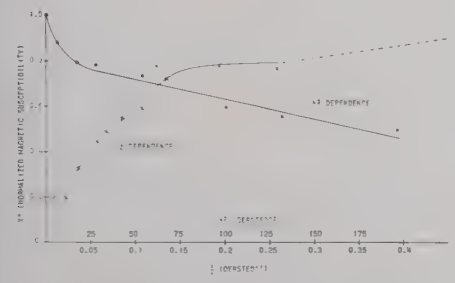

Fig. 7—Dependence of the magnetic susceptibility on the square of the RF field at low power levels, and on the reciprocal of the RF field at high power levels for type-414 material.

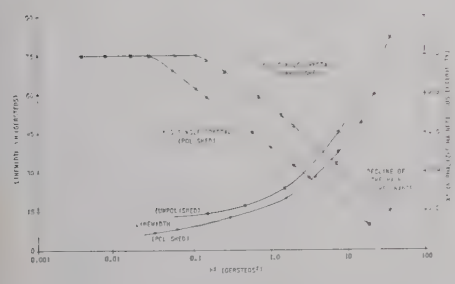

Fig. 8—Observed linewidth and decline of the main resonance as a function of incident power (square of RF field) for single crystal type-YIG material.

material is naturally reflected in its figure of merit [Table II, 8)] which, rather than decreasing in the expected manner, increases with incident power.

Type 447 material has been successfully used in high-power device applications. Since the linewidth and resonance absorption remain fairly constant with incident power, one would expect this material to provide satisfactory device characteristics at high power levels.

TABLE III
Critical RF Fields (h_c) and Corresponding Spin-Wave Resonance Linewidth (ΔH_k)

Material	$4\pi M_s$ Oersteds	ΔH Oersteds	h_c Oersteds	ΔH_k Oersteds
414	650	166	5.2	0.13
551-16	1100	143	4.9	0.16
YIG	1800	44	1.6	0.3
R1	2100	505	9.2	0.09
Y1-8	1800	56	1.8	0.23
Single-Crystal YIG, Unpolished	1750	13.5	0.33	0.13
Single-Crystal YIG, Polished	1750	6.5	0.17	0.16

$4\pi M_s$ = saturation magnetization
ΔH = linewidth of sample
h_c = RF field
ΔH_k = spin-wave resonance linewidth

The curves in Figs. 2 and 4 show an erratic behavior at "medium" field and power levels, which is not caused by experimental deviations. The fine structure noted in this region should be investigated further in order to determine the reason for the anomalous behavior.

Green and Schlömann[6] have shown that at fairly low power levels the susceptibility varies linearly with the square of the RF magnetic field strength, and that at high power levels, the susceptibility is inversely proportional to the amplitude of the RF magnetic field strength. The representative data presented in Figs. 5 and 6 tend, in general, to confirm these results.

The dependence of the susceptibility on $1/h$ at high power levels was compared to the linear relationship with the h^2 dependence at low power levels. The results for a representative sample are shown in Fig. 7. In all cases, the values for the magnetic susceptibility X'' are normalized to the low-power value.

The data presented can also be used to determine the critical field strength and the corresponding spin-wave resonance linewidth by use of the method of Schlömann, Saunders, and Servetz.[7] These values for the materials investigated are presented in Table III. It is interesting to note that the variations in ΔH_k are much smaller than those in ΔH.

The only single-crystal material investigated was yttrium-iron garnet. One sample of this material was checked both before and after it was polished. The results, which are given in Fig. 8, show the dependence of the linewidth and the decline of the main resonance on incident RF power. The results also show the expected effect of surface finish for narrow linewidth materials. The effectiveness of a polished surface in reducing linewidth is evident.

Conclusions

Information has been obtained concerning the dependence of linewidth and the decline of the main resonance on incident microwave power level for several common types of ferromagnetic materials.

The anomalous behavior noted in these experiments indicates the need for additional theoretical and experimental study. An indication has also been obtained of the direction to be taken in ferromagnetic material research in order to achieve optimized performance of microwave ferromagnetic devices, such as isolators, circulators, power limiters, and parametric amplifiers.

J. L. Carter
S. Dixon, Jr.
I. Reingold
U. S. Army Signal Res. and Dev. Lab.
Fort Monmouth, N. J.

[6] J. J. Green and E. Schlömann, "High Power Ferromagnetic Resonance at X-Band in Polycrystalline Garnets and Ferrites," Raytheon Co., Waltham, Mass., Tech. Memo. T-168; 1959.

[7] E. Schlömann, J. Saunders, and M. Servetz, "L-Band Ferromagnetic Resonance Experiments at High Peak Power Levels," Raytheon Co., Waltham, Mass., Tech. Memo. T-167; 1959.

Green's Function Techniques for Inhomogeneous Anisotropic Media*

In many problems involving the guiding and radiation of electromagnetic waves the solution for the field quantities at points in space is given in terms of integrals of the field quantities over their values on a closed surface. These integrals are often derived through the application of vector Green's theorems. The Green's function used in any particular application is usually determined by the special considerations of that problem, but it is convenient to use, as the Green's function, a solution of the vector wave equation which is singular at the point where the field is to be computed. In this article the concept is extended to include media which are anisotropic and may be inhomogeneous as well. Use is made of the generalized reciprocity relationships for anisotropic media.[1] This involves the use of the media of a given problem termed "original media" and those characterized by transposed tensor parameters and termed "transposed media."

If the media for a given problem are anisotropic with tensor constitutive parameters which are not necessarily symmetric, the following identity forms a convenient starting point:

* Received by the PGMTT, August 8, 1960; revised manuscript received November 28, 1960. This work is condensed from a chapter of a dissertation submitted in partial fulfillment of the requirements for the Ph.D. degree, Syracuse University, Syracuse, N. Y. It was performed at Syracuse University and was sponsored by the Office of Ordnance Res., U. S. Army, Contract No. DA-30-115-ORD-861.

[1] R. F. Harrington and A. T. Villeneuve, "Reciprocity relationships for gyrotropic media," IRE Trans. on Microwave Theory and Techniques, vol. MTT-6, pp. 308–310; July, 1958.

$$\iiint_V (\bar{B}\cdot\nabla\times[\tilde{\phi}]\nabla\times\bar{A} - \bar{A}\cdot\nabla\times[\phi]\nabla\times\bar{B})dv = \oiint_s (\bar{A}\times[\phi]\nabla\times\bar{B} - \bar{B}\times[\tilde{\phi}]\nabla\times\bar{A})\cdot d\bar{S}, \quad (1)$$

where $\bar{A}$ and $\bar{B}$ are vector functions of position, and the surface integral extends over the surface enclosing the volume V. Here $[\phi]$ is a tensor function of position and is not necessarily symmetric. The tilde indicates the transposed tensor. This identity may be derived by applying the divergence theorem to

$$\iiint_V \nabla\cdot(\bar{A}\times[\phi]\nabla\times\bar{B} - \bar{B}\times[\tilde{\phi}]\nabla\times\bar{A})dv, \quad (2)$$

and transforming the volume integral by the identity

$$\nabla\cdot(\bar{F}\times\bar{H}) = \bar{H}\cdot\nabla\times\bar{F} - \bar{F}\cdot\nabla\times\bar{H}. \quad (3)$$

Now let $\bar{B}\equiv\bar{E}$ and $\bar{A}\equiv\bar{G}$, where $\bar{E}$ is the desired electric field intensity due to sources outside of V, and $\bar{G}$ is arbitrary. If $[\phi] = [\mu]^{-1}/j\omega$, (1) becomes

$$\iiint_V (\bar{E}\cdot\nabla\times[\tilde{\mu}]^{-1}\nabla\times - \bar{G}\cdot\nabla\times[\mu]^{-1}\nabla\times\bar{E})dv = \oiint_s (\bar{G}\times[\mu]^{-1}\nabla\times\bar{E} - \bar{E}\times[\tilde{\mu}]^{-1}\nabla\times\bar{G})\cdot d\bar{S}. \quad (4)$$

Now let $\bar{G}$ be a solution of the equation

$$\nabla\times[\tilde{\mu}]^{-1}\nabla\times\bar{G} - \omega^2[\tilde{\epsilon}]\bar{G} = -\bar{u}_p\delta(|\bar{r}-\bar{r}'|), \quad (5)$$

where $\delta(|\bar{r}|)$ is the Dirac delta function and $\bar{r}'$ is within V. The tensors $[\mu]$ and $[\epsilon]$ are, respectively, the tensor permeability and permittivity of the original media in which the fields must be determined, $\bar{u}_p$ is a constant unit vector, and ω is the angular frequency. Time variations of the form $e^{j\omega t}$ are assumed. Since $\bar{G}$ is singular at $\bar{r}=\bar{r}'$, this point must be excluded from V by enclosing it within a small sphere of radius σ as in Fig. 1. In the remaining volume V_1, the volume integrand vanishes identically and the identity of (4) becomes

$$\iint_\sigma (\bar{G}\times[\mu]^{-1}\nabla\times\bar{E} - \bar{E}\times[\tilde{\mu}]^{-1}\nabla\times\bar{G})\cdot d\bar{S} = -\iint_s (\bar{G}\times[\mu]^{-1}\nabla\times\bar{E} - \bar{E}\times[\tilde{\mu}]^{-1}\nabla\times\bar{G})\cdot d\bar{S}. \quad (6)$$

On taking the limit of the left-hand side as $\sigma\to 0$, and in view of the singularity assumed in (5), one arrives at the result

$$\bar{u}_p\cdot\bar{E}(\bar{r}') = -\oiint_s (\bar{G}\times[\mu]^{-1}\nabla\times\bar{E} - \bar{E}\times[\tilde{\mu}]^{-1}\nabla\times\bar{G})\cdot d\bar{S}, \quad (7)$$

which is the component of $\bar{E}(\bar{r}')$ along the unit vector $\bar{u}_p$. Since $\bar{u}_p$ may be arbitrarily oriented, this amounts to a complete determination of $\bar{E}(\bar{r}')$. This expression is analogous to expressions occurring in the isotropic case with two important differences. First, $[\mu]$ is a tensor, and second, $\bar{G}$ now satisfies a vector wave equation in the transposed media rather than in the original media.

The foregoing was applied to a closed source-free region. It was found that the total field could be expressed in terms of the Green's function and of the fields on the surface bounding the region. Next consider a region with a source as shown in Fig. 2. The technique will be formulated for a point in V', the volume bounded by S and Σ. Call the volume bounded by σ, S and Σ, V_2, and let $\bar{J}^i$ be an impressed electric current density within V_2. Therefore in V' the electric field satisfies

$$\nabla\times[\mu_2]^{-1}\nabla\times\bar{E} - \omega^2[\epsilon_2]\bar{E} = -j\omega\bar{J}^i. \quad (8)$$

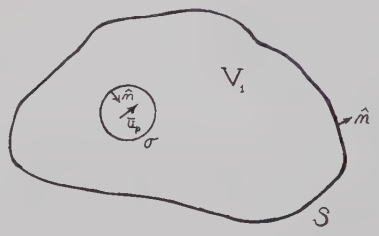

Fig. 1.

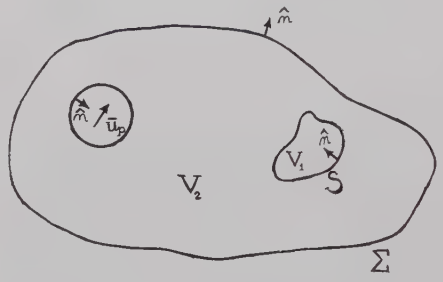

Fig. 2.

With these definitions a procedure similar to that above yields

$$\bar{u}_p\cdot\bar{E}(\bar{r}') = \iiint \bar{G}_2\cdot\bar{J}^i dv - \iint_{\Sigma+s} (\bar{G}_2\times[\mu_2]^{-1}\nabla\times\bar{E} - \bar{E}\times[\tilde{\mu}_2]^{-1}\nabla\times\bar{G}_2)\cdot d\bar{S}. \quad (9)$$

Thus, the field at $\bar{r}'$ in V' is completely determined. If Σ recedes to infinity it may be shown that the integral over this surface vanishes[2] with the result

$$\bar{u}_p\cdot\bar{E}(\bar{r}') = \iiint \bar{G}_2\cdot\bar{J}^i dv - \iint_s (\bar{G}_2\times[\mu_2]^{-1}\nabla\times\bar{E} - \bar{E}\times[\tilde{\mu}_2]^{-1}\nabla\times\bar{G}_2)\cdot d\bar{S}. \quad (10)$$

[2] J. R. Mentzer, "Scattering and Diffraction of Radio Waves," in Pergamon Sci. Ser., "Electronics and Waves," Pergamon Press, Inc., New York, N. Y., vol. 7, pp. 12–22; 1955.

Through the modified reciprocity theorem the first term on the right-hand side of (10) becomes

$$\iiint \bar{G}\cdot\bar{J}^i dv = \iiint \bar{u}_p\cdot\bar{E}^i(\bar{r})\delta(|\bar{r}-\bar{r}'|)dv = \bar{u}_p\cdot\bar{E}^i(\bar{r}'). \quad (11)$$

Thus, (10) becomes

$$\bar{u}_p\cdot\bar{E}(\bar{r}') = \bar{u}_p\cdot\bar{E}^i(\bar{r}') - \oiint_s (\bar{G}_2\times[\mu_2]^{-1}\nabla\times\bar{E} - \bar{E}\times[\tilde{\mu}_2]^{-1}\nabla\times\bar{G}_2)\cdot d\bar{S}. \quad (12)$$

This is an example of a modified Green's function technique which may be applied to anisotropic media. The only difference between this technique and that for isotropic media is that the Green's functions used satisfy equations for the transposed media.

Alfred T. Villeneuve
Hughes Aircraft Co.
Culver City, Calif.

N-Way Power Divider*

An N-way power divider is an $(N+1)$ port network with N equal outputs. If we assume the N outputs are symmetrical and the input port (1) is matched, then

$$S = \begin{bmatrix} 0 & S_{12} & S_{12} & S_{12}\cdots S_{12} \\ S_{12} & S_{22} & S_{23} & S_{23}\cdots S_{23} \\ S_{12} & S_{23} & S_{22} & \cdots\cdots S_{23} \\ S_{12} & S_{23} & S_{23} & \\ \cdots & \cdots & \cdots & \cdots S_{23} \\ S_{12} & S_{23} & S_{23} & S_{23}\cdots S_{22} \end{bmatrix}$$

which is a scattering matrix of the $(N+1)$th order. Since the device is lossless, the matrix is unitary. Therefore,

$$N|S_{12}|^2 = 1$$
$$|S_{12}|^2 + |S_{22}|^2 + (N-1)|S_{23}|^2 = 1$$
$$S_{11}S_{12}^* + S_{12}S_{22}^* + (N-1)S_{12}S_{23}^* = 0.$$

The solution to this simultaneous equation indicates that

$$|S_{12}|^2 = \frac{1}{N}$$
$$|S_{23}|^2 = \frac{1}{N^2}$$
$$|S_{22}| = \frac{N-1}{N}.$$

* Received by the PGMTT, December 13, 1960.

It can be concluded that the VSWR into any output port is

$$\underset{(N\neq 1)}{\mathrm{VSWR}_N} = \frac{1+|S_{22}|}{1-|S_{22}|} = 2N-1;$$

the isolation between any two output ports is

$$\mathrm{Isolation}_{(MN)} = 10\log\frac{1}{|S_{23}|^2} = 20\log N$$
$$(M\neq 1)$$
$$(N\neq 1)$$
$$(M\neq N)$$

the coupling between the input and any output port is

$$\underset{(N\neq 1)}{\mathrm{Coupling}_{1N}} = 10\log\frac{1}{|S_{12}|^2} = 10\log N.$$

It can be seen that when multi-outputs are required, say 10 or more, you can obtain some degree of isolation between the output ports. Directional couplers would be required only if there were a necessity for each output port to simulate a matched generator.

HERMAN KAGAN
Bogart Manufacturing Corp.
Brooklyn, N. Y.

Microwave Absorption Modulation by Electron Mobility Variation in *n*-Type Germanium*

Microwave-radiation attenuation in a dissipative medium such as germanium in which the conductivity and microwave frequency conditions $\sigma<\omega\epsilon$ and $\omega\tau<1$ are present has been shown by Gibson[1] to be attributed to the absorption constant relation

$$K = 1635\sigma/n \text{ db/meter}, \qquad (1)$$

where τ is the carrier relaxation time, ω the microwave angular frequency, and ϵ the permittivity. In the above equation, σ is the conductivity and n the index of refraction (4.05 in germanium).

Arthur, *et al.*,[2] previously reported that 37.5-kMc radiation absorption in *n*-type germanium could be modulated by a high external electric field across the crystal. Modulator operation depends on the phenomenon of electron-carrier mobility decreasing as a function of the electric field.[3,4] The semiconductor becomes transparent to the radiation when the carrier slope mobility dv/dE becomes zero in the saturated drift velocity region. Since information is limited on this new type of microwave modulator, a more extensive investigation was made. The present work proposes to investigate the radiation absorption modulation resulting from this effect at a lower frequency and, in addition, to observe the temperature and polarity conditions of the crystal that limit modulator operation.

The experimental arrangement is shown in Fig. 1. Fabrication of the slotted waveguide section through which the sample was inserted consisted of machining a nonradiating slot through each side of the broad section of the rectangular waveguide. The incident 24.2-kMc radiation power was set at 3 mw. An RF substitution method measured the attenuation changes. Measurements of the observed dc signal from a 1N26 crystal detector were made on a Tektronix 545 oscilloscope. The VSWR value with the sample in the microwave field was 1.3, which corresponds to a 0.07-db reflection loss. Polytetrafluoroethylene was placed between the crystal and waveguide section for electrical insulation.

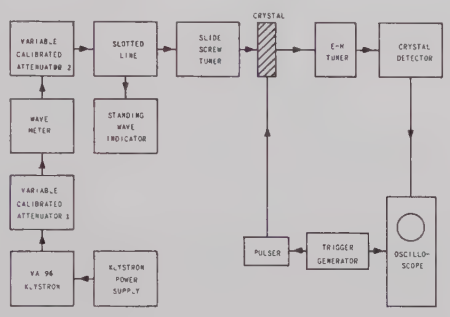

Fig. 1—Block diagram of the experimental apparatus.

Small pieces of 5-ohm-cm *n*-type germanium were sliced from the bulk single crystal and then lapped to the required thickness. The crystals were highly polished by etching[5] for two minutes in CP4 and rinsed successively in distilled water, ethyl alcohol, and carbon tetrachloride. To reduce hole injection from the positive-going end of each crystal, the wire lead on this end was mounted, using a n-n^+ junction. This junction was made with 95 per cent Sn—5 per cent Sb solder. The solder containing zinc-chloride flux was melted in an argon atmosphere and into this melt, the crystal end was immersed for five minutes at 600°C. This procedure produces alloying of the germanium and the Sn-Sb solder. Ordinary 90 per cent Pb-10 per cent Sn solder was applied for the negative-end connection. The excess flux was removed by placing the crystal in warm distilled water.

The germanium specimens had the form of a rectangular bar whose dimensions were 393 mils long, 125 mils wide, and 5 mils thick. When the crystal was inserted through the waveguide and no voltage pulse was applied, the power attenuated 4.5 db. The crystal was oriented so that the pulsed electric field would be parallel to the RF electric field vector. During operation the crystal was subjected to 0.5-μsec voltage pulses at a repetition rate of 40 pps and fan-cooled. An increase in RF power was detected as the voltage pulse was raised. The change in attenuation as the pulsed electric field across the crystal was increased is shown in Fig. 2. This curve indicates that

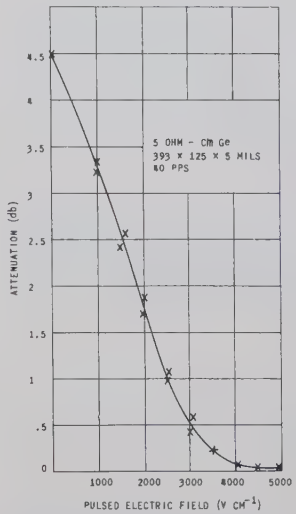

Fig. 2—Absorption variation vs electric field.

practically complete reduction of the 4.5-db attenuation occurs when the electric field across the sample was 4000 v/cm. This field strength represents the onset of the majority-carrier velocity saturation, which is in close agreement with observations made by Arthur.[2] The increase in the RF power when the pulsed electric field across the sample was 4000 v/cm is indicated by the pulse pattern shown in Fig. 3. The amplitude of the RF modulation pulse pattern remained the same when the electric field was increased from 4000 to 5000 v/cm. If the crystal was permitted to operate at a field strength of 3000 v/cm without being cooled, or if the pulse repetition rate was increased to 200 pps and cooling applied, the modulated RF power amplitude was quickly reduced. This microwave absorption effect could be caused by an increase in the carrier density due to thermal ionization. The occurrence, however, was nondestructive. The crystal returned to normal operation when cooling was restored or when the pulse rate of 40 pps was again applied. Fig. 4 indicates the results obtained when the n-n^+ junction was connected initially to the positive-voltage lead and then to the negative-voltage lead when the field strength was 2000 v/cm. From the oscillogram pattern, it is seen that hole injection will limit modulator operation if the n-n^+ junction is not connected to the crystal's positive-going end. It is further seen in Fig. 5 that some crystals with normal operating conditions (cooled and operated at 40 pps) exhibited two regions where RF power modulation changes occurred. These variations occurred

* Received by the PGMTT, October 28, 1960; revised manuscript received, December 23, 1960.

[1] A. F. Gibson, "The absorption of 39-kMc radiation in germanium," *Proc. Phys. Soc. (London) B*, vol. 69, pp. 488–490; March, 1956.

[2] J. B. Arthur, A. F. Gibson, and J. W. Granville, "The effect of high electric fields on the absorption of germanium at microwave frequencies," *J. Electronics*, vol. 2, pp. 145–153; September, 1956.

[3] E. J. Ryder, "Mobility of holes and electrons in high electric fields," *Phys. Rev.*, vol. 90, pp. 766–769; June, 1953.

[4] J. B. Gunn, "The field-dependence of electron mobility in germanium," *J. Electronics*, vol. 2, pp. 87–94; July, 1956.

[5] J. N. Shive, "Intermediate surface treatment," in "Transistor Technology," Bell Telephone Labs., Inc., vol. 1, pp. 393–406; September, 1952.

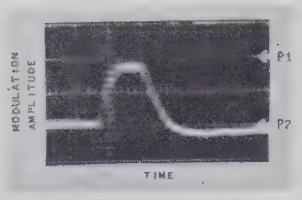

Fig. 3—Microwave absorption modulation pattern. P_1 and P_2 are the initial and absorption power levels respectively. Time scale = 0.25 μsec/division (E = 4000 v/cm, 40 pps).

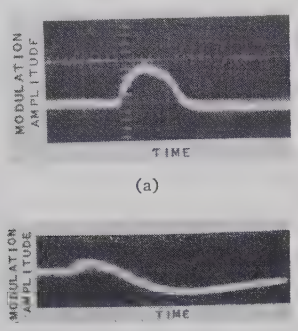

Fig. 4—Modulator operation dependence on junction polarity. Time scale = 0.5 μsecond/division (E = 2000 v/cm, 40 pps). (a) N-N^+ junction connected to positive-voltage lead. (b) N-N^+ junction connected to negative-voltage lead.

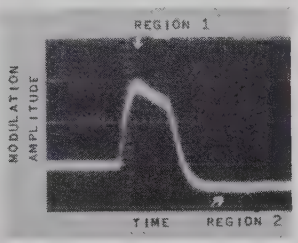

Fig. 5—Modulation changes due to minority carriers. Time scale = 0.5 μsec/division (E = 4000 v/cm, 40 pps).

both during and following the 0.5-μsec voltage-pulse application. This may be attributed to hole injection or to an ionization effect in these crystals. The region following the high-voltage pulse was of very long duration.

Milton Harmatz
USASRDL
Ft. Monmouth, N. J.

Coaxial to Strip Transmission Line Adapter*

Over the past few years, strip transmission line has shown itself capable of being utilized in a large number of microwave configurations which were previously constructed in coaxial line or waveguide. In many cases the components fabricated in strip transmission line are simpler to design and produce particularly where, as in the sandwich type of line, advantage may be taken of photo-etching techniques. This type of construction using copper-foil-clad dielectric material enables the foil to be used for both the center conductor and the ground planes.

However, the use of such thin conducting material with relatively poor adhesion between the metal and dielectric often leads to difficulties where the coaxial line is attached to the strip. The action of soldering the center pin of the coaxial line to the strip tends to destroy the adhesion between the foil and the dielectric. The first time the connection is made the results may be quite satisfactory, but in development work it is often necessary to assemble and dismantle a filter or other device many times to make adjustments and alterations. If a soldered connection is used in such a situation, the end of the strip is soon distorted and loosened to such an extent that measurements made through the junctions are meaningless. To overcome this difficulty, a solderless transition has been devised for use in our laboratory work. An exploded view of this transition showing the important dimensions is given in Fig. 1.

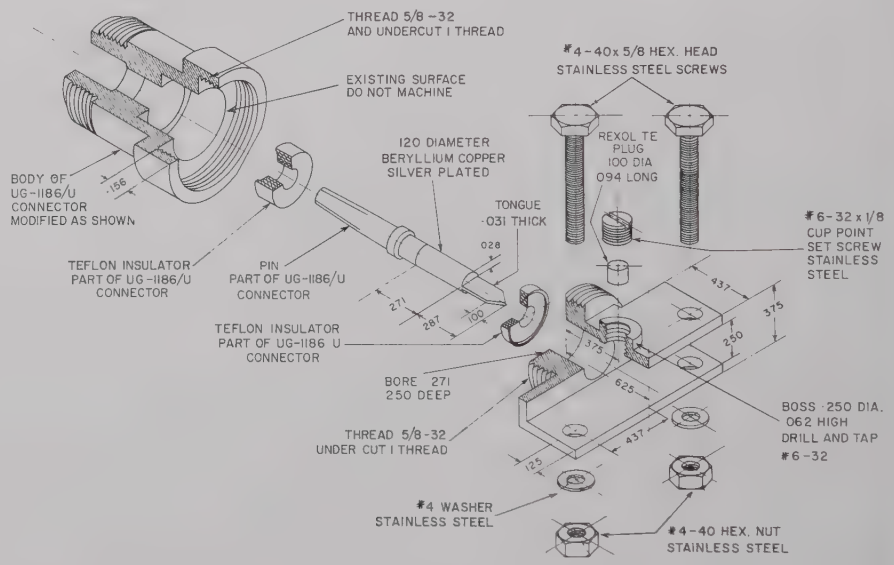

Fig. 1.

The adapter could have been of either the right-angle or in-line type, but the latter was chosen for mechanical strength and convenience, in addition to the fact that a symmetrical transition is less likely to introduce spurious modes. The channelled transition block is fastened to the stripline by two machine screws. This provides the mechanical attachment and the electrical connection to the ground planes. The flattened pin is accommodated in a slot milled in the lower surface of the upper dielectric sheet. The pin is pressed against the etched center conductor by a button of the same material as the dielectric of the line which is a loose fit in a hole in the upper dielectric sheet. A set screw in the threaded boss in the transition block holds the button tightly against the flattened pin, insuring good electrical contact between the pin and the center conductor.

The parts used for the coaxial end of the adapter were originally taken from a standard UG-1186/U connector with the body shortened and threaded as shown. However, after the initial connectors proved successful, a large quantity was made to our design by a manufacturer.

These connectors have been used over the range of frequencies from 300–6000 Mc and have given very satisfactory results. In order to confirm our opinion, measurements were made on a number of these connectors using the method of measuring a junction described by Wentworth and Barthel.[1]

Six adapters, taken at random from stock, were each measured with six different lengths of strip transmission line. This involved 36 assemblies and disassemblies of the transitions, but the uniformity of the results indicated that this had no adverse effect. At any frequency and with one particular length of line, the variation of the position of the voltage minima on the slotted line was less than ±0.2 mm with reference to the mean for the six transitions. This is of the same order as the expected experimental error and represents a spread of less than ±0.005 wavelength at the highest frequency. This close agreement between the measurements on the various adapters enabled the mean VSWR of the junctions to be computed from the average readings (Fig. 2). The true VSWR of a particular junction would not differ from this mean value by more than ±0.03.

* Received by the PGMTT, December 30, 1960.

[1] F. L. Wentworth and D. R. Barthel, "A simplified calibration of two port transmission line devices," IRE Trans. on Microwave Theory and Techniques, vol. MTT-4, pp. 173–175; July, 1956.

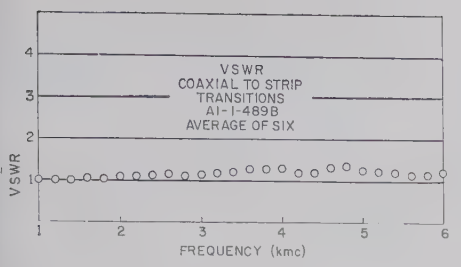

Fig. 2.

Our experience has shown that these connectors have a low enough VSWR to be adequate for all but the most critical situations and may be assembled and dismantled numerous times without damage to either the connector itself or to the strip to which it has been connected.

J. H. Craven
Radio & Elec. Engrg. Div.
Natl. Res. Council
Ottawa, Ont., Can.

A Note on Loaded Line Synthesis*

The purpose of this note is to present an alternate derivation of a formula for the synthesis of a loaded line. The problem is to determine the values of the normalized susceptances a and c mounted an exact quarter-wavelength apart along a uniform line. These are arranged in the order a, c, c, $\cdots$ c, a to achieve a loaded line with a given phase shift and perfect match. In order to analyze a particular loaded line design for standing-wave ratio and phase shift over a band of frequencies on a digital computer, it is worthwhile to know the values of the susceptances to many more decimal places than one would achieve from a simple graph.

In branch transmission line couplers, where the length of branches and the spacing between them are each exactly a quarter-wavelength long, the calculated response (standing-wave ratio and fraction of power out each arm) is symmetrical on a normalized frequency basis F where $F=f/f_0$ or $F=\lambda g_0/\lambda g$ when waveguide is used. For example, the response is the same at $F=0.80$ as it would be at $F=1.20$.

The response is not symmetrical in the case of a half-wave or quarter-wave rotating plate consisting of round waveguide loaded with a cascade of irises which are alternately all capacitive or all inductive as the guide is rotated. However, if the values of a and c are assumed to have a frequency variation which is reasonable (inductive varying as $1/F$ and capacitive varying as F), the difference in phase between the two positions of the plate does not change with frequency near the design center. That is, the phase shift of the plate, when it is used as a capacitive iris array minus that when it is an inductive iris array, has the desired value, and the rate of change of this value with respect to frequency is zero at the design center. The assumption is made that the magnitude of the susceptances are the same when the irises are inductive as when the irises are capacitive.

Consider a single shunt susceptance of normalized value, jc. Its matrix is

$$M = \begin{bmatrix} 1 & 0 \\ jc & 1 \end{bmatrix}. \quad (1)$$

For two such susceptances separated by a quarter wavelength of unity impedance line

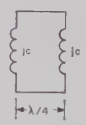

$$M = \begin{bmatrix} 1 & 0 \\ jc & 1 \end{bmatrix}\begin{bmatrix} 0 & j \\ j & 0 \end{bmatrix}\begin{bmatrix} 1 & 0 \\ jc & 1 \end{bmatrix} = \begin{bmatrix} -c & j1 \\ -j(c^2-1) & -c \end{bmatrix}. \quad (2)$$

For three susceptances

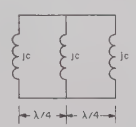

$$M = \begin{bmatrix} c^2-1 & j(-c) \\ -j(-c^3+2c) & c^2-1 \end{bmatrix}. \quad (3)$$

For n susceptances separated by $n-1$ quarter wavelength of line

$$M = \begin{bmatrix} S_{n-1}(-c) & jS_{n-2}(-c) \\ -jS_n(-c) & S_{n-1}(-c) \end{bmatrix} \quad (4)$$

where

$$\begin{aligned} S_{-1}(-c) &= 0 \\ S_0(-c) &= 1 \\ S_1(-c) &= -c \\ S_2(-c) &= c^2-1 \\ S_3(-c) &= -c^3+2c \end{aligned} \quad (5)$$

$$S_{n+1}(-c) = -cS_n(-c) - S_{n-1}(-c). \quad (6)$$

The polynomials $S_n(-c)$ are Chebyshev [2] polynomials of the second kind.

If a shunt susceptance ja is put a quarter-wavelength away from each end to achieve a matched condition, the matrix becomes

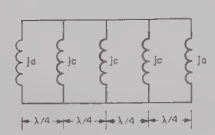

$$M = \begin{bmatrix} -aS_n(-c) - S_{n-1}(-c) & jS_n(-c) \\ -j(a^2S_n(-c) + 2aS_{n-1}(-c) + S_{n-2}(-c)) & -aS_n(-c) - S_{n-1}(-c) \end{bmatrix}. \quad (7)$$

This matrix represents a line of length θ and a normalized impedance of unity if each term in it is equal to those of a matrix of this length of line:

$$M = \begin{bmatrix} \cos\theta & j\sin\theta \\ j\sin\theta & \cos\theta \end{bmatrix}. \quad (8)$$

On equating matrix (7) with (8), the value of c can be found by setting $S_n(-c) = \sin\theta$ by inverse interpolation in the tables [2]. Then the value of a to give a matched line is

$$a = \left| \frac{|\cos\theta| - |S_{n-1}(-c)|}{\sin\theta} \right|. \quad (9)$$

There are two values of a which will match out the loaded line; the one which should usually be used is that with the smaller magnitude. The algebraic sign of a is the same as c and may be either positive or negative, depending on whether the resulting loaded line is to be effectively longer or shorter than the unloaded line.

An earlier contribution [3] has been based on using the value of a as exactly one-half that of c. The element spacing was then computed so that the differential phase shift was as desired. This scheme results in spacings which are not an exact quarter-wavelength and therefore may not give a symmetrical frequency response especially for small numbers of elements.

Appendix

The general circuit matrix of a dissipationless reciprocal symmetrical two-port network can be represented as

$$\begin{bmatrix} A & B \\ C & A \end{bmatrix}. \quad (10)$$

In this $A^2-BC=1$ and A is a purely real quantity and B and C are purely imaginary. The matrix of a cascade of n of these networks may be found by raising (1) to the nth power.

For $n=2$

$$\begin{bmatrix} A & B \\ C & A \end{bmatrix}^2 = \begin{bmatrix} 2A^2-1 & B(2A) \\ C(2A) & 2A^2-1 \end{bmatrix}. \quad (11)$$

For $n=3$

$$\begin{bmatrix} A & B \\ C & A \end{bmatrix}^3 = \begin{bmatrix} 4A^3-3A & B(4A^2-1) \\ C(4A^2-1) & 4A^3-3A \end{bmatrix}. \quad (12)$$

For the general case of n identical networks the matrix product may be expressed as [5]

$$M^n = \begin{bmatrix} T_n(A) & BU_{n-1}(A) \\ CU_{n-1}(A) & T_n(A) \end{bmatrix}. \quad (13)$$

$T_n(A)$ and $U_{n-1}(A)$ are Chebyshev polynomials of the first and second kind in A [2].

* Received by the PGMTT, October 29, 1959; revised manuscript received, January 3, 1961.

An alternate expression for this matrix product is

$$M^n = \begin{bmatrix} 1/2C_n(2A) & BS_{n-1}(2A) \\ CS_{n-1}(2A) & 1/2C_n(2A) \end{bmatrix}. \quad (14)$$

$C_n(2A)$ and $S_{n-1}(2A)$ are Chebyshev polynomials of the first and second kind normalized to $2A$ rather than A as in (13). Term-by-term identification of (13) and (14) serves to define the Chebyshev polynomials C_n and S_{n-1} in terms of Chebyshev polynomials T_n and U_{n-1}. The Chebyshev polynomials $C_n(x)$ and $S_n(x)$ are available [2] for $n=2(1)12$ (*i.e.*, from 2 to 12 in steps of one) for $x=0(0.001)2$ to 12 decimal places. In this reference $U_{n-1}(x)$ is employed where $U_n(x)$ is usually found [4], [5].

A useful quantity for reflection loss and the resulting standing-wave ratio of a periodic transmission line structure is the equivalent susceptance B_{eq} which would give the same VSWR or insertion loss in a unity impedance line. It is found by $jB_{eq}=B-C$ (15) for one stage or $jB_{eq}=(B-C)S_{n-1}(2A)$ (16) for n stages; the relation to voltage standing-wave ratio r is

$$B_{eq} = \frac{r-1}{\sqrt{r}} \quad (17)$$

and to power insertion loss is

$$L = 1 + \frac{B_{eq}^2}{4}. \quad (18)$$

These relations are valid in both the pass band $|A| \leq 1$ and the stop band $|A| \geq 1$.

John Reed
Raytheon Co.
Wayland, Mass.

Bibliography

[1] J. Reed, "The multiple branch waveguide coupler," IRE Trans. on Microwave Theory and Techniques, vol. MTT-6, pp. 398–403; October, 1958.
[2] "Tables of Chebyshev Polynomials ($S_n(x)$ and $C_n(x)$)," Natl. Bur. of Standards Appl. Math. Ser. No. 9, U. S. Govt. Printing Office; Washington, D. C.
[3] A. J. Simmons, "Phase shift by periodic loading of waveguide and its application to broad-band circular polarization," IRE Trans. on Microwave Theory and Techniques, vol. MTT-3, pp. 18–21; December, 1955.
[4] W. L. Pritchard, "Quarter wave coupled waveguide filters," *J. Appl. Phys.*, vol. 18, pp. 862–872; October, 1957.
[5] M. C. Pease, "The iterated network and its application to differentiators," Proc. IRE, vol. 40, pp. 709–711; June, 1952.

X-Band Diode Limiting*

Broad-band, matched, low power, instantaneous, passive, *X*-band diode limiting has been demonstrated. The limiter, which uses standard microwave components, is an outgrowth of point contact germanium diode microwave switch research. In fact, the hybrid-tee switch[1] makes a very good narrow-band limiter under the condition of zero bias voltage on the crystals (biasing terminals short circuited). The output power under these conditions is limited to 0.5 mw[2] for incident power up to 30 mw, deduced from Fig. 9 of Garver, *et al.*[1] However, the bandwidth of the hybrid-tee switch when used as a limiter is insufficient for many applications such as limiting the amplitude of a 0.2-μsec magnetron pulse or flattening a frequency-modulated klystron mode.

From our experience with the hybrid-tee switch, we concluded that any diode switch providing high isolation with diode conduction and low insertion loss with nonconduction will function passively as a limiter. Low RF power does not cause significant diode conduction, while high RF power results in conduction which changes the diode impedance, causing increasing attenuation. Thus a more broad-band switch is needed that provides high isolation with the diode in the conducting state.

Although the basic *X*-band diode switch using a point contact germanium diode such as the 1N263 is broad-band, it provides high isolation in the nonconduction state, and therefore does not fulfil the above criteria. In fact, with its biasing terminals short-circuited, this switch acts as an expander.

Using a technique developed by Sweet,[3] it is possible to make a broad-band switch having isolation with diode conduction and which is matched as well for all biases on the diode. Fig. 1 shows the block diagram for using Sweet's technique at *X*-band. If both arms containing diodes are identical reflectors, the properties of the 90°, 3-db coupler are such that the phases of the reflected waves add at the output arm and cancel at the input arm; thus all power reflected from the diodes comes out the output arm, and the input arm always appears matched. Using slide screw tuners next to the diodes, a switch has been made giving isolation greater than 20 db over a 400-Mc bandwidth with an insertion loss of 0.7 db or less. The isolation is greater than 30 db over a 150-Mc bandwidth. This is much better than the hybrid-tee switch isolation of greater than 30 db over a 20-Mc bandwidth.

When the short-slot hybrid junction switch with two diodes is used as a limiter, however, the output does not remain constant with increasing incident power but increases slightly. The action could be better described as compression. Better limiting is obtained by using power sensitive tuners behind the diodes instead of fixed tuners. A second 1N263 space $\frac{3}{4}\lambda_g$ from the first has been found to give the flattest limiting. As shown in Fig. 2, the output at the center frequency is limited to 0.43 mw $\pm$0.1 db for all incident power from 2 mw to 200 mw.[4] For pulsed power up to 10 watts peak, the output increases to 2 mw peak. Pulse energy greater than 1 watt μsec permanently damages the diodes so that the low power insertion loss of the limiter is increased above its typical value of 0.7 db.

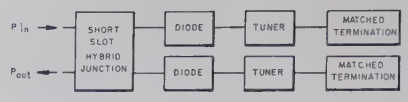

Fig. 1—Block diagram for making matched diode switch.

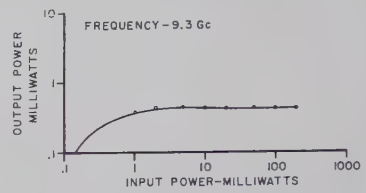

Fig. 2—Limiting using 4 1N263's and a short-slot hybrid junction.

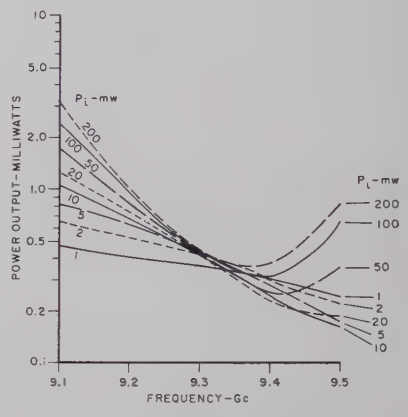

Fig. 3—Frequency dependence of limiting with diodes at $\frac{3}{4}\lambda_g$ spacing.

The frequency dependence of the limiting for $\frac{3}{4}\lambda_g$ spacing is shown in Fig. 3. For input power ranging from 2 mw to 200 mw, the output power is 0.45 mw $\pm$1 db over a 60-Mc bandwidth, and $\pm$2 db over a 120-Mc bandwidth. This limiter has been successfully used for suppressing the unwanted AM from an FM klystron.[5] Unless fringing effects forbit it, flat limiting should occur at one quarter wavelength between diodes. With the smaller spacing it is anticipated that only the abcissa of Fig. 3 would be changed, so that the data for 9.1 Gc would occur at 8.7 Gc and the data for 9.5 Gc would occur at 9.9 Gc, *i.e.*, the bandwidth should be tripled. To place the diodes one quarter-wavelength apart it will be necessary to redesign the diode mount so that it is smaller. Since the limiter does not require external biasing terminals or RF chokes, the dc shorts can be built into the diode mounts.

R. V. Garver
D. Y. Tseng
Ordnance Corps.
Diamond Ordnance Fuze Labs.
Washington, D. C.

* Received by the PGMTT, January 5, 1961.

[1] R. V. Garver, E. G. Spencer, and M. A. Harper, "Microwave semiconductor switching techniques," IRE Trans. on Microwave Theory and Techniques, vol. MTT-6, pp. 378–383; October, 1958. (See especially page 381.)

[2] Open-circuit bias terminals cause limiting at a higher output power level.

[3] L. Sweet, "Instantaneous Automatic Gain Control (IAGC) Techniques for Crystal Video Receivers," PRD Final Rept. 4.13, Contract No. AF 30(602)-1434/ Proj. No. 4505, Task No. 45215, ASTIA AD 148728; December 1, 1957.

[4] To obtain such flat output, it was necessary to use selected diodes. Diodes picked at random will give about 1 db variation in output. The characteristics were also slightly affected by diode rotation and seating.

[5] J. Samuel, "Diamond Ordnance Fuze Laboratories Workbook No. 1955." Unpublished.

A Note on the Difference Between Equiangular and Archimedes Spiral Antennas*

There seems to exist in the literature considerable confusion about the various types of spiral antennas, their characteristics, and their bandwidth capabilities. One evidence of this confusion appeared in a paper by Bower and Wolfe,[1] in which they state that the Archimedes spiral antenna can be specified in terms of angles and hence belongs in the class of "frequency-independent antennas." Frequency-independent antennas are relatively new; in fact, until 1955 there was no evidence that a "frequency-independent" antenna did, indeed, exist.[2] Therefore, it would appear appropriate to delineate the characteristics and the terminology of the antennas involved. Perhaps this brief report of some recent work at the University of Illinois Antenna Laboratory will aid in pointing up the differences in operation of the logarithmic (*i.e.*, equiangular) and Archimedean spiral antennas.

It has long been recognized that the log-spiral curve is specified by an angle, α, the angle between the position vector to a point on the curve and a tangent to the curve at that point. This property of the curve leads to the alternate name, equiangular spiral. It was pointed out by Rumsey[3,4] in 1954 that this property of the log-spiral makes it possible to specify an antenna based upon this curve entirely by angles except for a necessary arm length; hence, such an antenna might possibly be a frequency-independent structure. It has been shown[5] that frequency-independent operation of log-spiral antennas is indeed possible over bandwidths limited only by precision of construction. Rumsey also pointed out that magnification of the log-spiral curve is equivalent to a rotation so that a change in the operating wavelength of a log-spiral antenna can be exactly compensated by a rotation of the antenna. For loosely wound spirals in a plane (small α) the radiation patterns are not rotationally symmetric and a rotation of the elliptic cross section of the beam is observed with frequency.[5] For tightly wound spirals this rotation is unobservable because of the symmetry of the beam.

The Archimedean spiral is *not* specified by any one angle. The angle α between the position and tangent vectors on this curve is a function of position on the curve. (It can be easily shown that $\alpha = \arctan \phi$, where ϕ is the azimuthal angle swept out in generating the curve.) For very tightly wound spirals this angle, far from the origin, is a *slowly-varying* function. If, as is widely believed, the radiation from the Archimedean spiral occurs from a localized band on the antennas, then in these few turns of a tight spiral sufficiently far from the origin the angle α will be relatively constant, and the Archimedean spiral is a very close approximation to a tightly wound log-spiral. In fact, the Archimedean spirals which have been utilized over broad bandwidths are so tightly wound that the angle α changes little over the entire radiating structure so that the operation likewise changes little over the operating bandwidths. This difference in the two spiral curves is the principal reason why an Archimedean spiral antenna must have many closely spaced turns to operate successfully while planar log-spiral antennas can be constructed with only $1\frac{1}{2}$ or 2 turns in a relatively loose spiral.

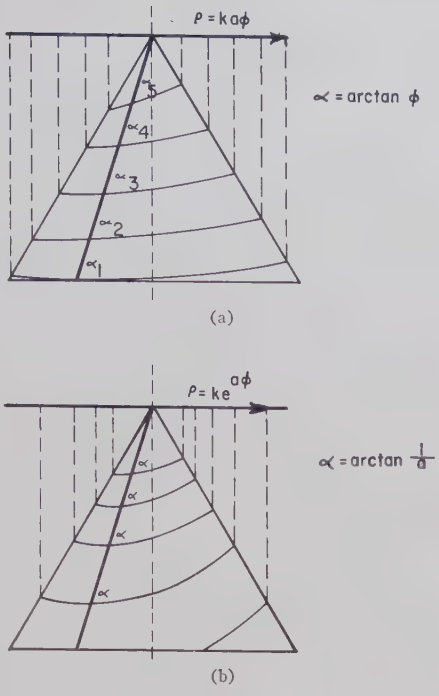

Fig. 1.

In order to point out the difference between Archimedean and log-spirals it is therefore necessary to magnify the changing α of the Archimedean curve. This could be done by constructing a loosely spiraled planar antenna. However, it can also be shown by constructing an Archimedean spiral antenna on a conical surface.

It has been previously shown[6] that the conical log-spiral is a useful antenna because it has a frequency-independent unidirectional radiation pattern. One of the characteristics of the conical log-spiral antenna is that the beamwidth is directly related to the angle α and since this angle is a constant for a given antenna the beamwidth can likewise be held relatively constant as a function of frequency. Similar unidirectional patterns can be obtained from the conical Archimedean spiral. Planar Archimedean spiral curves, which would describe a balanced antenna with well formed bidirectional patterns, may be orthogonally projected onto a conical surface as shown in Fig. 1(a). A similar projection is shown for the log-spiral in Fig. 1(b). In a particular case observed, the angle α for the conical Archimedean spiral antenna varied between approximately 45 degrees and 85 degrees whereas the log-spiral antenna constructed on the same cone has a fixed α of 85 degrees. The effect of the changing α on the radiation pattern of the Archimedean spiral as compared with the frequency-independent pattern of the log-spiral is shown in Fig. 2. The variation of the beamwidth of the conical Archimedean spiral with frequency is contrasted with the constant beamwidth of the conical log-spiral in Fig. 3. A similar contrast between Archimedean- and log-spiral operation has been obtained when using four-arm spirals to produce conical beams.[7]

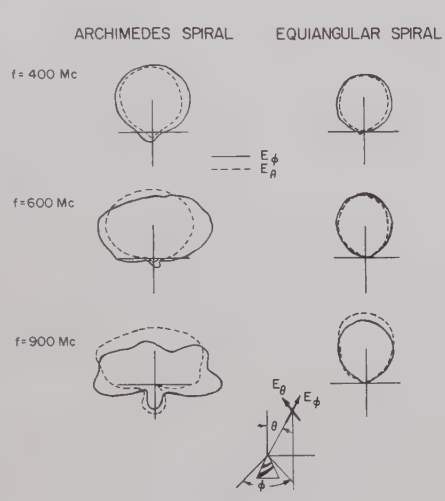

Fig. 2.

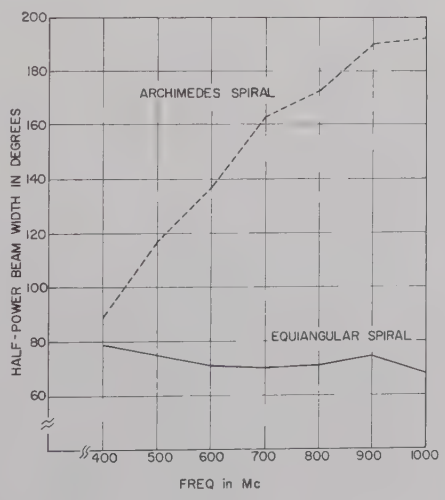

Fig. 3.

The above comments are not intended to detract in any way from the merit of the

* Received by the PGMTT, August 8, 1960.

[1] R. Bawer and J. J. Wolfe, "A printed circuit balun for use with spiral antennas," IRE TRANS. ON MICROWAVE THEORY AND TECHNIQUES, vol. MTT-8, pp. 319–325; May, 1960.

[2] J. D. Dyson, "The equiangular spiral antenna," *Proc. 5th Ann. Symp. on the USAF Antenna Res. and Dev. Program*, University of Illinois, Monticello, Ill.; October, 1955 (classified).

[3] V. H. Rumsey first proposed in September, 1954, that the log-spiral geometry be investigated.

[4] V. H. Rumsey, "Frequency independent antennas," 1957 IRE NATIONAL CONVENTION RECORD, Pt. 1, pp. 114–118. Also, Antenna Lab., University of Illinois, Tech. Rept. No. 21, Contract AF33(616)-3220; October, 1957.

[5] J. D. Dyson, "The equiangular spiral antenna," IRE TRANS. ON ANTENNAS AND PROPAGATION, pp. 181–187; April, 1959. Also, Antenna Lab., University of Illinois, Tech. Rept. No. 21, Contract AF33(616)-3220; September, 1957.

[6] J. D. Dyson, "The unidirectional equiangular spiral antenna," IRE TRANS. ON ANTENNAS AND PROPAGATION, vol. AP-7, pp. 329–334; October, 1959. Also, Antenna Lab., University of Illinois, Tech. Rept. No. 33, Contract AF33(616)-3220; July, 1958.

[7] J. D. Dyson and P. E. Mayes, "New circularly polarized frequency independent antennas with conical beam or omnidirectional patterns," submitted for publication in the IRE TRANS. ON ANTENNAS AND PROPAGATION. Also, Antenna Lab., University of Illinois, Tech. Rept. No. 46, Contract AF33(616)-6079; June, 1960.

Archimedean spiral antenna. The Archimedean spiral was a significant contribution to broad-band antennas and the work of Turner[8] on this antenna preceded that on the log-spirals at Illinois. However, there are basic differences in the Archimedean and log-spiral structures and in their characteristics, such as radiating efficiency and ultimate bandwidth capabilities. To loosely group all spiral antennas together and assume that the characteristics associated with one type are automatically to be found in the other can lead to erroneous conclusions.

P. E. Mayes
J. D. Dyson
Elec. Engrg. Dept.
University of Illinois
Urbana, Ill.

Rebuttal

Naturally, we were quite interested in Mayes and Dyson's letter on the difference between the equiangular and Archimedean spiral antennas, and we appreciate their calling our attention to a controversial statement in our paper.[1] We implied that, except for diameter, the Archimedean spiral is *completely described* by angles, and hence belongs to the class of so-called frequency-independent antennas. We are afraid, however, that some of the remarks in the correspondences cannot pass unanswered, and we should like to comment on three points:

1) the statement in our paper,
2) the meaning of frequency independent antennas, and
3) the comparative data given in the correspondence.

As the note so aptly points out, the Archimedean spiral is *not specified* by any one angle. In fact, had this spiral been capable of such a description, namely, that the angle between position vector and the tangent to any point on the curve is constant, Archimedes himself would probably have called it the equiangular spiral. We do admit, and apologize, for a poor choice of words, but hasten to add that there is a distinct difference between the statement as we made it, and the statement attributed to us in the correspondence; the words "specify" and "describe" are not synonymous, in either the vernacular or the mathematical sense.

With respect to our having included the planar Archimedean spiral in the class of frequency-independent antennas, Mayes and Dyson's comments are far more apropos. There is, indeed, widespread confusion about the term "frequency-independent antennas." For our part, there is no confusion; a frequency-independent antenna is just that—none of its characteristics exhibit *any* change with frequency. It is indeed unfortunate that the term was applied to a physical structure in the first place. The confusion stems entirely from the fact that many authors have associated the term "frequency-independent antenna" with the fact that the *characteristics* of the antenna are frequency-independent, and with a *geometry* which *theoretically* gives rise to an antenna which has frequency-independent characteristics. The two descriptions are not the same.

Mayes and Dyson properly point out that, in contrast to the equiangular spiral, the angle α between the position and tangent vectors for Archimedean spiral is a function of position on the curve. However, they go on to say that "this difference in the two spiral curves is the principal reason why an Archimedean spiral antenna must have many closely spaced turns to operate successfully, while planar log-spiral antennas can be constructed with only $1\frac{1}{2}$ to 2 turns in a relatively loose spiral." With respect to the effect of α on the characteristics of log-spirals, we quote from Dyson's paper,[5] in which he states that ". . . the more tightly spiraled antennas, and the antennas with wider arms, tend to have smoother and more uniform patterns." He later states, with reference to a particular antenna: "the variation in beamwidth is held within 4 degrees by antenna reorientation when the frequency is varied from 2 to 5.18 kMc . . . compared with the variation of approximately 50 degrees over the same band of frequencies without reorientation." In other words, for pattern or rotational symmetry corresponding to small beamwidth variations *without reorientation*, the log-spiral *must* be tightly wound—a conclusion quite analogous to that made for the Archimedean spiral.

Mayes and Dyson go on to say that in order to point out the difference between the two spirals, it is necessary to magnify the changing α of the Archimedean curve, and proceed to illustrate their point by constructing spirals on a conical surface. Now in our opinion, conclusions drawn from the conical surface are *not* directly applicable to the planar case in question. The data shown in Fig. 3 of the correspondence are of little value in the absence of further qualifications; and even if suitably qualified, they might have little bearing on the more appropriate comparison based on planar spirals.

To illustrate what can be done with planar Archimedean spirals, we call your attention to Figs. 4 and 5 which show actual

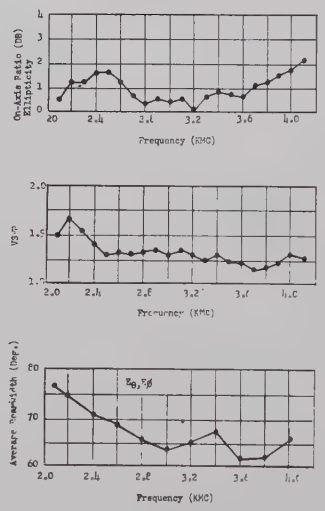

Fig. 4—Typical spiral antenna characteristics.

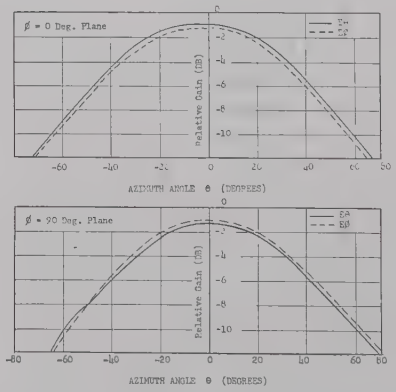

Fig. 5—Spiral antenna radiation patterns at 2800 Mc.

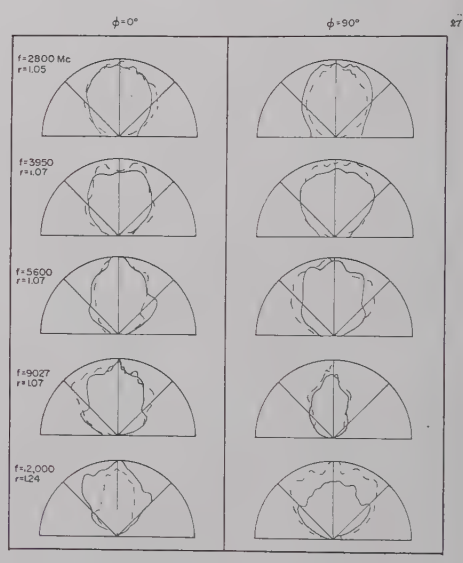

Fig. 6—Radiation patterns of antenna 2M15-C. $a=0.30$; $K=0.62$; solid line indicates E_θ; dashed line indicates E_ϕ.

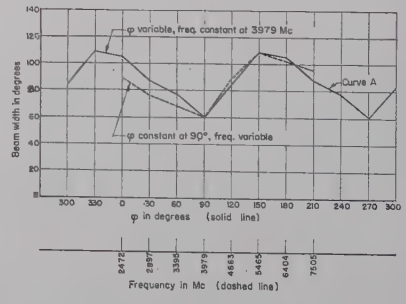

Fig. 7—Rotation of radiated field with a change in frequency (antenna M-10-3 slot length, 33 cm).

[8] E. M. Turner, "Sprial slot antenna," Wright Air Dev. Ctr., Wright-Patterson AFB, Ohio, Tech. Note WCLR-55-8; June, 1955.

data[9] taken on a cavity-backed Archimedean spiral; these data are typical of what has been observed on similar units over the frequency range from 200 through 5000 Mc. The antenna shown is *not* frequency-independent, although its characteristics might easily be termed "broad-band."

In contrast, data obtained by Dyson[5] for a bidirectional, planar, equiangular spiral antenna (no cavity) are reproduced in Figs. 6 and 7. These are the antennas which Dyson and others have called "frequency-independent." The fact is, any antenna whose pattern is asymmetrical and rotates with frequency or which yields data as shown above, is simply not frequency-independent (with *or* without quotes).

To continue to describe the equiangular spiral antenna as frequency-independent may not lead to erroneous conclusions, but will consistently and continually lead to confusion.

R. Bawer
Radiation System Inc.
Alexandria, Va.
J. I. Wolfe
Aero Geo Astro Corp.
Alexandria, Va.

[9] R. Bawer and J. J. Wolfe, "The spiral antenna," 1960 IRE International Convention Record, pt. 1, pp. 84–95;

A Further Note on the Equiangular and Archimedes Spiral Antennas

The intent of the original note was to point out basic differences between the two types of spiral antennas and that, although they have many similar characteristics, conclusions reached about one of the types do not necessarily apply to the other.

In regard to the "rebuttal" by Bawer and Wolfe to the note, we would like to make only four short comments:

1) The pattern rotation of the equiangular spiral antenna has been adequately covered in paragraph two and in our references.[2,4–6] In fact, the graph which Bawer and Wolfe reproduce as Fig. 7 was originally chosen and published[5] to point out this fact.
2) On the plane or on the cone the angle α, the angle between the position vector and a tangent to the curve, is a constant parameter for the equiangular spiral and a changing parameter for the Archimedes spiral.
3) The objection to the use of the term "frequency independent" as applying to *any* physical structure has some merit. However the logarithmic (*i.e.*, equiangular) spiral antennas are certainly in a class apart from the structures normally associated with the term broad band as it has been used over the years. Further, the conical logarithmic spiral has many characteristics which *are* essentially frequency independent over bandwidths which are limited only by practicality of construction and not by any basic parameter of the spiral.

   A new term is required which conveys the idea that the bandwidth, over which pattern and impedance characteristics of an antenna are essentially constant, is theoretically unlimited. We, and others, have been using the term "frequency-independent" in this sense for several years. Perhaps this question of terminology should be decided by an IRE Standards Committee.
4) Bawer and Wolfe need not have felt that they must defend the Archimedes spiral antenna. As we indicated in the final paragraph of our original note, it is an excellent antenna for many applications.

P. E. Mayes
J. D. Dyson
University of Illinois
Urbana, Ill.

Contributors

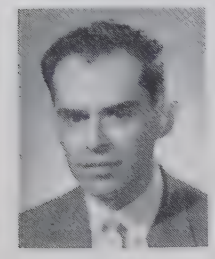

G. Boudouris

G. Boudouris (SM'58) was born in Kyparissia, Greece, on September 11, 1919. He studied mechanical and electrical engineering from 1937 to 1941 and in 1946, at the Polytechnic Institute of Athens, Greece, where he received the diploma in mechanical and electrical engineering. He went to Paris in 1950 and obtained the diploma of radio engineer at the Ecole Supérieure d'Electricité in 1952. Continuing his studies at the Sorbonne, University of Paris, he received the degree of "Docteur ès Sciences" in physics in 1958.

He is now on the research staff of the Laboratoire de Spectroscopie Hertzienne at the Centre National de la Recherche Scientifique, in Paris.

❖

R. E. Collin

Robert E. Collin (M'54) was born on October 24, 1928, in Donalda, Alberta, Canada. He received the B.S. degree in engineering physics from the University of Saskatchewan, Saskatoon, Canada, in 1951. The following two and a half years were spent in graduate work at Imperial College, London, England, from which he received the Ph.D. degree and the diploma of Imperial College in 1954.

Upon returning to Canada, he worked from 1954 to 1958 at the Canadian Armament Research and Development Establishment, Quebec. Since 1958, he has been on the professorial staff of the Electrical Engineering Department at Case Institute of Technology, Cleveland, Ohio.

Dr. Collin is a member of Sigma Xi.

❖

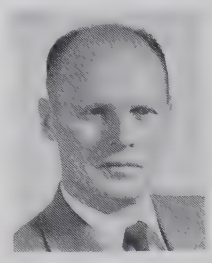

W. Culshaw

William Culshaw (SM'57) was born on February 5, 1914, in Lancashire, England. He received the B.Sc. degree in physics from the university of Sheffield, England, in 1941, the B.Sc. degree in mathematics from the University of London in 1947, and the Ph.D. degree from the University of London, in 1952.

From 1952 to 1954 he was a staff member of the Telecommunications Research Establishment, Malvern, England, where he was with the Microwave Receiver, and Millimeter Wave Divisions. From 1954 to 1956 he was a member of the Radio Physics Laboratory, Ottawa, Canada, where he worked on scattering, and antenna problems. He joined the staff of the National Bureau of Standards, Boulder Laboratories, Boulder, Colo., in 1956, and is now chief of the Millimeter Wave Research Section.

Dr. Culshaw is a member of the Scientific Research Society of America.

❖

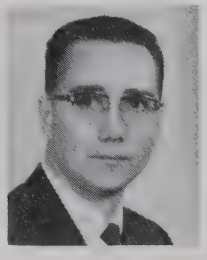

B. C. De Loach, Jr.

Bernard C. De Loach, Jr. (M'57) was born in Birmingham, Ala., on February 19, 1930. He received the B.S. and M.S. degrees from Auburn University, Auburn, Ala., in 1951 and 1952, respectively, and the Ph.D. degree from Ohio State University, Columbus, in 1956, all in physics.

Since 1956, he has been associated with Bell Telephone Laboratories, Holmdel, N. J., where he has been concerned with microwave filters and high-frequency parametric amplifiers.

❖

W. H. Eggimann

Wilhelm H. Eggimann was born in April, 1929, in Zurich, Switzerland. He received the diploma in electrical engineering in 1954 from the Swiss Federal Institute of Technology, Zurich. From 1954 to 56, he worked as an instructor and research assistant at the same institute. In 1956, he entered Case Institute of Technology, Cleveland, Ohio, working as an instructor. He received the M.S.E.E. degree in 1959 from Case Institute, where he is now studying towards the Ph.D. degree. He is presently engaged in research work on ferrites in microwave applications and artificial dielectrics.

Mr. Eggimann is an associate member of Sigma Xi.

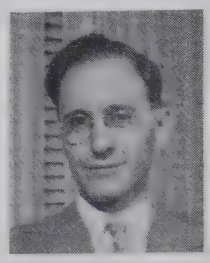

P. Foldes

Peter Foldes (M'58) was born in Budapest, Hungary, on April 8, 1928. He received the B.S. degree in electrical engineering from the Technical University of Budapest in 1950.

From 1950 to 1956, he was a research engineer at the Hungarian Telecommunication Research Institute, and from 1953 to 1956, on a part-time basis, was also a lecturer on antennas at the Technical University of Budapest. In 1957, he joined RCA Victor Company, Ltd., Montreal, Canada, as a project engineer. His work has been mostly in the field of antenna, propagation and system engineering studies. Since 1958, he has been responsible for the theoretical aspects of the microwave subsystem in a wide band microwave communication equipment. Recently he has made some theoretical and experimental investigations on low-noise antenna systems.

❖

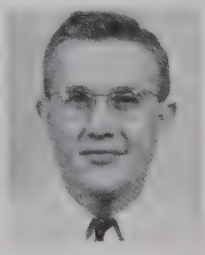

N. Gothard

Nicholas Gothard was born in Pecs, Hungary, in 1933. He received the B.Sc. degree from Budapest Technical University in 1956.

He then came to Canada, where he worked for Radio Communications Equipment and Engineering Ltd., Montreal, and was engaged on development of a radar target simulator. He joined RCA Victor Company, Ltd., in Montreal in 1958, and participated in the design of the MM-600 microwave radio relay equipment, of which he was concerned mainly with the design of antennas, waveguide and RF filters.

❖

D. J. Ilias (M'59) was born in Kymi, Greece, on January 21, 1922. He received the B.S. degree in physics and a post graduate certificate in electronics engineering degree from the University of Athens, Greece, in 1952 and 1953, respectively, and the "diplome d'études supérieure de science physiques" from the Sorbonne, University of Paris, France, in 1959.

From 1952 to 1953 he worked as an assistant at the University of Athens, and

from 1953 to 1956 he was a professor at the Radio-technical School of Athens and also did research work on semiconductors. From 1956 to 1960, he was working in the Laboratorie de Physique de l'Atmosphere, of the Faculty of Sciences, the Sorbonne, where his research concerned microwave spectroscopy. He is now a research physicist in charge of the Ionospheric Institute of Athens observatory.

D. J. Ilias

Mr. Ilias is a member of the Greek Electronics Engineer Association and the Société Francaise des Électronicien et des Radioeléctronicien.

❖

Kenneth M. Johnson, for a photograph and biography, please see page 576 of the September, 1960, issue of these Transactions.

❖

Richard Y. Y. Lee was born on August 26, 1937, in Shanghai, China. He was educated in elementary schools in Shanghai, and graduated from high school in Hong Kong in July, 1955. He spent one year at Taiwan University, Formosa, majoring in electricalengineering, and from February, 1957, to February, 1960, was an undergraduate at The University of Michigan, Ann Arbor, from which he received the B.S.E. degree in electrical engineering and mathematics in 1960. Since February, 1960, he has been a graduate student in physics at The University of Michigan.

R. Y. Y. Lee

He is a member of Eta Kappa Nu, Phi Kappa Phi, the American Physical Society, and an associate member of Sigma Xi.

❖

Enrique A. J. Marcatili (M'56) was born on August 1, 1925, in Argentina. He received the Aeronautical Engineer and Electrical Engineer degrees from the University of Córdoba, Argentina, in 1947 and 1948, respectively.

E. A. J. Marcatili

He joined the technical staff of Bell Telephone Laboratories in 1954 after studies of Cherenkov radiation in Córdoba, and has been engaged in microwave research in Holmdel, N. J. Specifically, Mr. Marcatili has been concerned with theory and design of filters in multimode waveguides and lately with communication systems analysis.

Mr. Marcatili is a member of the Physical Association of Argentina.

❖

Frank A. Olson was born in Boise, Idaho, on February 12, 1933. He received the B.S.E.E. degree from Oregon State College, Corvallis, in 1955, during which time he also received the Westinghouse Achievement Award. He performed graduate studies under Sylvania's Honors Cooperative program and received the M.S. and Ph.D. degrees from Stanford University, Stanford, Calif., in 1957 and 1960, respectively.

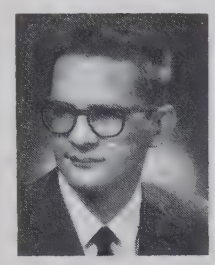

F. A. Olson

In 1955 he joined the Sylvania Electronic Defense Laboratory, Mountain View, Calif., working in the Applied Physics Group which later became the Microwave Physics Laboratory. There, he performed studies on plasmas, crossed-field tubes, and parametric devices. In 1958 he was a research assistant at Stanford Electronics Laboratories, working on parametric circuits. He is presently serving with the USAF at the Cambridge Research Laboratories, Bedford, Mass., engaged in studies of solid-state materials at microwave frequencies, principally the interaction of microwave phonons with ferrimagnetic materials.

Dr. Olson is a member of Sigma Xi, Phi Kappa Phi, Tau Beta Pi, and Eta Kappa Nu.

❖

J. E. Rowe (A'51–M'55) was born in Highland Park, Mich., in 1927. He received the B.S. degree in electrical engineering and in mathematics in 1951, the M.S. degree in electrical engineering in 1952, and the Ph.D. degree in electrical engineering in 1955, all from The University of Michigan, Ann Arbor.

J. E. Rowe

Since 1951, he has been associated with The University of Michigan Research Institute, engaging in fundamental research on microwave systems, microwave devices, electromagnetic field theory and plasmas. Formerly a lecturer, assistant professor, and associate professor of electrical engineering, he is now professor of electrical engineering and Director of the Electron Physics Laboratory at The University of Michigan.

Dr. Rowe is a member of the AIEE, the American Mathematical Society, and the Society for Industrial and Applied Mathematics; also, of Sigma Xi, Phi Kappa Phi, Tau Beta Pi, and Eta Kappa Nu.

❖

Elisabeth M. Rutz (SM'56) was born in Vienna, Austria, on August 28, 1912. She received the Diplom-Ingenieur degree and, in 1946, the Ph.D. degree, in applied physics from the Technical University, Vienna.

E. M. Rutz

In 1938 she joined the Research Laboratories of Siemens and Halske in Berlin, Germany, which later were transferred to Vienna. From 1938 to 1942 she was engaged in research and development of electro-acoustic transducers, and from 1942 to 1948 in research and development of microwave and commercial tubes. From 1950 to 1955 she worked part time as a research scientist at the Universities of Darmstadt, Germany and Aachen, Germany. After coming to the United States in 1955, she joined the Emerson Research Laboratories, Silver Spring, Md., where she first was in charge of research and development of microwave antennas and components. In 1959 she was transferred to the Advanced Systems Department where she is a Fellow Engineer in charge of applied research in the fields of propagation phenomena, microwave antennas and components, and of CW-FW systems.

❖

Sheldon S. Sandler was born in Cleveland, Ohio, on December 17, 1932. He received the B.S.E.E. degree from Case Institute of Technology, Cleveland, Ohio, in 1954. Under a Thomas A. Edison Fellowship at Yale University, New Haven, Conn., he received the M.E.E.E. degree in 1955. In 1958 he received the M.A. degree from Harvard University, Cambridge, Mass.

S. S. Sandler

From 1955 to 1956, he was a research associate in the Department of Physics, Horizons Inc., Cleveland. From 1956 to 1958, he was engaged in graduate study in the Department of Engineering and Applied Physics, Harvard University, Cambridge, Mass. From 1958 to 1959, he was a staff member of M.I.T. Lincoln Laboratory, Lexington, Mass. From 1959 to September, 1960, he was associated with Electronic Communications Inc., Timonium, Md., investigating problems in antenna theory and wave propagation in

ferrites at microwave frequencies. Currently he is a graduate student at Harvard University.

Mr. Sandler is a member of Tau Beta Pi and Eta Kappa Nu.

❖

Louis Stark (M'54–SM'60) was born in Detroit, Mich., on April 5, 1926. He received the B.S.E.E. and M.S.E.E. degrees from the Massachusetts Institute of Technology, Cambridge, in 1950 and 1952, respectively.

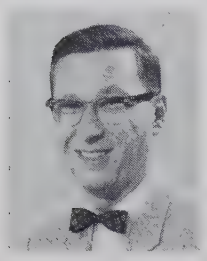

L. Stark

He worked at Hughes Research Laboratories from 1954–1957 on UHF and microwave antenna design. He then joined M.I.T. Lincoln Laboratory, Lexington, Mass., where he was assistant group leader in microwave circuits and antennas. In 1959, he joined Ground Systems Group, Hughes Aircraft Company, Fullerton, Calif., and is now Manager of the Microwave Department.

Mr. Stark is a member of Eta Kappa Nu and Sigma Xi.

❖

James E. Storer (A'54–SM'58) was born on October 26, 1927, in Buffalo, N. Y. He received the B.A. degree in physics from Cornell University, Ithaca, N. Y., in 1947, and the A.M. and Ph.D. degrees in 1948 and 1951, respectively, from the division of engineering sciences and applied physics, Harvard University, Cambridge, Mass.

From 1949 to 1951 he was an Atomic Energy Commission Fellow; from 1951 to 1952 he was a Research Fellow at Harvard, and from 1952 to 1953 a lecturer at Harvard. He was an assistant professor in the division of applied science at Harvard from 1953 to 1957, teaching courses in network analysis, network synthesis, microwave circuits, scattering, and graduate mathematics. He was a Guggenheim Fellow in 1956.

James E. Storer

Prior to joining Sylvania in Waltham, Mass., in 1957, he served as a consultant to the applied research laboratory at Sylvania, performing studies on both electronic countermeasures and airborne pulse-Doppler radar systems. Since becoming a member of the Applied Research Laboratory, he has been concerned with system design studies for electronic countermeasures on the ASD-1 program and on the GLR-4 reconnaissance program. In addition, he has carried out studies on error rates in advanced binary communications systems, secure communications systems, and on optimum correlation codes for long pulse radar. He is the author of several books and papers.

Dr. Storer is a member of Sigma Xi, the American Association of Physics Teachers, and the American Institute of Physics.

❖

Thomas W. Thompson (S'58) was born on May 25, 1936, in Canton, Ohio. He received the B.S. degree in engineering science from Case Institute of Technology of Cleveland, Ohio, in 1958 and the M.E. degree in electrical engineering from Yale University, New Haven, Conn., in 1959.

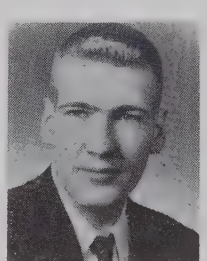

T. W. Thompson

At the present time, he is employed at the Waltham Laboratories of the Sylvania Electric Products, Waltham, Mass., and is engaged in work on a multimode transmission line study.

Mr. Thompson is a member of Sigma Xi and Tau Beta Pi.

❖

Glen Wade (S'51–A'55–SM'57) was born in Ogden, Utah, on March 19, 1921. He served in the U. S. Navy in World War II as an electronics technician and later as an electronics officer. He received the B.S.E.E. and M.S.E.E. degrees from the University of Utah, Salt Lake City, in 1948 and 1949, respectively. After working at the Naval Research Laboratory, Washington, D. C., he returned to graduate studies at Stanford University, Stanford, Calif., where he was first a Sperry Fellow and then an RCA Fellow in electronics. He received the Ph.D. degree from Stanford in 1954, and was then employed as a research associate by the General Electric Microwave Laboratory there.

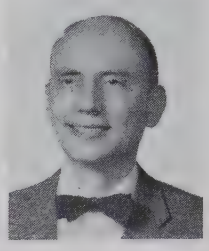

G. Wade

Until recently, he was an associate professor of electrical engineering at Stanford University and a senior staff member of the Stanford Electronics Laboratories. He also served as a consultant for the Zenith Radio Corporation, Philco Corporation, and Diamond Ordnance Fuze Laboratory. Early in 1960, he joined the Raytheon Company, Spencer Laboratory, Burlington, Mass., as associate director of engineering for general research.

Dr. Wade received an Eta Kappa Nu Award for "Outstanding Young Electrical Engineer" in 1955 and a National Electronics Conference Annual Award in 1959. He is a member of the American Physical Society, Phi Kappa Phi, Tau Beta Pi, Eta Kappa Nu, and Sigma Xi.

PGMTT National Symposium

SHERATON PARK HOTEL, WASHINGTON, D.C., MAY 15–17, 1961

Monday Morning

8:00 A.M.
Registration

10:15 A.M.
Opening Address—Robert O. Stone, *Symposium Chairman.*

10:20 A.M.
Keynote Address—Andre G. Clavier, Retired, International Telephone and Telegraph Labs., Nutley, N. J.

10:45 A.M. Session I—Millimeter Waves

Chairman—Robert O. Stone, National Bureau of Standards, Washington, D. C.

10:45 A.M.
"Quasi-Optical, Surface-Waveguide, and Other Components for the 100 to 300 KMC Region," F. Sobel and J. C. Wiltse, Electronic Communications, Inc., Timonium, Md.

Analytical and experimental studies were performed to evaluate various components and techniques from 100 to 300 kMc. Phase-corrected Fresnel zone plates were studied in detail; some properties and applications of these plates are presented.

11:10 A.M.
"A Millimeter Wave Fabry-Perot Maser," W. Culshaw and R. C. Mockler, National Bureau of Standards, Boulder, Colo.

The characteristics and design considerations for the use of a Fabry-Perot resonator as part of a maser are presented. State-selection problems and the minimum number of molecules required for maser oscillation and amplification are discussed.

11:35 A.M.
"Broadband Isolators and Variable Attenuators for Millimeter Frequencies," C. E. Barnes, Bell Telephone Labs., Murray Hill, N. J.

Faraday rotators with rotation independent of frequency in a band greater than 20 per cent centered at 55 kMc have been developed. Broadband isolators and variable attenuators have been designed using these rotators.

Monday Afternoon

2:00 P.M. Session II—Parametric Devices

Chairman—W. W. Mumford, Bell Telephone Labs., Whippany, N. J.

2:00 P.M.
"Transmission Phase Relations of Four-Frequency Parametric Devices," D. B. Anderson and J. C. Aukland, North American Aviation, Anaheim, Calif.

The transmission phase properties of parametric amplifiers are discussed. This matter is of extreme importance in angular detection systems, such as monopulse radars and interferometers, which use parallel signal channels. The analysis follows the matrix representation of a nonlinear capacitive reactance, four-frequency device and is comprehensive in its covering of the various types of parametric amplifiers.

"A Traveling-Wave Parametric Amplifier," T. H. Lee, Lockheed Aircraft Corporation, Sunnyvale, Calif.

This paper presents an analysis of a broad-band traveling-wave parametric amplifier in which the variable capacitance diodes are connected in series with the signal line rather than in shunt, resulting in a structurally and operationally simpler amplifier.

"An Electronically Tuneable Traveling-Wave Parametric Amplifier," R. C. Honey, Stanford Research Inst., Menlo Park, Calif.

This paper discusses a TW parametric amplifier incorporating several novel features which enable it to amplify in a narrow band that can be electronically tuned over a very wide frequency range by changing the pump frequency. A theoretical analysis and a graphical design technique is presented. A completed version with selected pill varactors which is capable of being tuned from very low frequencies to 2.25 kMc is also discussed.

3:15 P.M.
"Practical Design and Performance of Nearly Optimum, Wideband, Degenerate Parametric Amplifiers," M. Gilden and G. L. Matthaei, Stanford Research Inst., Menlo Park, Calif.

The nearly optimum, wideband performance of a single diode, degenerate parametric amplifier is obtained by using a series-resonated diode (rather than shunt) in an almost lumped constant network, and a separate pump resonator which is very lightly coupled to the diode and signal circuits. At 1 kMc, the amplifier offers 15 db midband gain, 1 db double channel noise figure and 20 per cent bandwidth for the two-resonator type compared to 8 per cent using one resonator.

"Design Theory of Up-Converters for Use as Electronically Tuneable Filters," G. Matthaei, Stanford Research Inst., Menlo Park, Calif.

The single diode, upper or lower sideband up-converters discussed use a wideband filter at the signal port, a moderately wide-band filter at the pump port, and a narrow-band filter at the sideband output port, which permit selection of the input signal frequency by varying the pump frequency.

"Passive Phase-Distortionless Parametric Limiters," I. T. Ho and A. E. Siegman, Stanford University, Stanford, Calif.

This paper presents the theoretical analysis and experimental results of a parametric limiter at *S*-band under CW or pulsed excitation. Theoretical expressions for the limiting threshold, bandwidth and dynamic range in terms of varactor diode characteristics are compared with experimental results.

Monday Evening

7:30 P.M.
"The Business of Inventing," Jacob Rabinow, President, Rabinow Engineering Co., Washington, D. C.

Tuesday Morning

9:00 A.M. Session III—Ferrites

Chairman, Frank Reggia, Diamond Ordnance Fuze Lab., Washington, D. C.

9:00 A.M.
"Field Displacement Devices," G. J. Wheeler, Sylvania Electric Products, Mountain View, Calif.

The field displacement effect in a ferrite-loaded waveguide has been utilized to obtain an absorption modulator for high-speed switching or amplitude modulation of microwave energy. This ferrite modulator, when used as a microwave switch, is capable of high isolation and low insertion loss with small magnetic control fields.

9:25 A.M.
"A Field Displacement Isolator at 57 KMC," C. E. Fay and E. F. Kankowski, Bell Telephone Labs., Murray Hill, N. J.

This paper describes a field displacement isolator which makes use of oriented barium ferrite with a very high anisotropic field to considerably reduce the high field requirements of isolators at millimeter wavelengths. This isolator has an insertion loss of approximately 1 db in the forward direction and an isolation of 60 db in the reverse direction over the 56 to 58 kMc frequency range.

9:50 A.M.
"Solid State *X*-band Power Limiter," W. F. Krupke, T. S. Hartwick, and M. T. Weiss, Hughes Aircraft Co., Culver City, Calif.

This paper describes recent ferrite limiter results and reports on a new limiter concept which makes use of a reflection-type diode limiter and a ferrite limiter in tandem. These ferrite-diode combination limiters, which have an operation bandwidth of 700 Mc at X-band, have been successfully operated in the medium power range.

10:30 A.M.
"Frequency Doubling with Planar Ferrites and Isotropic Ferrites with Large Saturation Magnetizations," I. Bady,

USASC Research and Development Lab., Ft. Monmouth, N. J.

Experiments conducted with long thin ferrite slabs in rectangular waveguide show that planar ferrites are more efficient for frequency doubling than isotropic ferrites. This efficiency is increased further by making use of a traveling ring circuit. The fundamental frequencies used for the experiments ranged from 8500 Mc to 9400 Mc.

10:55 A.M.

"Octave Bandwidth UHF/*L*-Band Circulator," F. Arams, B. Kaplan, and B. Peyton, Airborne Instruments Lab., Melville, L. I., N. Y.

A broad-band four-port phase-shift-type circulator for the UHF/*L*-band has been developed which makes use of an aluminum-substituted yttrium-iron-garnet with a low saturation magnetization. This circulator has an insertion loss of 1 db or less, a minimum isolation of 20 db and an input VSWR of approximately 1.15 over the 665 Mc to 1320 Mc frequency range.

11:20 A.M.

"A New Balanced Type Ferrite Switch," T. Kuroda and A. Cho, Nippon Electric, Tokyo, Japan.

This paper describes a reactive microwave switch which makes use of a longitudinally-magnetized ferrite rod in a modified rectangular waveguide system. Two of these reactive ferrite devices are then used in conjunction with two hybrid junctions to obtain a balanced type microwave switch which makes use of noncritical control field and is insensitive to changes in temperature.

Tuesday Afternoon

2:00 P.M. Session IV—High Power Microwave Techniques Panel

Chairman, Clarence Jones, Massachusetts Institute of Technology, Cambridge, Mass.

"Spurious Outputs from High Power Microwave Tubes and Their Control," K. Tomiyasu, General Electric Company, Schenectady, N. Y.

"Windows," D. B. Churchill, Sperry Gyroscope Co., Great Neck, L. I., N. Y.

"High Power Duplexers," E. Muehe, Mass. Inst. Tech., Lincoln Laboratories, Lexington, Mass.

Panel Members

C. R. Beitz, Cornell Aeronautical Lab., Buffalo, N. Y.

J. B. Griemsman, Polytechnic Institute of Brooklyn, Brooklyn, N. Y.

L. Gould, Microwave Associates, Burlington, Mass.

2:00 P.M. Session V—Low-Noise Microwave Amplifiers

Chairman, G. Wade, Raytheon Company, Burlington, Mass.

"Traveling Wave Tubes," D. A. Watkins, Stanford University, Stanford, Calif.

"Parametric Amplifiers," R. D. Weglein, Hughes Aircraft Co., Malibu, Calif.

"Masers," H. E. D. Scovil, Bell Telephone Labs., Murray Hill, N. J.

Panel Members

K. K. N. Chang, RCA Labs., Princeton, N. J.

J. W. Meyer, Mass. Inst. Tech., Cambridge, Mass.

J. Weber, University of Maryland, College Park, Md.

Tuesday Evening

7:00 P.M. **Banquet**

Speaker, Dr. John R. Pierce, Director of Research, Communications Principles, Bell Telephone Labs., Murray Hill, N. J.

Wednesday Morning

9:00 A.M. Session VI—Plasma

Chairman, N. Marcuvitz, Polytechnic Institute of Brooklyn, Brooklyn, N. Y.

9:00 A.M.

"Microwave Instrumentation for Plasma Research," E. G. Schwartz and H. H. Grimm, General Electric Co., Syracuse, N. Y.

Instrumentation has been developed to make extensive microwave measurements on shock introduced plasmas, each of which exists for a small number of milliseconds. The equipment operates at two frequencies, one near 8 kMc and the other near 60 kMc. All the components are capable of withstanding 100 kw peak power levels at 8 kMc.

9:25 A.M.

"Precision Measurements of Plasma Afterglows," E. H. Holt, K. C. Stotz, and S. Pike, Rensselaer Polytechnic Inst., Troy, N. Y.

The general problem of plasma study becomes simplified by the removal of any energy input. The plasma "decays" by processes of radiation and various types of particle interactions. The paper describes a scheme to determine two to three orders of magnitude change in the plasma density by detection of very small rapidly changing phase shifts.

9:50 A.M.

"Electromagnetic Properties of Weakly Ionized Argon" F. L. Tevelow and H. D. Curchack, Diamond Ordnance Fuze Lab., Washington, D. C.

Electromagnetic properties of weakly ionized argon are determined by approximating that the gas is a dielectric slab inclosed in a waveguide. The measurements are made in a shock tube at 10 kMc and are time resolved with total test time less than 300 microseconds. Curves of electron density, complex propagation constant and reflection coefficient are given as a function of distance behind a shock front for shock Mach numbers 7 to 9.

10:30 A.M.

"The Radiation Field and Q of a Resonant Cylindrical Plasma Column," W. D. Hershberger, University of California at Los Angeles, Calif.

A cylindrical plasma column placed across a waveguide or situated in free space in such a fashion that the electric field of an incoming wave is perpendicular to the axis of the column displays a series of resonant responses constituting a reflection and absorption spectrum. The paper discusses the electromagnetic field associated with the assumed electronic motion for the principal member of the spectrum and the factors which determine the width of the resonant response of this member.

10:55 A.M.

"A Plasma Guide Microwave Selective Coupler," W. H. Steier and I. Kaufman, Space Technology Lab., Canoga Park, Calif.

A selective plasma guide coupler is described. The coupling of plasma guide coupler can be continuously varied from less than −40 db to 8.5 db and it is believed that maximum coupling can be increased still further. Pulse power levels of greater than 100 watts at X-band can be handled.

Wednesday Afternoon

1:30 P.M. Session VII—System and Receiver Noise Performance Clinic

Chairman, Herman Haus, Mass. Inst. Tech., Cambridge, Mass.

Speakers

"Measurement of System and Receiver Performance," R. S. Engelbrecht, Bell Telephone Labs., Whippany, N. J.

The concept of operating noise temperature is employed in order to compare the noise performance of various receiving systems in terms of their environment (sky noise, etc.), component characteristics (noise figure, effective input noise temperature, gain, bandwidth, etc.), and intended use (one or two channel, radar or radiometry, etc.).

"Some Typical Examples," Robert Adler, Zenith Radio Corporation, Chicago, Ill.

Parametric amplifiers accept signal and noise inputs on more than one channel. To evaluate their weak-signal performance in a given installation we must know not only about the amplifier itself but also about the antenna system and the type of signal. The last two factors have surprisingly large effects and may swing the balance in favor of one or another type of amplifier. This is illustrated by practical examples.

"Commentary on Methods of Measurements," M. T. Lebenbaum, Airborne Instruments Lab., Melville, L. I., N. Y.

The general methods of noise figure measurement will be briefly reviewed. The special problems introduced by the peculiarities of negative resistance devices are emphasized, and some precautions suggested. Hot and cold body loads for measurement of very low noise temperature systems are described.

INSTITUTIONAL LISTINGS

The IRE Professional Group on Microwave Theory and Techniques is grateful for the assistance given by the firms listed below, and invites application for Institutional Listing from other firms interested in the Microwave field.

AIRTRON, INC.
A Division of Litton Industries
200 East Hanover Ave., Morris Plains, N.J.

Designers and Producers of Complete Line of Microwave Electronic and Aircraft Components

ALFORD MANUFACTURING COMPANY
299 Atlantic Ave., Boston 10, Mass.

RF Instruments, Coaxial Components, Antennas and Air Navigation Aids

CASCADE RESEARCH
Div. of Lewis & Kaufman Electronics Corp.
5245 San Fernando Rd., Los Angeles, Calif.

Research, Development, Production: Microwave Ferrite Devices, Microwave Components & Subsystems

EIMAC TUBES, EITEL-McCULLOUGH, INC.
301 Industrial Way, San Carlos, Calif.

Microwave Tubes, TWT-VTM-Reflex Klystrons, Power Grid Tubes, Amplifier Klystrons

FXR, INC.
25-26 50th Street, Woodside 77, N.Y.

Precision Microwave Test Equipment, High Power Microwave Electronics, Microwave Components & Instrumentation

HUGHES AIRCRAFT CO.
Florence and Teale Sts., Culver City, Calif.

Res., Dev., Mfg.: Radar Systems and Components, Microwave Devices and Components, Antennas, Tubes

ITT FEDERAL LABORATORIES
500 Washington Ave., Nutley 10, N.J.

Line-of-Sight and Over-the-Horizon Microwave Systems; Test Equipment and Components

MICROWAVE ASSOCIATES, INC.
South Avenue, Burlington, Mass.

Waveguide Devices, Microwave Diodes, Magnetrons, Duplexers, TWT's, Ferrite & Solid-State Devices

(See outside back cover for additional listings.)

The charge for an Institutional Listing is $50.00 per issue or $210.00 for six consecutive issues. Applications for Institutional Listings and checks (made out to The Institute of Radio Engineers, Inc.) should be sent to Robert A. Rivers, PGMTT Advertising Editor, Aircom Inc., 354 Main St., Winthrop 52, Mass.

INSTITUTIONAL LISTINGS

(See inside back cover for additional listings.)